**Band**
**434**

Verlagsschriftenreihe des Heinz Nixdorf Instituts
Prof. Dr.-Ing. Christoph Scheytt (Hrsg.)
Schaltungstechnik

Stephan Kruse

# Photonic Radar Circuits and Systems for Coherent mm-Wave Large Aperture Phased Array MIMO Systems

HEINZ NIXDORF INSTITUT
UNIVERSITÄT PADERBORN

Stephan Kruse

# Photonische Radar Schaltungen und Systeme für Kohärente mm-Wellen Phasengesteuerte MIMO Systeme mit Großer Apertur

# Photonic Radar Circuits and Systems for Coherent mm-Wave Large Aperture Phased Array MIMO Systems

**Bibliografische Information Der Deutschen Bibliothek**
Die Deutsche Bibliothek verzeichnet diese Publikation in der Deutschen Nationalbibliografie detaillierte bibliografische Daten sind im Internet über `http://dnb.ddb.de` abrufbar

Band 434 der Verlagsschriftenreihe des Heinz Nixdorf Instituts

ISSN (Online): 2365-4422
ISBN: 978-3-947647-53-8

Satz und Gestaltung: Stephan Kruse

UNIVERSITÄT
PADERBORN

FAKULTÄT FÜR
ELEKTROTECHNIK,
INFORMATIK UND
MATHEMATIK

# Photonic Radar Circuits and Systems for Coherent mm-Wave Phased Array MIMO Systems

Von der Fakultät für Elektrotechnik, Informatik und Mathematik
der Universität Paderborn

zur Erlangung des akademischen Grades

Doktor der Ingenieurwissenschaften (Dr.-Ing.)

genehmigte Dissertation

von

Stephan Kruse, M. Sc.

Erster Gutachter: Prof. Dr.-Ing. J. Christoph Scheytt
Zweiter Gutachter: Prof. Dr.-Ing. Vadim Issakov

Tag der mündlichen Prüfung: 11.02.2026

Paderborn 2026

Diss. EIM-E/396

# Declaration of Authorship

I, Stephan Kruse, declare that this thesis titled, “Photonic Radar Circuits and Systems for Coherent mm-Wave Large Aperture Phased Array MIMO Systems” and the work presented in it are my own. I confirm that:

- This work was done wholly or mainly while in candidature for a research degree at this University.
- Where any part of this thesis has previously been submitted for a degree or any other qualification at this University or any other institution, this has been clearly stated.
- Where I have consulted the published work of others, this is always clearly attributed.
- Where I have quoted from the work of others, the source is always given. With the exception of such quotations, this thesis is entirely my own work.
- I have acknowledged all main sources of help.
- Where the thesis is based on work done by myself jointly with others, I have made clear exactly what was done by others and what I have contributed myself.

Signed: Stephan Kruse

Date: 11.11.2025

The following artificial intelligence tools have been used for the creation of this thesis:
Die folgenden künstlichen Intelligenzen wurden für die Erstellung dieser Arbeit genutzt:

| Producer<br>Hersteller | Name<br>Name | Model<br>Modell | Usage<br>Einsatz |
|---|---|---|---|
| Microsoft | Copilot | GPT-5 | Spelling, grammar and wording improvement.<br>Verbesserung von Rechtschreibung, Grammatik und Formulierung. |

# Vorwort

**1965** schrieb Gordon E. Moore: "Selbst im Mikrowellenbereich werden die Strukturen, die in der Definition der integrierten Elektronik enthalten sind, immer wichtiger werden. Die Fähigkeit, Komponenten herzustellen und zu montieren, die im Vergleich zu den beteiligten Wellenlängen klein sind, wird zumindest bei den niedrigeren Frequenzen den Einsatz von Design mit pauschalen Parametern ermöglichen. Zum jetzigen Zeitpunkt lässt sich nur schwer vorhersagen, in welchem Umfang die integrierte Elektronik in den Mikrowellenbereich vordringen wird. Die erfolgreiche Realisierung von z.B. Phased-Array-Antennen, die eine Vielzahl von integrierten Mikrowellenstromquellen nutzen, könnte das Radar völlig revolutionieren.' [1].

Heute, 60 Jahre später, wissen wir, dass Moores Vorhersage richtig war. Radar ist allgegenwärtig geworden, mit Anwendungen, die von der adaptiven Geschwindigkeitsregelung (ACC) [2] und der Notbremsunterstützung [3] in der Automobilindustrie über Wetterradarsysteme [4] bis hin zu zahlreichen industriellen Anwendungen reichen, wie z. B. der Füllstandsmessung in Tanks [5], der Materialcharakterisierung [6] und der Schwingungsüberwachung in Windturbinenblättern [7]. Man kann mit Fug und Recht behaupten, dass die Radartechnologie heute in fast alle Bereiche des täglichen Lebens integriert ist.

Eine wesentliche Einschränkung der modernen Radarsysteme ist die Winkelauflösung. Nach dem heuristischen Rayleigh-Kriterium ist der Winkelradius $\theta$ der zentralen Scheibe gegeben durch

$$\theta \approx 1.2197 \frac{\lambda}{2R} \tag{1}$$

wobei $\lambda$ die Wellenlänge des Lichts und $2R$ den (Durchmesser der) Apertur darstellt' [8]. In Phased-Array-/multiple input multiple output (MIMO)-Radarsystemen wird der Durchmesser der Apertur durch erhebliche Übertragungsverluste eingeschränkt. 60 Jahre nach Moores ursprünglicher Vorhersage haben wir jedoch nicht nur die Integration von Elektronik, sondern auch die gemeinsame Integration von Elektronik und Photonik auf einem einzigen Siliziumchip erreicht. Da faseroptische Verbindungen im Vergleich zu ihren elektronischen Gegenstücken deutlich geringere Verluste aufweisen, ermöglicht dieser Ansatz die Realisierung von Phased-Array/MIMO-Radarsystemen mit großer Aperture in nahezu beliebigem Maßstab.

Aufbauend auf den in dieser Arbeit präsentierten Erkenntnissen und unter Ausnutzung moderner technologischer Fortschritte kann Moores Vorhersage wie folgt umformuliert werden: Die Kombination von Photonik und Mikrowellenelektronik wird zunehmend an Bedeutung gewinnen. Inwieweit die Integration von Elektronik und Photonik auf einem einzigen Chip den Mikrowellenbereich beeinflussen wird, lässt sich zum jetzigen Zeitpunkt nur schwer vorhersagen. Die erfolgreiche Realisierung von kostengünstigen elektronisch-photonischen Radarchips mit hoher Ausbeute und erschwinglichen Faser-Chip-Verbindungen könnte jedoch beispielsweise das Radar völlig revolutionieren.

*— Stephan Kruse*
*November 2025*
*Paderborn*

# Preface

In 1965, Gordon E. Moore wrote: 'Even in the microwave area, structures included in the definition of integrated electronics will become increasingly important. The ability to make and assemble components small compared with the wavelengths involved will allow the use of lumped parameter design, at least at the lower frequencies. It is difficult to predict at the present time just how extensive the invasion of the microwave area by integrated electronics will be. The successful realization of such items as phased-array antennas, for example, using a multiplicity of integrated microwave power sources, could completely revolutionize radar.' [1].

Today, 60 years later, we know that Moore's prediction was accurate. Radar has become ubiquitous, with applications ranging from adaptive cruise control (ACC) [2] and emergency braking assistance [3] in the automotive industry, to weather radar systems [4], and numerous industrial uses such as tank level probing [5], material characterization [6], and vibration monitoring in wind turbine blades [7]. One could reasonably claim that radar technology is now embedded in nearly every facet of daily life.

A major limitation of state-of-the-art radar systems is angular resolution. According to the heuristic Rayleigh criterion, 'the angular radius $\theta$ of the central disk is given by

$$\theta \approx 1.2197 \frac{\lambda}{2R} \tag{2}$$

in which $\lambda$ represents the wavelength of the light, and $2R$ the (diameter of the) aperture' [8]. In phased-array/MIMO radar systems, the aperture diameter is constrained by substantial transmission losses. However, 60 years after Moore's original forecast, we have not only achieved the integration of electronics but also the co-integration of electronics and photonics within a single silicon chip [9]. Because fiber-optic interconnects exhibit significantly lower losses compared to their electronic counterparts, this approach enables the realization of large-aperture phased-array/MIMO radar systems at nearly arbitrary scales.

Building on the findings presented in this work and leveraging modern technological advances, Moore's prediction can be reformulated as follows:

Combining photonics with microwave electronics will become increasingly important. It is difficult to predict at the present time how far the integration of electronics and photonics into a single chip will influence the microwave domain. However, the successful realization of low-cost, high-yield electronic-photonic radar chips and affordable fiber-to-chip connections could, for example, completely revolutionize radar.

*— Stephan Kruse*
*November 2025*
*Paderborn*

# List of Publications

## Journal Publications

- S. Kruse, S. Gudyriev, T. Schwabe, P. Kneuper, H. G. Kurz, and J. C. Scheytt, “Silicon Photonic Radar Transmitter IC for mm-Wave Large Aperture MIMO Radar Using Optical Clock Distribution,” *IEEE Microwave and Wireless Components Letters*, vol. 31, no. 6, pp. 783–786, 2021. DOI: `10.1109/LMWC.2021.3062112`
- S. Kruse, S. Gudyriev, P. Kneuper, T. Schwabe, M.-M. Meinecke, H. G. Kurz, et al., “Silicon Photonic Radar Receiver IC for mm-Wave Large Aperture MIMO Radar Using Optical Clock Distribution,” *IEEE Microwave and Wireless Components Letters*, vol. 32, no. 12, pp. 1447–1450, 2022. DOI: `10.1109/LMWC.2022.3186432`
- S. Kruse, J. C. Greitens, T. Schwabe, P. Kneuper, M.-M. Meinecke, H. G. Kurz, et al., “A Narrowband Four-Quadrant Electro-Optical Mixer for Microwave Photonics,” *IEEE Microwave and Wireless Technology Letters*, vol. 33, no. 11, pp. 1552–1555, 2023. DOI: `10.1109/LMWT.2023.3315315`
- S. Kruse, L. Serino, P. Folge, D. E. Oviedo, A. Bhattacharjee, M. Stefszky, et al., “A Pulsed Lidar System With Ultimate Quantum Range Accuracy,” *IEEE Photonics Technology Letters*, vol. 35, no. 14, pp. 769–772, 2023. DOI: `10.1109/LPT.2023.3277515`
- T. Schwabe, C. Kress, B. Sadiye, S. Kruse, and J. Christoph Scheytt, “Analysis and Design of Forward Biased Silicon Photonics Phase Shifter Equalizer Circuits,” *IEEE Access*, pp. 1–1, 2025. DOI: `10.1109/ACCESS.2025.3629385`
- T. Schwabe, C. Kress, S. Kruse, M. Weizel, H. Rhee, and J. C. Scheytt, “Forward-Biased Silicon Phase Shifter Modeling for Electronic-Photonic Co-Simulation and Validation in a 250 nm EPIC BiCMOS Technology,” *Journal of Lightwave Technology*, vol. 43, no. 1, pp. 255–270, 2025. DOI: `10.1109/JLT.2024.3450949`
- M. S. Amjad, C. Tebruegge, A. Memedi, S. Kruse, C. Kress, J. C. Scheytt, et al., “Towards an IEEE 802.11 Compliant System for Outdoor Vehicular Visible Light Communications,” *IEEE Transactions on Vehicular Technology*, vol. 70, no. 6, pp. 5749–5761, 2021. DOI: `10.1109/TVT.2021.3075301`

## Conference Publications

- S. Kruse, P. Kneuper, T. Schwabe, H. G. Kurz, M.-M. Meinecke, M. A. Gonzalez-Huici, et al., “Phase Noise Analysis of Photonic Radar Systems with Optical LO Distribution,” in *ICMIM 2024; 7th IEEE MTT Conference*, 2024, pp. 57–60
- S. Kruse, J. Brockmeier, P. Kneuper, T. Schwabe, H. G. Kurz, M.-M. Meinecke, et al., “Doppler Analysis of a Lidar-Photonic Radar Combined Sensor System,” in *2024 International Radar Symposium (IRS)*, 2024, pp. 70–73

- S. Kruse, T. Schwabe, P. Kneuper, H. G. Kurz, M.-M. Meinecke, and J. C. Scheytt, "Analysis and Simulation of a Photonic Multiband FMCW Radar Sensor System Using Nyquist Pulses," in *2024 15th German Microwave Conference (GeMiC)*, 2024, pp. 201–204. doi: `10.23919/GeMiC59120.2024.10485320`
- S. Kruse, M.-M. Meinecke, P. Kneuper, T. Schwabe, H. G. Kurz, and J. C. Scheytt, "Analysis and Simulation of a Coherent FMCW Lidar-Photonic Radar Combined Sensor System for Large Aperture Phased Array MIMO," in *2023 20th European Radar Conference (EuRAD)*, 2023, pp. 419–422. doi: `10.23919/EuRAD58043.2023.10289439`
- S. Kruse, P. Kneuper, T. Schwabe, M.-M. Meinecke, H. G. Kurz, and J. C. Scheytt, "Distributed System Architecture for Software-Defined Radio / Radar with Optical Signal Distribution," in *2023 24th International Radar Symposium (IRS)*, 2023, pp. 1–8. doi: `10.23919/IRS57608.2023.10172470`
- C. Greiff, D. Mateos-Núñez, R. Simoni, M. González-Huici, S. Kruse, J. C. Scheytt, et al., "Calibration of Large Coherent MIMO Radar Arrays: Channel Imbalances and 3D Antenna Positions," in *2023 24th International Radar Symposium (IRS)*, 2023, pp. 1–10. doi: `10.23919/IRS57608.2023.10172475`
- S. Kruse, T. Schwabe, P. Kneuper, M.-M. Meinecke, H. G. Kurz, and J. Christoph Scheytt, "Nonlinear S-Parameter Behavioral Model of a Photonic Radar Transceiver Chipset for Automotive Applications," in *2023 24th International Radar Symposium (IRS)*, 2023, pp. 1–10. doi: `10.23919/IRS57608.2023.10172395`
- S. Kruse, C. Kress, H. G. Kurz, T. Schneider, and J. C. Scheytt, "Analysis and Simulation of a Wireless Phased Array System with Optical Carrier Distribution and an Optical IQ Return Path," in *2020 German Microwave Conference (GeMiC)*, 2020, pp. 140–143
- S. Kruse, M. Bahmanian, P. Kneuper, C. Kress, H. G. Kurz, T. Schneider, et al., "Phase Noise Investigation for a Radar System with Optical Clock Distribution," in *2020 17th European Radar Conference (EuRAD)*, 2021, pp. 26–29. doi: `10.1109/EuRAD48048.2021.00018`
- S. Kruse, J. C. Scheytt, and H. G. Kurz, "An Area Efficient 19.25 GHz to 77 GHz Gilbert Cell Frequency Quadrupler with 55% Shrinked Delay Lines in 130nm SiGe BiCMOS," in *2019 IEEE MTT-S International Microwave and RF Conference (IMARC)*, 2019, pp. 1–5. doi: `10.1109/IMaRC45935.2019.9118726`
- V. S. Shroff, M. Bahmanian, S. Kruse, and J. C. Scheytt, "Design of an Ultra-Low Phase Noise Broadband Amplifier in 130 nm SiGe BiCMOS Technology," in *2024 IEEE BiCMOS and Compound Semiconductor Integrated Circuits and Technology Symposium (BCICTS)*, 2024, pp. 262–265. doi: `10.1109/BCICTS59662.2024.10745663`
- T. Mager, J. Diri, P. Kneuper, S. Kruse, and C. Scheytt, "Integration of a 77GHz automotive radar system into plastic surfaces using MID-technology," in *AmEC 2024 – Automotive meets Electronics & Control; 14. GMM Symposium*, 2024, pp. 89–94
- S. Kruse, M. Bahmanian, S. F. Fard, M.-M. Meinecke, H. G. Kurz, and J. C. Scheytt, "A Low Phase Noise 77 GHz Frequency Synthesizer for Long Range

Radar," in *2022 19th European Radar Conference (EuRAD)*, 2022, pp. 289–292. DOI: `10.23919/EuRAD54643.2022.9924677`

- S. Abughannam, S. Kruse, M. Iftekhar, and J. C. Scheytt, "Design and Measurements of a Low-power Low-Date-rate Direct-detection Wireless Receiver with Improved Co-channel Interference Robustness," in *2022 14th German Microwave Conference (GeMiC)*, 2022, pp. 192–195

- P. Kneuper, S. Kruse, B. Luchterhandt, J. Tünnermann, I. Scharlau, and J. C. Scheytt, "Sensory Substitution Device for the Visually Impaired Using 122 GHz Radar and Tactile Feedback," in *2020 17th European Radar Conference (EuRAD)*, 2021, pp. 90–93. DOI: `10.1109/EuRAD48048.2021.00034`

- M. S. Amjad, C. Tebruegge, A. Memedi, S. Kruse, C. Kress, C. Scheytt, et al., "An IEEE 802.11 Compliant SDR-Based System for Vehicular Visible Light Communications," in *ICC 2019 - 2019 IEEE International Conference on Communications (ICC)*, 2019, pp. 1–6. DOI: `10.1109/ICC.2019.8761960`

- J. Koepe, C. Kaltschmidt, M. Illian, R. Puknat, P. Kneuper, S. Wittemeier, et al., "Poster: First Performance Insights on Our Novel OFDM-based Vehicular VLC Prototype," in *2018 IEEE Vehicular Networking Conference (VNC)*, 2018, pp. 1–2. DOI: `10.1109/VNC.2018.8628322`

- S. Kruse, V. S. Shroff, M. Bahmanian, J. Brockmeier, and J. C. Scheytt, "An Ultra Low Phase Noise Frequency Synthesizer with Optical Output for 77 GHz Photonic Radar," in *2025 16th German Microwave Conference (GeMiC)*, 2025, pp. 148–151. DOI: `10.23919/GeMiC64734.2025.10979013`

- S. Kruse, J. Brockmeier, T. Schwabe, and J. C. Scheytt, "A Visible Light FMCW Lidar System Based on LEDs," in *2025 16th German Microwave Conference (GeMiC)*, 2025, pp. 372–375. DOI: `10.23919/GeMiC64734.2025.10979119`

- J. Brockmeier, S. Kruse, and J. C. Scheytt, "A Mach-Zehnder-Modulator based FMCW Lidar Emulator in C-Band," in *2025 16th German Microwave Conference (GeMiC)*, 2025, pp. 49–52. DOI: `10.23919/GeMiC64734.2025.10979164`

- S. Kruse, J. Diri, T. Mager, C. Kress, and J. C. Scheytt, "Electrooptical Integration of an Electronic Photonic Integrated Circuit into Plastic Substrates using MID-Technology," in *2025 55th European Microwave Conference (EuMC)*, 2025, pp. 1–4

- S. Kruse, J. Brockmeier, S. Max, S. Tobias, and J. C. Scheytt, "A Photonic Assisted Visible Light FMCW Lidar System for Large Aperture Phased Array MIMO Based on LEDs," in *2025 55th European Microwave Conference (EuMC)*, 2025, pp. 1–4

## Patents Granted

- S. KRUSE and J. C. SCHEYTT, "Elektrooptischer Balun und System zur Generierung eines pseudodifferentiellen Signals aufweisend einen solchen elektrooptischen Balun," DE102022201069B4, 2022

- S. KRUSE and J. C. SCHEYTT, "Elektrooptischer Mischer," DE102022201070B4, 2023

- M.-M. Meinecke, H. G. Kurz, C. Scheytt, and S. Kruse, “Verfahren zum Betreiben einer elektrooptischen Übertragungsvorrichtung für beliebige Signale, Computerprogrammprodukt sowie Datenübertragungsvorrichtung,” DE102022201312B4, 2022
- S. KRUSE and J. C. SCHEYTT, “Optoelektronischer Oszillator und Anordnung mehrerer elektrooptischer Wandlereinheiten weiterhin aufweisendend einen solchen optoelektronischen Oszillator,” DE102022214163B4, 2022
- S. KRUSE and J. C. SCHEYTT, “Elektrooptische PLL,” DE102023203698B4, 2023
- H. G. Kurz, M.-M. Meinecke, T. Schwabe, S. Kruse, and C. Scheytt, “Mehrband-Software-Defined-Radio-System zur Umfelderfassung, sowie Verfahren und Kraftfahrzeug,” DE102023204352B4, 2023
- C. Silberhorn, B. Brecht, and S. Kruse, “Optisch basierter Analog-Digital-Umsetzer,” DE102023209622B3, 2023
- C. Silberhorn, B. Brecht, S. Kruse, and T. Schwabe, “Optisch basierter Digital-Analog-Umsetzer,” DE102023212604B3, 2023

## Patents Pending

- S. KRUSE and J. C. SCHEYTT, “System mit optischer Trägerverteilung,” DE102020202771A1, 2020
- S. KRUSE and J. C. SCHEYTT, “Elektrooptischer Regelkreis,” DE102020207050A1, 2020
- S. KRUSE and J. C. SCHEYTT, “Elektrooptischer Mischer,” DE102020213283A1, 2020
- S. Kruse, C. Scheytt, M.-M. Meinecke, and H. G. Kurz, “Funk-Optisches Sensorsystem für die Umfelderfassung,” DE102022212165A1, 2022
- M.-M. Meinecke, A. Aal, H. Kurz, S. Kruse, and C. Scheytt, “Radarsystem mit CMOS-Elektronikkomponenten,” DE102023200606A1, 2023
- B. Brecht, C. Silberhorn, S. Kruse, and L. Serino, “Quantenoptisch-unterstütztes Sende-/Empfangssystem,” DE102023203697A1, 2023
- H. G. Kurz, M.-M. Meinecke, T. Schwabe, S. Kruse, and C. Scheytt, “Mehrband-Sensorsystem zur Umfelderfassung, sowie Verfahren und Kraftfahrzeug,” DE102023204354A1, 2023
- M.-M. Meinecke, H. G. Kurz, T. Gisder, S. Kruse, and C. Scheytt, “Verfahren zum Erzeugen eines frequenzmodulierten Sendesignals für eine Sendeeinrichtung, Computerprogrammprodukt, computerlesbares Speichermedium, Sendeeinrichtung sowie Detektionsvorrichtung,” DE102023205100A1, 2023
- M.-M. Meinecke, T. Gisder, R. Simoni, M. A. González-Huici, C. Greiff, D. Mateos-Nunez, et al., “Antennenvorrichtung zum Aussenden von elektromagnetischer Strahlung für ein Kraftfahrzeug sowie Kraftfahrzeug,” DE102023208400A1, 2023

- S. KRUSE and J. C. SCHEYTT, "ELEKTROOPTISCHER MISCHER," EP000004457561A1, 2023
- S. Kruse and C. Scheytt, "OPTOELEKTRONISCHER OSZILLATOR," EP000004639762A1, 2024
- H. G. Kurz, T. Gisder, M.-M. Meinecke, S. Kruse, and C. Scheytt, "Sendeempfängeranordnung und Verfahren zum Betreiben einer Sendeempfängeranordnung," DE102024206575A1, 2024
- H. G. Kurz, T. Gisder, M.-M. Meinecke, S. Kruse, and C. Scheytt, "Sensorfrontend, Sensorsystem und Verfahren zum Betreiben eines Sensorfrontends," DE102024206576A1, 2024

## Supervised Bachelor Theses

- O. Reimer, "Design and Implementation of a Hardware Frontend for Space Division Multiple Access in Vehicular Visible Light Communication Systems," Paderborn University, 2020
- C. Benefader, "Beiträge zur Mikrowelleninduzierten Hyperthermie zur Bekämpfung von Karzinomen mittels optischer Taktverteilung," Paderborn University, 2021
- M. J. Wigand, "Design and Implementation of a Single-Beam 1550 nm FMCW LiDAR Transceiver System," Paderborn University, 2022
- A. Makejkin, "Entwurf und Implementierung einer digitalen Mikrocontroller-basierten Echtzeit Übertragungsstrecke mit sichtbarem Licht," Paderborn University, 2025

## Supervised Master Theses

- J. Okocha, "77 GHz Downconversion IQ Mixer in SiGe BiCMOS for Automotive Radar Applications," M.S. thesis, Paderborn University, 2019
- A. H. Venkateshaiah, "Design and Designmethodology of Broadband Integrated Baluns for E- and W-Band using SiGe BiCMOS Technology," M.S. thesis, Paderborn University, 2019
- M. Ritter, "Entwurf und Entwurfsmethodik eines 154 GHz-Leistungsverstärkers mit integrierter Sendeantenne in einer 250 nm SiGe BiCMOS Technologie," M.S. thesis, Paderborn University, 2019
- A. Balke, "Selbstdiagnose von Radarkomponenten mithilfe eines Leistungsdetektors bei 77 GHz," M.S. thesis, Paderborn University, 2019
- P. Kneuper, "Design and Designmethodology of a 154 GHz Radar Front-End in a 45 nm RF SOI CMOS Technology," M.S. thesis, Paderborn University, 2020
- J.-C. Greitens, "Design of Critical Components of a 77 GHz Radar Front-End in a 22 nm FD-SOI CMOS Technology," M.S. thesis, Paderborn University, 2022

- J. Brockmeier, “Design and Implementation of a Radar-LiDAR Receiver with Optical Phased Array and IQ Downconversion Mixer in 45 nm CMOS SOI,” M.S. thesis, Paderborn University, 2023
- M. Schwengelbeck, “Design and Designmethodology of an Ultra-Low Phase Noise 240 GHz OFDM Transmitter for 6G Distributed MIMO Applications,” M.S. thesis, Paderborn University, 2025

# Zusammenfassung

*Photonische Radar Schaltungen und Systeme für Kohärente mm-Wellen Phasengesteuerte MIMO Systeme mit Großer Appertur*

Die Winkelauflösung einer phasengesteuerten Gruppenantenne ist umgekehrt proportional zur Aperturgröße. Die hohen elektrischen Verluste begrenzen die Aperturgröße moderner rein elektronischer Radarsysteme auf wenige cm. Dies stellt ein erhebliches Problem für eine Vielzahl von Anwendungen dar, insbesondere für Radarsysteme mit einer hohen Winkelauflösung.

In dieser Doktorarbeit werden verschiedene neuartige photonische Radarsysteme vorgestellt und mathematisch analysiert. Darüber hinaus werden die unterschiedlichen Systeme in der optischen Entwurfsumgebung Lumerical Interconnect simuliert. Da alle weiteren vorgestellten photonischen Radararchitekturen auf dem FMCW-MIMO-Radarsystem mit optischer LO-Verteilung und optischem Rückpfad basieren, wird dieses System ebenfalls in der elektrischen Entwurfsumgebung ADS simuliert.

Nach einer erfolgreichen Analyse werden neuartige Schaltungstopologien für die verschiedenen photonischen Radarsysteme vorgestellt, darunter ein neuartiger optoelektronischer Mischer. Anschließend wird der weltweit erste Transceiver-Chipsatz eines photonischen Radarsystems mit optischer LO-Verteilung präsentiert. Ein darauf basierender Demonstrator mit einer Aperturgröße von $50\,\mathrm{cm}$ erzielt eine Winkelauflösung von $0.4°$, was nahe an der theoretisch möglichen Grenze von $0.3°$ liegt.

Im Anhang dieser Arbeit werden zudem zwei $77\,\mathrm{GHz}$-Frequenzsynthesizer mit extrem niedrigem Phasenrauschen vorgestellt – einer mit optischem Ausgang, der andere mit elektrischem Ausgang. Darüber hinaus enthält der Anhang weiterführende mathematische Betrachtungen.

# Abstract

*Photonic Radar Circuits and Systems for Coherent mm-Wave*
*Large Aperture Phased Array MIMO Systems*

The angular resolution of a phased array antenna is inversely proportional to it's aperture size. The high electrical losses limit the aperture size of modern all-electric radar systems to a few $\mathrm{cm}$. This poses a significant problem for a variety of applications, especially for high resolution radar systems.

In this doctoral thesis, various novel photonic radar systems are presented and mathematically analyzed. Furthermore, the different systems are simulated in the optical design environment Lumerical Interconnect. Since all other photonic radar architectures presented are based on the FMCW MIMO radar system with optical LO distribution and optical return path, this system is also simulated in the electrical design environment ADS.

After a successful analysis, novel circuit topologies for the different photonic radar systems will be presented, including an novel optoelectronic mixer. Subsequently, the first transceiver chipset of a photonic radar system with optical LO distribution will be presented. A demonstrator based on this chipset, with an aperture size of $50\,\mathrm{cm}$, achieves an angular resolution of $0.4^\circ$, which is close to the theoretically possible limit of $0.3^\circ$.

The appendix of this work also presents two $77\,\mathrm{GHz}$ frequency synthesizers with extremely low phase noise - one with an optical output, the other with an electrical output. In addition, the appendix contains further mathematical considerations.

# Acknowledgements

An dieser Stelle möchte ich einfach einmal Danke sagen. Mein besonderer Dank gilt Prof. Dr. Christoph Scheytt, der mir überhaupt erst die Möglichkeit eröffnet hat, meine Doktorarbeit in seinem Fachgebiet zu schreiben. Zudem danke ich ihm für das kritische Gegenlesen meiner Publikationen sowie seine wertvollen Optimierungsvorschläge.

Darüber hinaus möchte ich mich herzlich bei meinen Kolleginnen und Kollegen für die inspirierenden Diskussionen bedanken. Ein besonderer Dank geht an meinen Bürokollegen Tobias Schwabe sowie an Pascal Kneuper, Jan Brockmeier, Christian Kress, Vijayalakshmi Surendranath Shroff, Sergiy Gudyriev und Meysam Bahmanian.

Schließlich möchte ich meinen Eltern, Brigitte und Dr. Karl-Heinz Kruse, sowie meinen leider bereits verstorbenen Großeltern, Anna (genannt Anni) und Bernhard Holtgrewe, meinen tiefsten Dank aussprechen. Ohne ihre wertvolle Unterstützung wäre ich heute nicht dort, wo ich bin.

# Contents

*Photonic Radar Circuits and Systems for Coherent mm-Wave Large Aperture Phased Array MIMO Systems*

# List of Figures

# List of Abbreviations

| | |
|---|---|
| AD | analog to digital. |
| ADC | analog to digital converter. |
| ADS | Advanced Design System. |
| AM | amplitude modulation. |
| BB | baseband. |
| BiCMOS | bipolar complementary metal-oxide-semiconductor. |
| BP | band pass. |
| BPF | band-pass-filter. |
| BW | bandwidth. |
| CB | common base. |
| CE | common emitter. |
| CG | common gate. |
| CMOS | complementary metal-oxide-semiconductor. |
| CS | common source. |
| CW | continuous wave. |
| DDS | direct digital synthesizer. |
| DSP | digital signal processor. |
| DUT | device under test. |
| EDE | electronic design environment. |
| EO | electro-optical. |
| EOE | electro-opto-electronical. |
| EPIC | electronic photonic interated circuits. |
| ESD | electrostatic discharge. |
| FET | field-effect transistor. |
| FFT | fast fourier transform. |
| FMCW | freqeuncy modulated continous wave. |
| FPGA | field programmable gate array. |
| GC | grating coupler. |
| GSG | ground signal ground. |
| GSGSG | ground signal ground signal ground. |
| GSSG | ground signal signal ground. |
| GSSGSSG | ground signal signal ground signal signal ground. |
| HBT | Heterojunction bipolar transistor. |
| I | in phase. |

| | |
|---|---|
| IF | intermediate frequency. |
| IQ | in phase quadrature phase. |
| LD | laser diode. |
| LNA | low noise amplifier. |
| LO | local oscilator. |
| LPF | low-pass-filter. |
| MIMO | multiple input multiple output. |
| MLL | mode locked laser. |
| MMI | multimode interferometer. |
| MOS | metal oxide semiconductor. |
| MZM | Mach-Zehnder modulator. |
| NB | narrowband. |
| NF | noise figure. |
| OE | opto-electronical. |
| OEPLL | opto-electronic phased locked loop. |
| OMA | optical modulation amplitude. |
| OPA | optical phased array. |
| PA | power amplifier. |
| PCB | printed circuit board. |
| PD | photodiode. |
| PIC | photonic integrated circuit. |
| PM | phase modulation. |
| Q | quadrature phase. |
| radar | radio detection and ranging. |
| RF | radio frequency. |
| RIN | relative intensity noise. |
| RX | receiver. |
| S-parameter | scattering parameter. |
| SE | single ended. |
| SiGe | silicon germanium. |
| SNR | signal to noise ratio. |
| SOI | silicon on insulator. |
| TE | transversal electrical. |
| TIA | transimpedance amplifier. |
| TL | transmission line. |
| TRX | transceiver. |
| TX | transmitter. |
| VNA | vector network analyzer. |

# Chapter 1

# Introduction

## 1.1 Large Aperture Radar

Lidar, radar, and camera-based sensors are commonly used for the implementation of driver assistance systems. Each sensor type offers distinct advantages and disadvantages. For instance, radar surpasses lidar in terms of range, performance under adverse weather conditions, and the measurement of radial velocity. Conversely, lidar excels over radar in range resolution and angular resolution. Table 1.1 provides a comparison of the different sensor systems (from [10]).

| Sensor | Radar | Lidar | Camera |
|---|---|---|---|
| Range | ++ | + | ++ |
| Range resolution | + | ++ | 0 |
| Angular resolution | 0 | ++ | + |
| Works in bad weather | ++ | 0 | - |
| Works in dark | ++ | ++ | − |
| Works in bright | ++ | + | + |
| Color/contrast | − | − | ++ |
| Radial velocity | ++ | 0 | - |

Table 1.1: Comparison of different advanced driver assistance systems (from [10])

Nonetheless, high-resolution millimeter-wave imaging radar is considered a promising candidate for enabling Level-4 or Level-5 autonomous driving [11]. A key limitation of current high-resolution radar systems lies in their angular resolution. According to the Rayleigh criterion, ’the angular radius $\theta$ of the central disk is given by

$$\theta \approxeq 1.2197 \frac{\lambda}{2R} \tag{1.1}$$

in which $\lambda$ represents the wavelength of the light, and $2R$ the (diameter of the) aperture’ [8]. (In [8], an equal sign is used in Eq. 1.1. To ensure scientific accuracy, it has been replaced with an approximate sign.)

The system with the largest ground-based aperture was introduced in 2019 by the Event Horizon Telescope Collaboration et al. This system enabled the first-ever photograph of the shadow of the supermassive black hole in the galaxy M87. The maximum baseline length of the sparse array radiometer was approximately $10\,700\,\mathrm{km}$, resulting in a theoretical angular resolution of roughly $6 \cdot 10^{-9}$ ° [12].

For automotive applications, an aperture size of $10\,700\,\mathrm{km}$ is not feasible. Fortunately, such extreme angular resolution is also unnecessary for autonomous driving.

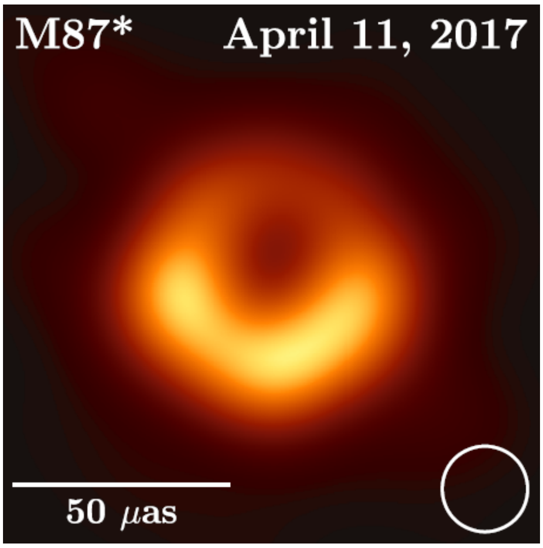

Figure 1.1: Shadow of the black hole M87 [12]

In the following chapter, the requirements—particularly regarding angular resolution—for an automotive radar system will be presented.

## 1.2 Automotive Radar with Large Aperture

### 1.2.1 Requirements

State-of-the-art lidar systems outperform radar systems in terms of range resolution and angular resolution [10]. This makes lidar systems particularly attractive for imaging applications. Table 1.2 presents performance specifications for automotive lidar systems [13].

| Parameter | Short Range | Long Range |
|---|---|---|
| Angular resolution | $\sim 1°$ | $0.1°$-$0.15°$ |
| Z resolution | a few cm | a few cm |
| Range | 20-30 $\mathrm{m}$ | 200-300 $\mathrm{m}$ |

Table 1.2: Automotive lidar performance specifications (from [13])

To the best of the authors' knowledge, the latest performance requirements for automotive radar systems were published in 2013 and are listed in table 1.3 [14].

| Parameter | Short Range | Long Range |
|---|---|---|
| Angular resolution | $\pm\ 2°$ | $\pm\ 0.1°$ |
| Z resolution | $\pm\ 5\,\mathrm{cm}$ | $\pm\ 10\,\mathrm{cm}$ |
| Range | 90 $\mathrm{m}$ | >200m |

Table 1.3: Automotive radar performance specifications (from [14])

State-of-the-art 77 GHz radar systems already meet the range requirements. For example, the Bosch Gen 5 front radar can detect objects at distances exceeding 200 m [15].

The radar resolution is primarily determined by its bandwidth. The frequency band from 76 GHz to 81 GHz has been approved for automotive use in nearly all countries [16]. The range resolution of a 77 GHz freqeuncy modulated continous wave (FMCW) radar, without any signal processing, is given by [17]:

$$\Delta R = \frac{c_0}{2 \cdot BW} \approx \frac{2.998 \cdot 10^8 \frac{m}{s}}{2 \cdot 5\,\mathrm{GHz}} \approx 30\,\mathrm{cm} \tag{1.2}$$

with $c_0$ the speed of light, and $BW$ the bandwidth. However, various publications have proposed signal processing techniques to improve range resolution beyond this baseline [17, 18].

Angular resolution, on the other hand, is constrained by the aperture size. Applying the Rayleigh criterion, the minimum aperture size required to achieve an angular resolution of $0.1°$ is:

$$R = 1.2197 \frac{\lambda}{2\theta} \approx 1.2197 \frac{3.89 \cdot 10^{-3}\mathrm{m}}{2 \cdot 0.001\,75\,\mathrm{rad}} \approx 1.36\,\mathrm{m} \tag{1.3}$$

This result indicates that the required aperture size is smaller than the front width of even compact cars.

### 1.2.2 Signal Distribution

In the previous section it was derived that a minimum aperture size of $1.36\,\mathrm{m}$ is necessary to achieve an angular resolution of $0.1°$. In state-of-the-art radar systems, it is difficult to distribute a high frequency electrical LO signal across such a large aperture. This limitation arises from the high losses associated with electrical interconnects—typically a few $\mathrm{dB/cm}$ at 77 GHz [19]. Additionally, coaxial cables are vulnerable to external environmental factors such as temperature fluctuations, mechanical stress, and electromagnetic interference, all of which can induce phase drift [20, 21]. Without phase stabilization, it becomes extremely challenging to operate multiple radar front ends coherently in harsh environments like those found in automotive applications.

In contrast, fiber-optic signal distribution offers significantly lower losses—e.g., $0.14\,\mathrm{dB/km}$ at 193 THz [22]—making it well-suited for large-aperture radar systems. Moreover, optical signal distribution provides enhanced immunity to electromagnetic interference [23]. Since the subsequent photodiode (PD), which performs the opto-electronical (OE) conversion, exhibits a $|E(t)|^2$ response characteristic [24], where $E(t)$ denotes the electric field of the optical signal, fiber-based systems demonstrate exceptional robustness against phase fluctuations of the optical signal after the OE conversion.

The combination of low transmission loss, immunity to electromagnetic interference, and resilience against phase drift makes fiber-optic signal distribution highly attractive for a coherent large aperture radar in harsh environments such as automotive applications.

### 1.2.3 Multiple Input Multiple Output Array

In the previous section, the focus was on the aperture size required to achieve an angular resolution of $0.1°$, as well as on strategies for enabling coherent signal distribution in harsh environments such as automotive applications.

However, to minimize grating lobes in a phased array system while maintaining a field of view of $180°$, the spacing between antenna elements should be $\frac{\lambda}{2}$ or less [25, 26]. For a 1D 77 GHz phased array radar system with an aperture size of $1.36\,\mathrm{m}$, at least

$$N = \frac{2 \cdot R}{\lambda} = \frac{2 \cdot 1.36\,\mathrm{m}}{3.89 \cdot 10^{-3}\mathrm{meter}} \approx 700 \tag{1.4}$$

antenna elements are required to achieve an angular resolution of $0.1°$ and a field of view of $180°$. For mass-market automotive applications, a system with 700 antennas is not practicable.

To address the high number of required antennas, a sparse array approach combined with MIMO signal processing can be employed, significantly reducing the number of antennas. Figure 1.2 illustrates a 2D sparse array configuration [27]. The physical array, shown on the left side of figure 1.2, consists of multiple transmit and receive antennas divided into two distinct sets [27]. Through discrete convolution of the transmit and receive antenna positions, the virtual array—depicted on the right side of figure 1.2—can be constructed [27]. A time-division multiplexing architecture is then used to ensure orthogonality between the different transmit antennas [27]. If the phase offsets between the various transmit and receive frontends, as well as the antenna positions, are known, the direction of arrival can be estimated using a discrete Fourier transform [28].

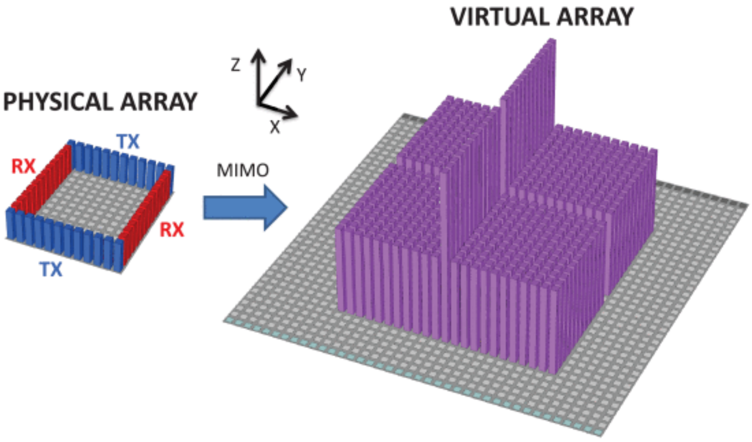

Figure 1.2: Schematic of the MIMO array configuration. Left: Physical 2D array with TX antennas (blue) and RX antennas (red); Right: Resulting virtual array. From [27]

It should be noted that in a sparse array with MIMO signal processing, the sidelobe level depends on the array geometry [29]. Consequently, several studies have proposed optimization strategies to reduce sidelobe levels, e.g., [29, 30].

### 1.2.4 Electronic Photonic Integrated Circuits

As presented in the previous section, the number of antennas can be significantly reduced by employing sparse array techniques. However, implementing a large-aperture phased array radar system using discrete components would be too costly for mass-market applications such as high-resolution automotive radar.

Historically, the integration of radar systems into cost-effective silicon-based technologies has enabled the production of multi-channel radar sensors [31]. Integrating electronic and photonic components into a single chip could similarly reduce the cost of large-aperture photonic FMCW radar systems with optical LO distribution.

In 2016 and 2017, S. Lischke et al. introduced a monolithic SiGe BiCMOS process that integrates electronic and photonic components on a single chip [32, 33]. The

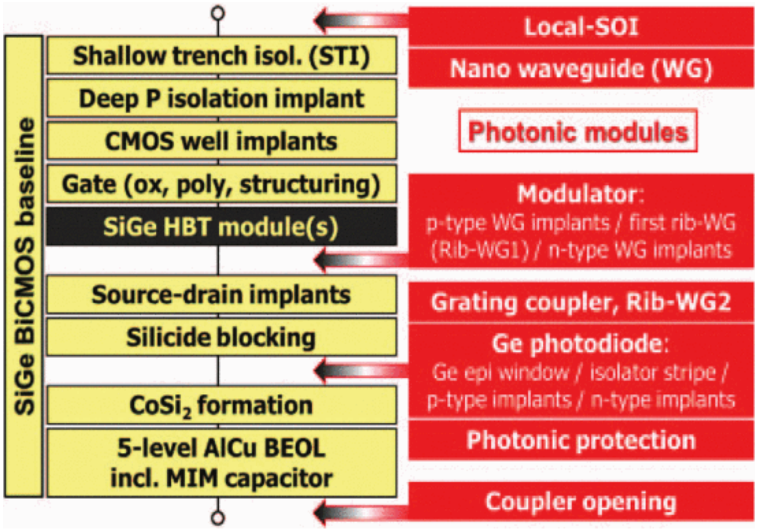

FIGURE 1.3: Electronic-photonic SiGe BiCMOS process flow. Red: Photonic Modules, Yellow: SiGe BiCMOS process. From [32]

process flow of the electronic-photonic BiCMOS technology is illustrated in figure 1.3 [32]. It begins with a local silicon on insulator (SOI) approach [34], used to implement silicon waveguides with a height of 220 nm on a 2 µm thick buried oxide. This approach also enables the fabrication of substrates tailored to the distinct requirements of high-speed electronics and photonics [32]. Furthermore, during the fabrication of the SiGe BiCMOS baseline, additional photonic modules are integrated to implement high-speed electro-optical modulators, grating couplers, and germanium PDs [32].

In addition to the monolithic electronic-photonic SiGe BiCMOS technology developed by IHP, GlobalFoundries introduced a monolithic electronic-photonic 45 nm complementary metal-oxide-semiconductor (CMOS) SOI technology in 2019 and 2020 [35, 36]. The proposed 45 nm CMOS platform enables high-volume, low-cost production of electronic-photonic integrated circuits on 300 mm wafers.

Both monolithic electronic-photonic integration technologies have the potential to enable low-cost, high-volume, large-aperture photonic FMCW radar systems with optical LO distribution.

## 1.3 State of the Art

Based on the performance requirements for automotive radar and applying the Rayleigh limit, the minimum aperture size required for high-resolution radar was calculated. The large number of antenna elements in a fully populated uniform linear phased array with $\frac{\lambda}{2}$ spacing highlights the need for a sparse array approach.

This section presents the state of the art in large-aperture millimeter-wave radar systems. Given that one of the main objectives of this thesis is the integration of a photonic millimeter-wave radar with optical LO distribution into a silicon photonic chipset, the current state of integrated photonic radar technologies will also be reviewed.

### 1.3.1 Large Aperture Radar Systems with Electrical Signal Distribution

Besides fiber-optic LO distribution, which is the focus of this work, several studies have proposed electronic synchronization techniques to align the elements of the array. A comprehensive overview of these techniques is beyond the scope of this section; therefore, only one synchronization protocol is introduced. Additionally, a satellite-based synchronization method will be briefly discussed.

One protocol frequently cited in the literature for synchronizing radar frontends is the White Rabbit protocol [37–39]. Originally developed by CERN and its partners for the Large Hadron Collider project, White Rabbit enables sub-nanosecond synchronization via optical fiber [37] or electrical cables [40]. It is based on the Precision Time Protocol (PTP, IEEE-1588) and Synchronous Ethernet (SyncE) [37], combining frequency synchronization from SyncE with an enhanced version of PTP clock synchronization [37]. In radar systems, the White Rabbit protocol is used to distribute a low-frequency signal, e.g., 10 MHz, to the various frontends [37]. Within each frontend, this 10 MHz signal is then used for synchronization.

Another method for synchronizing radar frontends involves the use of global navigation satellite systems (GNSS) [41]. GNSS-disciplined oscillators can synchronize multiple radar nodes using a low-jitter reference signal [41]. By leveraging GNSS synchronization, coherent bistatic radar measurements with transmitter (TX)-receiver (RX) baselines of up to 5 km have been demonstrated in the literature [42]. Several systems described in the literature utilize the 10 MHz clock output of GNSS-disciplined oscillators for clock synchronization. Similar to the White Rabbit approach, this clock signal is reused to synchronize the individual frontends.

### 1.3.2 Large Aperture mm-Wave Radar System with Optical Signal Distribution

In the field of large aperture mm-wave radar systems with optical signal distribution only one system was previously reported in the literature. This publication was part of the preliminary work for the Coala project, conducted on behalf of Volkswagen Konzernforschung within the Schneider working group at the Technical University of Braunschweig.

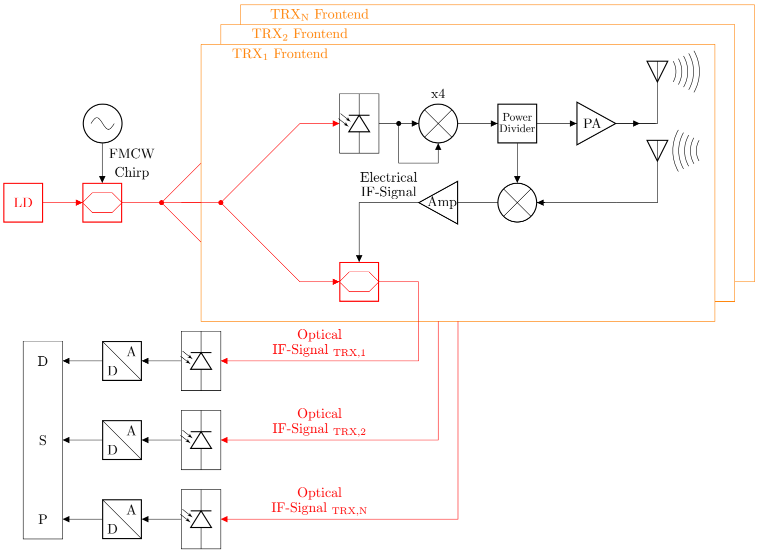

FIGURE 1.4: Block diagram of a photonic radar architecture with a single MZM. (Redrawn from [10, 43].)

Figure 1.4 shows the block diagram of the large aperture mm-wave radar with optical signal distribution [10, 43]. Within a central station, an FMCW signal generated by a signal generator drives a Mach-Zehnder modulator (MZM) fed by a continuous wave (CW) laser diode. The signal is split and sent to a transceiver (TRX) frontend. Within the TX, the optical signal is split into an LO path for the radar and an optical receive path. In the LO path, the optical signal is converted to an electrical signal by means of a PD before it is upconverted to the desired mm-wave frequency. In the TX branch, the mm-wave signal is amplified and transmitted via a transmit antenna. In the RX branch, the received signal, provided by a receive antenna, is directly downconverted. The LO signal for the downconversion is the upconverted mm-wave signal from the TX branch. The intermediate frequency (IF) signal is amplified to drive an MZM, which is fed by a portion of the optical LO signal that is bypassed off prior to the OE conversion within the TRX frontend. The optical signal is transmitted back to the central station via an optical receive path. Within the central station, the optical signal is converted to an electrical signal by means of a PD before the signal is further low pass filtered. The low pass filtered signal is converted to a digital signal before it is further processed by means of a digital signal processor (DSP) unit [10, 43].

The demonstrator consists of one master module, which generates the optical LO signal, and four slave modules that receive the optical signal, convert it into an electrical signal, and upconvert it to the 77 GHz band. Each module is equipped with six transmit and eight receive antennas. The demonstrator achieved an angular separation of 1.1° [10, 43].

### 1.3.3 Integrated Photonic Radar Chips

To the best of the author's knowledge, only five integrated photonic radar chips have been published in the literature. All previously proposed chips follow a hybrid approach, in which a photonic integrated circuit (PIC) contains the complete optical subsystem, while off-the-shelf components are commonly used for the electronic frontend. Table 1.4 provides an overview of the published photonic radar chips.

| Ref. | Technology | Purpose | Carrier Frequency [GHz] | Year |
|---|---|---|---|---|
| [44] | Hybrid: SOI PIC & Discrete Electronics | Combined Lidar-Radar System | 3.4 & 6.9 & 10.4 & 14.1 | 2021 |
| [45] | Hybrid: SOI PIC & Discrete Electronics | Inverse Synthetic Aperture Radar | 15 | 2020 |
| [46] | Hybrid: SOI PIC & Discrete Electronics | Multiband Radar | 3.4 & 6.9 & 10.4 & 14.1 | 2020 |
| [47] | Hybrid: SOI PIC & Discrete Electronics | Linear Frequency Modulated Radar | 2-18 | 2022 |
| [48] | Hybrid: InP & $Si_3N_4$ | Synthetic Aperture Radar RX | 9.65 | 2024 |

Table 1.4: State of the art of integrated photonic radar chip

All previously presented photonic radar chips operate below the millimeter-wave regime and follow a hybrid integration strategy. With the exception of [48], all designs require additional discrete electronics to drive the SOI PIC. In [48], no discrete electronics are needed, as the synthetic aperture radar RX is powered by external signal generators providing LO and radio frequency (RF) signals at 18 dBm and 10 dBm, respectively.

Finally, it should be noted that none of these photonic radar chips had been published at the starting point of this thesis in 2018.

## 1.4 Scope of the Thesis

In this thesis, a mathematical analysis—including phase noise—of a photonic FMCW radar system with optical LO distribution is presented for the first time. To this end, the mathematical system model and phase noise model of a radar system with electrical signal distribution are adapted to account for effects introduced by optical signal distribution. A key focus during phase noise modeling is the upconversion of baseband (BB) amplitude noise into phase noise caused by the electro-opto-electronical (EOE) conversion. To validate the mathematical analysis and gain deeper insights into system behavior, a system model of the proposed mm-wave photonic radar system is implemented in both an optical and an electronic design environment. Using this model, the compressive behavior of the electro-optical (EO) conversion in the optical receive path is analyzed. This compressive behavior leads to ghost targets in the subsequent OE conversion.

Novel circuit architectures that offer advantages for photonic FMCW radar systems with optical LO distribution are presented, analyzed, and validated.

Furthermore, the thesis introduces the world's first photonic radar TRX chipset implemented in low-cost, mass-market silicon technology. This TRX chipset enables the realization of the first 77 GHz large-aperture photonic radar system with optical LO distribution, operating with monolithic electronic-photonic integrated circuits.

In addition, the thesis presents extended system models beyond the photonic FMCW radar with optical LO distribution, including a photonic software-defined MIMO radar system with optical signal distribution, a photonic FMCW multiband radar system with optical LO distribution, and a combined lidar-radar sensor system.

To the best of the author's knowledge, these contributions represent the first detailed system analysis, modeling, and implementation of a millimeter-wave TRX chipset for a photonic FMCW radar with optical LO distribution, along with a system demonstrator. Additionally, this work presents—for the first time—the analysis and modeling of a photonic software-defined MIMO radar system with optical signal distribution, a photonic FMCW multiband radar system with optical LO distribution, and a lidar-radar combined sensor system. The results have been published in peer-reviewed journals and conferences and validated by the scientific community:[49–62]. Moreover, the novelty of the system has led to several patents in the field of photonic radar with optical signal distribution [63–76].

The thesis is organized as follows: Chapter 2 introduces the overall photonic FMCW radar system with optical LO distribution and explains the operating principles of the TX and RX frontends. Furthermore, in chapter 2.2 the mathematical analysis of the photonic FMCW radar system with optical LO is presented. The simulation of the system in both optical and electrical design environments and the behavioral model of the monolithic integrated photonic radar transceiver chipset is described in chapter 3. Chapter 4 introduces novel circuit architectures, including a narrowband optical receiver implemented in IHP's photonic SiGe BiCMOS technology and GlobalFoundries' 45 nm photonic CMOS SOI technology, as well as a narrowband four-quadrant electro-optical mixer. Within the chapters 5 and 6 the monolithic 77 GHz photonic radar transceiver chipset is presented. Chapter 7 showcases the first large-scale coherent MIMO photonic radar system with optical LO distribution based on this chipset.

Additional photonic radar architectures and a lidar-radar combined system are proposed in chapters 8 through 10. These system models are presented, mathematically analyzed, and their operating principles validated through simulations in an optical design environment.

Finally, Chapter 11 concludes the thesis, followed by supplementary information provided in the appendix.

# Chapter 2

# Photonic FMCW MIMO Radar Systems with Optical LO Distribution

## 2.1 System Overview

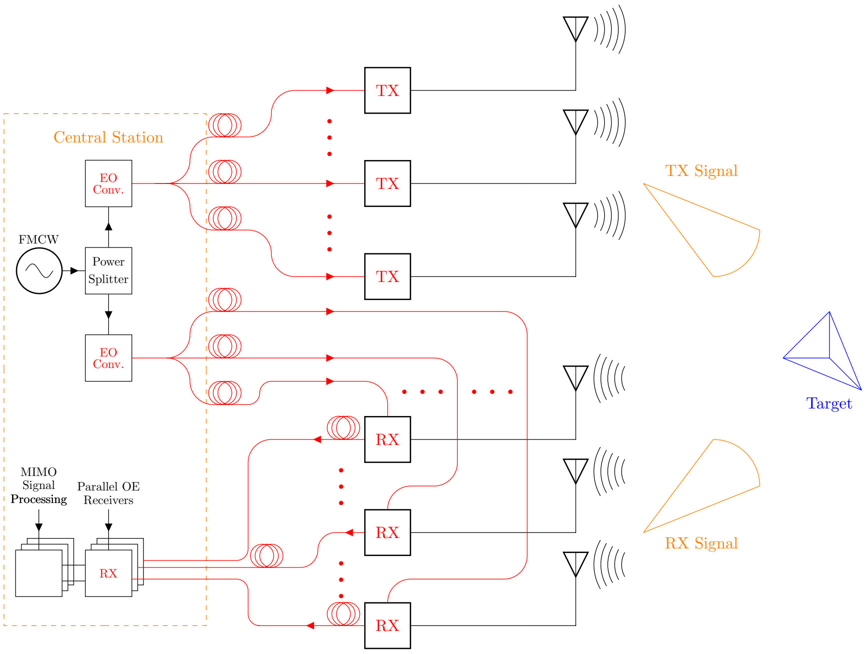

FIGURE 2.1: Simplified block diagram of the FMCW MIMO radar system with optical LO distribution and optical return path. The block diagrams of the TX and RX front ends are shown in figure 2.2.

The simplified block diagram of the FMCW radio detection and ranging (radar) system with optical LO distribution and optical receive path is shown in fig. 2.1. Similar to [10, 43], within a central station, a frequency synthesizer generates an FMCW signal, which is split to the TX and RX branches of the central station by means of a power splitter. Within each branch, the electrical ramp signal is converted to an optical FMCW ramp by one or several EO conversion blocks. In chapter 2.3, different OE conversion techniques will be compared, and it will be shown that the MZM approach provides the lowest additional phase noise, especially at high offset frequencies, among all the techniques. Therefore, for the rest of the thesis, it will be assumed that the EO conversion is realized by an MZM. After the EO conversion, the optical LO signal is distributed to the TX and RX arrays by means of optical fibers.

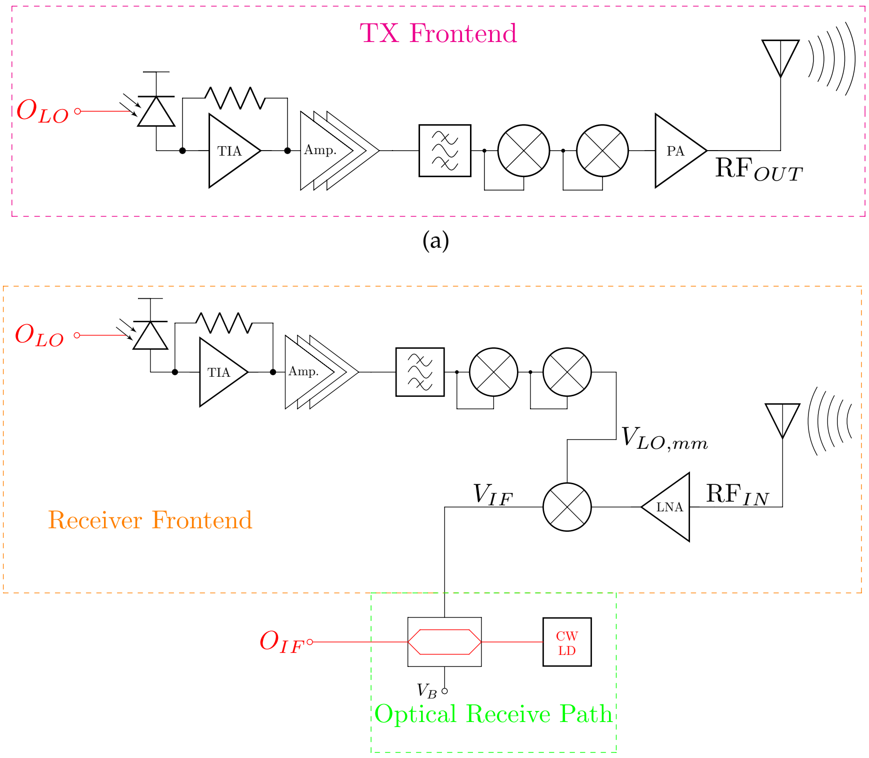

(a)

(b)

FIGURE 2.2: Simplified block diagrams of (a) the TX frontend; (b) the RX frontend with optical receive path.

The simplified TX and RX block diagrams are shown in fig. 2.2. In the TX frontend, the optical LO signal is converted to an electrical signal by means of a PD and a subsequent transimpedance amplifier (TIA). The weak electrical signal is further amplified by additional amplifiers. To avoid unwanted harmonics induced by the non-linear transfer function of the MZM, a bandpass filter selects the desired LO signal before upconversion to the mm-wave radar band. The mm-wave signal is amplified by a power amplifier (PA) before being transmitted by a transmit antenna.

The transmitted signal is reflected by an obstacle and received by a receive antenna in the RX frontend. The weak received signal is amplified by a low noise amplifier (LNA) before direct downconversion. The mm-wave reference LO signal for demodulation is generated from the optical LO signal, similar to the mm-wave transmit signal generation in the TX frontend. The low-frequency IF signal can be fed back to the central station via optical fibers. For this purpose, the electrical IF signal drives an MZM biased at the quadrature point. This optical receive path is highlighted in the green box of figure 2.2b.

The optical IF signal is transmitted back to the central station, where the optical signals are converted to electrical signals by a bank of parallel OE receivers before MIMO processing is performed.

## 2.2 Analysis of the Photonic FMCW Radar System with Optical LO Distribution

In the previous section, the photonic FMCW MIMO radar system with optical LO distribution was presented. In this section, the radar systems will be analyzed. For the further derivations, it will be assumed that the EO conversion is realized with an MZM, fed by a CW laser diode, and the OE conversion is realized with a PD.

Since the building blocks of the EO and OE conversion are used multiple times in the system, subsections 2.2.1& 2.2.2 will present the EO and OE conversion before the entire system is analyzed.

### 2.2.1 Electrooptical Conversion

The CW output intensity of the laser diode, feeding a subsequent MZM, is given as $\Psi_0$.

Via a bias voltage and an RF voltage, the operating point and the output intensity of the MZM can be manipulated. The output intensity of a lossless MZM is given by [77]:

$$\Psi_{MZM}(t) = \Psi_0 \cdot \left\{ 1 + \cos\left[ \frac{\pi\left(V_B + V_{IN}(t)\right)}{V_\pi} \right] \right\} \tag{2.1}$$

with the bias voltage $V_B$, the RF input voltage $V_{IN}(t)$, and the switching voltage of the MZM $V_\pi$.

Via the bias point, the MZM can be driven into any arbitrary operating point. Unless otherwise noted, the MZM is biased at the quadrature point in this thesis. Therefore, the bias voltage needs to be set to [78]:

$$V_B = -\frac{V_\pi}{2}. \tag{2.2}$$

Under this condition, the output intensity of the MZM simplifies to:

$$\Psi_{MZM}(t) = \Psi_0 \cdot \left\{ 1 + \sin\left[ \frac{\pi V_{IN}(t)}{V_\pi} \right] \right\}. \tag{2.3}$$

### 2.2.2 Optoelectronic Conversion

Neglecting the dark current, the PD generates a wavelength-dependent photocurrent which is proportional to the optical input intensity [79]:

$$I_{PD} = \mathcal{R}(\lambda) \cdot \Psi_0(t) \tag{2.4}$$

with the proportionality factor, namely the responsivity $\mathcal{R}(\lambda)$ of the PD. If the PD is fed by the output of an MZM, the photocurrent results by inserting eq. 2.3 into eq. 2.4 to:

$$I_{PD} = \mathcal{R}(\lambda) \cdot \Psi_0 \cdot \left\{ 1 + \sin\left[ \frac{\pi V_{IN}(t)}{V_\pi} \right] \right\}. \tag{2.5}$$

From textbooks, e.g. [80], it is known that the transimpedance of an ideal shunt feedback TIA, shown in figure 2.3 is given by

$$Z_T = \frac{V_{TIA}}{I_{PD}} = -\frac{G(j\omega)}{1 + G(j\omega)} \cdot \frac{Z_F(j\omega)}{1 + j\omega \frac{Z_F(j\omega) \cdot C_D}{G(j\omega)+1}} \tag{2.6}$$

$$Z_T = \frac{V_{TIA}}{I_{PD}} = -\frac{G(j\omega) Z_F(j\omega)}{1 + G(j\omega) + j\omega Z_F(j\omega) \cdot C_D} \tag{2.7}$$

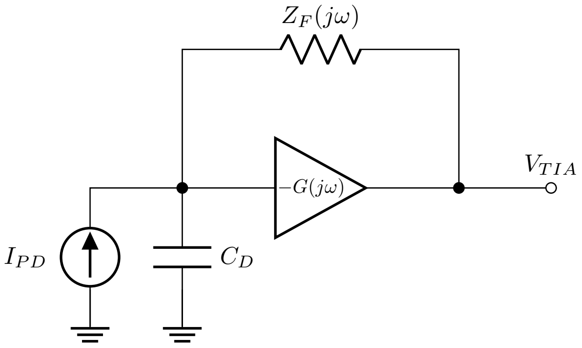

FIGURE 2.3: Shunt feedback TIA topology. (Redrawn with renaming from [80].)

with the capacitance of the PD $C_D = C_j + C_{diff}$, the junction capacitance of the PD $C_j$, the diffusion capacitance of the PD $C_{diff}$, the feedback impedance of the TIA $Z_F(j\omega)$, and the voltage gain of the core amplifier of the shunt feedback TIA $-G(j\omega)$. Since the PD is biased in reverse region, the diffusion capacitance of the PD is approximately $C_{diff} \approx 0$. Inserting eq. 2.5 into eq. 2.7 results, under the assumtion of a monochomatic system ($\mathcal{R}(\lambda) = \mathcal{R}$), to:

$$\begin{aligned} V_{TIA}(j\omega) = &-\frac{\mathcal{R}\Psi_0 G(j\omega) Z_F(j\omega)}{1 + G(j\omega) + j\omega Z_F(j\omega) \cdot C_D} \\ &\cdot \left[2\pi\delta(\omega) + \mathcal{F}\left\{\sin\left[\frac{\pi V_{IN}(t)}{V_\pi}\right]\right\}(j\omega)\right] \end{aligned} \tag{2.8}$$

with the dirac-delta distribution $\delta(\omega)$, and the Fourier transform $\mathcal{F}\{...\}(j\omega)$. Under the assumption that the RF input signal of the MZM is a sinusoidal signal

$$V_{IN} = V_0 \cdot \cos(\Xi) \tag{2.9}$$

with the amplitude $V_0$, and an arbitrary argument $\Xi$ of the sinusoidal function, and making use of the Jacobi-Anger expansion [81]

$$\sin(z \cdot cos(\theta)) = -2\sum_{n=1}^{\infty}(-1)^n J_{2n-1}(z)\cos[(2n-1)\theta] \tag{2.10}$$

with the Bessel function of the first kind and k-th order $J_k(...)$, eq. 2.8 results to

$$\begin{aligned} V_{TIA}(j\omega) = &\,2 \cdot \frac{\mathcal{R}\Psi_0 G(j\omega) Z_F(j\omega)}{1 + G(j\omega) + j\omega Z_F(j\omega) \cdot C_D} \\ &\cdot \left[-\pi\delta(\omega) + \mathcal{F}\left\{\sum_{n=1}^{\infty}(-1)^n J_{2n-1}\left(\frac{V_0\pi}{V_\pi}\right)\cos[(2n-1)\,\Xi]\right\}(j\omega)\right] \end{aligned} \tag{2.11}$$

In the following derivation, only the first-order Bessel function is considered. Equation 2.11 simplifies accordingly to:

$$\begin{aligned} V_{TIA}(j\omega) \approx &\,2 \cdot \frac{\mathcal{R}\Psi_0 G(j\omega) Z_F(j\omega)}{1 + G(j\omega) + j\omega Z_F(j\omega) \cdot C_D} \\ &\cdot \left[-\pi\delta(\omega) - \mathcal{F}\left\{J_1\left(\frac{V_0\pi}{V_\pi}\right)\cos[\Xi]\right\}(j\omega)\right] \end{aligned} \tag{2.12}$$

A detailed analysis of higher-order terms is provided in appendix A.

### 2.2.3 Transmit Part of the Central Station

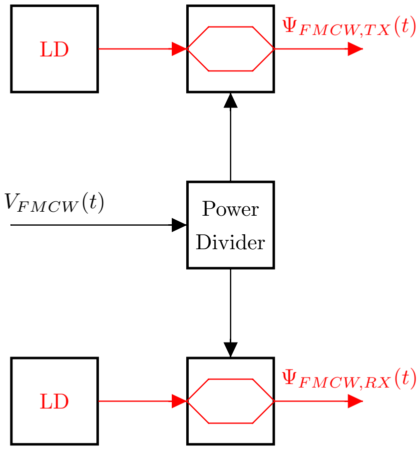

FIGURE 2.4: Block diagram of the TX part of the central station.

Within the TX part of the central station, the electrical LO is converted into the optical LO signal by means of MZMs. The electrical LO signal is given by

$$V_{FMCW}(t) = \sqrt{2}V_{FMCW,0}\cos\left(\left[\omega_{LO} + \frac{\mu t}{2}\right]t\right) \tag{2.13}$$

In the block diagram of the photonic FMCW MIMO radar system with optical LO distribution, shown in figure 2.1, the electrical LO signal is split into a TX and RX path. Under the assumption that the power divider is an ideal 3 dB divider, the optical LO signal in the TX and RX paths results by inserting eq. 2.13 into eq. 2.3 to:

$$\Psi_{FMCW,TRX}(t) = \Psi_0\left\{1 + \sin\left(\frac{\pi V_{FMCW,0}\cos\left(\left[\omega_{LO} + \frac{\mu t}{2}\right]t\right)}{V_\pi}\right)\right\} \tag{2.14}$$

### 2.2.4 TX Frontend

Within the TX frontend, shown in figure 2.2a, the optical LO signal is converted to an electrical one. By inserting $\Psi_{FMCW,TRX}(t)$ from eq. 2.14 into $\Psi_0(t)$ from eq. 2.4, and redo the analysis until eq. 2.12, the output voltage of the TIA results, neglecting the DC component, to:

$$\begin{aligned} V_{TIA}(j\omega) = 2 \cdot &\frac{G(j\omega)Z_F(j\omega)\mathcal{R}\Psi_0}{G(j\omega) + jZ_F(j\omega)C_D\omega + 1} \\ &\cdot \mathcal{F}\left\{-J_1\left(\frac{\pi V_{FMCW,0}}{V_\pi}\right)\cos\left[\left(\omega_{LO} + \frac{\mu t}{2}\right)t\right]\right\}(j\omega). \end{aligned} \tag{2.15}$$

Within the mm-wave part of the TX frontend, the electrical signal is upconverted to the mm-wave band by means of $k$ frequency multipliers. The mm-wave output signal of the frequency multipliers is filtered and amplified. The transmit signal is given by:

$$
\begin{aligned}
P_{TX}(j\omega) = -2 \cdot G_{TX}(j\omega) \cdot \frac{G(j\omega) Z_F \mathcal{R}(\lambda) \Psi_0}{G(j\omega) + jZ_F C_D \omega + 1} J_1 \left( \frac{\pi V_{FMCW,0}}{V_\pi} \right) \\
\cdot \mathcal{F} \left\{ \cos \left[ k \cdot \left( \omega_{LO} + \frac{\mu t}{2} \right) t \right] \right\} (j\omega). \qquad (2.16)
\end{aligned}
$$

### 2.2.5 RX Frontend

Within the RX frontend, shown in fig. 2.2b, the received signal, provided by a receive antenna, is filtered and amplified by an LNA before downconversion is performed. In mathematical words, this is a multiplication of the transmitted signal, given in eq. 2.16, with a time delayed version of the transmitted signal, given in eq. 2.16.

$$
\begin{aligned}
V_{IF}(j\omega) = 2 \cdot G_{TX}(j\omega) \cdot G_{RX}(j\omega) \cdot G_C(j\omega) \cdot \frac{G(j\omega) \cdot Z_F(j\omega) \cdot \mathcal{R}(\lambda) \Psi_0}{G(j\omega) + j\omega C_D Z_F(j\omega) + 1} J_1^2 \left( \frac{\pi V_{FMCW,0}}{V_\pi} \right) \\
\cdot \mathcal{F} \left\{ \left[ \cos \left[ k \cdot \left( \omega_{LO} + \frac{\mu t}{2} \right) t \right] \right] \cdot \left[ \cos \left[ k \cdot \left( \omega_{LO} + \frac{\mu (t - \tau)}{2} \right) (t - \tau) \right] \right] \right\} (j\omega) \\
(2.17)
\end{aligned}
$$

$$
\begin{aligned}
V_{IF}(j\omega) = G_{TX}(j\omega) \cdot G_{RX}(j\omega) \cdot G_C(j\omega) \cdot \frac{G(j\omega) \cdot Z_F(j\omega) \cdot \mathcal{R}(\lambda) \Psi_0}{G(j\omega) + j\omega C_D Z_F(j\omega) + 1} J_1^2 \left( \frac{\pi V_{FMCW,0}}{V_\pi} \right) \\
\cdot \left( \mathcal{F} \left\{ \cos \left[ k\mu\tau t + k\omega_{LO}\tau - \frac{k\mu\tau^2}{2} \right] \right\} (j\omega) \right. \\
\left. + \mathcal{F} \left\{ \cos \left[ 2k\omega_{LO} t + k\mu t^2 - k\omega_{LO}\tau - k\mu t\tau + \frac{k\mu\tau^2}{2} \right] \right\} (j\omega) \right) \qquad (2.18)
\end{aligned}
$$

with the free space path loss $G_C(j\omega)$, the overall gain of the RX frontend $G_{RX}(j\omega)$, and the round trip delay $\tau$. Applying low-pass filtering to eq. 2.18 yields:

$$
\begin{aligned}
V_{IF}(j\omega) = G_{TX}(j\omega) \cdot G_{RX}(j\omega) \cdot G_C(j\omega) \cdot \frac{G(j\omega) \cdot Z_F(j\omega) \cdot \mathcal{R}(\lambda) \Psi_0}{G(j\omega) + j\omega C_D Z_F(j\omega) + 1} J_1^2 \left( \frac{\pi V_{FMCW,0}}{V_\pi} \right) \\
\cdot \mathcal{F} \left\{ \cos \left[ k\mu\tau t + k\omega_{LO}\tau - \frac{k\mu\tau^2}{2} \right] \right\} (j\omega) \qquad (2.19)
\end{aligned}
$$

$$
\begin{aligned}
V_{IF}(j\omega) = \pi \cdot G_{TX}(j\omega) \cdot G_{RX}(j\omega) \cdot G_C(j\omega) \cdot \frac{G(j\omega) \cdot Z_F(j\omega) \cdot \mathcal{R}(\lambda) \Psi_0}{G(j\omega) + j\omega C_D Z_F(j\omega) + 1} J_1^2 \left( \frac{\pi V_{FMCW,0}}{V_\pi} \right) \\
\cdot \left[ e^{-j\left( k\omega_{LO}\tau - \frac{k\mu\tau^2}{2} \right)} \delta \left( \omega + k\mu\tau \right) + e^{j\left( k\omega_{LO}\tau - \frac{k\mu\tau^2}{2} \right)} \delta \left( \omega - k\mu\tau \right) \right] \qquad (2.20)
\end{aligned}
$$

In order to realize an optical receive path, the electrical IF signal is converted into an optical signal by means of an EO conversion unit.

### 2.2.6 Receive Part of the Central Station

Within the receive part of the central station, the optical IF signal is converted to an electrical signal by an OE conversion unit. The optical IF signal $\Psi_{IF}$ results from inserting eq. 2.19 into eq. 2.3. Inserting $\Psi_{IF}$ into $\Psi_0(t)$ from eq. 2.4, and redo the analysis until eq. 2.12, the output voltage of the TIA in the central station results to:

$$
\begin{aligned}
V_{TIA,RX,ECU} &= 2 \cdot \frac{G_{ECU}(j\omega) Z_{F,ECU}(j\omega) \mathcal{R}_{ECU} \Psi_{0,OR}}{G_{ECU}(j\omega) + j\omega C_{D,ECU} Z_{F,ECU}(j\omega) + 1} \\
&\cdot \left[ -\pi\delta(\omega) + \mathcal{F}\left\{ -J_1\left(\frac{V_0\pi}{V_\pi}\right) \cos\left[ k\mu\tau t + k\omega_{LO}\tau - \frac{k\mu\tau^2}{2} \right] \right\}(j\omega) \right]
\end{aligned}
\tag{2.21}
$$

$$
\begin{aligned}
V_{TIA,RX,ECU} &= 2 \cdot \frac{G_{ECU}(j\omega) Z_{F,ECU}(j\omega) \mathcal{R}_{ECU} \Psi_{0,OR}}{G_{ECU}(j\omega) + j\omega C_{D,ECU} Z_{F,ECU}(j\omega) + 1} \\
&\cdot \left[ -\pi\delta(\omega) - J_1\left(\frac{V_0\pi}{V_\pi}\right) \left[ e^{-j\left(k\omega_{LO}\tau - \frac{k\mu\tau^2}{2}\right)} \delta\left(\omega + k\mu\tau\right) \right.\right. \\
&\left.\left. + \; e^{j\left(k\omega_{LO}\tau - \frac{k\mu\tau^2}{2}\right)} \delta\left(\omega - k\mu\tau\right) \right]\right]
\end{aligned}
\tag{2.22}
$$

with $V_0 = G_{TX}(j\omega) \cdot G_{RX}(j\omega) \cdot G_C(j\omega) \cdot \frac{G(j\omega) \cdot Z_F(j\omega) \cdot \mathcal{R}(\lambda)\Psi_0}{G(j\omega) + j\omega C_D Z_F(j\omega) + 1} J_1^2\left(\frac{\pi V_{FMCW,0}}{V_\pi}\right)$, the voltage gain of the core amplifier of the shunt feedback TIA of the central station $G_{ECU}(j\omega)$, the feedback impedance of the TIA of the central station $Z_{F,ECU}(j\omega)$, the responsivity of the PD of the central station $\mathcal{R}_{ECU}$, the optical amplitude of the optical receive path $\Psi_{0,OR}$, and the capacitance of the PD of the central station $C_{D,ECU}$.

## 2.3 Phase Noise Analysis of a Photonic FMCW Radar System with Optical LO Distribution

Phase noise is a critical performance parameter for radar systems [82]. Within this section, the phase noise of a photonic radar system with optical LO distribution is analyzed. In section 2.3.1, the phase noise of the three commonly used EO conversion techniques are measured and compared. It turns out that the MZM approach adds the lowest additive phase noise of the different methods. In addition, an MZM can be integrated into a single chip for low-cost, high-volume mass production. Based on these two arguments, the MZM approach is the best candidate for the overall system.

### 2.3.1 Phase Noise Measurement

Starting point for the phase noise analysis are the three different most prominent EO conversion techniques [83]:

- Two laser beating within a PD [84].
- Intensity modulation of a CW laser by means of an MZM [85].
- Direct intensity modulation of a laser [86].

Figure 2.5 shows the block diagrams of the measurement setups for the three different EO conversion methods. For the two laser beating, the output signals of two locked lasers were combined and fed onto a high-speed PD with an integrated shunt resistor. The weak output signal is AC coupled to an amplifier before the phase noise is measured. For the intensity modulation of a CW laser by means of an MZM, biased at the quadrature point and driven by an RF signal generator, the output signal of the

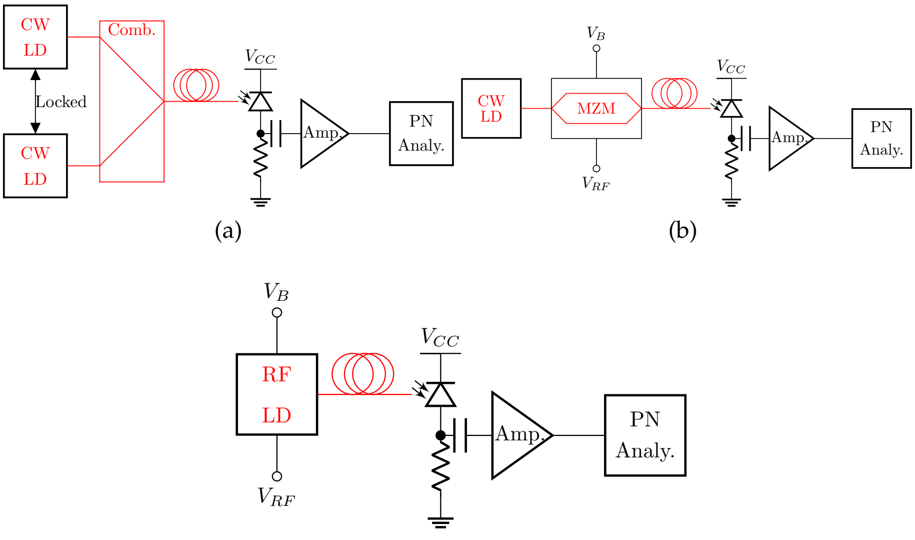

(a) (b)

(c)

FIGURE 2.5: Simplified block diagram of the phase noise measurement setup of (a) two laser beating in the PD; (b) intensity modulation of CW laser by means of an MZM; (c) direct intensity modulation of a laser.

MZM is directly fed to a high-speed PD with an integrated shunt resistor. Similar to the two laser beating case, the weak output signal is AC coupled to an amplifier before the phase noise is measured by means of a phase noise analyzer. The phase noise analysis for the direct intensity modulation of a laser is performed similarly. The laser diode is driven by an RF signal generator. Via an external bias, it is ensured that the laser remains in lasing mode even if the signal generator provides a high signal swing. As in the previous measurements, the output signal of the RF laser is directly fed to a high-speed PD with an integrated shunt resistor. The weak output signal is AC coupled to an amplifier before the phase noise is measured by means of a phase noise analyzer.

The measurement results for a 5 GHz LO signal are shown in figure 2.6. The two-laser approach with subsequent beating in a PD exhibits the highest phase noise of the three methods up to an offset frequency of approximately 20 MHz. The MZM and the RF laser are driven by the signal generator E8257D from Keysight with the ultra-low phase noise option. Both techniques approximately follow the phase noise of the reference signal generator up to an offset frequency of approximately 500 kHz. The spikes in the MZM approach are induced by the bias source used in the measurement. Other phase noise measurements do not show such spikes. Beyond 500 kHz, the MZM approach provides the lowest additional phase noise to the LO signal compared to the RF laser.

In addition to conventional signal generators, appendix D and appendix C present novel signal generators that may offer advantages for the photonic FMCW MIMO radar system with optical LO distribution.

### 2.3.2 Phase Noise Analysis

In the previous section, it was shown that an MZM-based EO conversion provides the lowest additional phase noise to the LO signal after the OE conversion. In this section, the phase noise of a photonic radar system with optical LO distribution will

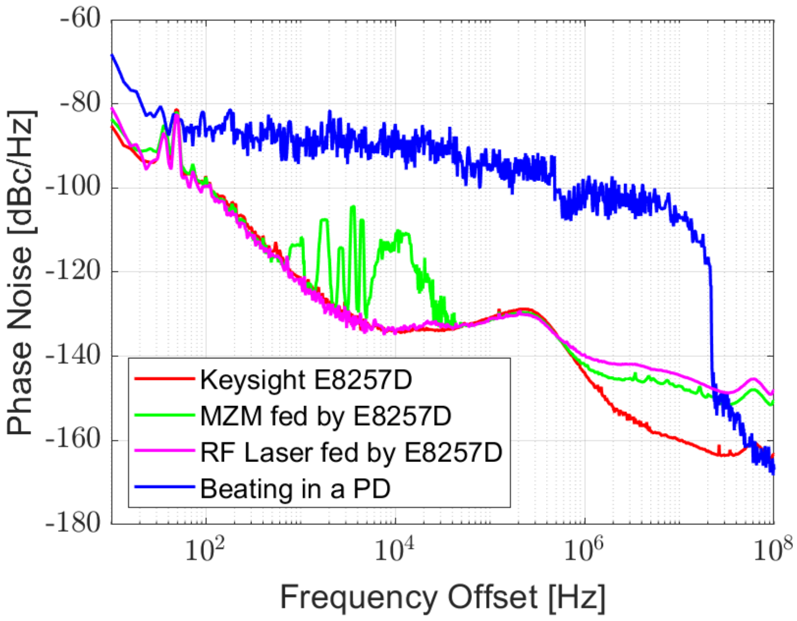

FIGURE 2.6: Phase noise measurement of the three common techniques of optical LO generation at 5 GHz.

be analyzed. Compared to pure electronic radar systems [87, 88], for phase noise analysis of a photonic radar system with optical LO distribution, the amplitude noise before the OE conversion has an impact to the overall phase noise [89] of the radar system. For simplicity, within this thesis, the additive phase noise and the amplitude modulation (AM) to phase modulation (PM) conversion within the components themselves will be neglected.

The electrical LO signal with amplitude fluctuations and phase noise is given by:

$$V_{FMCW}(t) = (V_{0,FMCW} + \Delta V_{FMCW}(t)) \cos\left(\left[\omega_{LO} + \frac{\mu t}{2}\right] t + \Delta\varphi_{FMCW}(t)\right) \quad (2.23)$$

with $V_{0,FMCW}$ the nominal amplitude of the FMCW chirp, $\Delta\varphi_{FMCW}(t)$ the phase perturbation of the FMCW chirp, and $\Delta V_{FMCW}(t)$ the amplitude perturbation of the FMCW chirp.

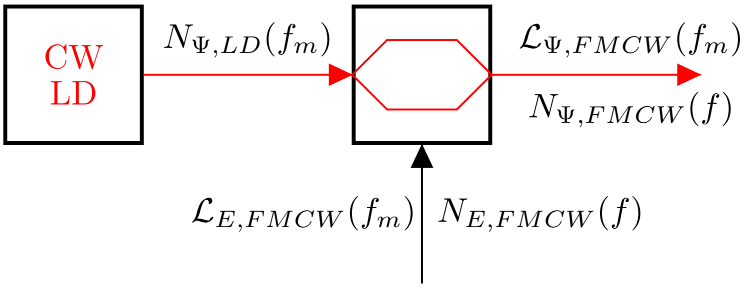

FIGURE 2.7: Illustration of the amplitude noise and phase noise of the optical LO generation.

The electrical FMCW LO signal drives an MZM, which is biased in the quadrature point, as shown in figure 2.7. The optical intensity has a nominal intensity $\Psi_0$ and a relative intensity noise $RIN(t)$. The product $\Psi_0 \cdot RIN(t)$, which represents the amplitude fluctuations of the CW laser, has the spectral properties $N_{\Psi,LD}$. The phase fluctuations of the optical THz signal do not affect the subsequent derivation, as the PD has an $|x|^2$ characteristic and $\left|e^{j\cdot\Xi}\right|^2 = 1$, where $\Xi$ is an arbitrary real-valued function. Assuming that the amplitude fluctuation of the bias voltage of the MZM can be neglected, the time domain optical FMCW signal is given by:

$$\Psi_{MZM}(t) = \Psi_0\left(1 + RIN(t)\right)\left[1 - \sin\left(\frac{\pi V_{FMCW}}{V_\pi}\right)\right] \tag{2.24}$$

Inserting eq 2.23 into eq. 2.24, and making use of the Jacobi-Anger expansions, the frequency domain representation for $\mu = 0$ is given by:

$$\begin{aligned}\Psi_{FMCW}(j\omega) = \Psi_0\pi\left(\delta(\omega) + RIN(j\omega)\right) * \left[\delta(\omega) + \left\{\sum_{m=1}^{\infty}(-1)^n J_{2m-1}\left(\frac{\pi V_{0,FMCW}(j\omega)}{V_\pi}\right)\right.\right.\\ \left.\left. * \left[\mathcal{F}\left(\left\{\cos\left([2n-1]\left[\omega_0 t + \Delta\varphi_{FMCW}(t)\right]\right)\right\}\right]\right\}\right]\end{aligned} \tag{2.25}$$

In formula eq. 2.25, the convolution indicates that the BB AM noise converts into BB AM noise and an additional band pass (BP) AM noise term around the fundamental and all odd-order higher harmonics. Due to this, the spectral properties of the intensity noise $N_{\Psi,FMCW}$ are no longer a linear superposition of the broadband laser $RIN$ and the wideband amplitude fluctuations.

For further derivations, it will be assumed that the convolution of the electrical FMCW phase noise to non-first-order-harmonics can be neglected. This is justified because the electrical phase noise typically has a narrowband $1/f^3$ characteristic close to the carrier [90], so the non first order harmonics of the FMCW phase noise do not influence the fundamental phase noise.

Since a fraction of the optical intensity fluctuations convert into phase fluctuations due to saturation [91] and other nonlinearities of the PD's semiconductor, the AM noise converts into phase noise of the LO signal after OE conversion [89]. The single sideband phase noise is given by [89]:

$$\mathcal{L}_{AM-PM}(f_m) = \frac{\Delta\Psi(f)}{\Psi_0} + 20\log\left(\alpha\right) - 3\,\mathrm{dB} \tag{2.26}$$

with the offset frequency from the carrier $f_m = f - \frac{\omega_0}{2\pi}$, the absolute intensity fluctuation $\Delta\Psi$, e.g. laser relative intensity noise (RIN), MZM bias point fluctuations, or FMCW chip amplitude fluctuations, and $\alpha$ the AM to PM conversion factor of the PD. $\alpha$ define the induced root mean square phase variations induced by fractional power fluctuations [89]. $\alpha$ depends on the bias voltage, average photocurrent and frequency [89]. Assuming that the optical AM noise is uncorrelated with the electrical PM noise of the FMCW chirp, the overall phase noise at the output of the PD is given by:

$$\mathcal{L}_{PD}(f_m) = \mathcal{L}_{AM-PM}(f_m) + \mathcal{L}_{FMCW}(f_m). \tag{2.27}$$

Within the TX frontend, the frequency is multiplied by a factor of $N$, leading to a phase noise increase by a factor of $N^2$ [87]. This results in the final phase noise of the transmitted signal being:

$$\mathcal{L}_{TX}(f_m) = \mathcal{L}_{AM-PM}(f_m) + \mathcal{L}_{FMCW}(f_m) + 20\log\left(N\right). \tag{2.28}$$

The phase noise diagram of the RX frontend is shown in figure 2.8. Within the RX frontend, the received signal is amplified and directly downconverted to the

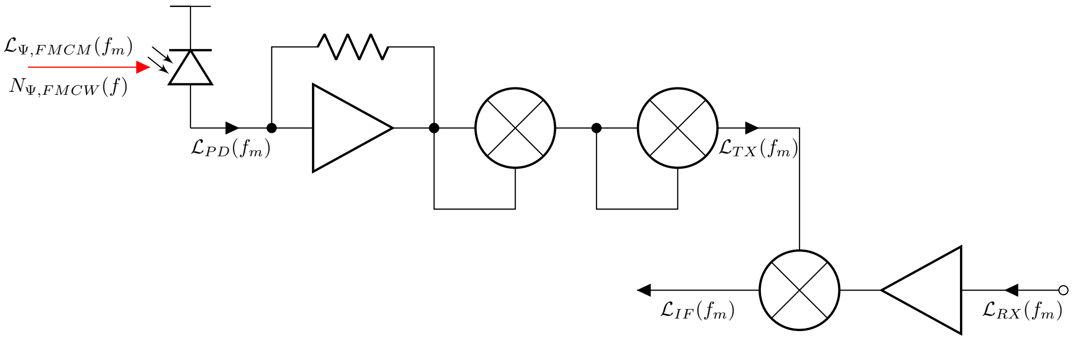

FIGURE 2.8: Illustration of the phase noise of the EO RX frontend chip.

baseband. Since the additive phase noise of the frequency multipliers is neglected within this work, it can be assumed that the LO signal in the RX frontend is a non-delayed replica of the one in the TX frontend. Making use of this simplification, the phase noise of the downconverted IF frequency is given by [87]:

$$\mathcal{L}_{IF}(f_m) = 2 \cdot \mathcal{L}_{TX}(f_m) \cdot [1 - \cos(2\pi f_m \Delta\tau)] \tag{2.29}$$

with $\Delta\tau$ being the round trip delay. In a mixer, phase noise cancellation occurs when the two input signals have a defined phase relationship with each other [88]. This phenomenon is described by the decorrelation term $\cos(2\pi f_m \Delta\tau)$ [88]. In pure electronic radar systems, this time difference would simply be the round trip delay of the radar signal. Due to the high losses of electronic interconnections, pure electronic radar systems cannot have a significant LO length offset of the interconnections. Due to the low-loss property of the fiber optical LO distribution, it is possible that the LO distribution adds an additional time offset. In this case, $\Delta\tau$ results in:

$$\Delta\tau = \frac{2R}{c_0} - \frac{\Delta L}{c_f} \tag{2.30}$$

with the distance to the target $R$, the speed of light $c_0$ in the medium where the radar measurement is performed, the length offset between the central station to the TX frontend and from the central station to the RX frontend $\Delta L$, and the speed of light in the fiber $c_f$. Applying $\Delta\tau$ to eq. 2.29 results in:

$$\mathcal{L}_{IF}(f_m) = 2 \cdot \mathcal{L}_{TX}(f_m) \cdot \left[1 - \cos\left(2\pi f_m \left\{\frac{2R}{c_0} - \frac{\Delta L}{c_f}\right\}\right)\right] \tag{2.31}$$

It should be noted that this result is only correct if, and only if, the time difference $\Delta\tau < \tau_c$, the coherence time of the LO [87].

In the case of an optical receive path, the AM to PM conversion due to the EO and OE conversion results in a single sideband phase noise of [89]:

$$\mathcal{L}_{AM-PM,RX}(f_m) = \frac{\Delta\Psi_{RX}(f)}{\Psi_0} + 20\log(\alpha) - 3\,\text{dB} \tag{2.32}$$

with $\Delta\Psi_{RX}$ being the absolute intensity fluctuations in the optical receive path. The overall phase noise after the optical receive path is given by:

$$\mathcal{L}'_{RX}(f_m) = \mathcal{L}_{AM-PM,RX}(f_m) + \mathcal{L}_{IF}(f_m). \tag{2.33}$$

The last part of the signal chain is the digitalization and processing. During the digitalization of the signal, an analog-to-digital converter adds some effects to the IF phase noise, which are presented in other works [92–94]. In this work, only the effect of the fast fourier transform (FFT) on the phase noise will be considered. Nevertheless, there exist several signal processing techniques to reduce the influence of the phase noise. It has been shown that the influence of the FFT on the phase noise properties of an arbitrary signal $\mathcal{L}_{\Xi}(f_m)$ is [87]:

$$\mathcal{L}_{FFT}(f_m) = \mathcal{L}_{\Xi}(f_m) \cdot \frac{F_S}{M} \tag{2.34}$$

with the number of samples M within a timeframe $T_{OBS}$, and the sampling rate $F_S$.

For a photonic radar system without an optical receive path, the overall phase noise results in:

$$\mathcal{L}_{FFT}(f_m) = \frac{N^2 F_S}{M} \left[\mathcal{L}_{AM-PM} + \mathcal{L}_{FMCW}(f_m)\right] \cdot \left[1 - \cos\left(2\pi f_m \left\{\frac{2R}{c_0} - \frac{\Delta L}{c_f}\right\}\right)\right] \tag{2.35}$$

and for a system with an optical receive path:

$$\begin{aligned}\mathcal{L}_{FFT}(f_m) = {} & \frac{N^2 F_S}{M} \left[\mathcal{L}_{AM-PM} + \mathcal{L}_{FMCW}(f_m)\right] \\ & \cdot \left[1 - \cos\left(2\pi f_m \left\{\frac{2R}{c_0} - \frac{\Delta L}{c_f}\right\}\right)\right] + \frac{F_S}{M}\mathcal{L}_{AM-PM,RX}(f_m)\end{aligned} \tag{2.36}$$

In both cases, the additional term due to the AM to PM conversion in the optoelectronic path adds up to the overall phase noise of the entire system.

To visualize the upconversion of the AM noise to the desired LO and its harmonics, and the AM to PM conversion, simulations were performed. In these simulations, the laser $RIN$ is modeled as [95]:

$$RIN(j\omega_m) = \frac{RZ^2(1 + A\omega_m^2)}{Z^2\left(Y^2 - 2Z\right)\omega_m^2 + \omega_m^4} \tag{2.37}$$

with $\omega_m$ the offset frequency from the optical carrier, and the fitting parameters A,R,Y,Z. Table 2.1 [95] provide the fitting parameter for the laser RIN used in the simulations. A frequency of $5\,\mathrm{GHz}$ was selected to visualize the overlap of phase noise induced by the upconversion of laser RIN. At the target LO frequency of $19.25\,\mathrm{GHz}$, this overlap would not be observable.

| $f_0$ | $\alpha$ | A | R | Y | Z | $\mu$ | $V_\pi$ |
|---|---|---|---|---|---|---|---|
| $5\,\mathrm{GHz}$ | $1.41$ | $1.037 \cdot 10^{-19}$ | $7.983 \cdot 10^{-15}$ | $5.306 \cdot 10^{9}$ | $2.041 \cdot 10^{20}$ | $0$ | $5\,\mathrm{V}$ |

TABLE 2.1: Simulation and fitting parameter for the laser RIN [95]

Figure 2.9a illustrates the phase noise induced by laser RIN as a function of angular frequency for various drive voltage amplitudes applied to the MZM. Equation 2.25 predicts the upconversion of BB noise to the desired LO frequency and its harmonics. As the drive voltage increases, a greater portion of BB noise is upconverted to the desired LO frequency, reaching a maximum around $\frac{3}{4}V_\pi$. Beyond this point, additional BB noise is predominantly upconverted to higher-order harmonics, whose influence on the desired LO band is sufficiently attenuated.

The phase noise induced by MZM drive voltage fluctuations is shown in figure 2.9b as a function of the standard deviation of white Gaussian noise with a mean

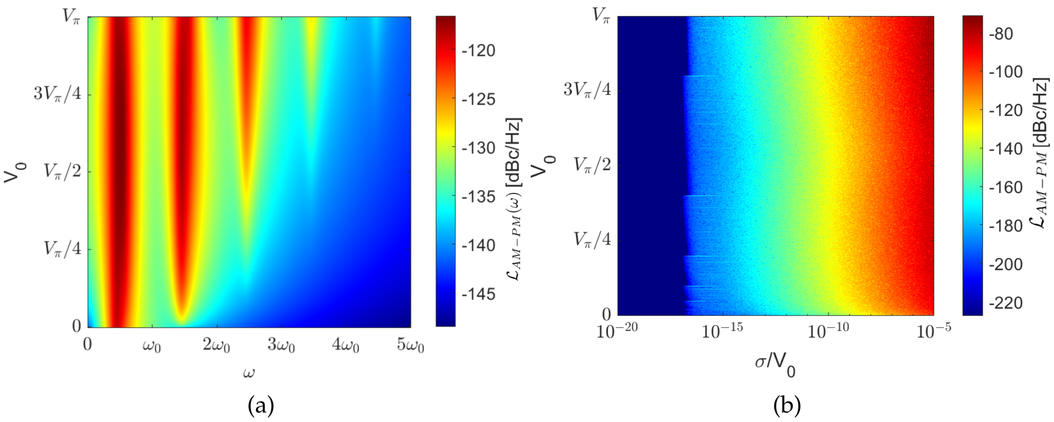

(a) (b)

Figure 2.9: Simulated phase noise induced by (a) laser RIN as function of the angular frequency ($\omega_0 = 2 \cdot \pi \cdot 5\,\mathrm{GHz}$) for different MZM drive voltages for $\alpha = 1.41$ (see eq.2.32); (b) MZM drive voltage fluctuations for $\alpha = 1.41$ (see eq.2.32), and an offset frequency of 1 Hz.

value of zero for different drive voltages of the MZM at $\omega = \omega_{LO} + 1\,\mathrm{Hz}$. Below a standard deviation of $\sigma = 10^{-10}$, the AM to PM conversion induced by the drive voltage fluctuations is below that induced by laser RIN.

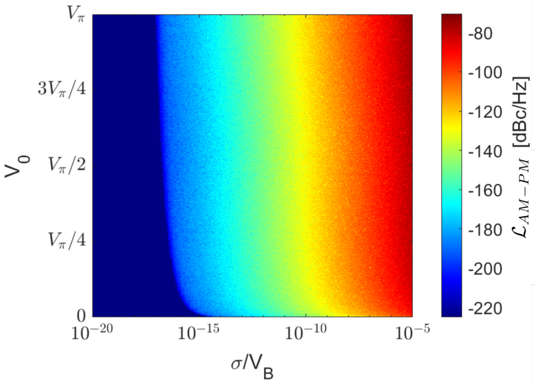

Figure 2.10: Simulated phase noise induced by MZM bias point fluctuations for $\alpha = 1.41$, and an offset frequency of 1 Hz.

In the previous derivations, the phase noise induced by bias point fluctuations of the MZM was neglected. Figure 2.10 illustrates the phase noise as a function of the standard deviation of white Gaussian noise with a mean value of zero for different drive voltages of the MZM at $\omega = \omega_{LO}$. Similar to the drive voltage noise, for a standard deviation below $\sigma = 10^{-10}$, the AM to PM conversion induced by the bias voltage fluctuations is below that induced by laser RIN.

## 2.4 Conclusion

Within this chapter, the central station along with the TX and RX frontends of the proposed photonic FMCW MIMO radar system with optical LO distribution are presented. The FMCW signal is generated and the EO conversion is carried out in the transmit section of the central station.

In both the TX and RX frontends, the optical LO signal is first converted into an electrical signal, followed by upconversion to the mm-wave band. In the TX frontend, the resulting mm-wave signal is amplified prior to transmission.

In the RX frontend, the received signal is downconverted to the BB and subsequently transmitted back to the central station via an optical receive path.

Within the receive section of the central station, OE conversion and MIMO signal processing are performed.

Subsequently, the proposed photonic FMCW MIMO radar system with optical LO distribution was analyzed. To simplify the analysis, only the first-order Bessel function was considered. For an argument of the Bessel function $\frac{V_0 \pi}{V_\pi} \leq 1.4$ the error is below 10 %. Under this approximation, the photonic FMCW MIMO radar system with optical LO distribution produces approximately the same IF signal as a purely electronic radar.

As a preparatory step for the phase noise analysis, the phase noise of the three most prominent EO conversion techniques was measured: optical beating of two lasers, intensity modulation of a CW laser using a MZM, and direct intensity modulation. The results showed that the MZM approach introduces the least additional phase noise into the system.

For the phase noise analysis of the photonic FMCW MIMO radar system with optical LO distribution, an additional term must be included to account for AM-to-PM conversion effects arising from the EO and OE conversion processes.

Parts of the content presented in this chapter have previously been published by the author [49, 52, 61].

# Chapter 3

# System and Circuit Simulation

Within the previous chapters, the photonic FMCW MIMO radar system with optical LO distribution was presented and analyzed. In order to optimize wireless systems, an accurate system model is essential. In this chapter the photonic FMCW MIMO radar system with optical LO distribution is modeled.

Several electronic design environments (EDEs) are available on the market for various use cases. For the modelling of a photonic radar system, an EDE must support both electronic and photonic system and circuit design. Current EDE software tools support either electronic or photonic system and circuit design, but not both. Therefore, the photonic radar system is implemented in Lumerical-Interconnect from Ansys for the photonic system and circuit design and in Keysight's ADS for the electronic system and circuit design.

In the first section, the photonic radar system is implemented in the optical design environment Lumerical-Interconnect from Ansys. With this model, the working principles of the architecture shall be validated.

A more realistic system model of the photonic FMCW MIMO radar system with optical LO distribution is presented in the second section of this chapter. The entire system is modeled in ADS from Keysight. This EDE allows detailed modeling of the nonidealities of the electronic components of the radar system. However, ADS does not inherently support or offer optical models. To overcome the limitations of the EDE, Verilog-A models are used to implement the optical components [96]. The modular approach of the proposed system model allows to exchange the generic building blocks with the post layout results to validate the performance of the designed components in the entire system.

In the last section of this chapter, a behavioral model of a monolithic integrated photonic radar transceiver chipset is presented. With such a model, the influences of parameter variations, such as PD bandwidth fluctuations, can be analyzed without performing time-consuming Monte Carlo simulations.

## 3.1 Modelling in an Optical Design Environment

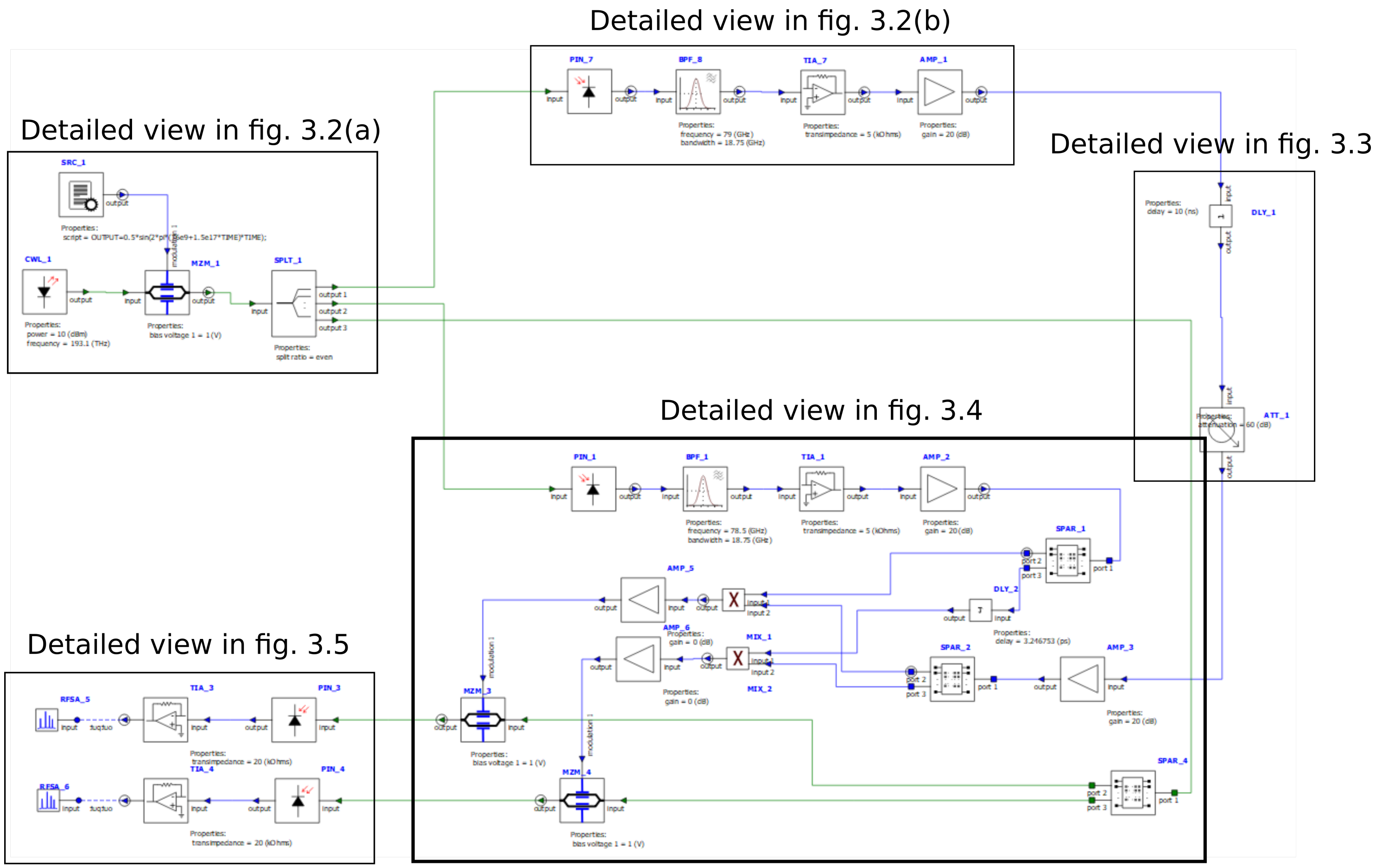

FIGURE 3.1: Overall simulation setup of the photonic FMCW radar system with optical LO distribution and optical IQ return path. (High resolution images in [97].)

Figure 3.1 shows the overall simulation setup of the photonic FMCW radar system with optical LO distribution in the optical design environment Lumerical Interconnect. The setup includes the optical LO generation, the TX frontend, the noiseless channel, the RX frontend with optical IQ return path, and the IQ receiver in the central station.

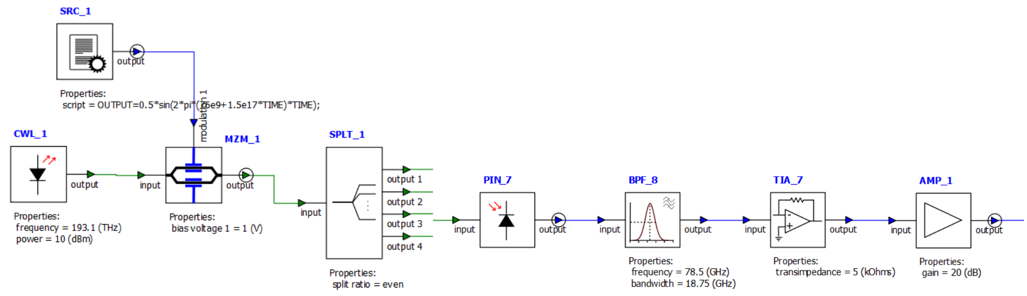

(a) (b)

FIGURE 3.2: Implementation of the (a) optical LO generation; (b) TX frontend in Lumerical Interconnect.

Figure 3.2a shows the optical LO generation. A scripted electrical source (SRC_1) drives an MZM (MZM_1), which is biased at the quadrature point and fed by a CW laser (CWL_1). The scripted electrical source generates a 77 GHz FMCW chirp with the amplitude $V_0/V_\pi = 1/8$, and $\mu = 7.5 \cdot 10^{16}\,\mathrm{s}^{-2}$. The high chirp rate is motivated by the finite frequency resolution of Lumerical Interconnect. The optical signal is split into four channels: one for the TX frontend, one for the LO distribution of the RX frontend, one for the optical receive path, and one for the coherent detection in the receiver part of the central station.

Within the TX frontend, the optical signal is converted into an electrical signal using a PD (PIN_7) and a TIA (TIA_7). To suppress higher-order harmonics generated by the MZM, a band-pass-filter (BPF) (BPF_8) is inserted between the PD and TIA. The electrical signal provided by the TIA is further amplified by an amplifier block (AMP_1), which represents the PA in the real forntend.

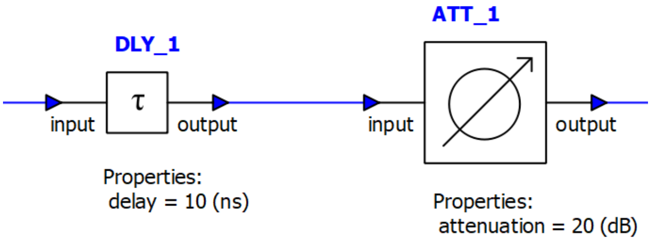

FIGURE 3.3: Implementation of the noiseless channel in Lumerical Interconnect.

Figure 3.3 shows the implemented noiseless channel. The time of flight is implemented with a delay element (DLY_1), and the free space path loss, antenna gain, and reflection coefficient of the obstacle are realized with an attenuator block (ATT_1) with a damping of 20 dB.

Figure 3.4 shows the implementation of the RX frontend with optical in phase quadrature phase (IQ) return path. The RX frontend uses the same PD (PIN_1), BPF (BPF_1), TIA (TIA_1), and amplifier (AMP_2) architecture as the TX frontend for the OE conversion of the LO signal. Since no electrical 90° hybrid couplers or electrical phase shifters are available in Lumerical Interconnect, an ideal 3 dB coupler, implemented by an S-parameter component (SPAR_1) and a delay element (DLY_2), was used to generate the electrical IQ LO signal.

The weak received input signal is amplified by an amplifier (AMP_3) and split by the S-parameter component (SPAR_2). The output signal of the splitter is mixed with the IQ LO signal by means of two mixers (MIX_1 & MIX_2). The output signals of the mixers are further amplified via amplifier components (AMP_5 & AMP_6). The subsequent MZMs (MZM_3 & MZM_4) are driven by the output voltage and fed by the optical IQ signal. The IQ signal is generated by the optical S-parameter block (SPAR_4) fed by one channel of the optical LO generation block. Finally, the two optical signals transmitted back to the central station.

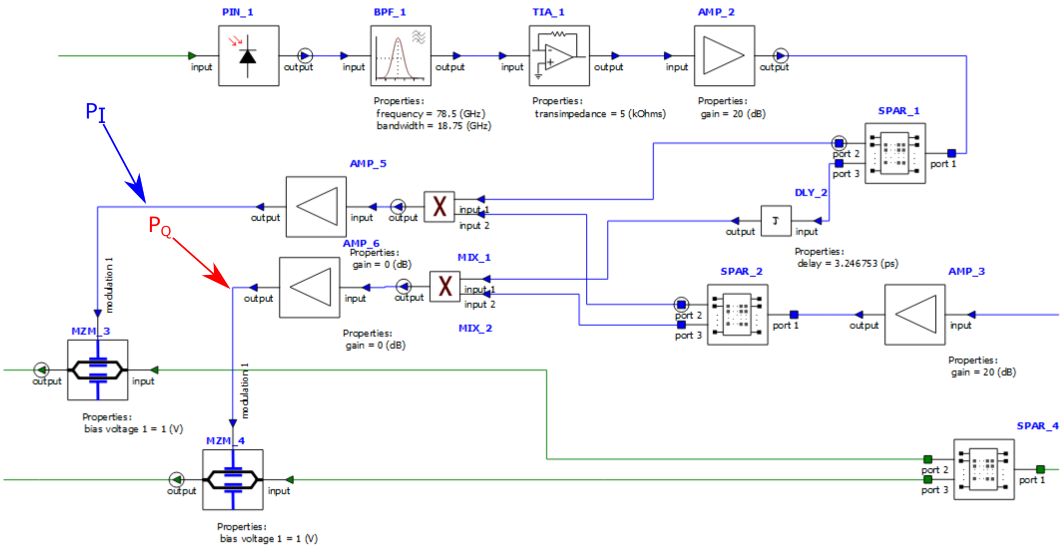

FIGURE 3.4: Implementation of the RX frontend with optical IQ return path.

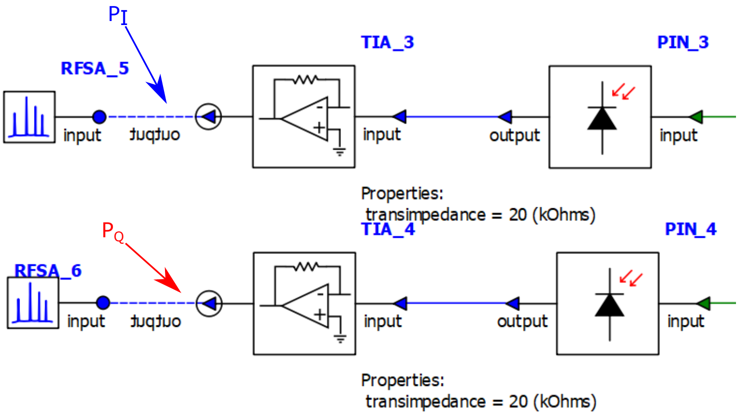

FIGURE 3.5: Implementation of the optical IQ receiver in the central station.

Figure 3.5 shows the optical IQ receive part in the central station. The two optical signals are converted into electrical signals using PDs (PIN_3–PIN_4) and TIAs (TIA_3–TIA_4). The spectrum of the resulting electrical IQ signal is then captured by the electrical spectrum analyzer components RFSA_5 and RFSA_6.

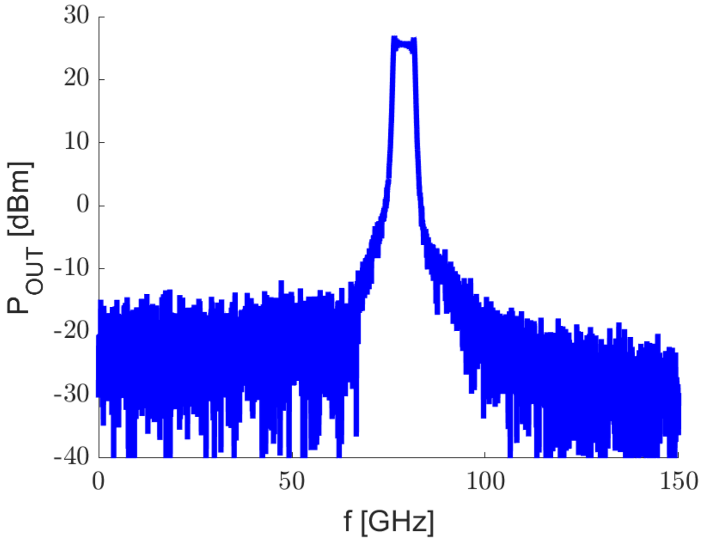

FIGURE 3.6: Simulated FMCW transmit chirp.

The simulated transmitted FMCW chirp in the frequency domain at the end of the TX frontend is shown in figure 3.6. The transmitted signal has a bandwidth of 3 GHz around a center frequency of 78.5 GHz. The FFT noise is at least 30 dB lower than the desired signal.

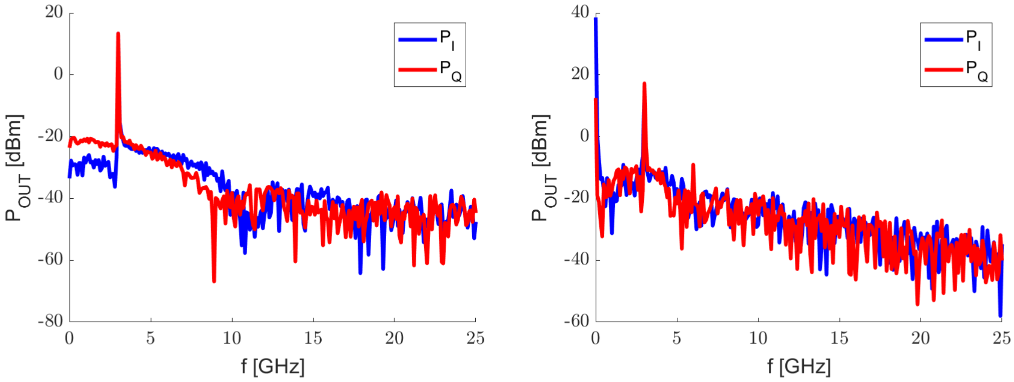

(a) (b)

FIGURE 3.7: Simulated IF signal in the (a) RX frontend before optical IQ receive path; (b) central station after optical IQ path.

The simulation results of the IF signals are shown in figure 3.7. The IF signal before the optical receive path, shown in figure 3.7a, clearly shows the target at the IF frequency of 3 GHz, which corresponds to the analytical solution. The signal to noise ratio (SNR) is above 30 dB. The IF signal after the optical IQ return path, shown in figure 3.7b, shows the same IF peak. In addition, the spectrum consists of a DC component and a second harmonic signal at 6 GHz, slightly above the noise level. Higher order harmonics induced by the nonlinear function of the MZM are masked by the FFT noise.

## 3.2 Modelling in an Electrical Design Environment

Within the previous section, the photonic FMCW MIMO radar system with optical LO distribution was modeled in an optical design environment. Within this section, the system is implemented in an electrical design environment.

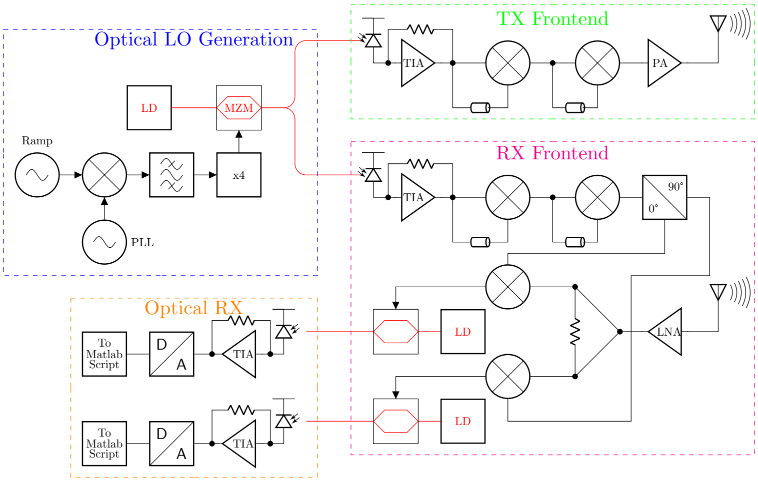

FIGURE 3.8: Simplified block diagram of the implemented photonic radar system.

The block diagram of the implemented photonic radar system is shown in figure 3.8. It consists of the optical LO generation, including the electrical FMCW signal generation, the TX frontend, the wireless channel, the RX frontend including an IQ downconversion mixer, and the optical receive part of the central station. The optical receive part also includes the analog to digital (AD) conversion and an interface to a MATLAB script. The overall simulation setup of the photonic FMCW radar system with optical LO distribution in the electronic design environment ADS Ptolemy from Keysight is shown in figure 3.9.

Figure 3.10 shows the implemented electrical LO generation in the electronic design environment Keysight ADS Ptolemy. The ramp block R1 generates an electrical voltage ramp with the repetition rate $t_{\text{Ramp}}$. The voltage ramp is converted into a frequency ramp by the frequency modulator block F1. The carrier signal is generated by a constant source (C1) and a second frequency modulator block (F2). The ramp signal and the carrier signal are multiplied by a mixer (MIX5). To suppress unwanted spurs, the output signal of the mixer is filtered by a BPF (BPF3). The output signal of the BPF is upconverted to the desired LO frequency by means of two mixers (MIX6 & MIX7). To suppress the DC output signal of the mixers, 90° phase shifters (PS4 & PS5) were inserted between the RF and LO ports of the mixer [98]. The unwanted mixing products are canceled by BPFs (BPF4 & BPF5). The LO signal at the desired frequency is split into two paths, one for the LO signal generation for the TX frontends, and one for the RX frontends.

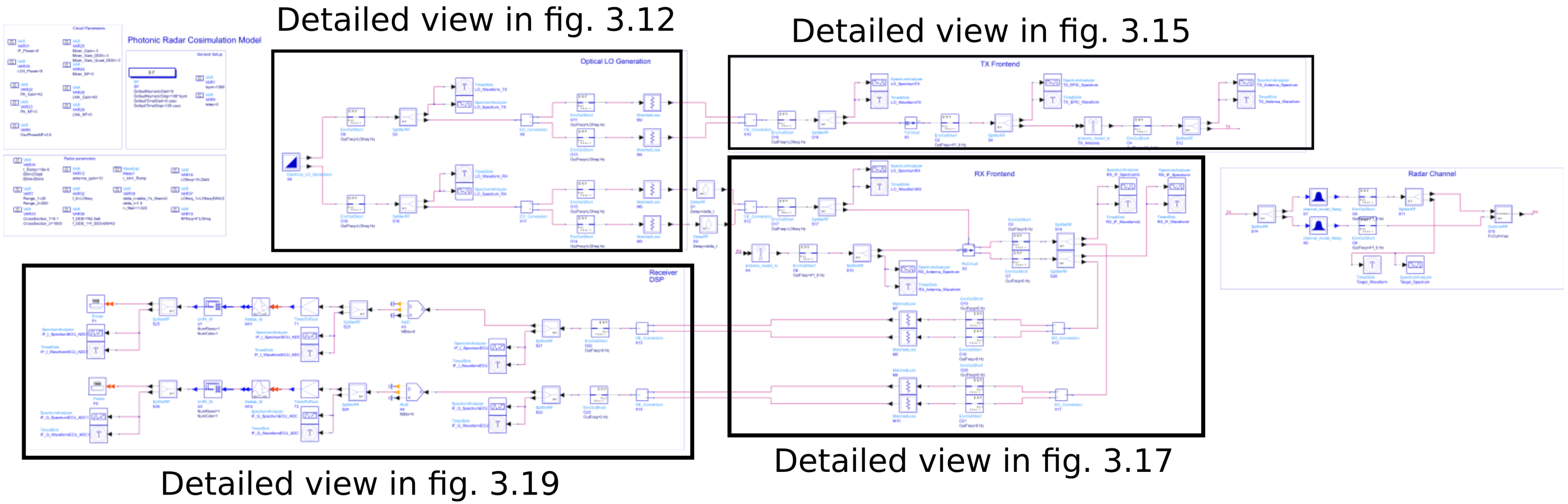

FIGURE 3.9: Overall simulation setup of the photonic FMCW radar system with optical LO distribution and optical return path in the electronic design environment Keysight ADS Ptolemy.

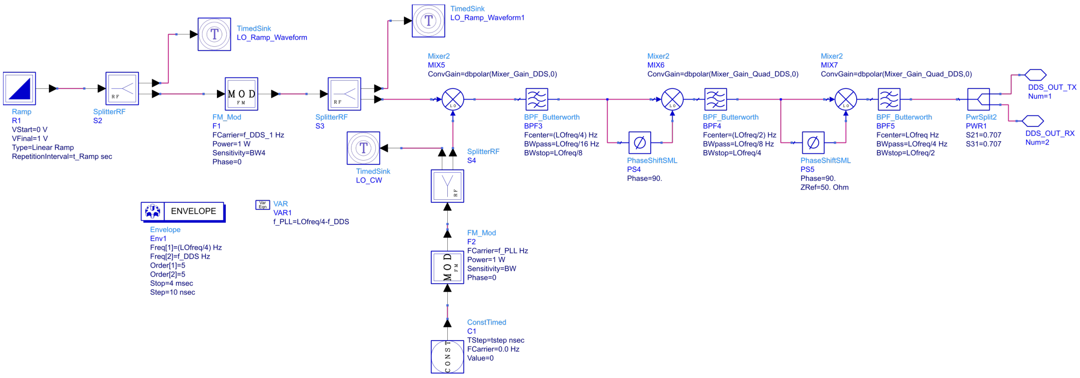

Figure 3.10: Implementation of the electrical LO generation in the electronic design environment Keysight ADS Ptolemy.

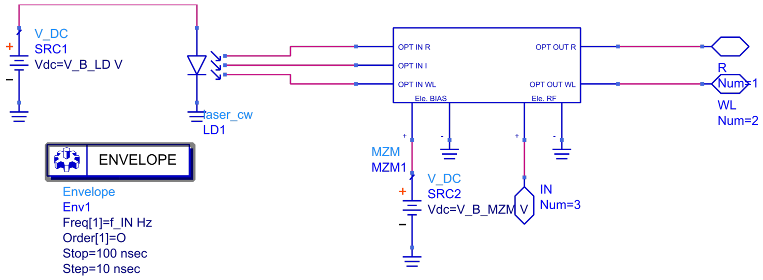

Figure 3.11: Implementation of the EO conversion in the electronic design environment Keysight ADS Ptolemy.

The implementation of the EO conversion in the electronic design environment Keysight ADS Ptolemy is shown in figure 3.11. Since no optical components are available in ADS, self-coded components which are based on [96] were implemented in Verilog-A. The codes are given in [99]. For the EO conversion, a CW laser generates a complex electric field with a specific wavelength, which feeds the MZM (MZM1). The output power of the CW laser is proportional to the electrical source SRC1. It should be noted that in a physical model, the output power of the laser would be proportional to the input current. The MZM has two electrical inputs. One is for the setup of the bias point and the other is for the electrical LO signal. Within the Verilog-A code, the two electrical ports have a low-pass behavior with different cutoff frequencies. This is motivated by the fact that the bias point is typically adjusted by thermal phase shifters in silicon-based MZMs [100], which have a much higher response time compared to the reverse biased, lateral PN phase shifters [100], which are commonly driven by the RF port in silicon-based MZMs. With the electrical source SRC2, the MZM is biased at the quadrature point. Via the node IN, an external RF drive voltage can be connected. Since the output current of the subsequent PD in the TX and RX frontend is proportional to the incident optical intensity, the MZM generates an optical output intensity proportional to the incident complex optical electric field. The amplitude of the optical output signal is controlled by the RF signal.

Figure 3.12 shows the implementation of the optical LO generation. It consists of the electrical LO signal generator X8 with its two output signals and the two EO conversion units X9 and X11. The EnvOutShort components (O9, O11, O13, O14, O15, & O16) are ideal shorts, needed for the simulator. The splitter blocks S3 and S18 with the time sink and the spectrum analyzer are inserted for observation purposes.

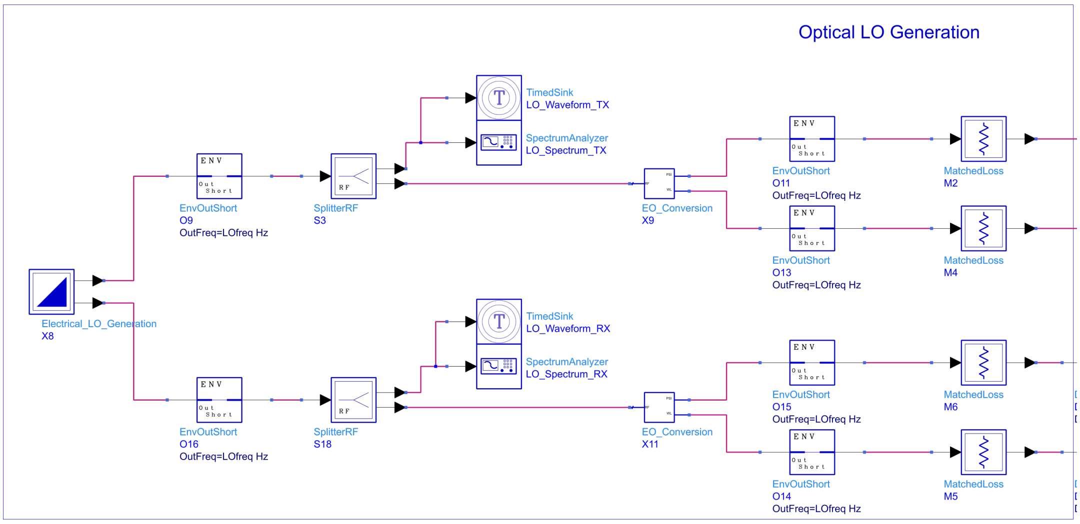

FIGURE 3.12: Implementation of the optical LO generation in Keysight's ADS Ptolemy.

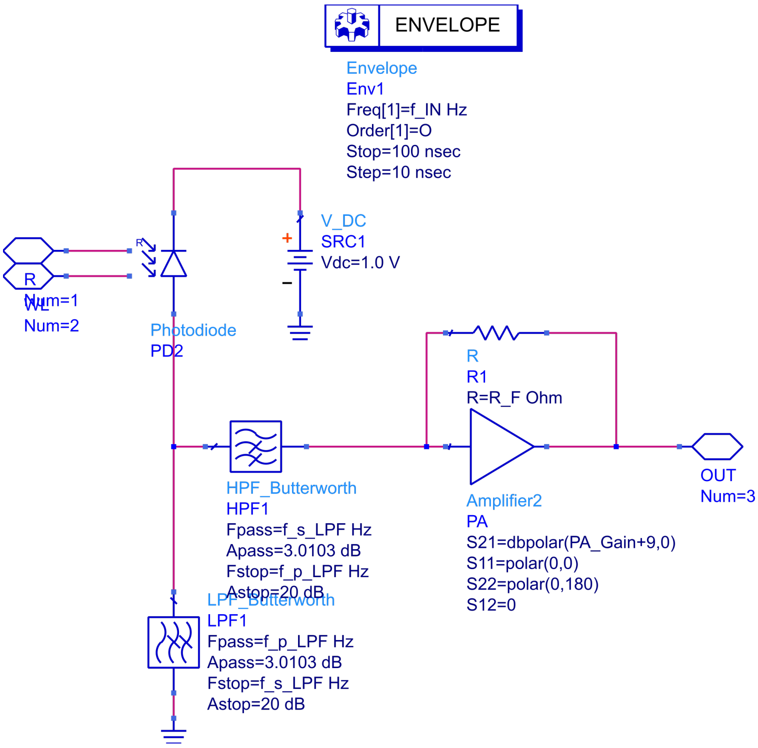

FIGURE 3.13: Implementation of the OE conversion in Keysight's ADS Ptolemy.

The implementation of the OE conversion in the electronic design environment ADS Ptolemy from Keysight is shown in figure 3.13. It consists of a reverse-biased PD, implemented via a Verilog-A script. The DC current of the PD is shorted via a low-pass-filter (LPF) (LPF1), while the LO signal is fed to a TIA. The TIA consists of an amplifier (PA) and a feedback resistor $R_F$.

Figure 3.14 shows the implemented electronic components of the TX electronic photonic interated circuits (EPIC) in Keysight's ADS Ptolemy. It consists of the frequency upconversion to the desired mm-wave frequency band, implemented by means of mixers (MIX5 & MIX6). Similar to the electrical LO generation, $90°$ phase

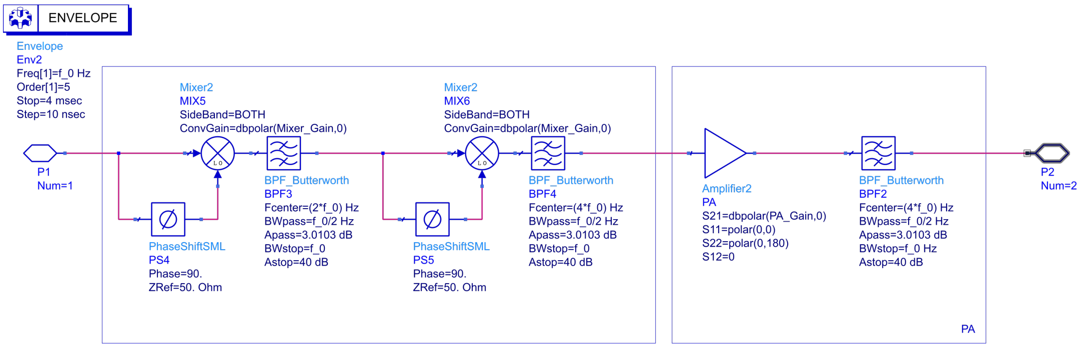

Figure 3.14: Implementation of the electronic components of the TX EPIC in Keysight's ADS Ptolemy.

shifters were inserted between the RF and the LO port of the mixer to suppress the unwanted DC component at the output of the mixer [98]. Furthermore, the unwanted mixing products are canceled by BPFs (BPF3 & BPF4). The PA is implemented by means of an amplifier (PA). The unwanted harmonics generated by the PA are canceled by the output BPF (BPF2).

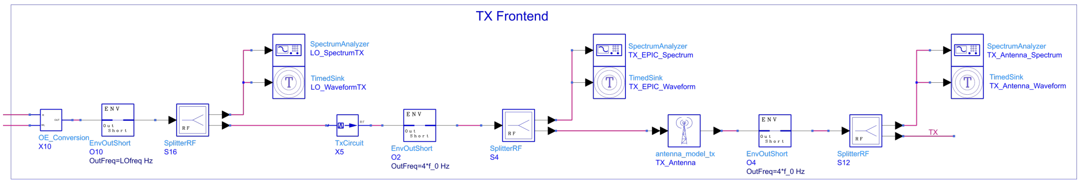

Figure 3.15: Implementation of the entire TX frontend in Keysight's ADS Ptolemy.

The implemented entire TX frontend in the electronic design environment ADS Ptolemy from Keysight is shown in figure 3.15. The optical input signal is converted to an electrical signal by means of the OE conversion block (X18). The electrical LO signal is fed into the block containing the electrical components of the TX EPIC, followed by the model of the transmit antenna (TX_Antenna). The transmit antenna is modeled as an amplifier with gain equal to the antenna gain.

The model of the noisy wireless channel is similar to the one in [101], shown in figure 3.16a. Within the channel, the Doppler shift is added to the transmitted signal via a single sideband mixer. In order to model the free space path loss the signal is attenuated with the loss $G_C(j\omega)$. In addition to [101], a noise source is added at the output of the wireless channel.

Figure 3.16b shows the implemented noisy wireless channel in the electronic design environment ADS Ptolemy from Keysight. The left-hand side of the block diagram features a single-sideband modulator [102] for applying the Doppler shift. Therefore, the input signal is split into an in-phase and a quadrature-phase path by means of a power divider (PWR1) and two phase shifters (PS1 & PS2). In each path, the input signal is multiplied by multiplier blocks (MULT1 & MULT2) with the signal provided by the sources SRC1 and SRC2. The two sources are $90^\circ$ out of phase. The output signals of the two multipliers are summed up by a power combiner (PWR2) before the signal is attenuated by an amplifier block (AMP1). The attenuation factor models the free-space path loss. The noise is added by an additive noise source (SRC3).

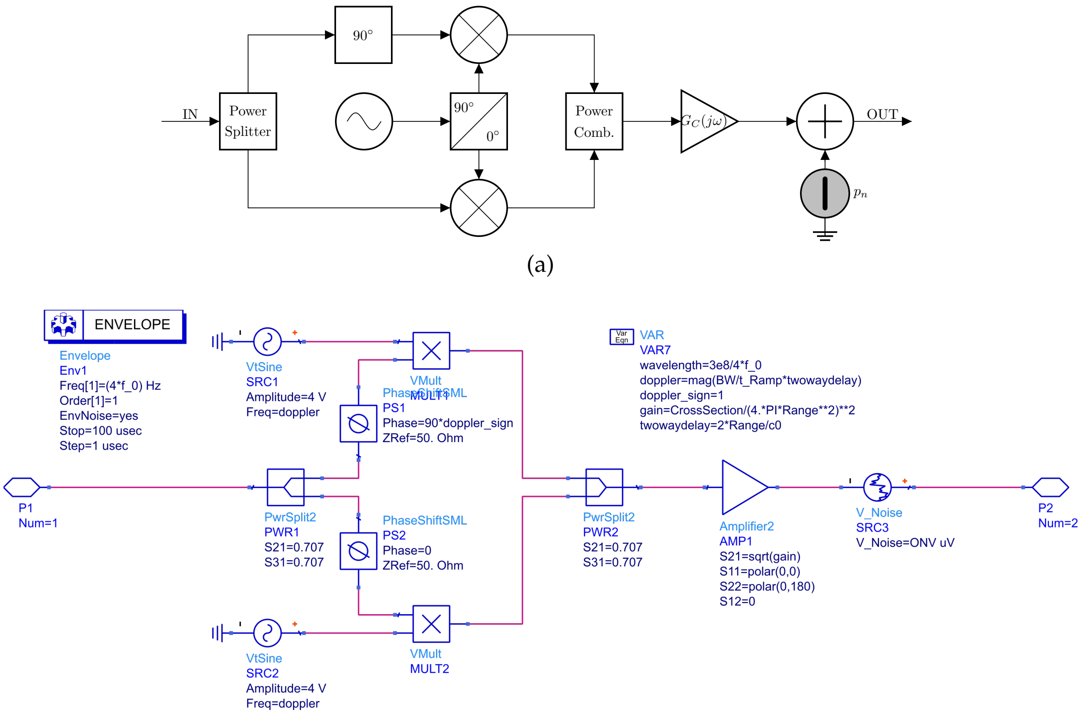

(a)

(b)

Figure 3.16: (a) Block diagram of the noisy wireless channel with Doppler shift; [101](b)Implementation of the noisy wireless channel with Doppler shift in Keysight's ADS Ptolemy.

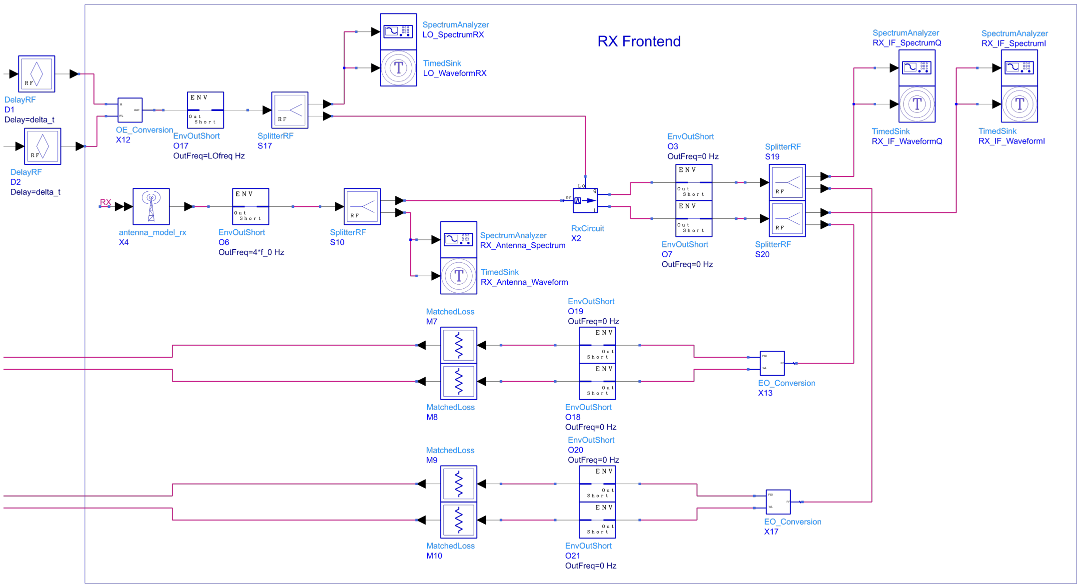

Figure 3.17: Implementation of the RX frontend in Keysight's ADS Ptolemy.

Figure 3.17 shows the implemented RX frontend in the electronic design environment ADS Ptolemy. Since the losses of a fiber can be neglected, an arbitrary length offset can be introduced between the TX and RX frontend. This length offset leads to an offset in the IF frequency. Otherwise, in the case of an optical return path, the IF frequency of nearby targets could fall below the lower cut off frequency of the MZM. This length offset is implemented by the delay blocks (D1 & D2). The optical LO signal is converted to an electrical signal by means of an OE conversion block (X12) before it is fed into the LO port of the electronic part of the RX frontend (X2). The received signal, which is amplified in the antenna model block X4, representing the antenna gain, is fed into the RF port of X2. The IQ output signals of X2 are converted back to the optical domain by means of two individual EO blocks (X13 & X17).

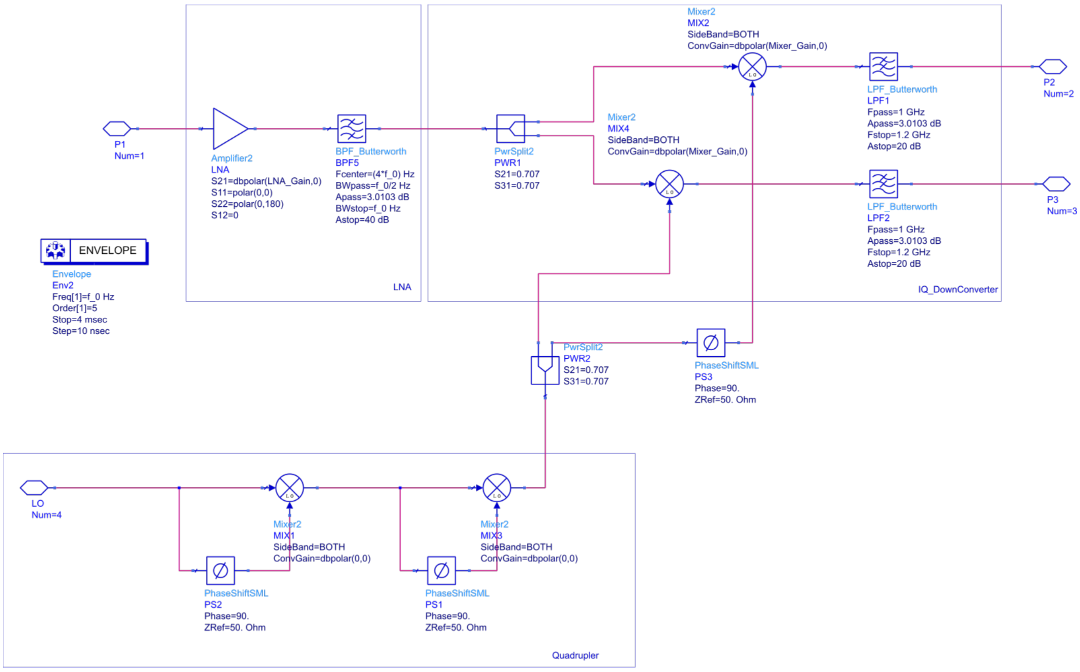

Figure 3.18: Implementation of the electronic part of the RX frontend in Keysight's ADS Ptolemy.

The electronic part of the RX frontend is shown in figure 3.18. The upconversion of the LO signal to the desired frequency band is implemented similarly to the TX frontend by means of mixers (MIX1 & MIX3) and phase shifters (PS1 & PS2). The LO signal at the desired frequency is split into an IQ signal by means of a power splitter (PWR2) and a phase shifter (PS3).

The RF input signal, provided at the RF port, is amplified by an amplifier block (LNA) and filtered by a BPF (BPF5). The signal is split into two paths. In each path, the received signal is amplified with the in-phase or quadrature signal. To cancel the high-frequency component, LPFs (LPF1 & LPF2) are inserted at the output of the mixers. The output signal of the LPFs are connected to the output ports of the electronic part of the RX frontend.

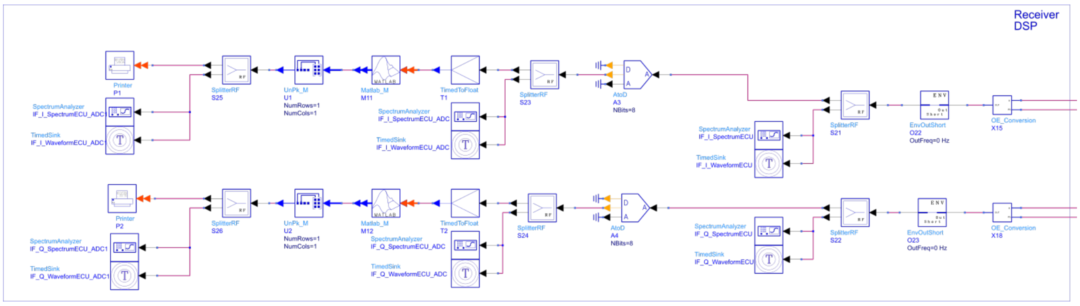

Figure 3.19: Implementation of the receive part of the central station in Keysight's ADS Ptolemy.

Figure 3.19 illustrates the receiving part of the central station, implemented in the electronic design environment ADS Ptolemy. The downconverted optical signal is converted into an electrical signal using OE conversion blocks (X15 & X18). Since the LPF in the OE conversion block, shown in figure 3.13, shorts the DC photocurrent, the LPFs must have a cutoff frequency lower than the minimum expected input frequency. To account for the quantization noise of the analog to digital converter (ADC) in the model, the electrical signal is quantized using ADC blocks (A3 & A4).

For the realization of the Matlab interface, the data format needs to be adjusted. Since ADS Ptolemy uses the data format 'timed', while Matlab expects data in the format 'float', data format conversion blocks (T1 & T2) are placed between the ADC and the Matlab block. Without loss of generality, the Matlab code multiplies the input data with a constant number $> 1$. Since ADS assumes that Matlab delivers an output matrix, while ADS Ptolemy needs a data stream, matrix to serial blocks (U1 & U2) are used. Finally, the data are stored by the printer blocks P1 and P2.

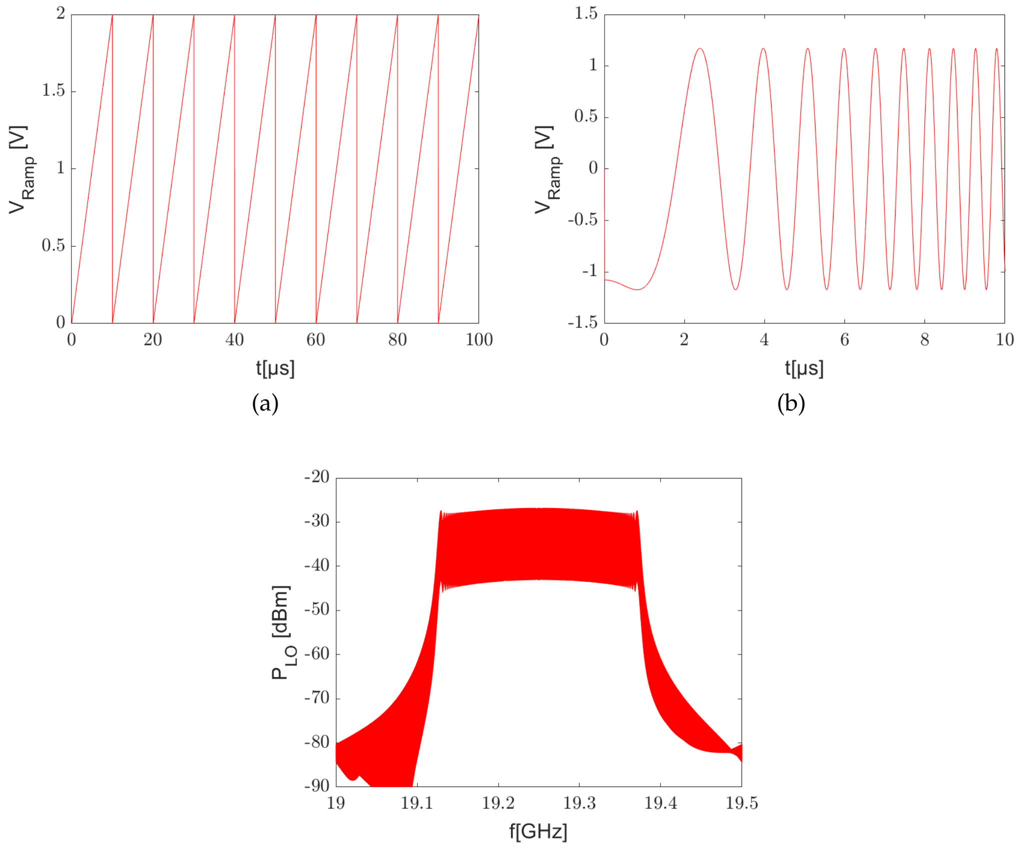

(a)

(b)

(c)

FIGURE 3.20: (a) Drive voltage of the frequency modulator block in the time frame $0\,\mathrm{s} \leq t \leq 100\,\mu\mathrm{s}$; (b) Time domain signal of the FMCW chirp in the time frame $0\,\mathrm{s} \leq t \leq 10\,\mu\mathrm{s}$; (c) Spectrum of the electrical LO signal in the base station.

Figure 3.20 shows the simulation results of the LO signal generation. The electrical ramp generator synthesizes a sawtooth signal with the repetition rate of $10\,\mu\mathrm{s}$. The time domain signal is shown in figure 3.20a. The corresponding FMCW chirp in the time frame $0\,\mathrm{s} \leq t \leq 10\,\mu\mathrm{s}$ is shown in figure 3.20b. For visualization purposes, the bandwidth in figure 3.20b was reduced to $1\,\mathrm{MHz}$ instead of $250\,\mathrm{MHz}$. The LO spectrum with the target bandwidth 250 MHz with a carrier of 19.25 GHz is shown in figure 3.20c. After upconversion to the mm-wave band in the TX frontend, the spectral properties fit into the 77 GHz radar band.

In chapter 2.2 the nonlinear behavior of the entire photonic assisted radar system with optical receive path was derived. To validate the theory, a two-target scenario with targets at different positions and with different radar cross-sections was simulated in the electronic design environment. Within this scenario, it is assumed that the EO modulator, which generates the optical LO signal, is operating in the linear region.

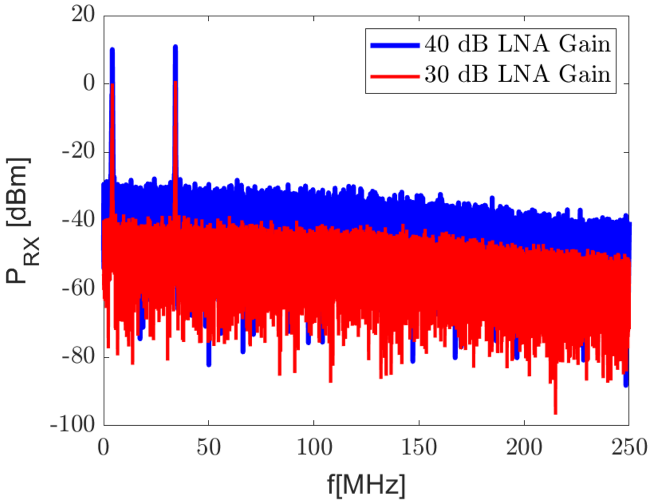

FIGURE 3.21: Simulation results of the downconverted in-phase signal at the output of the RX frontend before OE conversion. Blue: 40 dB LNA gain; Red: 30 dB LNA gain.

The simulation results of the downconverted signal at the output of the RX frontend before the OE conversion are shown in figure 3.21. The two desired targets occur at an IF frequency of 10 MHz and 40 MHz. The radar cross-sections of the different targets were chosen in such a way that both signals have the same amplitude. In addition, both IF signals have an SNR of approximately 40 dB. The noise floor is limited by the FFT noise and the noise of the wireless channel. For further analysis of the nonlinear effects of the optical receive path, two simulations with different LNA gains were performed. In the further simulations, an LNA gain of 30 dB leads to linear behavior, while an LNA gain of 40 dB leads to nonlinear behavior.

The IF spectrum after the optical receive path to the central station is shown in figure 3.22. If the MZM operates in the linear region, the received IF signal in the central station has the same spectral properties as the one before the optical receive path. If the MZM operates in the nonlinear region, five additional ghost targets occur in the IF spectrum. The first ghost target is located at the second harmonic of the first target and is just above the noise floor. The second and third ghost targets are located symmetrically around the second harmonic of the IF signal. The spacing of the ghost target spectrum to the desired carrier is twice the IF frequency of the first target. The last two ghost targets are located symmetrically around the second harmonic of the second target. The spacing between these two ghost targets is twice the IF frequency of the first target. These second to fifth ghost targets are generated due to a convolution of the nonlinear effects of intermodulation distortion and cross-modulation.

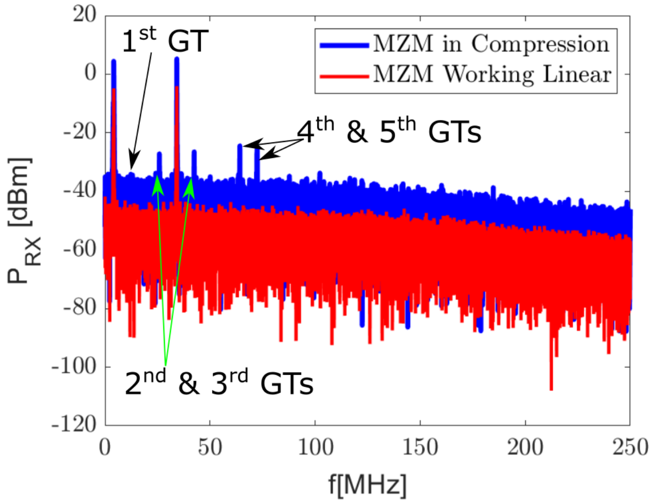

FIGURE 3.22: Simulation results of the downconverted in-phase signal after the optical receive path to the central station. Blue: MZM in compression; Red: MZM operates linearly.

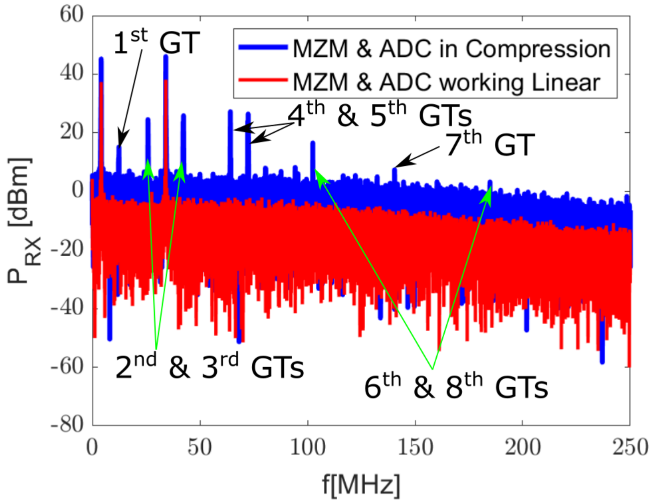

FIGURE 3.23: Simulation results of the downconverted in-phase signal after the ADC and the Matlab script. Blue: MZM & ADC in compression; Red: MZM & ADC operate linearly.

The quantized signal after the ADC and the Matlab interface is shown in figure 3.23. The IF spectrum contains eight ghost targets: The initial five from the nonlinear characteristic of the MZM, multiplied by a constant factor greater than one, and additional three ghost targets at even harmonics of the IF frequency of the second target. These additional ghost targets were previously masked by the noise floor of the FFT. In addition, the compressive behavior of the ADC also adds some intensity to these ghost targets.

## 3.3 Behavioural Model of a Monolithic Integrated Photonic Radar Transceiver Chipset

The previous sections of this paper focused on the modeling of the photonic FMCW MIMO radar system with optical LO distribution in optical or electronic design environments. This section presents more accurate device models, which can be included in the photonic radar system models in the optical or electrical design environment for high-accuracy system modeling for digital prototyping before costly system implementation.

The model of the photonic radar TRX chipset is based on a behavioral description of the S-parameters with subsequent gain compression. Instead of the complex modeling of the entire chipset at once, the chipset is subdivided into its building blocks, which can be modeled as two ports or three ports. Figure 3.24a shows the signal flow graph of an OE and electrical two-port, consisting of a linear two-port described by its S-parameters and subsequent gain compression blocks.

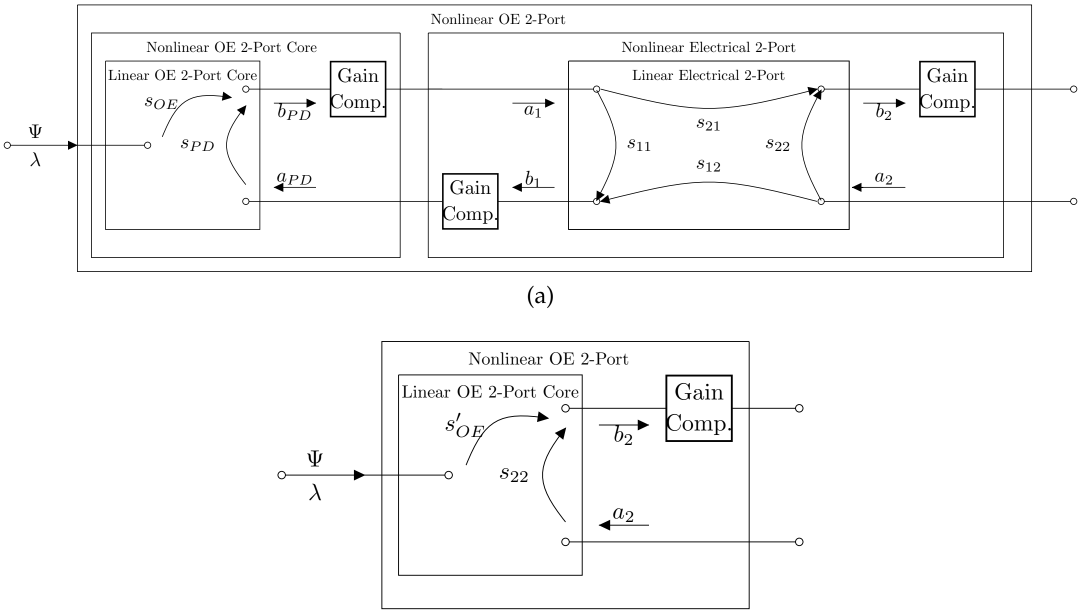

(a)

(b)

FIGURE 3.24: Signal flow graph of the OE model. (a) Detailed with OE core (e.g., PD) and electrical core (e.g., TIA) and (b) simplified using a combined OE block.

For the TIA and PD, a combined S-parameter block is used. This is motivated by the fact that the PD bandwidth has a direct effect on the overall TIA bandwidth, which needs to be taken into account. The simplified signal flow graph of a combined OE two-port is shown in figure 3.24b.

### 3.3.1 Behavioural Optoelectronic S-Parameter Model

According to S-parameter theory, the reflected wave vector $\vec{b}$ of a two-port is the superposition of the product of the incident wave vector $\vec{a}$ and its scattering matrix $\underline{S}$:

$$\vec{b} = \underline{S} \cdot \vec{a}. \tag{3.1}$$

For a single port $j$, this can be expressed by:

$$b_j = \sum_{i=1}^{n} S_{ji} a_i \quad \forall i. \tag{3.2}$$

To expand this formalism to unilateral OE systems, the reflected wave of port $j$ is given for $m$ optical inputs by:

$$b_j = \sum_{i=1}^{n} S_{e,ji}(j\omega) a_i + \sum_{k=1}^{m} S_{O,jk}(\lambda) \Psi_k, \tag{3.3}$$

where $\Psi_k$ is the optical incident intensity of port $k$.

The implementation of eq. 3.3 is based on the previously published controlled voltage source approach.

In the past, several methods were proposed for accurate S-parameter extraction. These parameters fit only for a single realization of a component. Within this thesis, the S-parameters are approximated by a finite-order transfer function:

$$S = \frac{\sum_{n=0}^{m} x_n s^n}{\sum_{d=0}^{k} y_d s^d}. \tag{3.4}$$

The order of the numerator and denominator depends on the subcomponent and the acceptable mismatch. Within this thesis, narrowband filter functions like bandpass or bandstop filters were used to describe the behavior of the S-parameters.

Besides the simplification using filter functions, nonlinear S-parameters were only used when necessary, such as for frequency doublers or the IQ downconversion mixer. In this case, the nonlinear S-parameters represent the relationship between an incident signal at a specific frequency and a reflected wave at another frequency.

### 3.3.2 Gain Compression

Gain compression can be modeled using high-order nonlinear S-parameters. Within this thesis, the number of nonlinear terms of the S-parameters is fixed to an absolute lower limit. As shown in figure 3.24b, a subsequent gain compression block limits the output signal [103]. In the past several publications proposed models to model the compressive behavior [104–106] with reasonable fitting to the measurement results. In this thesis a hyperbolic tangent is proposed. Based on the difference between the instantaneous output power and the saturated output power $P_{\text{OUT,Sat}}$, a hyperbolic tangent function generates a saturation limit. Eq. 3.5 shows the proposed approach [107]:

$$P_{\text{OUT,I}} = \frac{P_{\text{OUT,U}}}{2} \left\{ 1 - \tanh \left[ \alpha \left( P_{\text{OUT,U}} - P_{\text{OUT,Sat}} \right) + \gamma \left( P_{\text{OUT,U}} - P_{\text{OUT,Sat}} \right)^3 \right] \right\} \tag{3.5}$$

with $\alpha$ and $\gamma$ as weighting coefficients of the first and third order gain compression, and $P_{\text{OUT,I}}$ as the incident leveled output power.

In comparison to [104], the proposed model is also capable of capturing the declining behavior via the $\gamma$ term. Additionally, since the inner transistor—such as a heterojunction field-effect transistor—with its compressive characteristics can be modeled using a hyperbolic tangent function [107], the proposed model is well suited to model the compressive behavior of transistor based building blocks.

### 3.3.3 Noise Sources

The spectral properties of the input-referred noise source are generated similarly to the S-parameters using a behavioral spectral tailoring with a finite-order transfer function. This transfer function is used to manipulate the spectral properties of a white Gaussian noise source. The output is additively added as a source to the input of the circuit. The mathematical representation is given in eq. 3.6, eq. 3.7, and eq. 3.8 for a noisy voltage, current, and optical intensity source, respectively.

$$v_n = WN\,[V]\,\frac{\sum_{n=0}^{m} a_n s^n}{\sum_{d=0}^{k} b_d s^d} \tag{3.6}$$

$$i_n = WN\,[A]\,\frac{\sum_{n=0}^{m} c_n s^n}{\sum_{d=0}^{k} e_d s^d} \tag{3.7}$$

$$p_n = WN\,[W]\,\frac{\sum_{n=0}^{m} f_n s^n}{\sum_{d=0}^{k} g_d s^d} \tag{3.8}$$

with $WN$ as white Gaussian noise in the unit $[X]$, and the fitting coefficients $a_n$, $b_n$, $c_n$, $e_n$, $f_n$, and $g_n$.

### 3.3.4 Model Implementation and Verification

For the verification, the model was implemented in Verilog-A. Verilog-A was chosen due to its interoperability with different electrical or optical design environments like Keysight's ADS, Cadence Virtuoso, Synopsys, Lumerical Interconnect, and non-electronic design automation suites like Matlab. In addition, Verilog-A allows for simulating electrical and optical properties simultaneously [96].

A simplified pseudocode of a noisy optoelectronic component is shown in listing 3.1. The real code is given in [99]. It shows exemplary how the electronic and photonic properties, including the noise, were implemented in Verilog-A and how the optoelectronic conversion, the nonlinear behavior, the S-parameters, and the gain suppression are implemented.

```
’include "constants.vams"
’include "disciplines.vams"
//Module Definition
module OE_Comp (INPUT_1, ..., INPUT_N,
OUTPUT_1, ..., OUTPUT_M, GND);
//Input Port Definition
input INPUT_1, ... INPUT_N;
//Output Port Definition
output OUTPUT_1, ..., OUTPUT_M;
//InOut Definition
inout GND;
// External Photonic Node Definition
photonics INPUT_j, ...;
// External Electric Node Definition
electrical OUTPUT_i, Res_i, ...;
// Internal Photonic Node Definition
photonics PSI_internal_j, ...;
// Internal Electric Node Definition
electrical V_internal_i;
```

```
// Parameter Definition
parameter real c_i=1;
...
//Branches of the Electrical Noiseless Ports
branch (OUTPUT_i,Res_i) Source_i;
branch (OUTPUT_i,GND) OUT_i;
branch (Res_i, GND) Load_i;
...
// Optical Input Referred Noise Currents
branch (INPUT_j, PSI_internal_j) Psi_Noise_j;

analog begin
// White Noise Generation
wn=white_noise(noise, "noise");
//Frequency behaviour of the input referred optical
   noise
I(Psi_Noise_j)=laplace_nd(wn,n_n,d_n);

// Optical power calculated of the input signal
optical_power=EF(OPTIN);
// Optoelectronic conversion
I_PD=responsivity*laplace_nd(optical_power,n_PD,d_PD)
   ;

//Current in Resistor i
I_L_i=I(Load_i);
//Voltage over Resistor i
V(Load_i)<+Z_i*I(Load_i);
// Internal Voltage of a node
V(internal_i)<+ V(OUT_i)+V(Load_i);

// Calculation of s_ij^n
//For i=j:
V(Source_i)<+lapalce_nd(pow(V(internal_i),n),n_ii_n,
   d_ii_n);
//For i!=j:
OUT_i=lapalce_nd(pow(V(internal_j),n),n_ij_n,d_ij_n);

//Calculation of the power without gain supression
//Ouput Power of Port i
P_Port_i=-V(Load_i)*I_L_i+sum(V_IJ)*I_L_i;
//Output power of port i in dBm
P_Port_i_dBm=10*log(abs(P_Port_i)/1e-3);
//Gain suppression
//Calculation of the saturated source power
OUT_i=OUT_i/2*(1-tanh(alpha*(P_Port_i_dBm-P_i_sat)
+gamma*pow((P_Port_i_dBm-P_isat),3)));

//Adding saturated s_ij^n to the source.
V(Source_i)<+OUT_i;
end
```

```
endmodule
```

Listing 3.1: Simplified Verilog-A pseudocode of a noisy OE component

After each electronic, photonic, and optoelectronic component was implemented in Verilog-A, the parameters of the model were fitted to the post-layout simulation results.

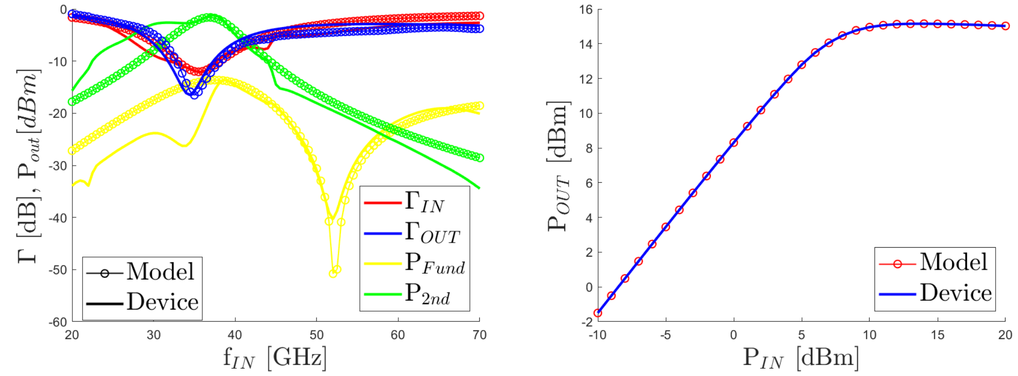

(a) (b)

Figure 3.25: Comparison of the model with post-layout harmonic-balance simulation results of (a) the 38.5 GHz to 77 GHz frequency doubler, and (b) the gain compression of the PA.

Figure 3.25 compares the model and the post-layout simulation results of the 38.5 GHz to 77 GHz frequency doubler, and the PA of the TX frontend. In figure 3.25a, it can be observed that the model of the input and output reflection coefficient $\Gamma$, the leakage of the input signal, and the desired output signal of the 2nd harmonic of the frequency doubler fits nearly perfectly with the post-layout simulation results. Moreover, the hyperbolic tangent approach for the gain compression compares favorably with the post-simulation results of the PA, as shown in figure 3.25b.

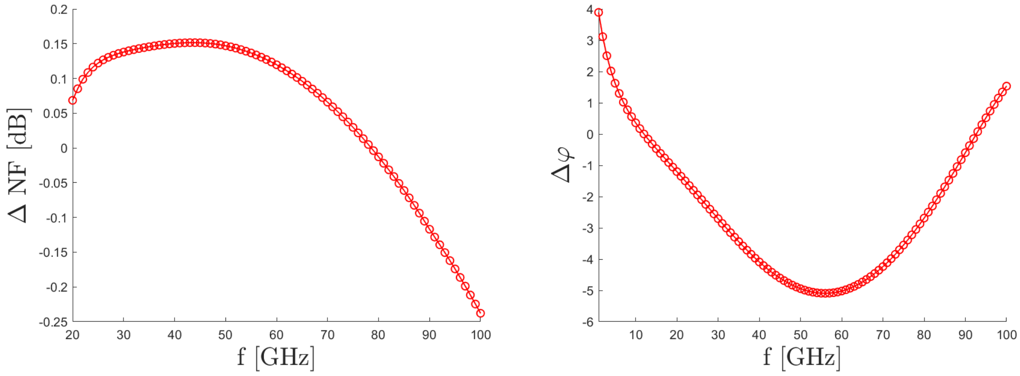

(a) (b)

Figure 3.26: Mismatch between the behavioral model and post-layout S-parameter simulation results of (a) the noise figure of the LNA, and (b) the phase difference of the IQ-mixer.

The mismatch between the behavioral model and the post-layout simulation results of critical components of the RX frontend is shown in figure 3.26. In the entire frequency band from 20 GHz to 100 GHz, the mismatch between the post-layout simulation results and the modeled noise figure (NF) of the LNA, shown in figure 3.26a, is below ±0.25 dB, and at the desired 77 GHz radar band, it is below $\pm 2 \cdot 10^{-2}$dB. Figure 3.26b presents the phase mismatch between the behavioral model and the post-layout simulation results of the IQ-mixer. In the entire frequency range from close to DC up to 100 GHz, the phase difference between the model and post-layout simulation results is below ±5°, and at the desired 77 GHz radar band, it is $-3°$.

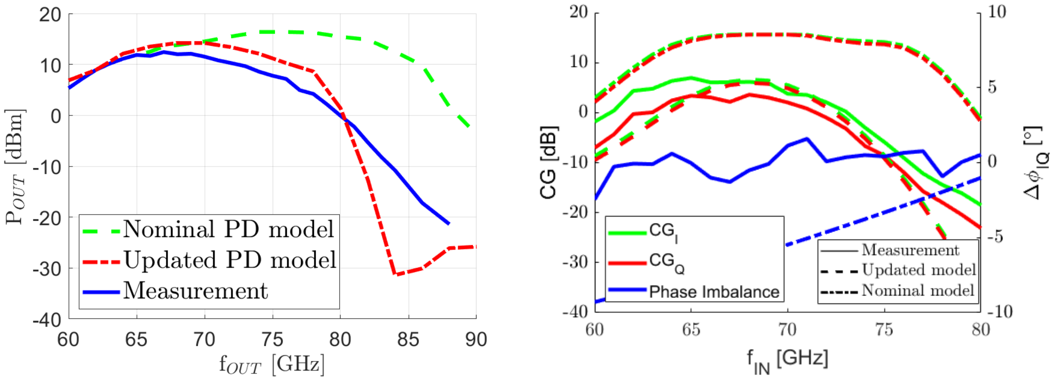

(a) (b)

FIGURE 3.27: Comparison of the behavioral model and measurement results of (a) the TX EPIC, and (b) the RX EPIC.

The comparison of the measurement results of the first monolithic integrated photonic radar TRX chipset and the simulation results of the behavioral model is shown in figure 3.27. It can be clearly observed that the measurement results differ significantly from the simulation results using the nominal PD model with the nominal PD bandwidth (BW). Due to a decrease in the PD BW within the fabrication process, leading to a reduction of the overall TIA BW, the frequency at the maximum output power of the TX EPIC and the maximum conversion gain of the RX EPIC is reduced by 10 GHz. Considering the reduced PD BW, leading to an updated PD and TIA model, the simulation results of the behavioral TRX model fit nearly perfectly with the measured ones. For detailed results of the TX and RX EPIC, refer to chapter 5.2 and chapter 6.2.

## 3.4 Conclusion

In this chapter, the proposed photonic FMCW radar system with optical LO distribution and optical return was simulated using the optical design environment Lumerical Interconnect from Ansys. The simulation validated both the principles of operation described in chapter 2.1 and the analysis presented in chapter 2.2.

Beyond optical simulation, the system was also modeled in the electronic design environment ADS-Ptolemy from Keysight. This hardware-oriented system model was used to investigate the effects of the MZM and ADC operating in compression. It was shown that the resulting IF signal contains several ghost targets, induced by the compressive behavior of both the MZM and the ADC. Additionally, the model provides deeper insights into the parameters of individual components and enables a more detailed representation of the central station.

Furthermore, a behavioral model of the monolithically integrated photonic radar transceiver chipset was introduced. The chipset was divided into its constituent building blocks, which were implemented in Verilog-A and fitted against post layout simulation results of each block. This model confirmed that the degraded chipset performance was due to a reduction in the PD BW during the fabrication process, which in turn led to a decrease in the overall TIA BW.

The content of this chapter was partially presented in the authors' publications [52, 56, 57, 61]. In addition, a journal publication on the model within the electronic design environment ADS-Ptolemy by Keysight is currently in preparation.

# Chapter 4

# Novel Circuit Architectures

## 4.1 Narrowband Optical Receiver

Within this section, a novel narrowband (NB) optical RX is presented. For the OE conversion of the high-frequency LO signal, performed in every previously presented photonic radar architecture, a NB optical RX is advantageous compared to a BB architecture because it reduces noise and harmonics. In addition, the novel NB optical RX architecture achieves higher gain and lower sensitivity to variations in the PD BW, thus improving the robustness of the optical RX against process, voltage, and temperature variations. Due to process variations, the peak transmit power and the maximum conversion gain of the first monolithic integrated photonic radar TRX chipset, presented in chapter 5, was reduced by $10\,\mathrm{GHz}$. With the novel optical RX architecture, such shifts can be reduced.

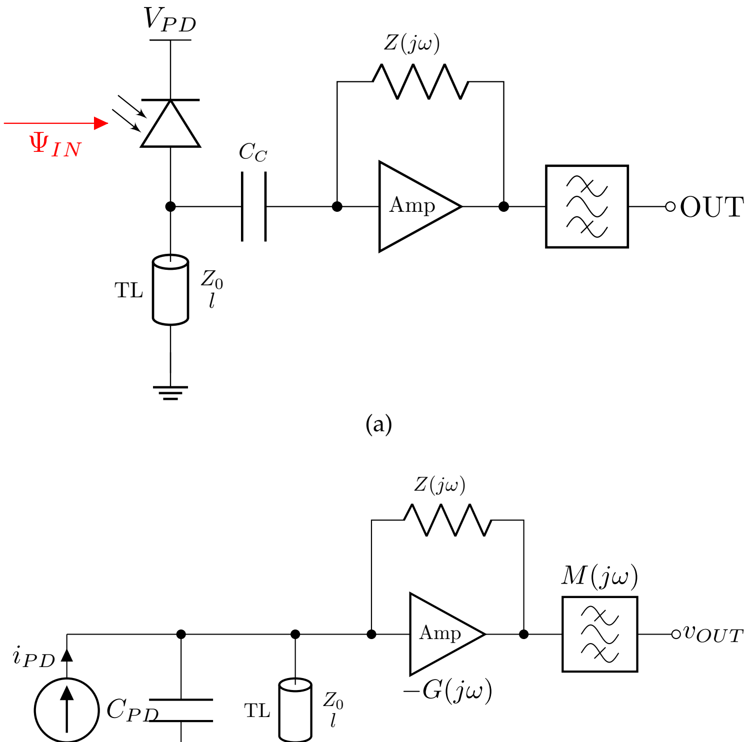

FIGURE 4.1: (a) Block diagram of the proposed NB optical RX architecture and (b) its small signal equivalent circuit.

The simplified block diagram of the NB optical RX and its small signal equivalent circuit is shown in figure 4.1. The PD is reverse biased by means of a transmission line (TL) with the length of [102]

$$0 \ll l \leq \frac{c}{\omega_{LO}} \cot^{-1}\left(C_{PD} Z_0 \omega_{LO}\right) = l_{max} \tag{4.1}$$

with $c$ being the speed of the electromagnetic wave in the TL, $C_{PD}$ as the capacitance of the PD, and $Z_0$ as the characteristic impedance of the transmission line. If $l$ is $l = l_{max}$, the inductive behaviour of the shorted TL cancels the capacitive behaviour of the reverse biased PD. In comparison to an inductor, the TL shorts also all unwanted signals with an angular frequency of

$$\omega_s = \frac{n\pi c}{l};\ n \in \mathbb{N}. \tag{4.2}$$

The desired LO signal is coupled to the input of the NB optical RX core by the high-value capacitor $C_C$. The NB optical RX core consists of an amplifier with the voltage gain $-G(j\omega)$ and a feedback impedance $Z(j\omega)$. The NB output impedance matching network can be modelled as a bandpass filter with the transfer function $M(j\omega)$.

The further theoretical analysis of the NB optical RX is based on the transimpedance. For the derivation of the transimpedance $Z_T$, the small signal equivalent circuit of the NB optical RX, shown in figure 4.1b, is analyzed. The output voltage after the matching network is given as

$$v_{OUT} = M(j\omega) \cdot v^{'}_{OUT} \tag{4.3}$$

with $v^{'}_{OUT}$ as the voltage after the amplifier, and before the output matching network. The input voltage of the amplifier can be written as its output voltage divided by the voltage gain:

$$v_{IN} = -\frac{{v_{OUT}}'}{G(j\omega)} = -\frac{v_{OUT}}{G(j\omega)M(j\omega)} \tag{4.4}$$

Kirchhoff's current law at the PD node of the equivalent circuit leads, under the assumption that the input current of the amplifier is zero, to

$$i_{PD} = i_{C_{PD}} + i_{TL} - i_{Z(j\omega)}. \tag{4.5}$$

Under the assumptions that the transmission line acts as an inductor and the circuit is in a steady state, the current in eq. 4.5 can be expressed by its component equations

$$i_{PD} = j\omega \cdot C_{PD} \cdot v_{IN} + \frac{v_{IN}}{j\omega L_{TL}} - \frac{v^{'}_{OUT} - v_{IN}}{Z(j\omega)}. \tag{4.6}$$

Substituting $v_{IN}$ and $v^{'}_{OUT}$ in eq. 4.6 with $v_{OUT}$ by eq. 4.4 results in

$$i_{PD} = -\frac{j\omega \cdot C_{PD} \cdot v_{OUT}}{G(j\omega) \cdot M(j\omega)} - \frac{v_{OUT}}{j\omega \cdot L_{TL} \cdot G(j\omega) \cdot M(j\omega)} - \frac{v_{OUT} + \frac{v_{OUT}}{G(j\omega)}}{Z(j\omega) \cdot M(j\omega)}. \tag{4.7}$$

Excluding $v_{OUT}$, and multiplying the numerator and denominator of the last summand of eq. 4.7 with $G(j\omega)$ leads to

$$\frac{i_{PD}}{v_{OUT}} = -\frac{j\omega \cdot C_{PD}}{G(j\omega) \cdot M(j\omega)} - \frac{1}{j\omega \cdot L_{TL} \cdot G(j\omega) \cdot M(j\omega)} - \frac{1 + G(j\omega)}{Z(j\omega) \cdot G(j\omega) \cdot M(j\omega)}. \tag{4.8}$$

Inverting eq. 4.8, and excluding $G(j\omega) \cdot M(j\omega)$ results in

$$Z_T = \frac{v_{OUT}}{i_{PD}} = G(j\omega) \cdot M(j\omega) \cdot \left\{ -j\omega \cdot C_{PD} - \frac{1}{j\omega \cdot L_{TL}} - \frac{1 + G(j\omega)}{Z(j\omega)} \right\}^{-1}. \tag{4.9}$$

Multiplying the numerator and denominator of the first summand of eq. 4.9 with $j\omega L_{TL}$, and excluding the $-1$ results in

$$Z_T = \frac{v_{OUT}}{i_{PD}} = -G(j\omega) \cdot M(j\omega) \cdot \frac{1}{\frac{1+G(j\omega)}{Z(j\omega)} + \frac{1-\omega^2 L_{TL} C_{PD}}{j\omega L_{TL}}}. \tag{4.10}$$

Multiplying the numerator and the denominator of eq. 4.10 with $\frac{Z(j\omega)}{1+G(j\omega)}$ finally results in

$$Z_T = \frac{v_{OUT}}{i_{PD}} = -\frac{G(j\omega) \cdot M(j\omega)}{1 + G(j\omega)} \cdot \frac{Z(j\omega)}{1 + \frac{Z(j\omega)(1-\omega^2 L_{TL} C_{PD})}{j\omega L_{TL}(1+G(j\omega))}}. \tag{4.11}$$

with

$$L_{TL} = \frac{Z_0}{\omega} \tan\left(\frac{l\omega}{c}\right). \tag{4.12}$$

If $l \to l_{max}$, eq. 4.11 simplifies for $\omega \approx \omega_{LO}$ to

$$Z_T(j\omega_{LO}) \approx -\frac{G(j\omega_{LO}) \cdot M(j\omega_{LO})}{1 + G(j\omega_{LO})} \cdot Z(j\omega_{LO}) \tag{4.13}$$

with

$$G_{T,I}(j\omega_{LO}) = -\frac{G(j\omega_{LO}) \cdot M(j\omega_{LO})}{1 + G(j\omega_{LO})} \tag{4.14}$$

it follows

$$Z_T(j\omega_{LO}) \approx G_{T,I}(j\omega_{LO}) \cdot Z(j\omega_{LO}). \tag{4.15}$$

In this case, the transimpedance is completely independent of the PD capacitance.

If PD capacitance variations occur ($C_{PD} = C_{PD,0} + \Delta C_{PD}$), e.g., due to temperature drifts, the transimpedance results in

$$Z_T(j\omega_{LO}) \approx G_{T,I}(j\omega_{LO}) \cdot \frac{Z(j\omega_{LO})}{1 - \frac{Z(j\omega_{LO})\Delta C_{PD}\omega_{LO}}{j(G(j\omega_{LO})+1)}}. \tag{4.16}$$

If the amplifier gain is sufficiently large ($|G(j\omega) + 1| \gg |Z(j\omega)\Delta C_{PD}\omega|$) at $\omega = \omega_{LO}$, eq. 4.16 simplifies to eq. 4.15, which is already independent of the PD capacitance.

For the simulative verification of the proposed analysis of the NB optical RX, a two-stage stacked FET inverter was used as the core amplifier. Such an inverter

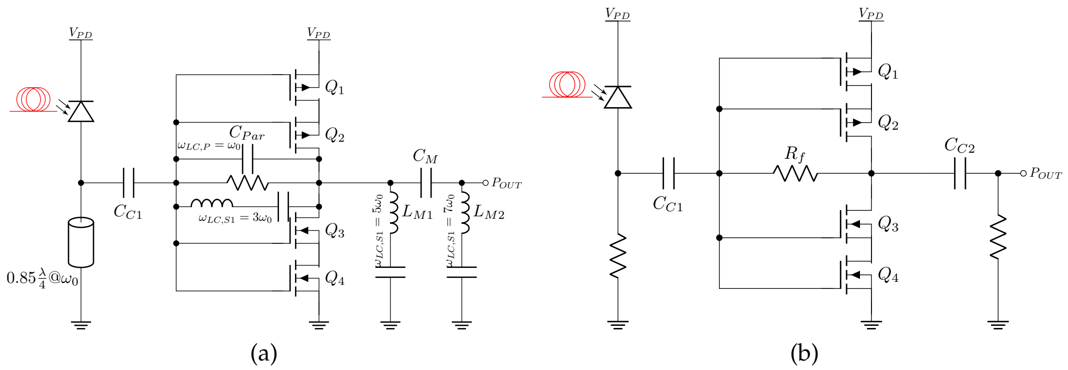

FIGURE 4.2: Simplified schematic of the (a) NB optical RX core (b) BB optical RX core test circuit.

exhibits higher gain compared to other CMOS inverter architectures, leading to a higher DC gain of the amplifier. The bandstop filter feedback was implemented as an RLC parallel tank, which provides high impedance at the resonance frequency. The resistor in the RLC tank is needed to provide stability for the proposed NB optical RX. Figure 4.2a shows the schematic of the NB test circuit. The implementation of the inverter-based optical RX is presented in section 4.1.1.

For the validation of the NB optical RX and a comparison to a BB optical RX, a two-stage stacked inverter TIA was implemented. The BB feedback of the BB optical RX, shown in figure 4.2b, was realized with a resistor.

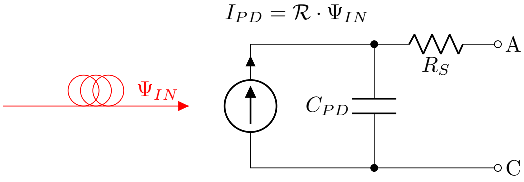

FIGURE 4.3: Voltage controlled current source model of the integrated PD used for the simulations [79].

In the simulation setup, the PD model shown in figure 4.3 [79] was used. It consists of a controlled current source, which provides a photocurrent proportional to the incident optical intensity. The PD capacitance is modeled parallel to the controlled current source. In the previous derivations, the series resistance $R_S$ was neglected. In the model, the series resistor is modeled as a lumped component. The shunt resistance of the PD junction $R_J$ can be neglected at high frequencies ($R_J \gg \frac{1}{j\omega C_{PD}}$) [108].

The simulation results of the NB optical RX and the BB optical RX are shown in figure 4.4. The optoelectronic conversion gain ($CG_{OE} = P_{el}/\Psi_{opt}$) of the BB and NB optical RX are shown in figure 4.4a. In this simulation, the BB optical RX was designed with a 3 dB BW of 19.25 GHz, while the NB optical RX was designed with a peak conversion gain at 19.25 GHz with nominal PD parameters. It can be clearly observed that the peak $CG_{OE}$ of the NB optical RX is approximately 25 dB larger compared to the BB optical RX. Besides the peak $CG_{OE}$, the NB optical RX shows a higher conversion gain for almost two octaves compared to the BB optical RX. The edge in the graph of the NB RX at 20 GHz can be explained by an insufficient step size.

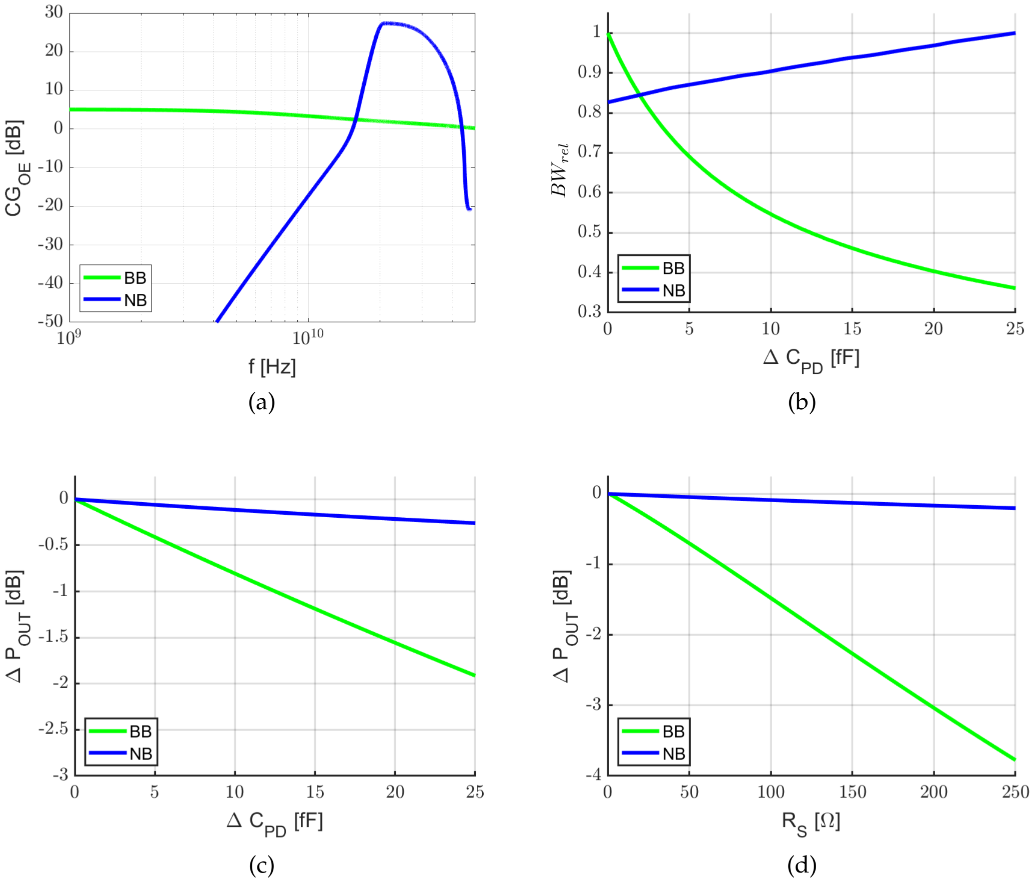

(a) (b)

(c) (d)

FIGURE 4.4: (a) Simulated conversion gain of an inverter-based BB optical RX and a NB optical RX; Simulated relative (b) bandwidth reduction of an inverter-based BB and NB optical RX as a function of the PD capacitance variations; (c) output power reduction of an inverter-based BB and NB optical RX as a function of the PD capacitance variations; (d) output power reduction of an inverter-based BB and NB optical RX as a function of the PD series resistance.

The simulated relative BW ($BW_{rel} = BW/BW_{max}$) as a function of the PD capacitance variations is shown in figure 4.4b. The bandwidths of the NB optical RX and the BB optical RX were normalized to the 3 dB BW over the different PD capacitance values. For the BB optical RX, it can be observed that the BW drops to 30 % of the peak BW if the capacitance varies from $\Delta C = 0\,\text{fF}$ to $\Delta C = 25\,\text{fF}$ with a nominal capacitance $C_{PD,0} = 50\,\text{fF}$. In contrast, the NB optical RX increases its bandwidth from 82 % at $\Delta C = 0\,\text{fF}$ to the maximum bandwidth at $\Delta C = 25\,\text{fF}$. Only positive values for $\Delta C$ were investigated, since the BW of the BB optical RX would increase with decreasing PD capacitance, but drastically decrease with increasing PD capacitance. In this special architecture of the NB optical RX, the peak gain of the NB optical RX reduces slightly, while the gain-BW product remains approximately the same. This leads to an overall bandwidth increase of the NB optical RX even if the BW of the PD decreases.

The relative output power ($\Delta P_{OUT} = P_{OUT}/P_{OUT,max}$) at 19.25 GHz of the BB optical RX and the NB optical RX as a function of the PD capacitance variations is shown in figure 4.4c. The output powers of the NB optical RX and the BB optical RX were normalized to the maximum peak output power, which occurs at PD capacitance variations of $\Delta C = 0\,\mathrm{fF}$. For increasing PD capacitance variations, the output power of the BB optical RX drops by $1.95\,\mathrm{dB}$, while the output power of the NB optical RX drops only by $0.25\,\mathrm{dB}$.

The impact of the series resistance of the PD is shown in figure 4.4d. It shows the relative output power at $19.25\,\mathrm{GHz}$ of the BB and the NB optical RX as a function of the series resistance of the PD. Similar to the effect of the PD capacitance variation, the output power of the NB and BB optical RX were normalized to the peak output power, which occurs at a series resistance of $0\,\Omega$. With increasing series resistance, the relative output power of the BB optical RX decreases by $3.8\,\mathrm{dB}$, while the relative output power of the NB optical RX drops only by $0.2\,\mathrm{dB}$ when the series resistance varies from $0\,\Omega$ to $250\,\Omega$.

All performed simulations validate that the NB optical RX provides higher gain and simultaneously high immunity against PD variations.

### 4.1.1 Implementation in a 45nm Photonic CMOS SOI Technology

The novel NB optical RX was implemented in GlobalFoundries $45\,\mathrm{nm}$ photonic CMOS SOI technology [35, 36]. Modern SOI technologies allow the integration of high-performance CMOS components and high-quality optics monolithically. The $45\,\mathrm{nm}$ silicon photonics technology supports optical signals in the optical C-($1530\,\mathrm{nm}$-$1565\,\mathrm{nm}$), L-($1565\,\mathrm{nm}$-$1625\,\mathrm{nm}$), and O-($1260\,\mathrm{nm}$-$1360\,\mathrm{nm}$) bands. In addition, the foundry provides optical waveguides and components for wavelengths around $1310\,\mathrm{nm}$ and $1550\,\mathrm{nm}$. In the following subsections, the implemented photonics and electronics will be presented in detail.

#### Photonics

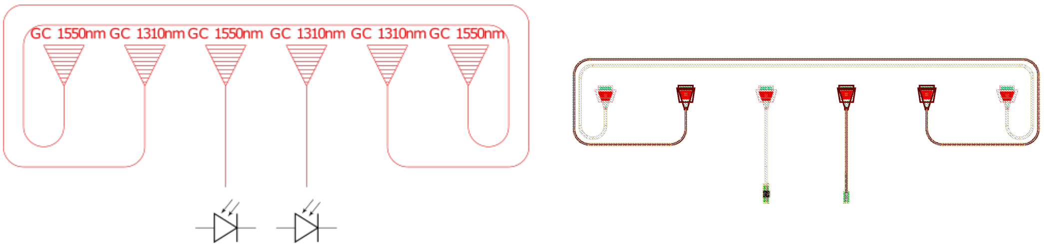

(a) (b)

FIGURE 4.5: (a) Block diagram of the integrated photonic, and (b) the realization on chip.

The simplified block diagram of the integrated photonics and its realization on the chip is shown in figure 4.5. The optical signals are coupled to the chip by means of focusing grating coupler (GC)s, optimized for $\lambda = 1550\,\mathrm{nm}$ and $\lambda = 1310\,\mathrm{nm}$, respectively. The optical signals can be coupled to the chip by means of a single fiber or a fiber array. For the optimization of the optical alignment of the fiber array and the optimization of the polarization, pilot lines were implemented into the chip. Pilot lines are optical waveguides that short two GCs optimized for one wavelength [24]. Since optical waveguide crossings have a high crosstalk [109], the optical interconnects are routed above the GCs to avoid waveguide crossings.

The optical interconnections are realized by rib waveguides optimized for the specific optical band. Above the waveguides, no metal plates are placed to reduce the losses.

The OE conversion is performed by lateral germanium epitaxy pin-PDs, also optimized for the different optical bands. The PDs offers a 3 dB BW of 50 GHz and a responsivity of 0.9 A/W, while the dark current is below 40 nA [36].

### Electronics

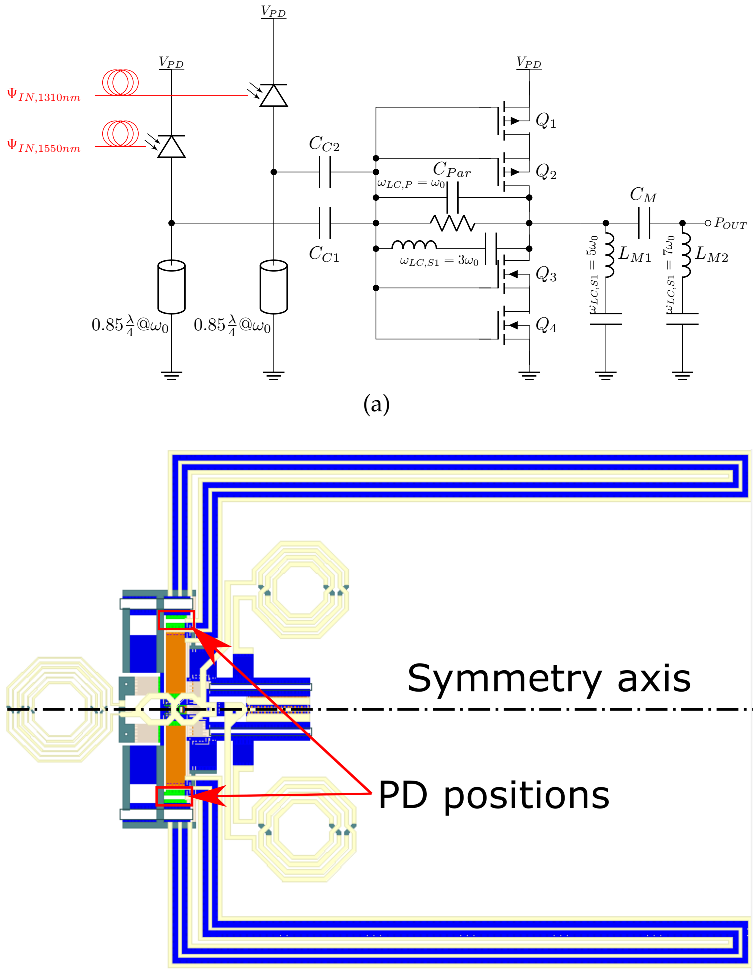

(a)

(b)

FIGURE 4.6: Simplified (a) schematic, and (b) layout of the implemented NB optical RX core.

The simplified circuit diagram of the implemented NB optical RX core is shown in figure 4.6a. The optical input signal $\Psi_{IN}$ is detected by means of PDs, whose positions are highlighted in figure 4.6b. The shorted TL was implemented as a coplanar backed line with a length of $l \approx 0.85 \cdot \lambda/4 \approx l_{max}$ and $Z_0 = 70\,\Omega$. In the layout of the NB optical RX core, shown in figure 4.6b, it can be observed that the two TLs are placed symmetrically around the symmetry axis. The distance between the two TLs was set in a way that the subsequent buffer stages can be placed between them. The electrical signal is coupled into the NB optical RX core with metal-oxide-metal capacitors. Such metal-oxide-metal capacitors with a small width to length ratio have a low self-resonance frequency, which causes a high impedance for unwanted higher order harmonics.

The NB optical RX core is based on a CMOS stacked field-effect transistor (FET) inverter architecture, with a parallel RLC feedback tank and a Π-shape output matching network. The CMOS stacked FET architecture features a high input-output slope, leading to an increased optical RX gain. The RLC feedback tank was designed with a resonance frequency of $\omega_{LO}$. An RLC feedback was chosen due to its NB behavior and finite impedance at $\omega_{LO}$. In addition, the resistor leads to a higher stability factor of the architecture. To provide DC isolation and cancel higher order harmonics induced by the MZM, an LC series resonator is used in the feedback tank, which shorts, in conjunction with the parallel capacitors, the unwanted harmonics at $3 \cdot \omega_{LO}$. The lossless output matching network is implemented as a Π-matching network with an LC series tank instead of a single inductor. These tanks provide the desired inductance at $\omega_{LO}$ and act as shorts at $k \cdot \omega_{LO}, k \in 5, 7$. The even harmonics are partially shorted via the TLs [110].

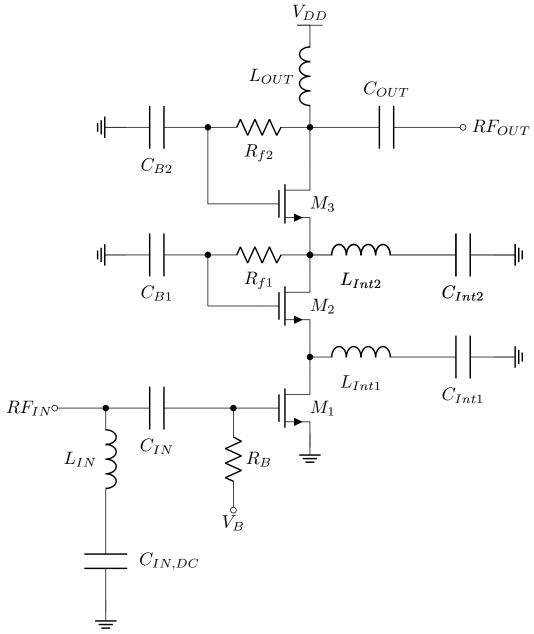

FIGURE 4.7: Simplified schematic of the buffer stage.

To increase the gain of the NB optical RX, a three-stage output NB buffer, biased in class AB mode, follows the NB optical RX core. The simplified schematic is shown in figure 4.7. Each buffer stage consists of a three-stage stacked FET architecture with inductive interstage matching. The interstage matching is implemented by means of LC series tanks, which provide the desired inductance at $\omega_{LO}$ while simultaneously isolating at DC. The input and output matching networks are implemented as LC series tanks at the input node. These LC tanks filter the unwanted harmonics at $2\omega_{LO}$. The input and output inductors were realized with multiturn squared inductors, while the inductors for interstage matching were realized as single-turn octagon inductors.

The common source (CS) FET is biased via a high-ohmic biasing resistor $R_B$ and a gate-degenerated current mirror architecture, while the common gate (CG) FETs are self-biased via a high-ohmic feedback resistor $R_{fx}, x \in 1, 2$ from the drain to the gate node.

The NB optical RX chip has a ground signal ground (GSG) output terminal configuration with RF electrostatic discharge (ESD) protection. The ESD protection is implemented by means of an LC parallel tank, which eliminates the capacitive behavior of the RF bondpad and an additional on-chip spiral inductor between the ground and signal bondpad [111]. To achieve a symmetric layout and to reduce the ESD stress of the inductors, two multiturn octagon inductors were implemented, each with an inductance value of $2 \cdot L_P$. For a proper capacitance to the ground potential, a ground plate was routed at the lowest metal layer under the signal bondpad. In addition, a via stack from each of the two ground bondpads connects the ground plate with the ground bondpads.

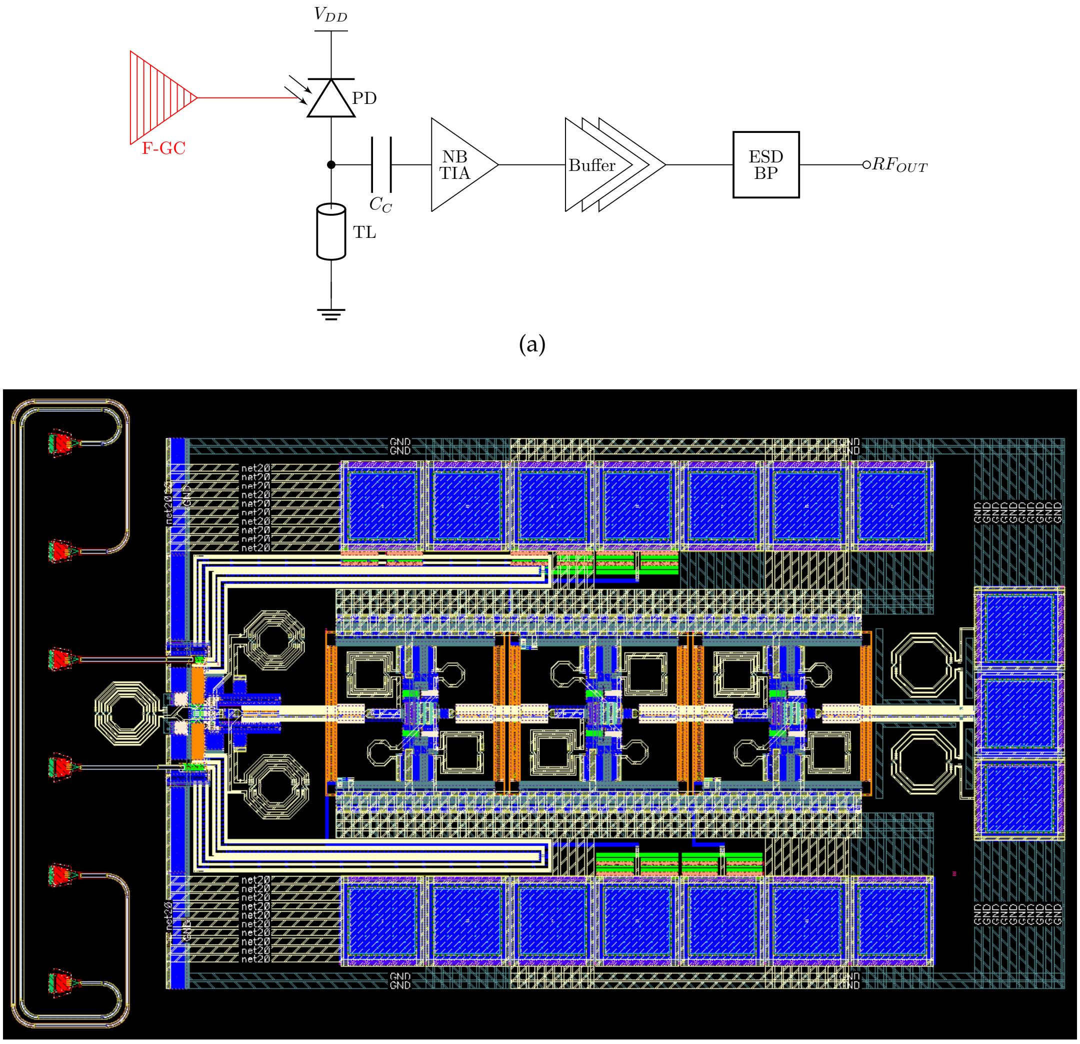

(a)

(b)

Figure 4.8: Simplified (a) block diagram and (b) layout of the implemented NB optical RX chip.

The simplified block diagram and the layout of the entire NB optical RX chip is shown in figure 4.8. The chip was implemented in GlobalFoundries $45\,\mathrm{nm}$ silicon photonics technology 45SPCLO [35, 36]. The photonic CMOS SOI technology provides transistors with $f_T$ and $f_{MAX}$ of $280\,\mathrm{GHz}$ and $340\,\mathrm{GHz}$ for the NFET and $230\,\mathrm{GHz}$ and $290\,\mathrm{GHz}$ for the PFET, respectively [36]. In addition, the technology offers silicon and silicon nitride optical waveguides, and eight copper layers and one aluminum layer [36]. The entire NB optical RX chip consists of the photonic inputs and pilot lines, the NB optical RX core, a three-stage buffer, and the RF ESD bondpad [111].

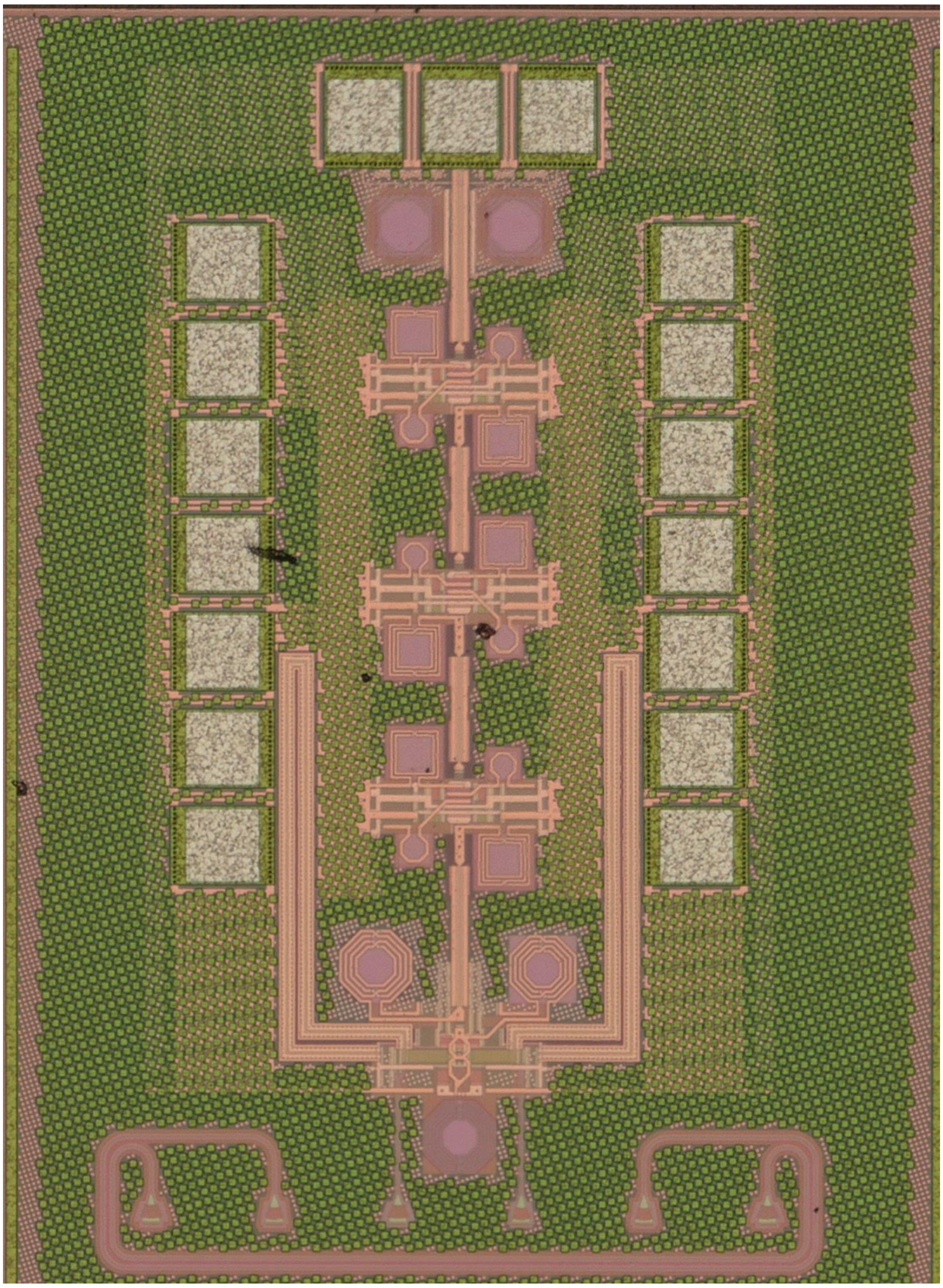

FIGURE 4.9: Microphotograph of the fabricated NB oRX

The microphotograph of the fabricated monolithic integrated NB optical RX chip is shown in figure 4.9. The NB optical RX consumes a chip area of $0.94\,\mathrm{mm}^2$ with an active core area of $233.7\,\mu\mathrm{m}^2$. The NB optical RX core and the PD dissipate $230\,\mu\mathrm{W}$ from a $1\,\mathrm{V}$ power supply with no optical input power and $655\,\mu\mathrm{W}$ from a $1\,\mathrm{V}$ power supply at maximum available optical input power. The additional power consumption comes from the DC current induced in the PD.

Each output buffer dissipates $48.2\,\mathrm{mW}$ from a $2.5\,\mathrm{V}$ power supply, leading to an overall power dissipation of the three-stage buffer of $144.6\,\mathrm{mW}$. The power dissipation of the bias voltages of the CS transistors of the buffers was below $2\,\mu\mathrm{W}$.

The EO measurement setup of the NB optical RX chip is shown in figure 4.10. A CW laser diode (LD) is connected to a lithium-niobate MZM, biased in the quadrature point. A signal generator is used to amplitude modulate the optical carrier with the electrical LO signal. Since only transverse electric polarized light can couple into the EPIC chip, a polarization-maintaining MZM is used, and only polarization-maintaining fibers are used in the setup. In addition, the CW LD provides a transverse electric polarized signal. Via a polarization-maintaining single-mode fiber, which is aligned by micro positioners with a self-designed fiber holder, the light is fed into the NB optical RX chip.

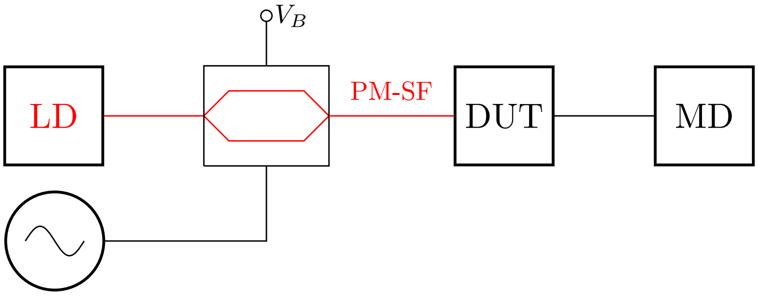

FIGURE 4.10: Simplified measurement setup of the NB optical RX chip.

The polarization-maintaining single-mode fiber was located slightly above the surface of the EPIC and no gluing was performed. The output signal of the NB optical RX was fed to the measurement device by means of an RF GSG probe and $1\,\mathrm{mm}$ coaxial cables. Both the cable and the probe have a cut-off frequency of $110\,\mathrm{GHz}$. Except the mismatch at the interceonnects, all results were deembedded.

The measurement results of the NB optical RX are presented in figure 4.11. The $3\,\mathrm{dB}$ BW of the implemented NB optical RX in 45nm photonic CMOS SOI spans the frequency range from $17.01\,\mathrm{GHz}$ to $19.81\,\mathrm{GHz}$. For the BW measurement, the signal generator held the frequency for $5\,\mathrm{s}$ while the spectrum analyzer measured the corresponding peak output power. Since the measurement lasted over half an hour, mechanical vibrations of the single-mode fiber in the measurement setup caused an unstable coupling efficiency between the fiber and the chip. This instability resulted in dips in the BW measurement, as shown in figure 4.11a.

The SNR measurement is shown in figure 4.11b. In the frequency range from $15\,\mathrm{GHz}$ to $24\,\mathrm{GHz}$, an SNR of $67.5\,\mathrm{dBc}$ is measured with respect to the desired LO signal at $19.25\,\mathrm{GHz}$. This value is limited by the noise floor of the spectrum analyzer used.

In addition, up to an optical modulation amplitude (OMA) [112]

$$OMA_{dB} = 10 \cdot log_{10}\left(\frac{\Psi_{high} - \Psi_{low}}{1\,\mathrm{mW}}\right) = -12\,\mathrm{dBm} \tag{4.17}$$

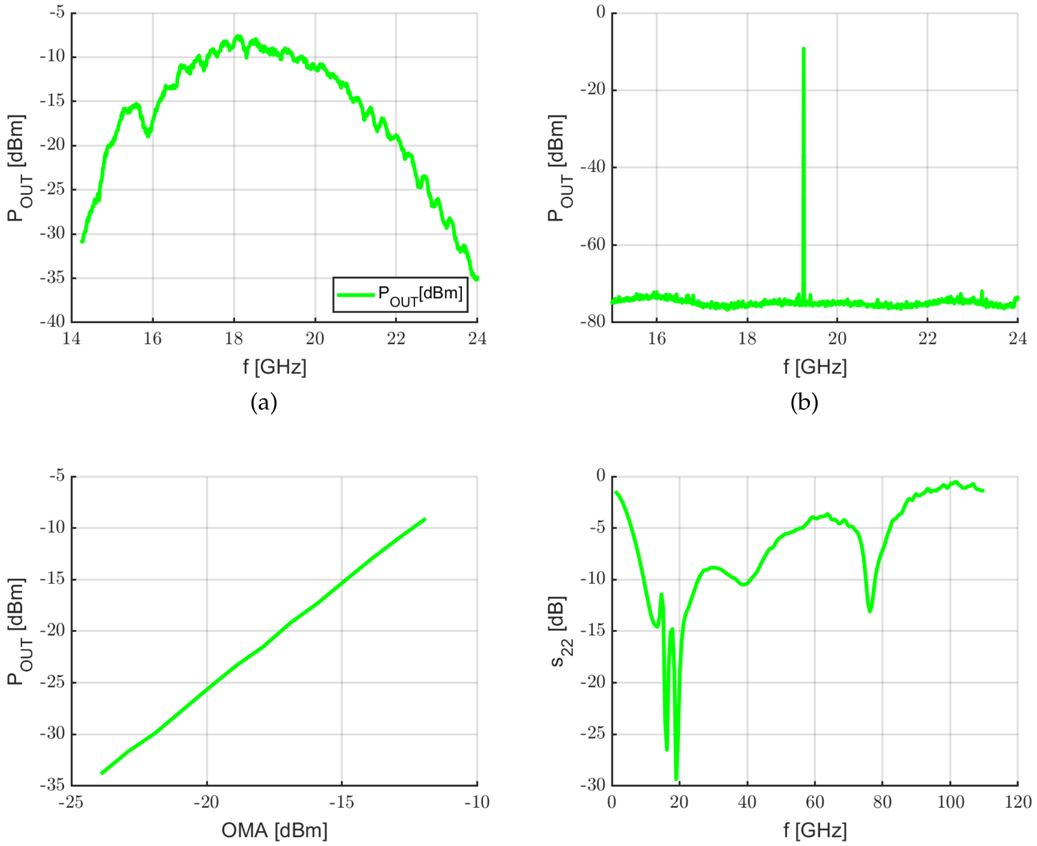

(a) (b)

(c) (d)

FIGURE 4.11: (a) Output power as a function of the LO frequency; (b) SNR measurement at 19.25 GHz, noise floor limited by measurement device; (c) Linearity measurement with respect to the OMA; (d) Output S-parameter measurement of the NB optical RX.

with $\Psi_{high}$ being the maximum optical power level, and $\Psi_{low}$ being the minimum optical level in a sinusoidal waveform, no gain compression occurs, which indicates that the high-order harmonic rejection technique implemented in the feedback tank and the output matching network works properly. In the measurement a higher OMA could not be tested due to a lack of optical laser power and limited coupling efficiency. Furthermore, the NB optical RX provides gain for an $OMA_{dB} > -15\,\text{dBm}$ and reaches a peak gain of $G = 4\,\text{dB}$. In appendix B, it is proven analytically that the OE power gain $G = P_{EL,OUT}/P_{OPT,IN} = P_{EL,OUT}/OMA_{lin}$ of any TIA, including BB TIAs, is $< 1/0\,\text{dB}$ up to a certain input power. This means that this behavior is not caused by a lack of the implementation, it is a physical rule.

The measured output scattering parameter (S-parameter) of the NB optical RX is shown in figure 4.11d. In the entire 3 dB BW of the NB optical RX, the output S-parameter is below $-15\,\text{dB}$, reaching a minimum of approximately $-29\,\text{dB}$ at 19.5 GHz. The dip in the middle of the band is caused by a slight mismatch between the output stage buffer and the ESD bondpad.

### 4.1.2 Implementation in a 250nm Photonic SiGe BiCMOS Technology

A second implementation of the novel NB optical RX was carried out in IHP's $250\,\mathrm{nm}$ photonic SiGe BiCMOS technology [32, 33]. Additionally, a BB optical RX was implemented in IHP's $250\,\mathrm{nm}$ photonic SiGe BiCMOS technology for the validation of the advantages of the novel NB optical RX architecture. Modern photonic SiGe BiCMOS technologies allow the integration of high-performance Heterojunction bipolar transistor (HBT)s and high-quality optics, such as optical waveguides and PDs, monolithically. In comparison to GlobalFoundries' photonic CMOS SOI technology, IHP offers optical waveguides and PDs which are simultaneously optimized for the optical C-band and O-band, respectively. In the following subsections, the implemented photonics and electronics will be presented in detail.

#### Photonics

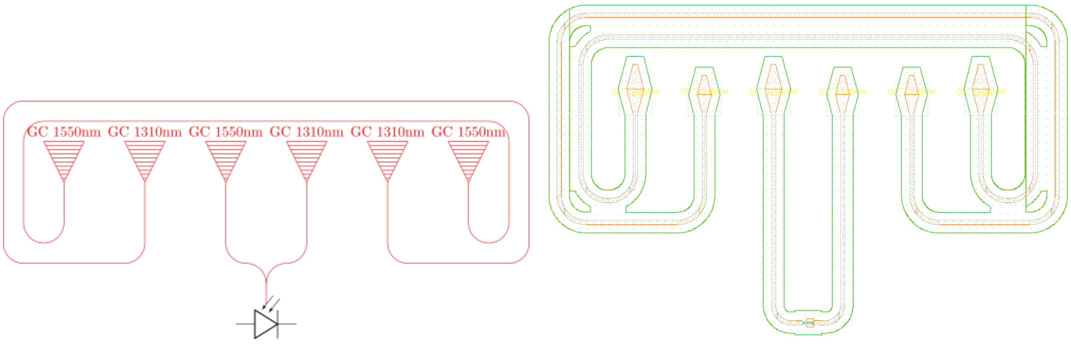

(a)

(b)

FIGURE 4.12: (a) Block diagram of the integrated photonics, and (b) the realization on chip.

The simplified block diagram of the integrated photonics and its realization on the chip is shown in figure 4.12. Similar to the implementation in the $45\,\mathrm{nm}$ CMOS SOI, the optical signals are coupled to the chip by means of focusing GCs, optimized for $\lambda = 1550\,\mathrm{nm}$ and $\lambda = 1310\,\mathrm{nm}$, respectively. Additionally, pilot lines for fiber array alignment [24] were implemented in the $250\,\mathrm{nm}$ demonstrator. The optical interconnections are realized by rib waveguides optimized for the specific optical band.

In comparison to the previously demonstrated NB optical RX in $45\,\mathrm{nm}$ photonic CMOS SOI, IHP's $250\,\mathrm{nm}$ photonic SiGe BiCMOS technology offers one PD for both optical bands with two optical input ports. To reduce the complexity of the optical RX core, each optical band is routed to one side of the PD.

The OE conversion is performed by lateral germanium epitaxy pin-PDs, optimized for both optical bands. The PD offers a nominal $3\,\mathrm{dB}$ BW of $35\,\mathrm{GHz}$ and a responsivity of $0.5\,\mathrm{A/W}$, both at a reverse voltage of $0\,\mathrm{V}$, while the dark current is below $400\,\mathrm{nA}$.

#### Electronics

The simplified circuit diagram of the implemented NB and BB optical RX cores is shown in figure 4.13. In both optical RXs, the optical input signal $\Psi_{IN}$ is detected by means of PD.

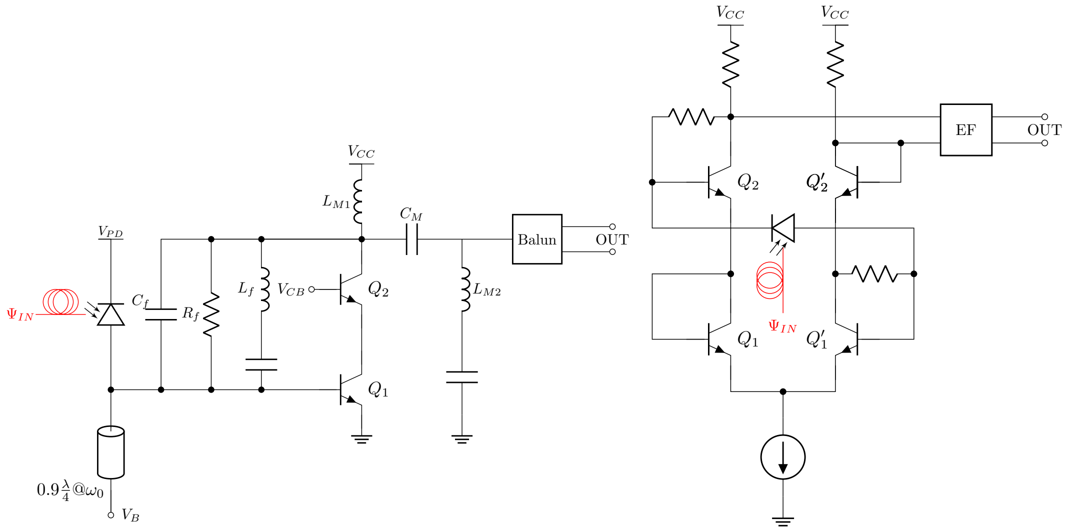

(a) (b)

FIGURE 4.13: Simplified schematic of the implemented (a) NB; (b) BB optical RX core.

The shorted transmission line of the NB optical RX was implemented as a coplanar backed line with a length of $l \approx 0.9 \cdot \lambda/4 \approx l_{max}$. Besides compensating for the capacitive behavior of the PD, the common emitter (CE) transistor is biased via the TL.

The NB optical RX core is based on a cascode amplifier, with a parallel RLC feedback tank, and Π-shape output matching network. Since the Miller effect is minimized in cascode amplifiers [113], they provide high voltage gain, high bandwidth, and improved linearity, leading to an increased optical RX gain and improved OE linearity. Similar to the implementation in the photonic CMOS SOI technology, the RLC feedback tank was designed with a resonance frequency of $\omega_{LO}$, and RLC feedback was chosen due to its NB behavior and finite impedance at $\omega_{LO}$. Additionally, the resistor contributes to a higher stability factor for the architecture. The implementation of the NB optical RX in the photonic BiCMOS technology uses a similar LC series resonator in the feedback and output matching network to cancel unwanted harmonics induced by the MZM, and providing DC isolation. The lossless output matching of the NB optical RX core is implemented by a Π-matching network, in which the inductor $L_{M1}$ provides the DC feed and $C_M$ the DC decoupling. The single-ended output of the NB optical RX core is transformed into a differential output by means of an LC lattice type balun [114].

The BB optical RX core consists of a fully differential, DC-coupled, and self-biased TIA structure [115]. The main advantage of this structure is that the PD is directly DC-biased due to the special architecture. The feedback of the BB optical RX core was implemented by means of high-ohmic feedback resistors. The 3 dB BW of the BB optical RX core was designed to be 19.25 GHz.

To increase the gain of the NB and BB optical RX, a three-stage NB differential amplifier follows the optical RX core. The simplified schematic is shown in figure 4.14. Each buffer stage consists of a differential cascode amplifier with lossless L-shape input and output matching. The L-shape input matching networks are implemented as LC series tanks. The CE amplifier of the cascode stage is biased via a high-ohmic biasing resistor $R_B$ and a base-degenerated current mirror architecture.

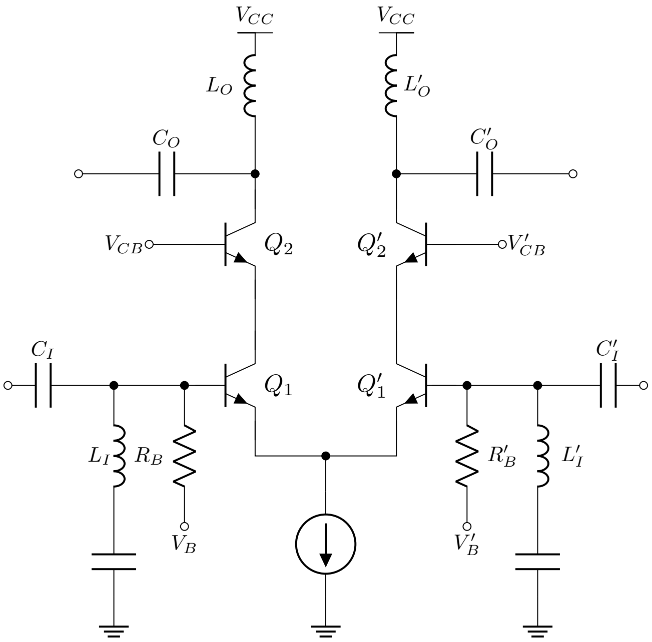

FIGURE 4.14: Simplified schematic of the differential amplifier stage.

The optical RX architectures in the photonic BiCMOS technology have ground signal signal ground (GSSG) output terminal configuration with RF ESD protection [111] similar to the implementation of the NB optical RX in the photonic CMOS SOI technology.

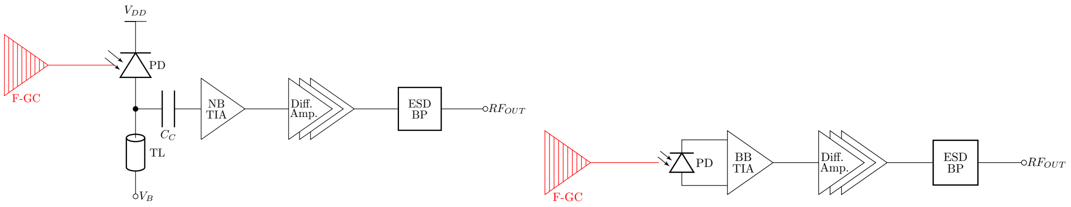

(a) (b)

FIGURE 4.15: Simplified block diagram of the implemented (a) NB; (b) BB optical RX chip.

The simplified block diagram of the entire NB and BB optical RX chip is shown in figure 4.15. The chips were implemented in IHP's $250\,\mathrm{nm}$ SiGe BiCMOS technology SG25H5 [32]. The photonic BiCMOS technology provides npn-HBTs with $f_T$ and $f_{MAX}$ of $200\,\mathrm{GHz}$ and $280\,\mathrm{GHz}$, respectively. In addition, the technology offers silicon based optical waveguides, and three thin and two thick aluminum layers. Both the NB and the BB optical RX chips consist of the photonic inputs and pilot lines, the optical RX core, a three-stage differential amplifier, and the RF ESD bondpad [111]. From figure 4.15, it can be observed that the only difference between the NB and BB optical RX chip is the optical RX core.

The microphotograph of the fabricated monolithic integrated NB and BB optical RX chip is shown in figure 4.16. The NB optical RX consumes a chip area of $1.63\,\mathrm{mm}^2$ with a core area of $0.32\,\mathrm{mm}^2$, while the BB optical RX consumes a chip area of $1.41\,\mathrm{mm}^2$ with a core area of $0.27\,\mathrm{mm}^2$. The NB optical RX core and the PD dissipate $4.3\,\mathrm{mW}$ and the BB optical RX core and the PD dissipate $8.4\,\mathrm{mW}$ from a $3.3\,\mathrm{V}$ supply.

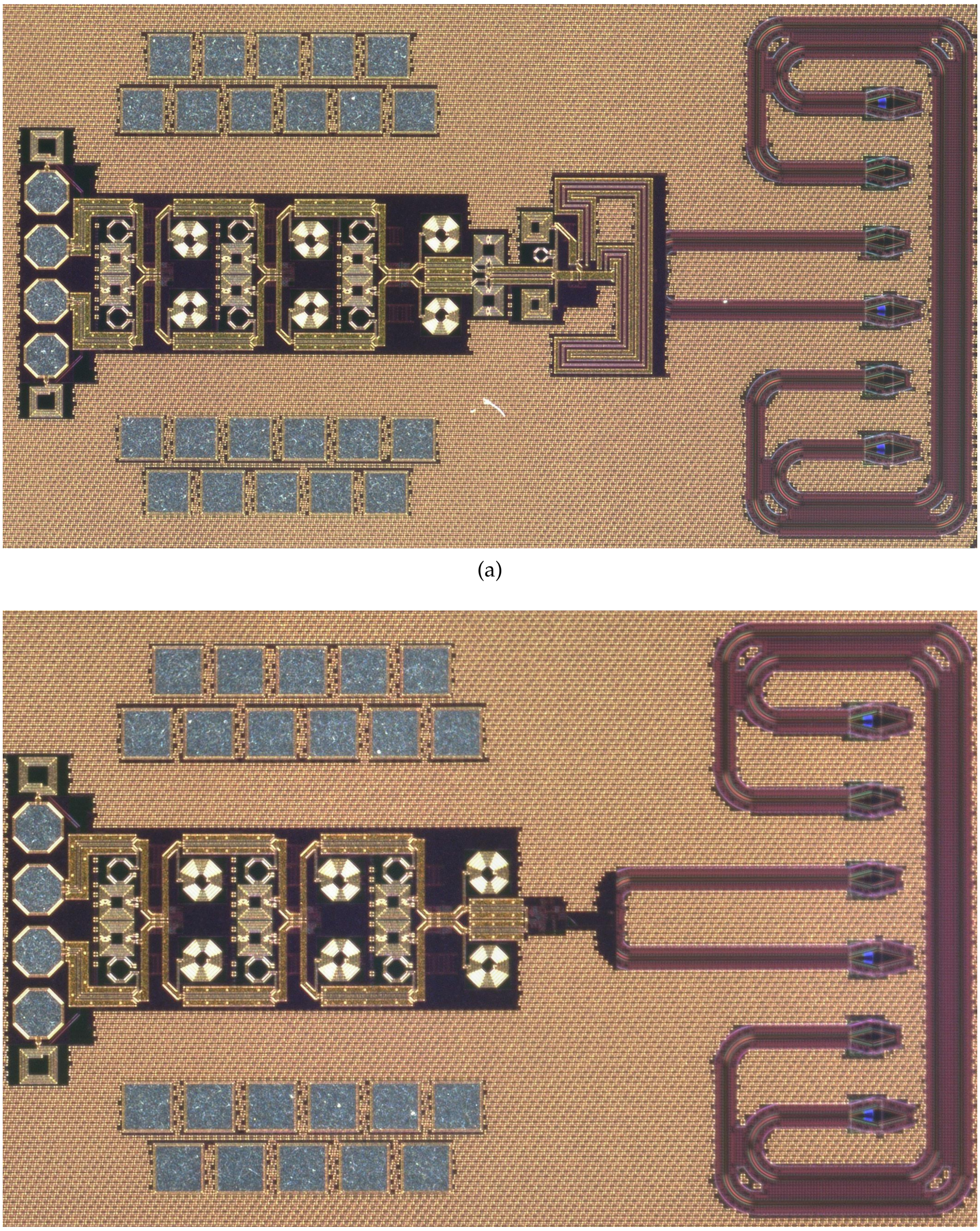

(a)

(b)

Figure 4.16: Microphotograph of the monolithic integrated (a) NB; (b) BB optical RX chip.

Each differential amplifier dissipates $8\,\mathrm{mW}$ from a $3.3\,\mathrm{V}$ power supply, leading to an overall power dissipation of the three-stage differential amplifier of $24\,\mathrm{mW}$. No further off-chip supply voltages are needed since all bias voltages are generated on-chip.

The EO measurement setup is exactly the same as the one for the NB optical RX in the photonic CMOS SOI technology, shown in figure 4.10, and already described in section 4.1.1.

The measurement results of the NB and BB optical RX are shown in figure 4.17.

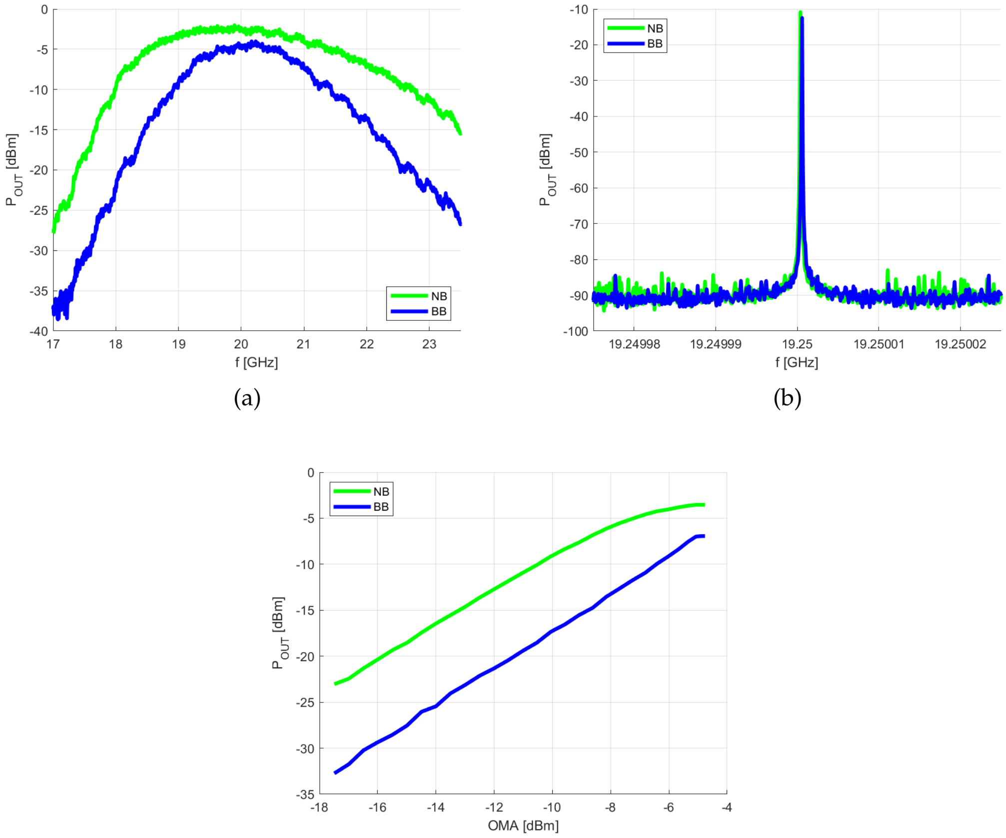

(a) (b)

(c)

Figure 4.17: Measurement results of the NB (green) and BB (blue) optical RX: (a) Output power as a function of the LO frequency; (b) SNR measurement at 19.25 GHz. Noise floor limited by measurement device; (c) Linearity measurement with respect to OMA.

The 3 dB BW of the implemented NB optical RX covers the frequency range from 18.5 GHz to 21.5 GHz, while the BB optical RX covers the frequency range from 19.3 GHz to 20.9 GHz. The BP behavior of the BB optical RX is caused by the subsequent NB differential amplifiers after the BB optical RX core. It can be clearly observed in figure 4.17a that for low frequencies, the slope of the NB and BB optical RX chips is approximately the same. For low frequencies, the NB differential amplifier is the limiting element in terms of BW. For high frequencies, it can be clearly observed that the output power of the BB optical RX decreases much faster with respect to frequencies than the NB optical RX. For high frequencies, the bandwidth of the BB optical RX core is the limiting element. The dips in the BW measurement, shown in figure 4.17a, are induced by mechanical vibrations of the single-mode fiber within the measurement setup, leading to an unstable coupling efficiency from the fiber to the device under test, similar to the measurement setup of the NB optical RX chip in the photonic CMOS SOI technology.

The SNR measurement is shown in figure 4.17b. The SNR is below 81 dB for the NB optical RX, and 77 dB for the BB optical RX, respectively. The value is limited by the noise floor of the spectrum analyzer used. A lower noise floor compared to the one shown in figure 4.11b could be achieved since another spectrum analyzer with a lower noise floor was used. Still, the value is limited by the noise floor of the spectrum analyzer used.

In addition, up to an OMA of $OMA = -6.4\,\text{dBm}$ for the NB optical RX chip, and up to an OMA of $OMA = -5\,\text{dBm}$ for the BB optical RX chip, no gain compression occurs. Furthermore, the NB optical RX provides gain for $OMA > -11\,\text{dBm}$ and reaches a peak gain of $G = 2.23\,\text{dB}$ at an OMA of $OMA = -6.4\,\text{dBm}$. The BB optical RX provides no gain and reaches only a peak gain of $G = -1.92\,\text{dB}$ at an OMA of $OMA = -5\,\text{dBm}$. It should be noted that a higher OMA could be achieved compared to the one shown in figure 4.11c, since the coupling efficiency of the photonic BiCMOS optical RX chipset was better compared to the NB optical RX in the photonic CMOS SOI technology. Since the OMA is also deembedded, except the unknown coupling efficiency, the coupling efficiency has a direct impact on the maximum achievable OMA.

In the entire frequency range from $18\,\text{GHz}$ to $21.7\,\text{GHz}$, the measured output S-parameter is below $-15\,\text{dB}$ and reaches a minimum of approximately $-22\,\text{dB}$. Since the output S-parameters are dominated by the ESD bondpad and the NB differential amplifiers, almost no output S-parameter variations could be observed between the NB and BB optical RX chip.

## 4.2 Narrowband Four-Quadrant Electro-Optical Mixer

Within this section, a novel circuit architecture of a NB four-quadrant EO mixer is presented. Such a NB mixer can be used as a frequency doubler as an initial stage of the upconversion of the optical LO signal to the desired mm-wave band, or as a TIA-less implementation of mixing arbitrary signals with the mm-wave signal in the photonic software-defined MIMO radar system with optical signal distribution (see chapter 8.1).

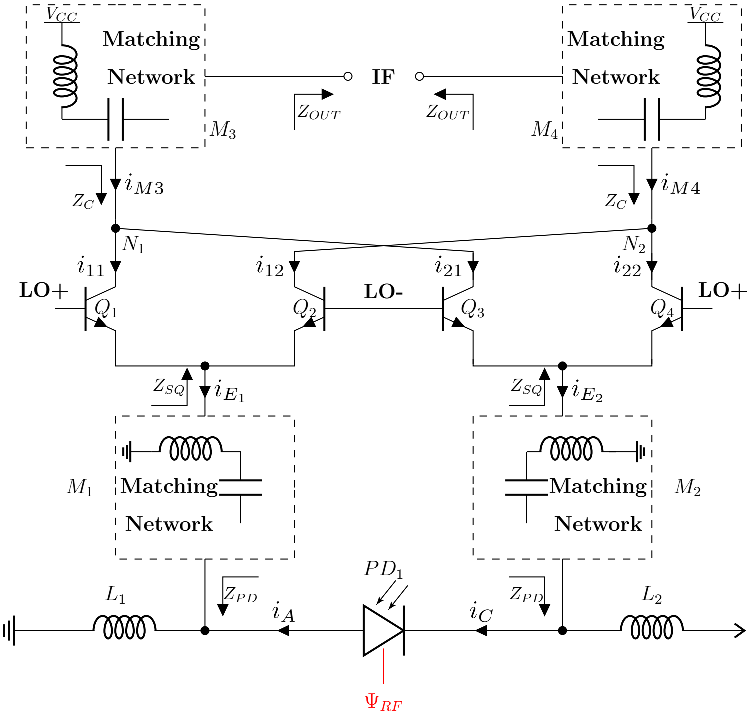

Figure 4.18: Simplified schematic of the NB four-quadrant EO mixer.

The simplified schematic of the novel NB four-quadrant EO mixer architecture is shown in figure 4.18. The optical input signal is converted to an electrical signal via a PD, which is reverse biased by the inductors $L_1$ and $L_2$. If the optical input signal is sufficiently narrow-band, these inductors can be implemented as transmission lines. The inductors act as open circuits for the desired RF signal so that the RF signal can only couple into the matching networks $M_1$ and $M_2$, or the inductors are part of a $\Pi$ matching network. These lossless matching networks maximize the power transfer into the switching quad, implemented by transistors $Q_1$ to $Q_4$ of a transconductance stage-less Gilbert cell mixer. If the differential LO signal is sufficiently strong, the switching quad steers the photocurrent to either node $N_1$ or $N_2$. In the case of a DC-free IF signal, the collector impedances $Z_C$ and $Z'_C$ are complex conjugate-matched to the output impedance $Z_{OUT}$ by means of $M_3$ and $M_4$ to provide maximum power transfer to the output IF port of the mixer. For an IF signal at or close to DC, these matching networks would be replaced by an impedance.

In the following subsections, the NB mixer architecture is analyzed. Therefore, it will be assumed that $V_{LO} \gg 3 \cdot V_T$, with $V_{LO}$ the LO voltage, and $V_T$ the threshold voltage of the transistors. In addition, it is assumed that the PD is operating linearly.

### 4.2.1 Optoelectronic Conversion Gain

The RF anode and cathode photocurrent of the PD is given by [79]

$$i_A = i_C = \mathcal{R} \cdot \Psi = \mathcal{R} \cdot (\Psi_0 + \Psi_{RF}) \tag{4.18}$$

with the DC part of the optical power $\Psi_0$ and the RF part of the optical power $\Psi_{RF}$. Since the inductors $L_1$ and $L_2$ act as open circuits for the RF signal and as shorts for the DC current, the DC current of the PD is shorted, while the RF current is fed into the lossless matching networks $M_1$ and $M_2$. The electrical power of at the PD node and at the emitter node is given by

$$P_{PD} = i^2_{A,C} Z_{PD} \tag{4.19}$$

$$P_E = i^2_{E_{1,2}} Z_{SQ} \tag{4.20}$$

For a lossless matching network, the power before the matching network is equal to the power after the matching network. For the maximum power transfer the matching networks have to transform the complex conjugated of the source impedance to the load impedance [102]. This leads to

$$i^2_{A,C} Z^*_{PD} = \mp i^2_{E_{1,2}} Z_{SQ} \tag{4.21}$$

$$i_{E_{1,2}} = \mp \sqrt{\frac{Z^*_{PD}}{Z_{SQ}}} i_{A,C} \tag{4.22}$$

Taking into account the losses of a real lossless matching network, and inserting the RF part of eq. 4.18 into eq. 4.22 reuslts to

$$i_{E_1} = -Q_1 \sqrt{\frac{Z^*_{PD}}{Z_{SQ}}} \mathcal{R} \cdot \Psi_{RF} \tag{4.23}$$

$$i_{E_2} = Q_2 \sqrt{\frac{Z^*_{PD}}{Z_{SQ}}} \mathcal{R} \cdot \Psi_{RF} \tag{4.24}$$

with the quality factor $Q_{1,2}$ of the matching networks $M_1$ and $M_2$.

For $V_{LO} \gg 3 \cdot V_T$, the current flow out of node $N_1$ would be $i_{11} = i_{E_1}$, and at node $N_2$ the discharge current would result in $i_{22} = i_{E_2}$.

$$i_{M3} = i_{11} = i_{E_1} = -Q_1 \sqrt{\frac{Z_{PD}^*}{Z_{SQ}}} \mathcal{R} \cdot \Psi_{RF} \tag{4.25}$$

$$i_{M4} = i_{22} = i_{E_2} = Q_2 \sqrt{\frac{Z_{PD}^*}{Z_{SQ}}} \mathcal{R} \cdot \Psi_{RF} \tag{4.26}$$

For the opposite half-wave of the LO signal, $V_{LO} \ll -3 \cdot V_T$, the current flow out of node $N_1$ would be $i_{21} = i_{E_2}$, and at node $N_2$ the discharge current would result in $i_{12} = i_{E_1}$.

$$i_{M3} = i_{21} = i_{E_2} = Q_2 \sqrt{\frac{Z_{PD}^*}{Z_{SQ}}} \mathcal{R} \cdot \Psi_{RF} \tag{4.27}$$

$$i_{M4} = i_{12} = i_{E_1} = -Q_1 \sqrt{\frac{Z_{PD}^*}{Z_{SQ}}} \mathcal{R} \cdot \Psi_{RF} \tag{4.28}$$

The lossless matching networks $M_3$ and $M_4$ transform the current finally into a voltage

$$P_{IF\pm} = \frac{v_{IF\pm}^2}{Z_{OUT}} \tag{4.29}$$

$$P_{M3,4} = Z_C i_{M3,4} \tag{4.30}$$

$$\rightarrow v_{IF\pm} = \sqrt{Z_C^* Z_{OUT}} \cdot i_{M3,4} \tag{4.31}$$

Under the assumptions $Q_1 = Q_2 = Q_{12}$, and the quality factor of the matching networks $M_3$ and $M_4$ $Q_3 = Q_4 = Q_{34}$, the IF voltage results in

$$v_{IF} = -2 \cdot Q_{12} \cdot Q_{34} \cdot \sqrt{\frac{Z_C^* Z_{OUT} Z_{PD}^*}{Z_{SQ}}} \cdot \mathcal{R} \cdot \Psi_{RF} \cdot \text{sign}\left(V_{LO}\right). \tag{4.32}$$

Applying the first-order Taylor series under the assumption that the LO voltage is given as follows:

$$V_{LO} = V_{LO,0} \cdot \sin\left(\omega_{LO} t\right) \tag{4.33}$$

and the current of the PD after the matching networks $M_1$ and $M_2$ is given by

$$i_{E_2} = -i_{E_1} = \mathcal{R} \Psi_{RF,0} \cos\left(\omega_{RF} t\right) \tag{4.34}$$

and the output matching network has a bandpass filter behavior with the passband at $\omega_{IF} = \omega_{RF} \pm \omega_{LO}$, equation 4.32 simplifies to

$$v_{IF} \approxeq -\frac{4}{\pi} \cdot Q_{12} \cdot Q_{34} \cdot \sqrt{\frac{Z_C^* Z_{OUT} Z_{PD}^*}{Z_{SQ}}} \cdot \mathcal{R} \cdot \Psi_{RF,0} \cdot \cos\left(\left[\omega_{RF} \pm \omega_{LO}\right] t\right). \tag{4.35}$$

This leads to the OE conversion gain of

$$A_{OE} = \frac{v_{IF}}{\Psi_{RF,0} \cdot \cos\left(\left[\omega_{RF} \pm \omega_{LO}\right] t\right)} \tag{4.36}$$

$$= -\frac{4}{\pi} \cdot Q_{12} \cdot Q_{34} \cdot \sqrt{\frac{Z_C^* Z_{OUT} Z_{PD}^*}{Z_{SQ}}} \cdot \mathcal{R} \tag{4.37}$$

It is obvious from equation 4.37 that the conversion gain of the proposed NB OE mixer is proportional to the responsivity of the PD $\mathcal{R}$, the quality factors of the matching networks, the PD impedance, the output impedances, the collector impedances of the switching quad, and is inversely proportional to the impedance seen in the emitter nodes of the switching quad.

### 4.2.2 Optoelectronic Linearity

In a solely electronic double-balanced mixer topology, the linearity depends on the linearity of the transconductance stage and on the $V_{DS}$ for MOS transistors, and $V_{CE}$ in the case of bipolar transistors in the switching quad [113]. Since the transconductance stage is replaced with a PD within the NB OE mixer topology, the PD linearity is an important factor for the overall OE linearity of the mixer. Nevertheless, several works have presented highly linear PD structures [116–118]. Since the assumption was made that the PD is working in the linear range, the linearity of the NB OE mixer architecture is limited by the switching quad linearity. Adapting the results [113] to the NB OE mixer topology, the linearity limit of the proposed architecture is

$$V_{N_1-N_2} = V_{CE}(Q_1) - V_{CE,Sat} \tag{4.38}$$

with the difference voltage $V_{N_1-N_2}$ between the nodes $N_1$ and $N_2$, $V_{CE}(Q_1)$ the collector-emitter voltage of transistor $Q_1$, and $V_{CE,Sat}$ the saturated collector-emitter voltage of transistor $Q_1$.

### 4.2.3 Isolation

It is well known from Gilbert cell mixer theory that the LO to IF isolation, and the LO to RF isolation depend on the mismatch of the transconductance stage current [113]. Within the novel NB OE mixer architecture, the transconductance stage is replaced by a PD and the DC emitter current of the switching quad is set externally. Under the assumption that no photocurrent flows into the PD substrate, the anode and cathode terminal impedance is equal, and all transistors and matching networks are equal, the LO signal does not leak to the IF port. In addition, PDs have an extremely high reverse isolation, leading to an almost infinite LO to RF port isolation of the novel NB OE mixer architecture, even if a device mismatch occurs.

### 4.2.4 2.45 GHz ISM Band Prototype & Measurement Results

The simplified schematic and the photograph of the realized printed circuit board (PCB) prototype are shown in figure 4.19. Due to the long wavelength at 2.45 GHz, the PD reverse biasing was realized via inductors instead of transmission lines. Together with the DC decoupling capacitors and the emitter DC feed inductor, the three passive components form a Π-shaped matching network. To reduce the LO leakage induced by the asymmetry of the discrete PD, the matching network was optimized for the anode and cathode terminals of the PD. In modern CMOS or BiCMOS, the

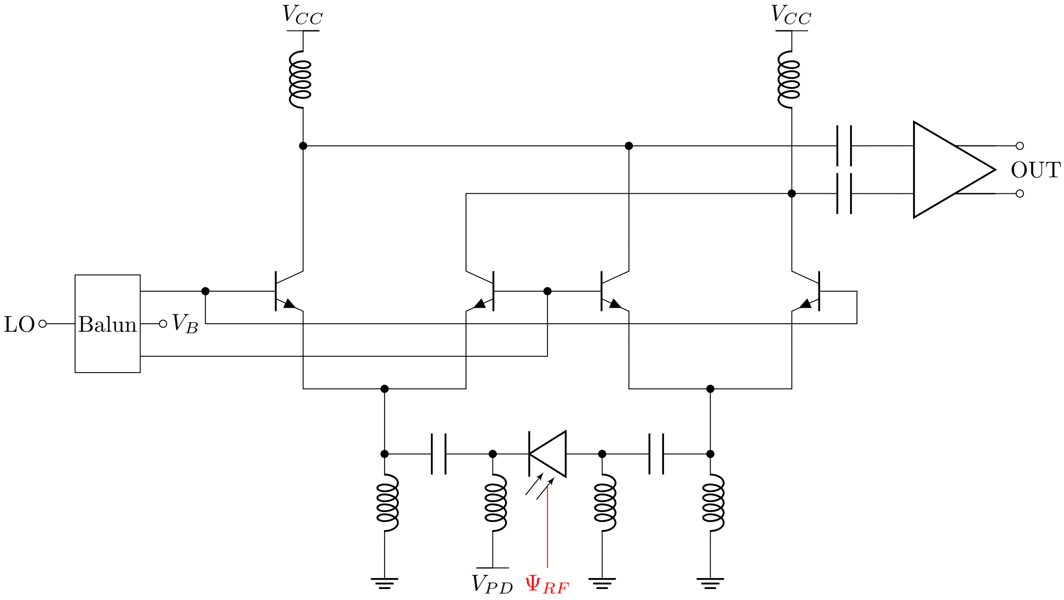

(a)

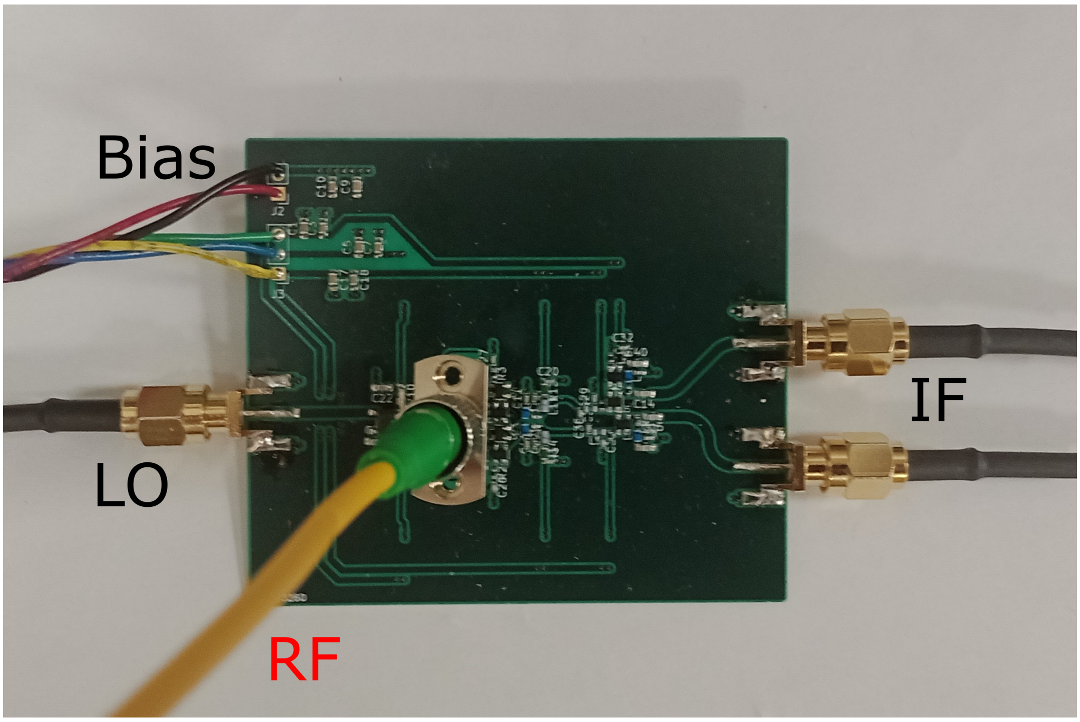

(b)

FIGURE 4.19: (a) Simplified schematic of the 2.45-GHz ISM band demonstrator. (b) Photograph of the PCB realization.

PD is commonly integrated as a waveguide-integrated PD [119]. For a waveguide-integrated PD, the anode and cathode currents and the anode and cathode parasitics are equal, which leads to a PD and matching network independent isolation.

The single-ended LO signal is converted to a differential one by means of a on PCB transformer-based balun. The center tap on the differential side of the balun is used to provide the bias voltage to the switching quad. The output matching is implemented as an L-shape matching network, consisting of DC feed inductors and

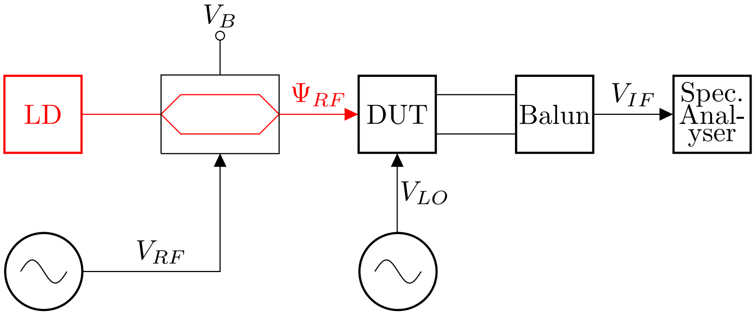

FIGURE 4.20: Simplified measurement setup of the NB EO mixer.

decoupling capacitors. To improve the gain of the NB OE mixer, a 50 Ω output buffer with a gain of 4 dB was implemented at the output of the NB OE core. This amplifier is implemented as a cascode amplifier, biased in class A mode. The demonstrator is implemented on a 0.5 mm thick RO4350B base material from Rogers. All input and output traces are implemented as 50 Ω microstrip lines. An FCI-InGaAs-120 PD with a junction capacitance of 2 pF was used for the NB OE mixer. For the transistors, the BFP540 npn transistor was chosen, which offers an $f_T = 30\,\text{GHz}$. To reduce LO leakage caused by fabrication tolerances of the discrete transistors, all used transistors were from the same batch.

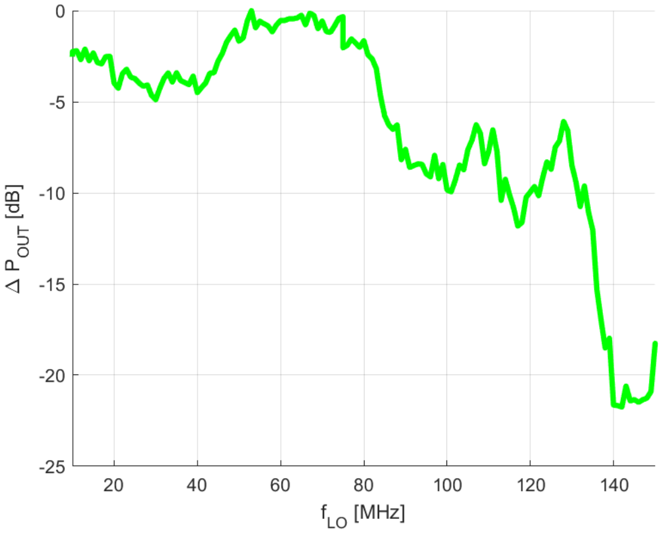

FIGURE 4.21: Measured relative output power with respect to the global maximum as a function of the LO frequency at an RF frequency of 2.45 GHz.

The measurement setup of the NB OE mixer is shown in figure 4.20. The RF signal is generated from a 1550 nm laser diode signal by means of a lithium niobate MZM, with a $V_\pi = 5\,\text{V}$, biased at the quadrature point. The MZM is driven by an electrical RF signal with an output power of 15 dBm. The optical RF signal and the electrical LO signal are fed to the NB OE mixer (device under test (DUT)). The IF spectrum is then measured by means of a spectrum analyzer.

An RF 3 dB bandwidth of more than 180 MHz was achieved with the implemented NB OE mixer. The measurement results of the LO bandwidth are shown in figure 4.21. The 3 dB LO BW is 82 MHz. In the LO response, a small overshoot was observed in the frequency range from 50 MHz to 80 MHz. This results from a slightly detuned center frequency of the NB OE mixer. The NB OE mixer consumes 60 mW from a 2 V supply and achieves an OE conversion gain of −7 dB, after deembedding the measurement devices. The low conversion gain of the implemented mixer is caused by the low cutoff frequency of the used PD. The nonlinearity of the entire measurement setup was dominated by the nonlinearity of the MZM.

## 4.3 Conclusion

Within this chapter, a novel narrowband optical receiver and a novel narrowband four-quadrant electro-optical mixer were presented. The unique topology of the narrowband optical receiver shows a greatly reduced dependency on the variance of the capacitance of the PD. For verification purposes, the narrowband optical receiver was implemented using the 45 nm photonic CMOS SOI technology from GlobalFoundries [35, 36] and the 250 nm photonic SiGe BiCMOS technology from IHP [32, 33]. The measurement results validate the operating principle. A comparison with a broadband, fully differential, DC-coupled, and self-biased TIA [115] demonstrates that the novel NB receiver architecture achieves higher gain while maintaining comparable linearity to the conventional broadband design.

Currently a journal and a letter paper about the novel NB optical receiver are in preparation.

For the novel NB four-quadrant electro-optical mixer, key mixer parameters—including OE conversion gain, OE linearity, and isolation—were derived. To validate the architecture, a 2.45 GHz ISM band prototype was fabricated. The measurement results of the demonstrator confirm the potential of this technology.

The mixer was perviously published by the author in [51] and [69].

## Chapter 5

# 77 GHz Electronic Photonic Radar Transmitter Chip in 250 nm SiGe BiCMOS

In the previous chapters 2, and 3, the photonic FMCW MIMO radar system with optical LO distribution was presented, analyzed, and simulated. Within this chapter, an integrated photonic radar TX chip in silicon photonics technology is presented. The chip is implemented in the $250\,\mathrm{nm}$ SiGe BiCMOS technology from IHP [32, 33]. The chip integrates all photonic and electronic components to receive the optical LO signal and transmit a mm-wave radar signal.

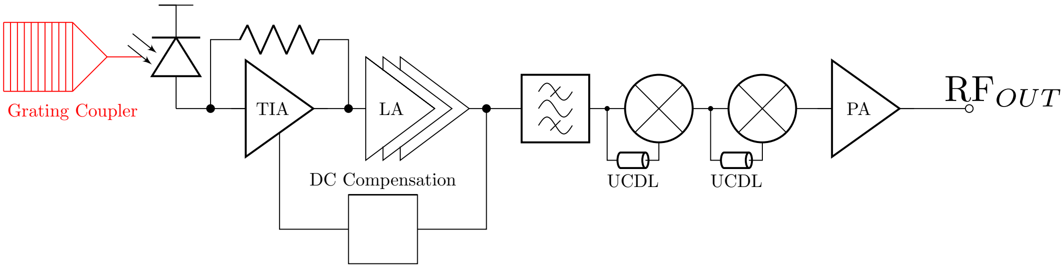

FIGURE 5.1: Block diagram of the photonic radar TX chip with optical LO distribution.

The simplified block diagram of the photonic TX radar chip with optical LO distribution is shown in figure 5.1. The principle of operation is given in chapter 2.1. In the following sections, the implemented photonics, the broadband TIA with DC compensation, the frequency quadrupler with ultra-compact delay lines, and the power amplifier with ESD bondpads will be presented in detail.

## 5.1 Implementation

### 5.1.1 Photonic Part

The photonic part of the TX and RX photonic radar EPIC is similar to the implementation of the NB optical RX in IHP's $250\,\mathrm{nm}$ photonic SiGe BiCMOS technology (4.1.2).

The simplified block diagram of the integrated photonics and its realization on the chip is shown in figure 5.2. In comparison to the previous NB optical RX EPIC, the optical signals are coupled to the chip by non-focusing GCs, optimized for $\lambda = 1550\,\mathrm{nm}$ and $\lambda = 1310\,\mathrm{nm}$, respectively. The optical interconnects are realized by rectangular

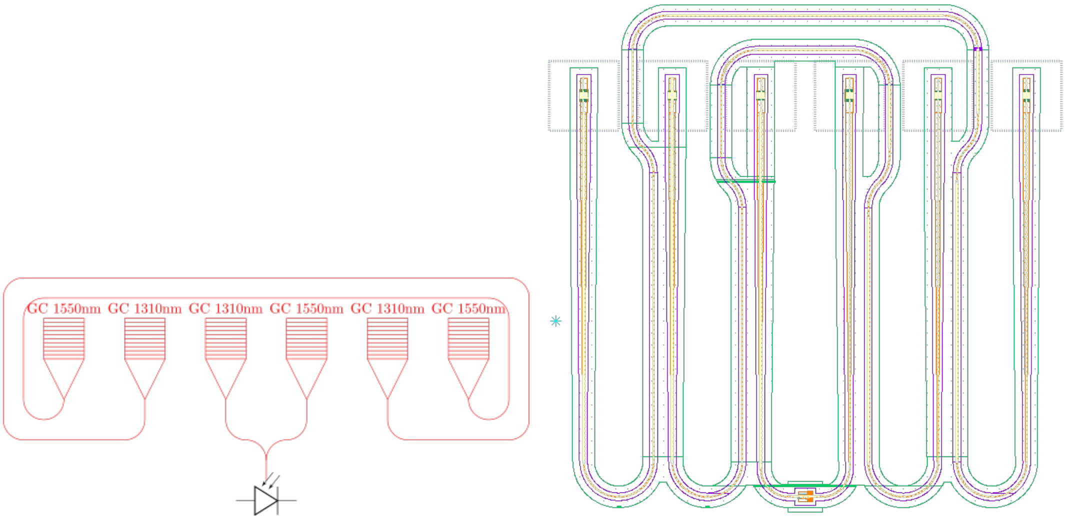

(a) (b)

Figure 5.2: (a) Block diagram of the integrated photonic, and (b) its realization on the chip.

waveguides optimized for the specific optical band. To align the wide rectangular waveguide cross-section, directly after the GCs, to the the regular rectangular waveguides with low cross-section, linear waveguide tapers are added between the GCs and the waveguides. In addition, pilot lines for fiber array alignment were also implemented in the EPIC [24].

Similar to the NB optical RX chip, each optical band is routed to one port of the PD. The nominal PD characteristics are given in chapter 4.1.2.

## 5.1.2 Electronic Part

### Broadband Optical Receiver with DC Compensation

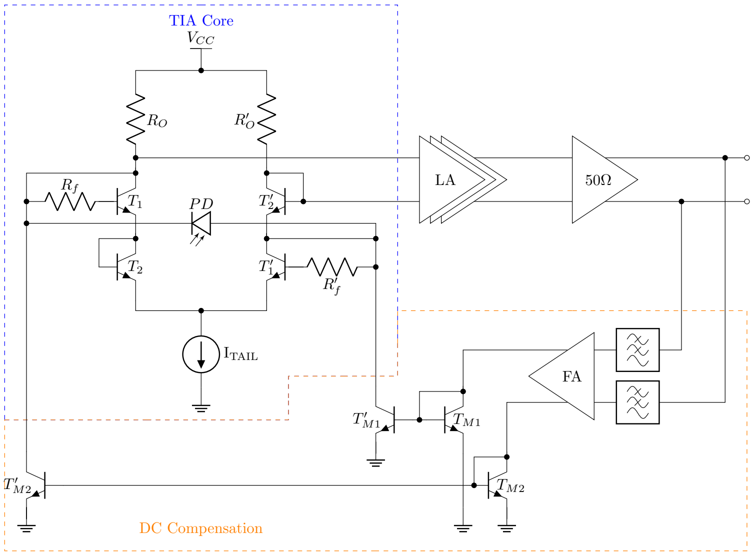

Figure 5.3: Simplified overall schematic of the broadband optical RX with DC compensation

The simplified overall schematic of the broadband optical RX with DC compensation is shown in figure 5.3. It consists of a PD with a TIA core, which form the optical RX core, limiting amplifier, and 50 Ω buffers. The feedback loop consists of LPFs, a feedback amplifier, and the biasing current mirrors.

The optical RX core is implemented as a fully differential, DC-coupled, and self-biased TIA [115], similar to the one shown in chapter 4.1.2. The TIA is based on a basic differential amplifier with the transistors $T_1$ and $T_1'$ acting as CE amplifiers and the feedback resistors $R_f$ and $R_f'$. The additional diode-connected transistors $T_2$ and $T_2'$ are added into each branch to provide the DC biasing voltage of $V_{BE}$ between the anode and cathode terminals of the PD.

Since no further components are needed at the input of the TIA to set the operating point of the PD and transistors, the compexity of the TIA is decreased instead of the NB oRX presented in chapter 4.1.

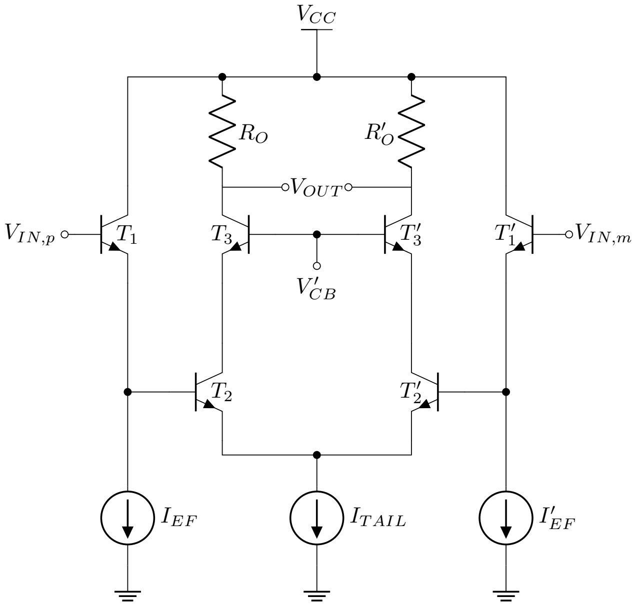

FIGURE 5.4: Simplified schematic of a single stage of the limiting amplifier and 50 Ω output buffer.

Figure 5.4 shows the simplified schematic of a single stage of the limiting amplifier and a 50 Ω output buffer. The transistors $T_1$ and $T_1'$ act as emitter followers. Instead of emitter resistors, current sources are used at the emitter node of the transistors. The transistors $T_2$ and $T_2'$ act as a differential common emitter pair with the common tail current source. A differential cascode topology with the common base transistors $T_3$ and $T_3'$ was chosen to reduce the Miller effect [113] and increase the gain and the bandwidth. All current sources are tunable to control the gain of each stage.

The simplified schematic of the feedback amplifier is shown in figure 5.5. The feedback amplifier is implemented as a differential folded cascode amplifier as the first stage, and a differential pair as the output stage. The architecture is useful down to small differential input voltages, which make it attractive as a feedback amplifier since it has to compensate for even small offset variations [120]. Due to the low cutoff frequency of the metal oxide semiconductor (MOS) transistors in IHP's 250 nm EPIC technology, the feedback amplifier also acts as a low pass filter with a cutoff frequency of 1 MHz [121]. It should be noted that a bypass option was also implemented in the EPIC to disable the automatic DC compensation and provide an external compensation current. This option was never used in the overall system.

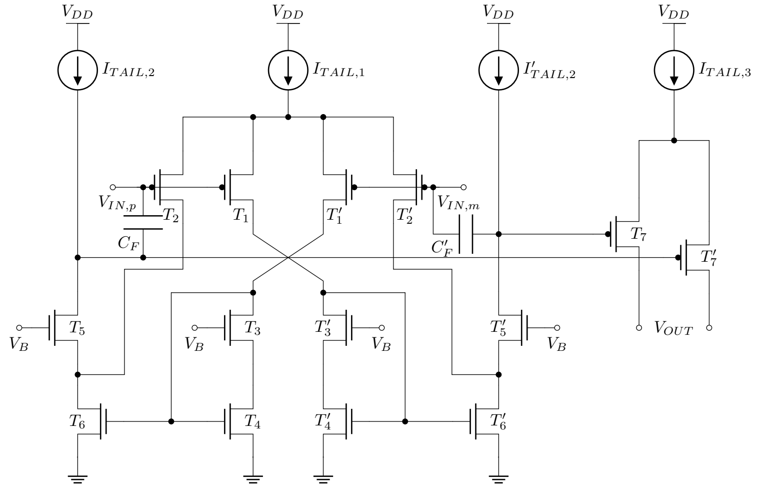

Figure 5.5: Simplified schematic of the feedback amplifier.

### Frequency Quadrupler with Ultra-Compact Delay Lines

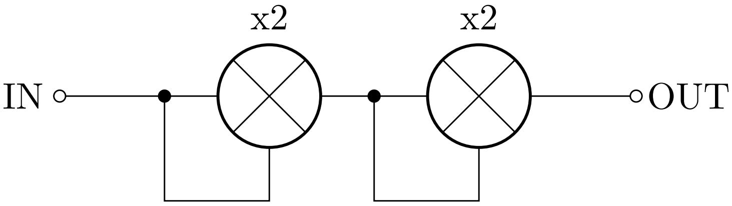

Figure 5.6: Simplified block diagram of the frequency quadrupler.

Figure 5.6 shows the simplified schematic of the frequency quadrupler. The quadrupler consists of two mixers where the RF and LO port are shorted.

Each mixer is implemented as a pseudo-differential bootstrapped Gilbert cell [122] with an additional output common base (CB) stage. The simplified schematic of a single stage of the quadrupler is shown in figure 5.7. The additional CB stage at the output of the switching quad increases the gain and bandwidth of the mixer. In addition, the CB stage provides high isolation [123]. Each port of the Gilbert cell is matched to $50\,\Omega$ single-ended / $100\,\Omega$ differential by lossless matching networks. The matching network of the RF port of the mixer is implemented as an L-matching network via $L_{RF}$, $L'_{RF}$, $C_{RF}$, and $C'_{RF}$. The L-matching network of the LO port consists of $L_{LO}$, $L'_{LO}$, $C_{LO}$, and $C'_{LO}$. The output matching network of the first stage is implemented as a Π-matching network, consisting of $L_{IF,1}$, $L_{IF,2}$, $C_{IF,1}$, $C_{IF,2}$, $L'_{IF,1}$, $L'_{IF,2}$, $C'_{IF,1}$, and $C'_{IF,2}$. The output matching network of the second stage is implemented as an L-matching network with $L_{IF,1}$, $C_{IF,1}$, $L'_{IF,1}$, and $C'_{IF,1}$. Via the capacitors $C_{IF,2}$ and $C'_{IF,2}$, a zero was added in the transfer function of the Π-matching network to suppress the fundamental frequency of $19.25\,$GHz. The DC operating point of the transistors is adjusted by base-degenerated current mirror topologies, where the current is mirrored via $R_{RF}$, $R'_{RF}$, $R_{LO}$, $R'_{LO}$, and $R_{CB}$ to the transistors $M_1$-$M'_4$.

The 90° TL between the CE amplifier and the switching quad of the Gilbert cell is implemented as a conductor-backed coplanar waveguide. The technology used offers three thin aluminum layers (M1-M3) and two thick aluminum layers (TM1-TM2). The conductor-backed coplanar waveguide was implemented on TM2 and M3. To reduce the effective chip area, capacitive loading [124], slow wave structures

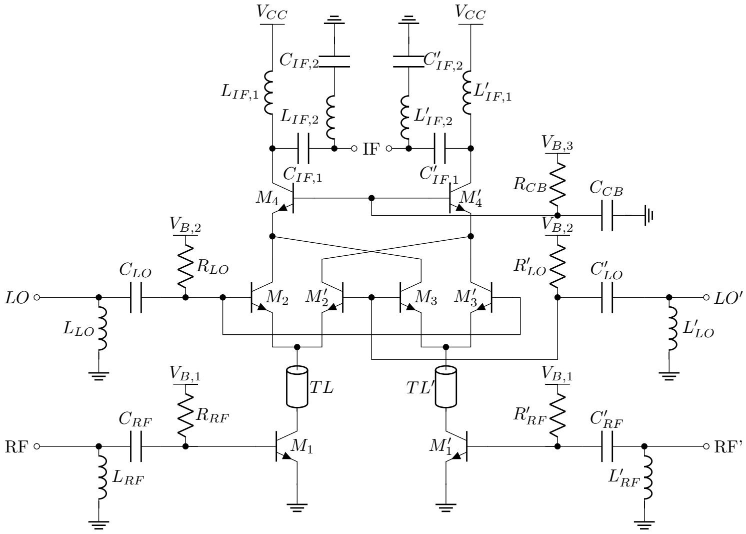

FIGURE 5.7: Simplified schematic of the Gilbert cell mixer

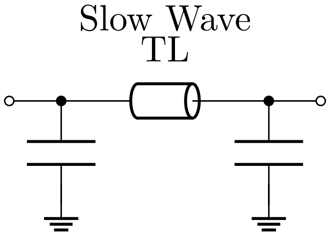

FIGURE 5.8: Simplified schematic of the ultra-compact delay line.

[125], and meandering [110] were used to build an ultra-compact delay line. Figure 5.8 shows the simplified schematic of the ultra-compact delay line. The ultra-compact delay line was implemented as a capacitive loaded slow wave transmission line.

The slow wave structure was realized by floating metal shield lines implemented in TM1 perpendicular to the signal line of the coplanar waveguide [125]. A 3D view of the slow wave transmission line is shown in figure 5.9a.

Figure 5.9b shows the losses and the electrical length of the different transmission lines with the different shrinking techniques. The conductor-backed coplanar waveguide without any length reduction techniques had an electrical length of $59.6°$ at $19.25\,\text{GHz}$ and a loss of $0.64\,\text{dB}$. The characteristic impedance of the transmission line is $Z_0 = 60.75\,\Omega$. The implementation of the slow wave structures slightly increases the losses to $0.65\,\text{dB}$ and increases the electrical length to $63.2°$ with a characteristic impedance of $Z_0 = 55.4\,\Omega$. In contrast, the capacitive loading without slow wave structures led to an electrical length of $87.3°$ and a loss of $0.84\,\text{dB}$. The characteristic impedance of the transmission line is $Z_0 = 52.23\,\Omega$. The combination of the two techniques finally leads to an electrical length of $89.7°$ with a characteristic impedance of $Z_0 = 49.6\,\Omega$ and a loss of $0.95\,\text{dB}$.

### Power Amplifier with ESD Bondpads

The simplified schematic of the PA is shown in figure 5.10. The power amplifier is implemented as a pseudo-differential cascode amplifier. The amplifier is biased in class AB mode. Therefore, the DC operating point of the transistors is adjusted by base-degenerated current mirror topologies, where the current is mirrored via $R_{B,1}$,

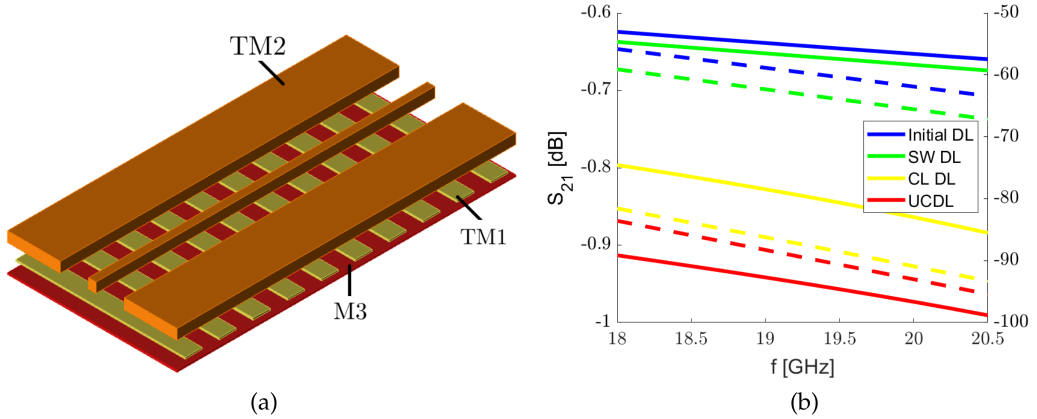

FIGURE 5.9: (a) 3D view of the slow wave delay line, and (b) simulation results of losses (solid) and phase (dashed) of the initial DL (blue), a delay line with slow wave structures (green), a capacitive loaded delay line (yellow), and the ultra-compact delay line (red).

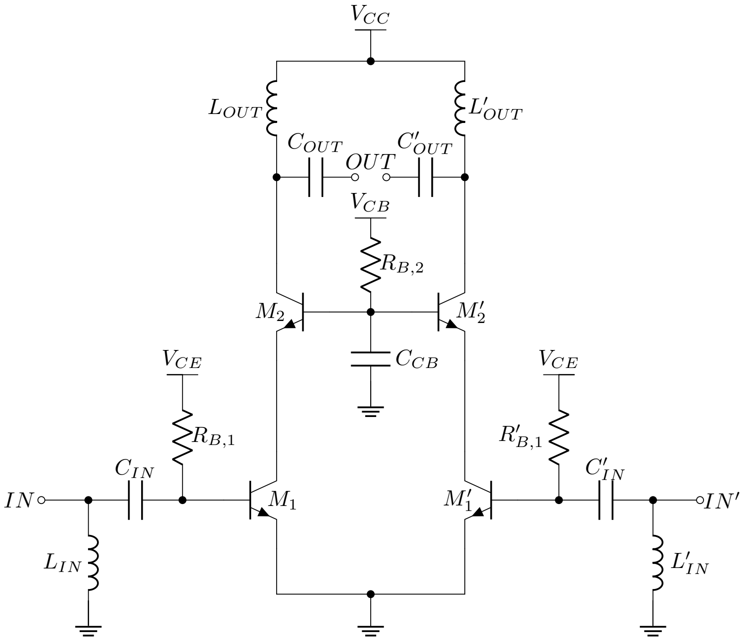

FIGURE 5.10: Simplified schematic of the 77 GHz PA.

$R'_{B,1}$, and $R_{B,2}$ to the transistors $M_1$-$M'_2$. The common base amplifiers are biased in weak avalanche region to increase the power added efficiency [126]. The input and output of the PA are matched to 50 Ω / 100 Ω differential by lossless L-matching networks. The input port is matched via $L_{IN}$, $L'_{IN}$, $C_{IN}$, and $C'_{IN}$. The output is matched by means of $L_{OUT}$, $L'_{OUT}$, $C_{OUT}$, and $C'_{OUT}$.

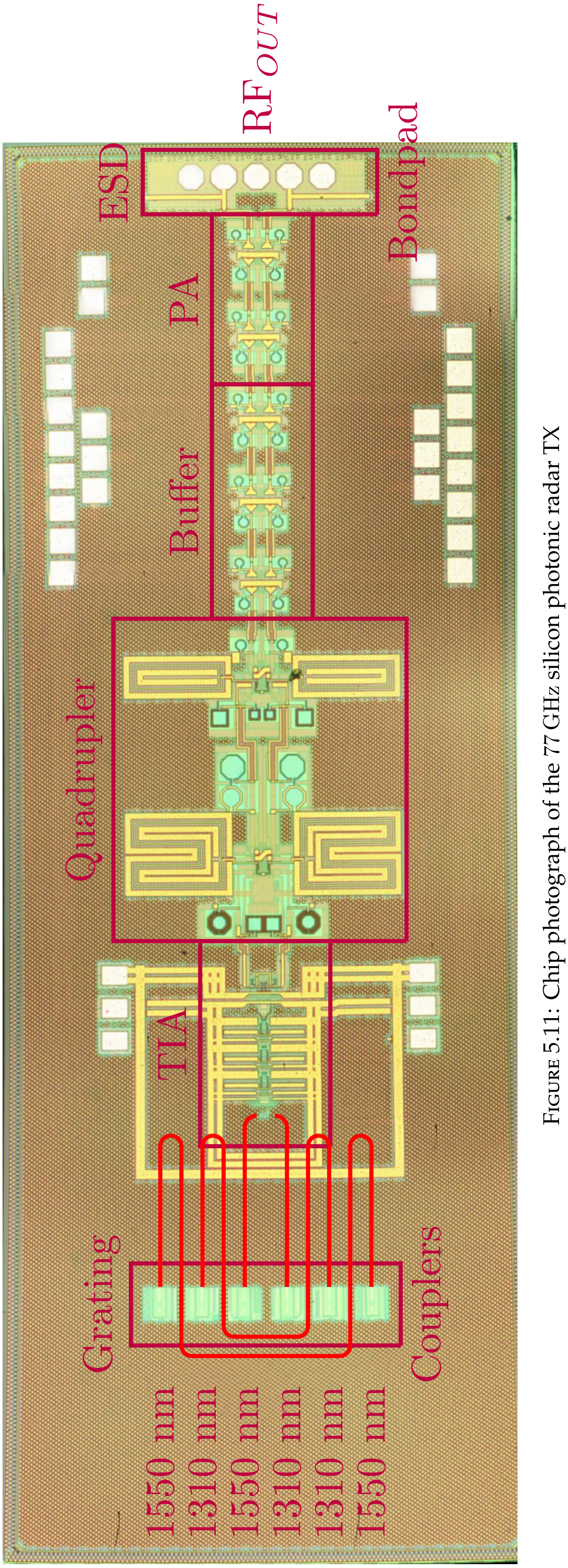

FIGURE 5.11: Chip photograph of the 77 GHz silicon photonic radar TX

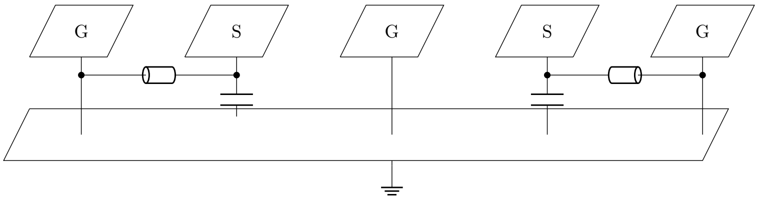

FIGURE 5.12: Simplified block diagram of the ESD bondpad.

The final stage of the TX chip is the 77 GHz bondpad to the off-chip transmit antenna. Figure 5.12 shows the simplified block diagram of the ESD bondpad [111]. The bondpad is implemented in ground signal ground signal ground (GSGSG) configuration. The ground pads are connected to the global ground of the chip. To guarantee a specific parasitic capacitance to the ground potential under all pads, a ground plane on the lowest metal plane was added. The parasitic capacitance of the signal bondpad, in conjunction with a shorted TL acting as an inductor, forms an LC parallel tank. At the resonance frequency, the impedance seen into the bondpad is the impedance from the subsequent stage. If an ESD event occurs, the low-frequency components of the event are shorted via the TL, and the high-frequency components are shorted via the parasitic capacitance to the ground potential. The remaining energy at the resonance frequency of the LC tank is sufficiently small to protect the circuit against ESD events.

## 5.2 Measurement Setup and Results

The chip was implemented in IHP's pre-production, photonic 250 nm SiGe:C BiCMOS technology [32, 33] with $f_t$ and $f_{MAX}$ of 200 GHz and 280 GHz, respectively. The chip microphotograph of the electronic photonic radar TX is shown in figure 5.11. The TX consumes a chip area of $6.65\,\mathrm{mm}^2$ with a core area of $1.09\,\mathrm{mm}^2$.

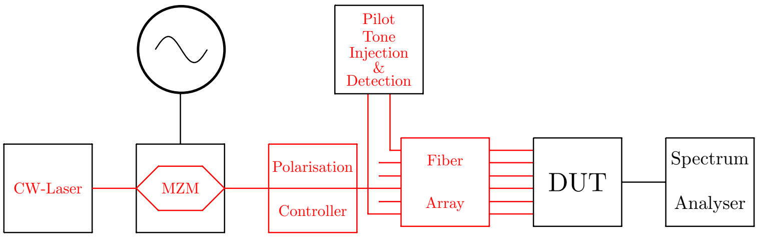

FIGURE 5.13: Measurement setup of the TX chip.

Figure 5.13 shows the measurement setup of the TX EPIC chip. A 1550 nm CW laser is connected to a lithium-niobate MZM driven by an RF signal generator. The RF signal generator, in conjunction with the MZM biased at the quadrature point, is used to amplitude modulate the optical carrier with the electronic LO signal. The polarization of the optical signal is controlled by means of a polarization controller, since only transversal electrical (TE) polarized light can couple to the chip. The optical power at the output of the polarization controller is 2.3 dBm, which is the reference for the input OMA. The TE polarized light is fed into a PM fiber array to couple the light into the chip. Via the pilot lines, a loss of 11.2 dB per grating coupler was observed. The single-ended output signal of the TX EPIC was detected by means of a spectrum analyzer and a vector network analyzer (VNA). The second output of the TX EPIC was terminated by a 50 Ω load. The results were deembedded, and 3 dB were added to calculate the differential performance.

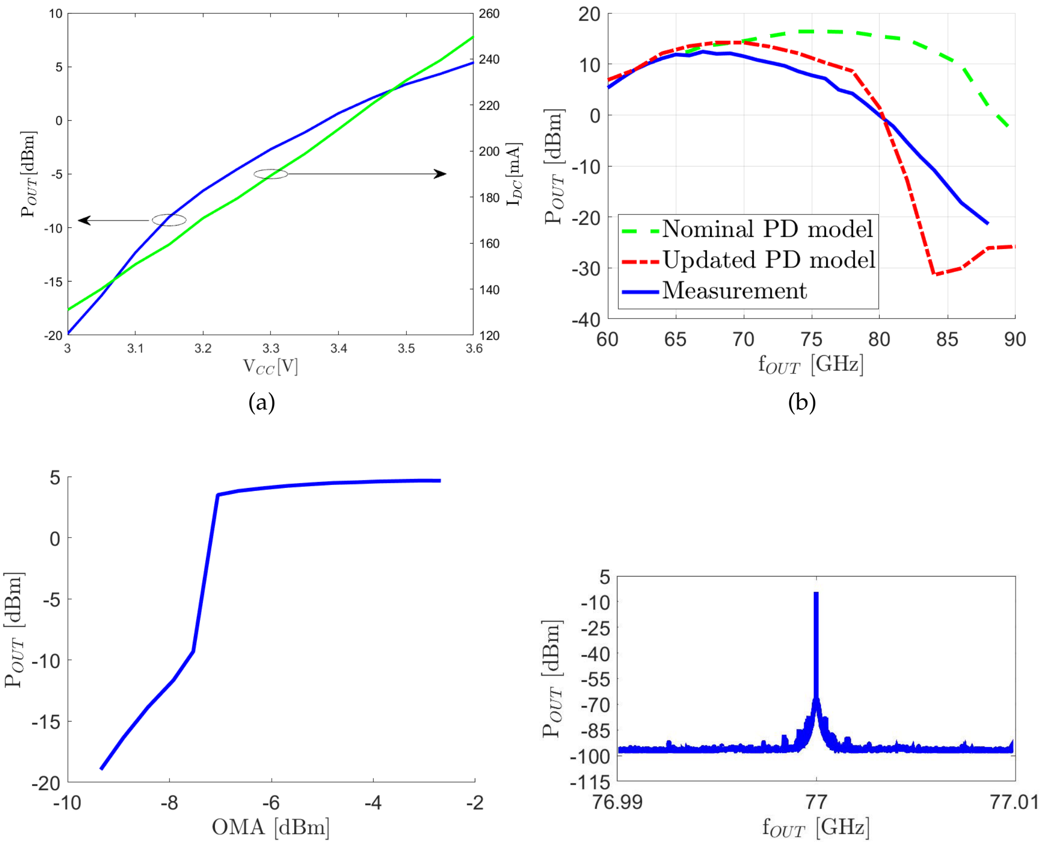

(a) (b)

(c) (d)

FIGURE 5.14: Measurement results of the TX EPIC frontend: (a) Output power and current consumption over supply voltage at 77 GHz, (b) Output power as a function of the output frequency at $-5\,\mathrm{dBm}$ OMA input signal at $V_{CC} = 3.6V$, (c) Output power as a function of OMA at 77 GHz at $V_{CC} = 3.6V$, and (d) Output spectrum at $V_{CC} = 3.6V$.

Figure 5.14 shows the measurement results of the TX frontend. The TX EPIC was designed to operate with a 3.3 V power supply and to deliver 14 dBm output power at 77 GHz. Unfortunately, the maximum output power shifted to 67 GHz, which is caused by a decrease in the germanium PD BW, thus reducing the overall TIA BW by 2.5 GHz, leading to a reduction of 10 GHz at the output of the frequency quadrupler. By increasing the supply voltage from 3.3 V to 3.6 V, the output power at 77 GHz could be increased from $-2.6$ dBm to 5 dBm. At a supply voltage of 3.6 V, the TX EPIC was designed to deliver 15.5 dBm at 77 GHz. The entire power consumption at 3.6 V is 900 mW. The output power and current consumption versus supply voltage are shown in figure 5.14a.

Figure 5.14b shows the measured output power of the TX EPIC over the output frequency of the chip. By making use of post-layout simulation results and the behavioral model (see section 3.3), it was validated that the BW reduction of the TX EPIC is caused by the PD BW reduction. The simulation results with the updated PD model fit favorably with the measurement. With the nominal PD BW, the TX EPIC would deliver 15.5 dBm output power at 77 GHz and a 3 dB BW of 17 GHz. Due to the PD BW reduction, the BW of the entire TX EPIC reduces to 11 GHz.

The measurement results of the TX EPIC power as a function of the LO OMA are shown in figure 5.14c. For an OMA above $-7\,\mathrm{dBm}$, the output power saturates to $5\,\mathrm{dBm}$ at 77 GHz. Below $-7\,\mathrm{dBm}$, the TIA does not provide sufficient power to drive the frequency doubler. Since $0.5\,\mathrm{dB}$ OMA steps were used for the measurements, a distinct edge can be observed in Figure 5.14c.

The RF output port of the TX EPIC with the ESD bondpad and the subsequent PA is matched ($S_{OUT} \leq -10\,\mathrm{dB}$) in the entire BW.

Figure 5.14d shows the output spectrum of the TX EPIC. The transmit signal exhibits excellent spectral purity with the largest side lobes $60\,\mathrm{dB}$ lower than the fundamental signal. At an offset frequency of $2\,\mathrm{MHz}$, the noise reaches the noise floor of the measurement device.

## 5.3 Conclusion

In this chapter, the monolithic integrated 77 GHz electronic-photonic radar TX chip implemented in $250\,\mathrm{nm}$ SiGe BiCMOS technology was presented. All electronic and photonic components integrated within the chip were described in detail. The TIA used in this chapter was designed by Sergiy Gudyriev, based on requirements provided by Stephan Kruse, while the remaining content of the chapter was contributed by Stephan Kruse. Electro-optical measurements were conducted to evaluate the chip's performance. The chip represents the first mm-wave monolithic integrated electronic-photonic radar TX chip.

Due to a reduction in the bandwidth of the germanium PD, combined with a BB optical receiver, the maximum transmit power shifted from 77 GHz to 67 GHz. Under an optical LO power of $-5\,\mathrm{dBm}$ OMA, the chip delivers $13\,\mathrm{dBm}$ at 67 GHz and $5\,\mathrm{dBm}$ at 77 GHz. The chip consumes $900\,\mathrm{mW}$ from a $3.6\,\mathrm{V}$ source.

The TX chip was previously published in [49].

## Chapter 6

# 77 GHz Electronic Photonic Radar Receiver Chip in 250 nm SiGe BiCMOS

In this chapter, a monolithically integrated photonic radar RX chip is presented. Like the TX chip, the RX chip is also implemented in a 250 nm SiGe BiCMOS technology [32, 33] which integrates all photonic and electronic components to receive the optical LO signal and IQ downconvert the mm-wave radar signal.

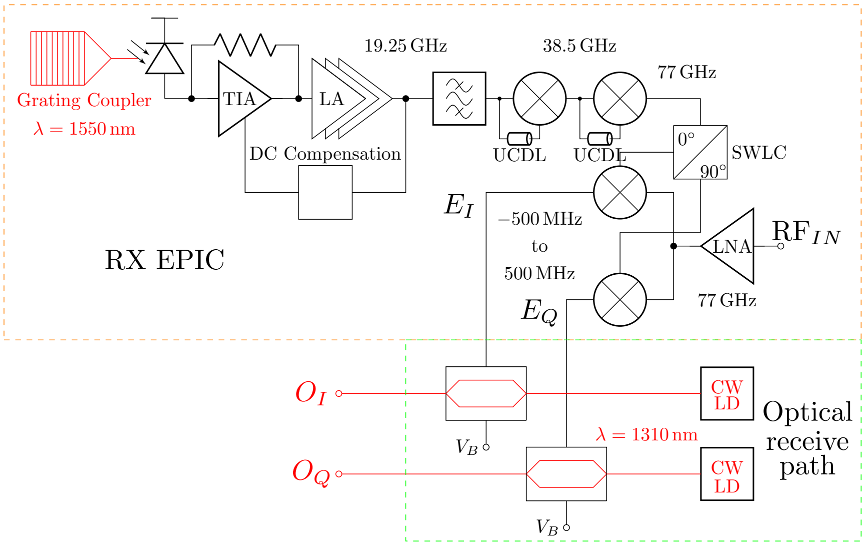

FIGURE 6.1: Block diagram of the photonic radar RX chip with optical LO distribution and optical receive path.

The simplified block diagram of the photonic RX radar chip with optical LO distribution and optical receive path is shown in figure 6.1. Since the photonics, the TIA, and the upconversion of the LO signal to the mm-wave band are the same as in the TX frontend chip, the following subsections will only present the implemented slow wave Lange coupler with the IQ-mixer, the LNA, and the off-chip optical receive path in detail.

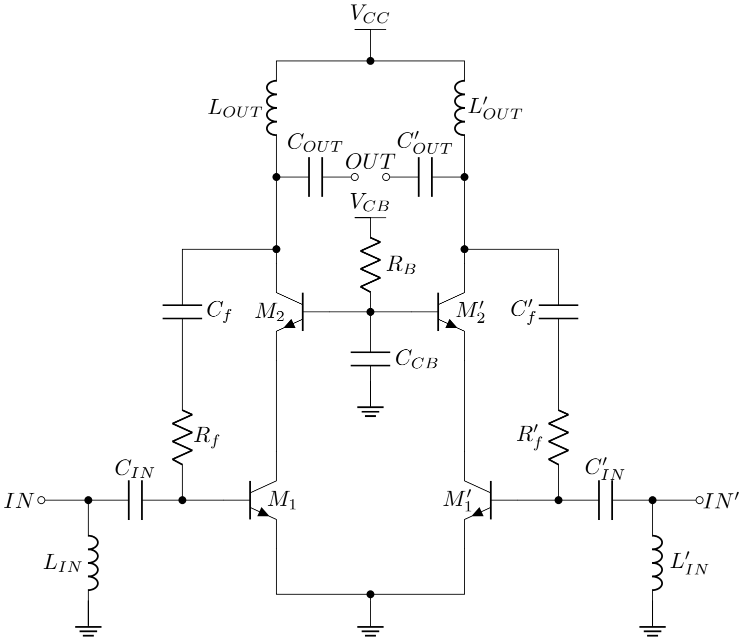

FIGURE 6.2: Simplified schematic of the LNA

## 6.1 Implementation

### 6.1.1 Low Noise Amplifier

The simplified schematic of the LNA is shown in figure 6.2. The LNA is implemented as a pseudodifferential cascode resistive feedback amplifier [102]. The resistive feedback is implemented via $R_f$ and $C_f$, or $R'_f$ and $C'_f$, respectively. Typically, a resistive feedback LNA offers wideband input and output matching without additional input and output matching networks [127]. The noise figure of the resistive feedback LNA depends on the transistor area of $M_1$ [127]. To reduce the noise figure, the maximum allowed transistor size for $M_1$ was selected. Since a larger transistor size reduces the matching properties of the resistive feedback LNA, input and output matching were performed. The components $L_{IN}$, $L'_{IN}$, $C_{IN}$, and $C'_{IN}$ form the input L-matching network, and $L_{OUT}$, $L'_{OUT}$, $C_{OUT}$, and $C'_{OUT}$ form the output L-matching network. Similar to the PA, the CB amplifier operates in weak avalanche area [126] to reduce the power consumption of the LNA. The CB stage of the LNA is biased via a base-degenerated current mirror with $R_B$.

### 6.1.2 IQ-Downconversion Mixer with Slow Wave Lange Coupler

The simplified schematic of the direct downconversion IQ-mixer is shown in figure 6.3. The IQ-mixer is implemented as a pseudodifferential Gilbert cell with a common transconductance amplifier for the in phase (I)- and quadrature phase (Q)-switching quad [128, 129], a common base amplifier for the differential I- and Q-signal, and a passive second-order low-pass current-to-voltage converter. Since the switching transistors have a high influence on the noise figure of the mixer, the current density of the switching transistors was chosen to be close to the maximum $f_T$ [130]. To further improve the noise figure, multifinger transistors were used in the pseudodifferential transconductance amplifier to reduce the base resistance [130]. Simultaneously, the current density of the transconductance amplifier was chosen to be close to the maximum $f_{max}$ to increase the gain of the mixer. The RF port

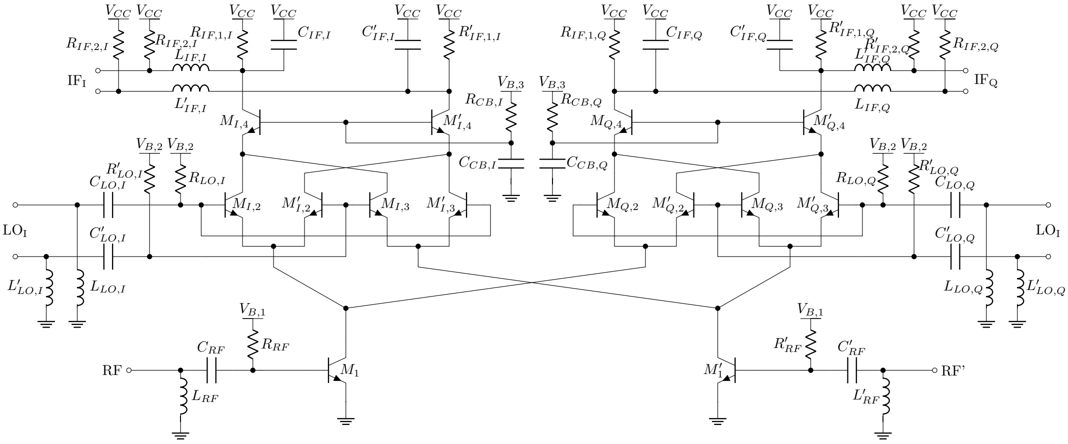

FIGURE 6.3: Simplified schematic of the IQ-mixer

is matched to $50\,\Omega$ single ended (SE) / $100\,\Omega$ differential with a lossless matching network. The components $L_{RF}$, $L'_{RF}$, $C_{RF}$, and $C'_{RF}$ form a differential L-matching network. Both the I- and the Q-LO ports are matched to $50\,\Omega$ SE / $100\,\Omega$ differential with a lossless matching network. The components $L_{LO,x}$, $L'_{LO,x}$, $C_{LO,x}$, and $C'_{LO,x}$ form a differential L-matching network for both the I- and Q-port. The common base amplifier is added to reduce the Miller effect and increase the isolation [113]. Each stage is biased via resistive degenerated current mirrors with $R_{RF}$, $R'_{RF}$, $R_{LO,x}$, $R'_{LO,x}$, and $R_{CB,x}$.

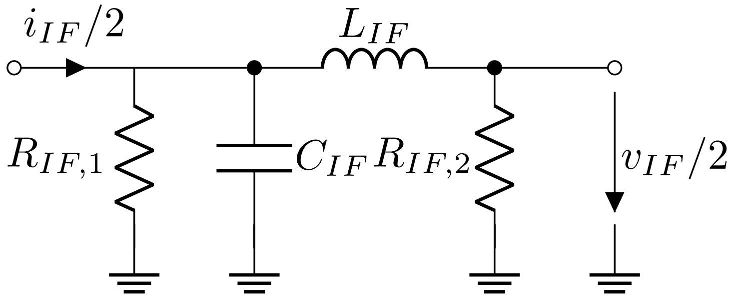

FIGURE 6.4: Small signal equivalent circuit of the second-order low-pass current-to-voltage converter.

The second-order low-pass current-to-voltage converter is used to cancel the unwanted high-frequency component of the signal. The circuit of the second-order current-to-voltage converter is shown in figure 6.4. The impedance of the filter is given by:

$$Z_F(j\omega) = \frac{R_{IF,1} \cdot \left(R_{IF,2}^2 + \omega^2 L_{IF}^2\right)}{R_{IF,1}R_{IF,2} + R_{IF,2}^2 + \omega^2 L_{IF}^2 + j\omega\left(C_{IF}R_{IF,1}R_{IF,2}^2 - L_{IF}R_{IF,2} + \omega^2 R_{IF,1}L_{IF}^2 C_{IF}\right)} \tag{6.1}$$

Close to DC, the I- and Q-port are matched to $50\,\Omega$ single-ended / $100\,\Omega$ differential. The cutoff frequency of the filter was chosen to be $500\,\mathrm{MHz}$.

The IQ-generator network was implemented by a slow wave Lange coupler. The signal lines were implemented in TM2 with the ground plane on M1 and a via fence from M1 to TM2. The cavities in M1 are needed to fulfill the design rules of IHP. The

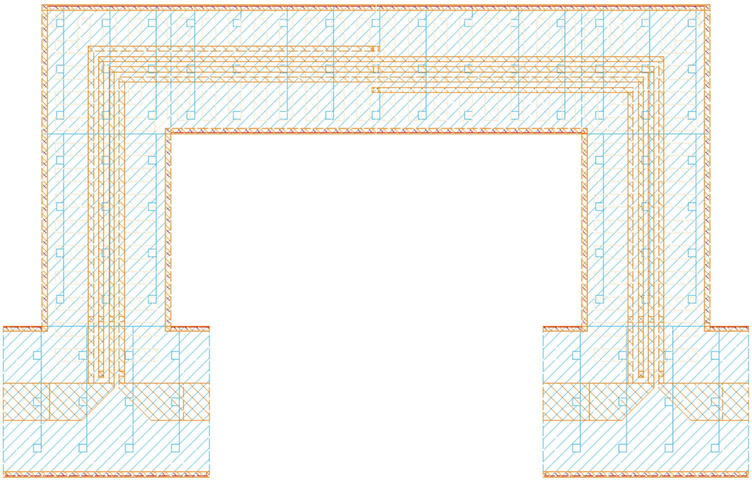

FIGURE 6.5: Top view of the slow wave Lange coupler

isolated port was terminated by a $50\,\Omega$ resistor. Similar to the ultra-compact delay lines (see chapter 5.1.2), the slow wave structure was realized by floating metal shield lines implemented in TM1 perpendicular to the signal line [125] of the Lange coupler [110]. The top view of the slow wave Lange coupler is shown in figure 6.5.

## 6.2 Measurement Setup and Results

The RX chip was fabricated in the same IHP's pre-production, photonic $250\,\mathrm{nm}$ SiGe:C BiCMOS technology [32, 33] run as the TX EPIC, with $f_t$ and $f_{MAX}$ of $200\,\mathrm{GHz}$ and $280\,\mathrm{GHz}$, respectively. The chip microphotograph of the electronic photonic radar RX is shown in figure 6.6. The RX consumes a chip area of $7.93\,\mathrm{mm}^2$ with a core area of $1.44\,\mathrm{mm}^2$.

Figure 6.7 shows the measurement setup of the RX EPIC with electrical and optical receive paths, respectively. Similar to the TX EPIC, a $1550\,\mathrm{nm}$ CW laser is connected to a lithium niobate MZM driven by a first signal generator providing the electrical LO signal. The first signal generator, in conjunction with the MZM, biased at the quadrature point, is used to amplitude modulate the optical carrier with the electrical LO signal. To provide TE polarized light to the grating couplers of the RX EPIC, the polarization is controlled by means of a polarization controller. The TE polarized light is fed into a PM fiber array to couple the optical LO signal into the chip. The optical power at the input of the PM fiber array is $2.3\,\mathrm{dBm}$, which is again the reference for the input OMA.

The differential $77\,\mathrm{GHz}$ RF signal is provided by a VNA, in CW signal generator configuration, and a magic tee in balun configuration. The derivation of the magic tee operating as a balun is provided in appendix I.1.

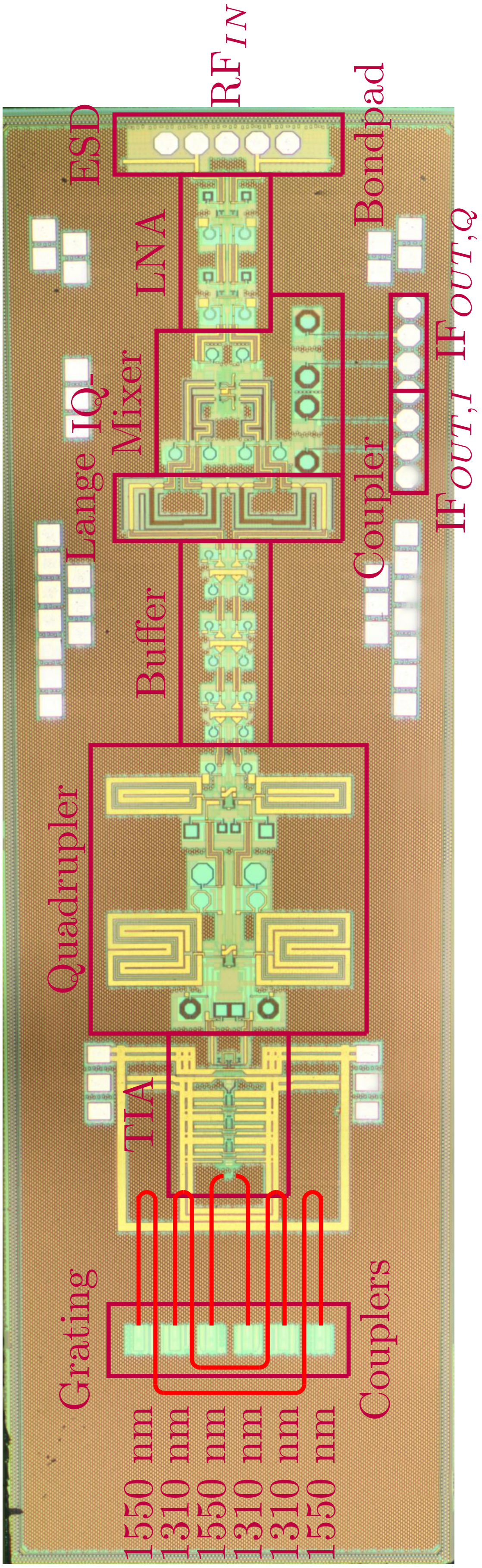

FIGURE 6.6: Chip photograph of the 77 GHz silicon photonic radar RX

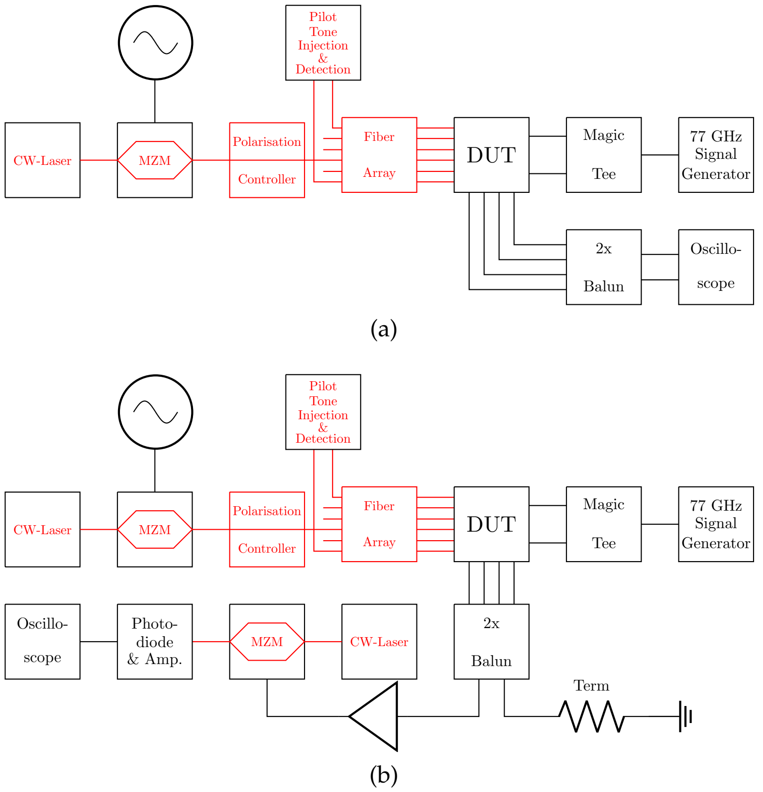

(a)

(b)

FIGURE 6.7: Measurement setup of the RX chip with (a) electrical receive path; (b) off-chip optical receive path.

The differential IQ IF signal is coupled out of the chip via a ground signal signal ground signal signal ground (GSSGSSG) pad configuration. The differential signal is converted to a single-ended signal using baluns. For the measurements of the RX EPIC with electrical receive path, shown in figure 6.7a, the single-ended output signals of the IQ signals are evaluated by an oscilloscope with an input impedance of 50 Ω. For the measurement of the RX EPIC with optical receive path, shown in figure 6.7b, the Q signal is terminated by a termination load, while the I signal is amplified before it modulates the amplitude of a 1310 nm CW laser by means of an off-the-shelf lithium niobate MZM, biased at the quadrature point, with 33 GHz EO BW and 4.5 V RF $V_\pi$. The optical signal is converted to an electrical one by means of an off-the-shelf waveguide integrated PD with an integrated 50 Ω resistor to convert the photocurrent into a voltage. The output signal of the PD is amplified by a LNA before it is observed by an oscilloscope.

The measurement results of the RX EPIC are shown in figure 6.8. The RX frontend was designed, like the TX EPIC, to operate with a 3.3 V power supply, and to achieve a conversion gain of 10 dB and a noise figure of 4.4 dB. Since the RX EPIC was fabricated in the same run as the TX EPIC, the maximum conversion gain of the RX EPIC was also shifted to 66 GHz, caused by the decreased germanium PD BW, thus reducing the overall TIA BW by 2.5 GHz. This leads to a reduction of 10 GHz at the output of the frequency quadrupler. As shown in figure 6.8a, by increasing the supply voltage from 3.3 V to 3.6 V, the output power at an input frequency of 77 GHz could be increased by 12 dB. At a supply voltage of 3.6 V, the RX EPIC was designed to achieve a conversion gain of 13 dB and a noise figure of 4.6 dB at an RF frequency of 77 GHz. The entire power consumption at 3.6 V is 770 mW. Figure 6.8a visualizes the output IF power and the current consumption of the RX EPIC. figure 6.8b shows

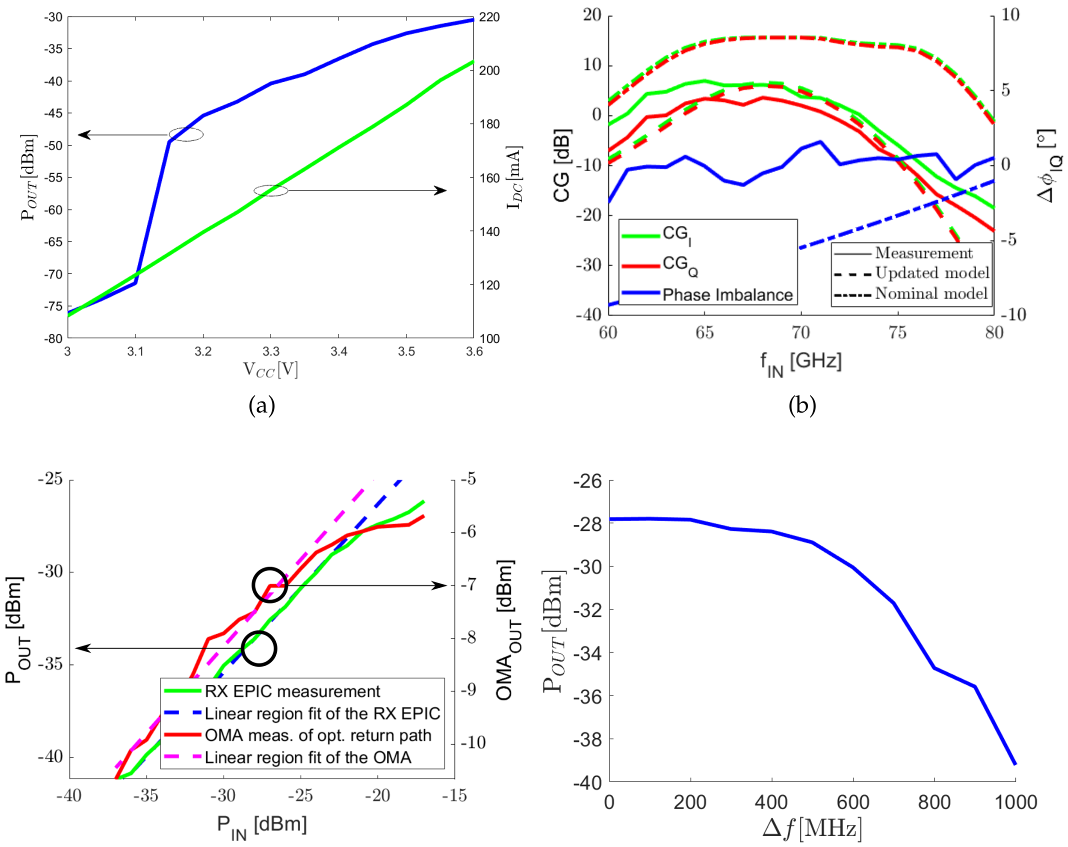

(a) (b)

(c) (d)

FIGURE 6.8: Measurement results of the RX EPIC frontend: (a) Output power and current consumption over supply voltage at an RF input frequency of 77 GHz and IF frequency of 1 MHz, (b) Conversion gain and phase imbalance of the IQ signal at $V_{CC} = 3.6\,\text{V}$ as a function of the RF frequency at $-17\,\text{dBm}$ RF power and 1 MHz IF frequency, (c) Electrical output power and OMA of the receive path and its linear region fit at $V_{CC} = 3.6\,\text{V}$ as a function of the RF input power and an IF frequency of 1 MHz, and (d) Output power at $V_{CC} = 3.6\,\text{V}$ as a function of the IF frequency for an RF frequency of 77 GHz.

the conversion gain and phase imbalance of the RX EPIC. The peak CG of 6.95 dB was achieved at 66 GHz, and a conversion gain of $-11.18\,\text{dB}$ was achieved at 77 GHz. An average amplitude imbalance of 3.53 dB with a peak value of 5.24 dB and an average phase imbalance of 0.023° with a peak value of 2.46° was observed. By making use of the post-layout simulation results and the behavioral model (see section 3.3), it was validated that the performance degradation of the RX EPIC is also caused by the PD BW reduction. With the nominal PD BW, the RX EPIC would achieve a conversion gain of 13 dB and a BW of 21 GHz. Due to the PD BW reduction, the BW of the entire RX EPIC reduces to 9 GHz.

The electrical output power of the electrical receive path of the RX EPIC and the OMA of the optical receive path at an RF frequency of 77 GHz and an IF frequency of 1 MHz are shown in figure 6.8c. The input referred 1 dB compression point of the RX EPIC with electrical or optical receive path is $-20\,\text{dBm}$. This indicates that the linearity of the optical receive path is not dominated by the non-linear EO characteristic of the MZM for an input amplitude of the MZM of $(1/3)V_\pi$. Furthermore, the saturated output power of the RX EPIC with the optical receive path is $17.7\,\mathrm{dB}$ higher than the output power of the electrical receive path and reaches $-6\,\mathrm{dB}$ OMA.

The output power of the RX EPIC as a function of the IF frequency is shown in figure 6.8d. It can be clearly observed that the RX EPIC reaches a single-sided $3\,\mathrm{dB}$ BW of $550\,\mathrm{MHz}$. Out of the band, the filter shows a high-order roll-off factor.

The measured RF input reflection coefficient ($s_{RF}$) is below $-10\,\mathrm{dB}$ in the entire E-band.

## 6.3 Conclusion

In this chapter, the $77\,\mathrm{GHz}$ electronic-photonic radar RX chip, implemented in $250\,\mathrm{nm}$ SiGe BiCMOS technology [32, 33], was presented. All electronic and photonic components integrated into the chip that were not part of the TX chip were described in detail. Electro-optical measurements were carried out to evaluate the chip's performance. The chip represents the first mm-wave monolithic integrated electronic-photonic radar RX chip.

As the RX chip was fabricated in the same process run as the TX chip, the reduced bandwidth of the germanium PD, in combination with a BB optical receiver, led to a shift in the maximum conversion gain from $77\,\mathrm{GHz}$ to $66\,\mathrm{GHz}$. At an IF frequency of $1\,\mathrm{MHz}$, the measured conversion gain was $6.95\,\mathrm{dB}$ at an RF frequency of $66\,\mathrm{GHz}$, and $-11.16\,\mathrm{dB}$ at $77\,\mathrm{GHz}$, with an optical LO power of $-5\,\mathrm{dBm}$ OMA and an RF input power of $-13\,\mathrm{dBm}$. The chip consumes $770\,\mathrm{mW}$ from a $3.6\,\mathrm{V}$ supply.

Furthermore, the chip was tested using an off-chip optical return path. The input-referred $1\,\mathrm{dB}$ compression point of the RX chip, both with and without the optical receive path, was determined to be $-20\,\mathrm{dBm}$.

The RX chip was previously published in [50].

# Chapter 7

# Large Coherent MIMO Radar System

## 7.1 System Implemntation

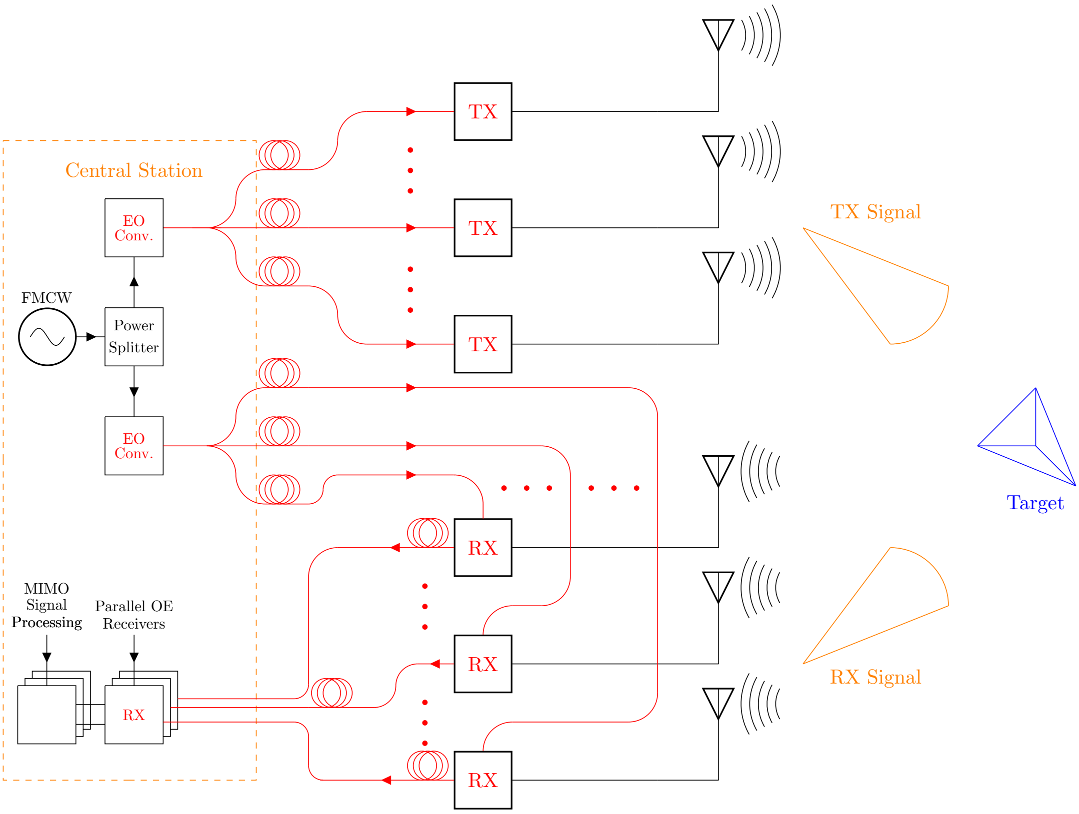

FIGURE 7.1: Simplified block diagram of the FMCW MIMO radar system with optical LO distribution and optical return path.

The simplified block diagram of the FMCW MIMO radar system with optical LO distribution and optical return path from chapter 2.1 is redrawn in figure 7.1. In the previous chapter 2.2, the theory of a FMCW MIMO radar system with optical LO distribution and optical return path was presented. Furthermore, a monolithically integrated radar TRX chipset with optical LO distribution and off-chip optical return path was presented in chapters 5 & 6. In this chapter, a FMCW MIMO radar demonstrator with eight TX and six RX frontends, using the first monolithic integrated radar TRX chipset from chapters 5 & 6, will be presented.

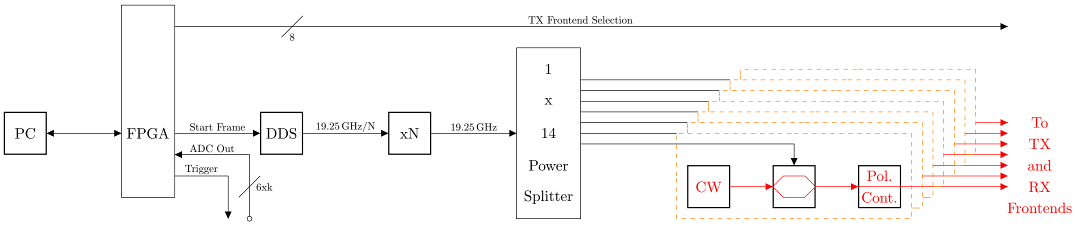

FIGURE 7.2: Block diagram of the transmit and control part of the central station of the 6x8 MIMO demonstrator.

A more detailed look at the control part and transmit part of the central station is shown in figure 7.2. Within the central station, provided by a consortial partner, a central PC controls and receives data from a field programmable gate array (FPGA). The FPGA selects a specific TX frontend which is active in the specific time frame. Subsequently, the FPGA triggers a direct digital synthesizer (DDS) which generates the FMCW chirp at a fraction of the desired frequency. The chirp is upconverted to the 19.25 GHz band by frequency multipliers. The 19.25 GHz signal is split into multiple paths, and in each path, the electrical LO signal is converted to an optical signal by means of MZMs fed by multiple 1310 nm CW lasers. Before each signal is distributed to the frontends, the polarization of each signal is adjusted by means of a polarization controller.

The block diagram of the TX and RX frontends is similar to the measurement setup of the TX EPIC (see chapter 5.2) and the RX EPIC with off-chip optical receive path (see chapter 6.2). Each TX frontend consists of the chip holder PCB, power supply, a TX EPIC from chapter 5 with a non-PM fiber array glued on the chip, a differential microstrip to WR-12 waveguide launcher, designed by a consortial partner, a short WR-12 waveguide from the chip holder PCB to the antenna PCB, and an antenna PCB with a microstrip patch transmit antenna, designed by a consortial partner. Similarly, each RX frontend consists of the chip holder PCB, power supply, a RX EPIC from chapter 6 with a non-PM fiber array glued on the chip, a differential microstrip to WR-12 waveguide launcher, a short WR-12 waveguide from the chip holder PCB to the antenna PCB, and an antenna PCB with a microstrip patch receive antenna. In addition, each RX frontend consists of IF amplifiers and an MZM to implement the optical receive path, provided by a consortial partner. The optical fiber from the central station to the TX frontend and from the central station to the RX frontend have a length offset. The offset is inserted to guarantee that for nearby targets, the IF frequency is above the cutoff frequency of the bias tee of the MZMs.

Figure 7.3 shows the simplified block diagram of the receive part of the central station. Within the central station, the optical IF signal from the RX frontends is converted into an electrical signal by means of a PD and TIA. When a trigger signal from the FPGA in the control unit of the central station is set, the ADCs start digitizing the analog IF signal. The digital IF signal is then transmitted back to the FPGA, which stores the data on the control PC where the MIMO signal processing is performed.

Figure 7.4 shows the front view of the 8x6 MIMO demonstrator, built up by a consortial partner. Eight TX frontends are placed above six RX frontends in two racks with a separation of 30 cm. The aperture size of the demonstrator is approximately 0.5 m. The array geometry in each rack is implemented as planar and linear. The antennas are placed sparsely and non-uniformly. The position is optimized according to the method described in [29] to achieve an azimuth far-field main lobe of 0.23° and a sidelobe level below 9.6 dB.

To enable coherent array processing, performed by a consortial partner, prior

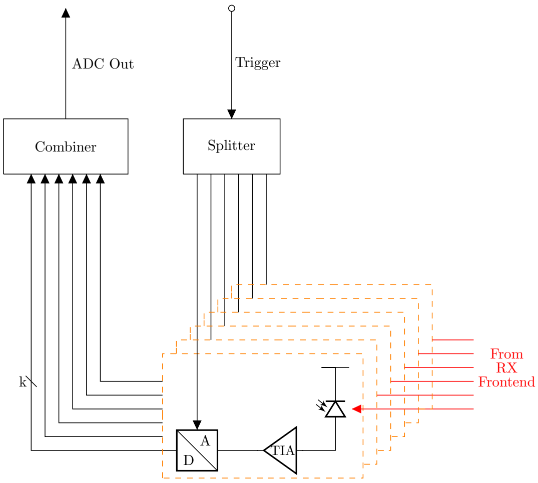

FIGURE 7.3: Block diagram of the receive part of the central station of the 6x8 MIMO demonstrator.

FIGURE 7.4: Front view of the MIMO demonstrator with eight TX and six RX frontends.

and online calibration are necessary, also performed by a consortial partner. For a simple parametric approach, at least the channel imbalances and antenna positions need to be determined. In addition, the time delays of the optical fibers need to be calibrated at least once to align peaks in the range profile. Further information on the calibration can be found in [62].

Measurements of the MIMO demonstrator were conducted in an anechoic chamber under controlled laboratory conditions. Within the chamber, metallic rods with a radius of $11\,\mathrm{mm}$ were positioned at a minimum distance of $2\,\mathrm{m}$ in front of the MIMO demonstrator. The 6×8 MIMO demonstrator is placed at the coordinates $x = 0$; $y = 0$. A simplified measurement setup is provided in figure 7.6a. The actual position of the metallic rods was measured using a crosshair laser installed between the TX and

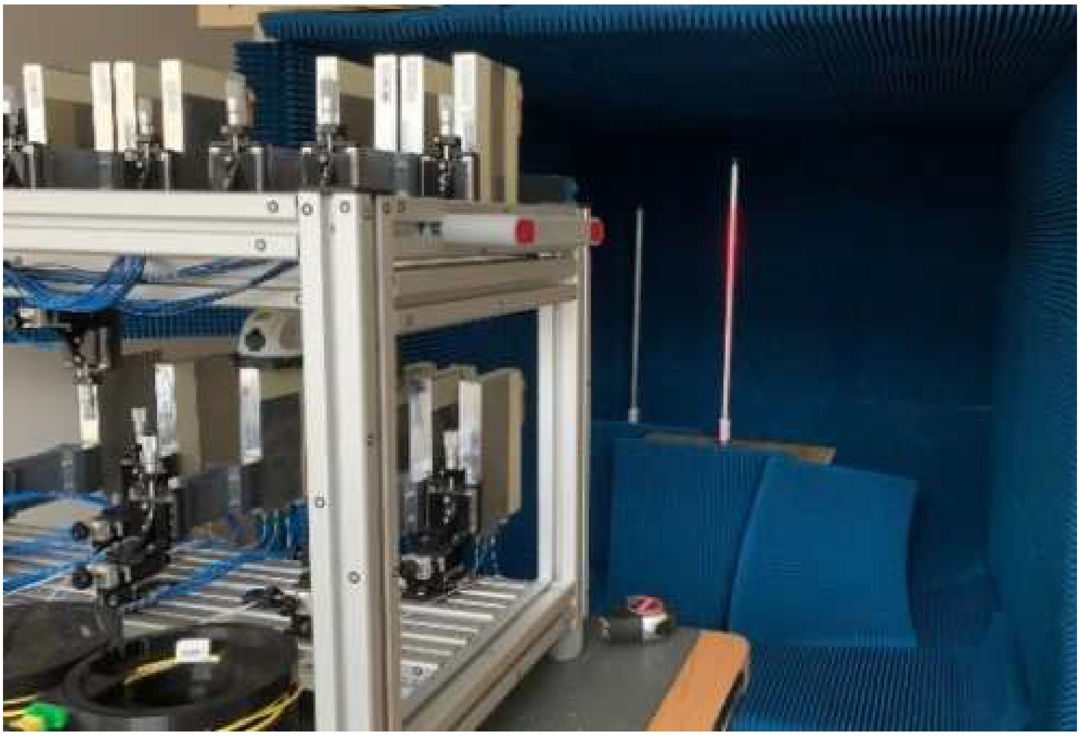

FIGURE 7.5: Measurement setup for the MIMO demonstrator.

RX frontends in the rack. Figure 7.5 shows the measurement setup for the MIMO demonstrator.

Figure 7.6 shows the measurement results of the 8x6 MIMO demonstrator. One metallic rod was at approximately $2\,\mathrm{m}$ distance and the other two metallic rods were at $2.3\,\mathrm{m}$. Figure 7.6b shows that even without the optimization of the antenna position, the three metallic rods result in three peaks in the two-dimensional map close to the actual positions of the metallic rods (marked with red circles). The angular resolution test is shown in figure 7.6c. The two targets at approximately $-19°$ with a separation of $0.5°$ can be easily distinguished. Further resolution tests with targets at various angles showed distinct peaks until $0.4°$, which is close to the theoretical limit of this demonstrator of $0.3°$.

## 7.2 Conclusion

In this chapter, a demonstrator featuring eight TX and six RX chips was presented. The aperture size of the demonstrator was approximately $0.5\,\mathrm{m}$, achieving an azimuth far-field main lobe width of $0.23°$ with a sidelobe level below $9.6\,\mathrm{dB}$. Measurements were conducted in an anechoic environment using three metallic rods. The demonstrator achieved an angular resolution of $0.4°$, which is close to its theoretical limit of $0.3°$.

The measurement setup and results were previously published by the author in [62].

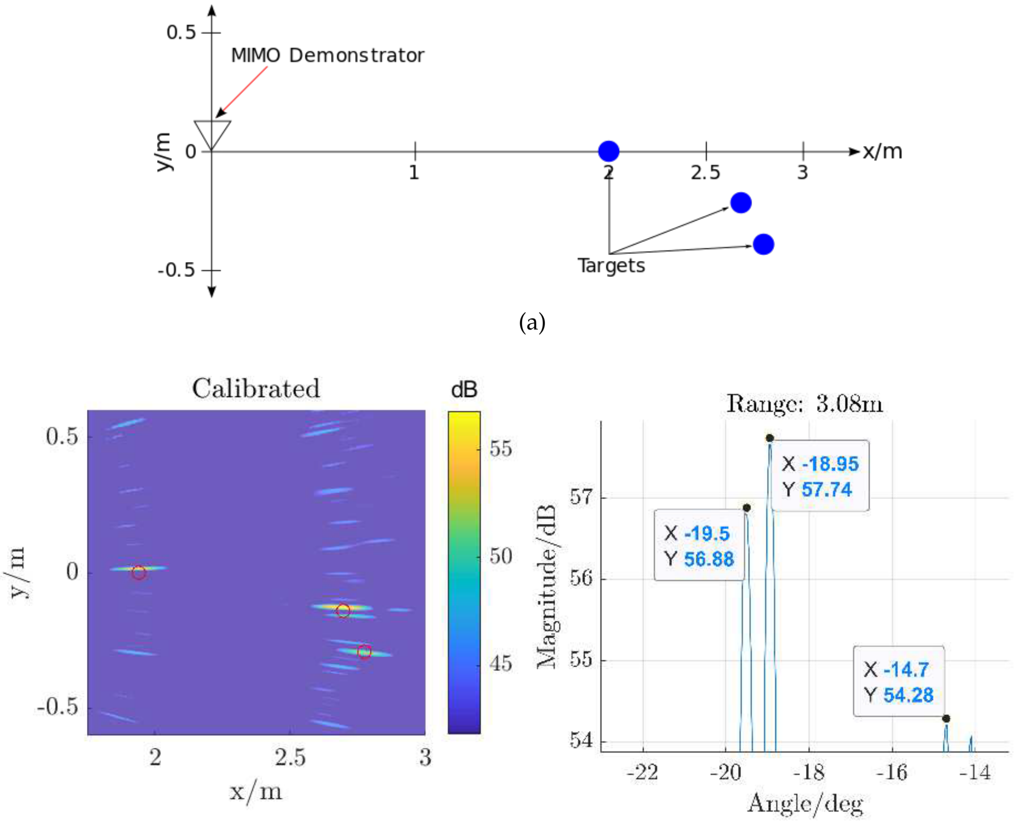

(a)

(b)

(c)

FIGURE 7.6: Measurement setup and results of the 8x6 MIMO demonstrator: (a) Measurement setup with three targets, (b) Two-dimensional distance map with three targets, and (c) Azimuth map with three targets.

# Chapter 8

# Photonic Software Defined MIMO Radar Systems with Optical Signal Distribution

In the previous chapters 2, 3, 5, 6, and 7, the photonic FMCW radar system with optical LO distribution were presented, analyzed, and modeled, and a demonstrator featuring a monolithically integrated TRX chipset was introduced. In this and the following chapters, additional novel photonic radar architectures for automotive applications with optical signal distribution will be presented, analyzed, and evaluated through simulations.

## 8.1 System Overview

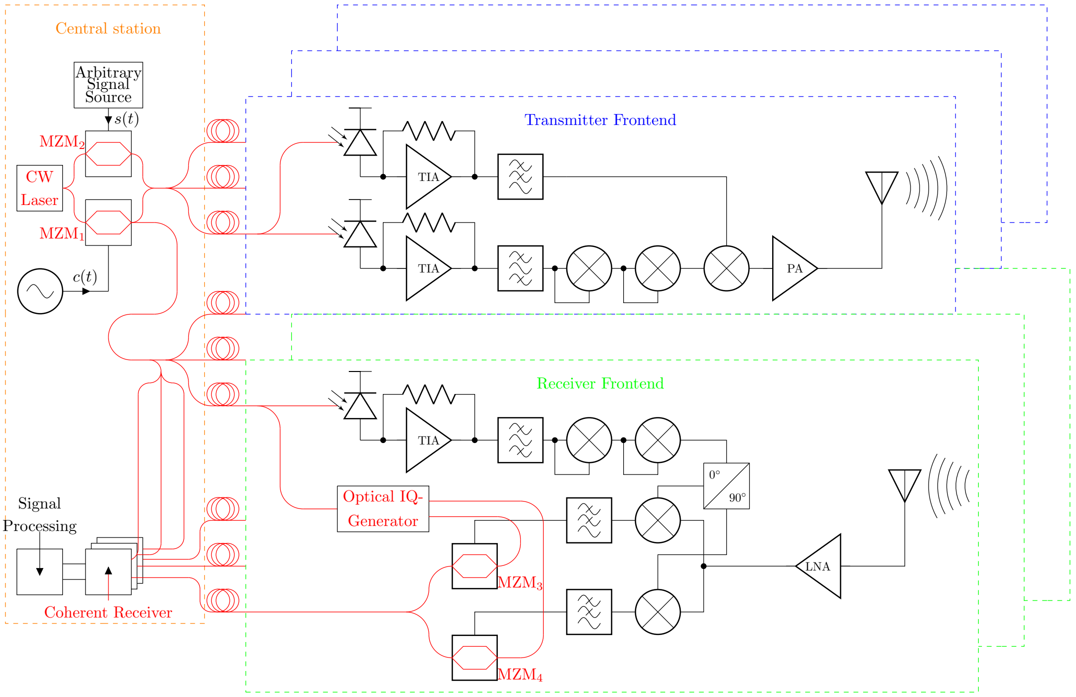

FIGURE 8.1: Simplified block diagram of the photonic software defined MIMO radar system with optical signal distribution and a self-coherent optical return path.

A photonic software-defined MIMO radar system with optical signal distribution is shown in figure 8.1. Within a central station, a CW laser generates the optical carrier which is split into two paths. In the upper path, the optical carrier is modulated by an IF signal $s(t)$, using a first MZM. In the lower part, a fraction of the desired mm-wave signal is modulated by a constant frequency carrier signal $c(t)$ using a second MZM. The two signals are summed, before the signal is divided and distributed to the TX and RX frontends. Additionally, a fraction of the signal is fed to the receive path of the central station to enable coherent demodulation of the received signal.

In the TX frontend, the optical signal is split into two different branches. In the lower branch, the optical signal is converted into an electrical signal by means of a PD and a TIA. The subsequent BPF in the lower arm suppresses the IF signal $s(t)$ and the wireless carrier $c(t)$ is upconverted to the desired mm-wave band. In the upper arm, the optical signal is also converted to an electrical signal by means of a PD and a TIA. The LPF in this arm suppresses the carrier signal $c(t)$, so that only the IF signal is mixed with the wireless carrier via a mixer. Alternatively, to reduce the hardware complexity of the system, the NB four-quadrant electrooptical mixer presented in chapter 4.2 can be used instead of the PD, TIA, BPF, and electrical mixer. The output signal of the mixer is amplified and transmitted via a transmit antenna.

The reflected signal is received by an antenna in the RX frontend. The RX frontend is similar to the RX frontend of the photonic FMCW MIMO radar systems with optical LO distribution presented in chapter 2.1. The optical signal is converted to an electrical signal and upconverted to the mm-wave band, similar to the TX frontend. The weak received signal is amplified by a LNA before IQ demodulation is performed. In comparison to the previously discussed architecture of the photonic FMCW MIMO radar systems with optical LO distribution, a fraction of the optically distributed signal is used to realize an optical IQ return path. It consists of an optical IQ generator and two EO modulators. The two signals are combined and transmitted via a single fiber back to the central station. In the central station, a coherent reception is performed using a fraction of the distributed optical signal. Finally, the regenerated electrical IQ signals are further processed by a signal processing unit.

## 8.2 Analysis

### 8.2.1 Photonic Software-Defined MIMO Radar System with Optical Signal Distribution

The starting point for the analysis of the photonic software defined MIMO radar system are the two MZMs in the central station, shown in fig. 8.1, fed by a continuous wave laser and driven by the sinusoidal carrier voltage $V_c(t)$ with the angular frequency $\omega_{LO}$, and arbitrary signal voltage $V_s(t)$. The output signals of the MZMs are [131]:

$$E_{MZM,1}(t) = \frac{E_0}{2} \cdot \cos\left(\frac{\pi\,(V_c(t) + V_B)}{2V_\pi}\right) e^{j\omega_{opt}t} = E_c(t) e^{j\omega_{opt}t} \tag{8.1}$$

$$E_{MZM,2}(t) = \frac{E_0}{2} \cdot \cos\left(\frac{\pi\,(V_s(t) + V_B)}{2V_\pi}\right) e^{j\omega_{opt}t} = E_s(t) e^{j\omega_{opt}t} \tag{8.2}$$

A fraction of the carrier signal $E_{MZM,1}$ is bypassed for the coherent optical receive path, before both signals are summed up and transmitted to the radar TX frontend. Within the frontend, the signals are split into two branches and in each of them, the optical signal is converted to an electrical signal by means of PDs. The output currents of the PDs are [24]:

$$I_{PD,1,2} = \mathcal{R}\left|k \cdot E_c(t)e^{j\omega_{opt}t} + E_s(t)e^{j\omega_{opt}t}\right|^2 \tag{8.3}$$

$$I_{PD,1,2} = \mathcal{R}\left|k \cdot E_c(t) + E_s(t)\right|^2 \cdot \left|e^{j\omega_{opt}t}\right|^2 \tag{8.4}$$

with $\left|e^{j\omega_{opt}t}\right|^2 = 1$ follows

$$\begin{aligned} I_{PD,1,2} = \frac{\mathcal{R}E_0^2}{8}&\left[k^2 \cdot \left(1+\cos\left(\frac{\pi\left(V_c(t)+V_B\right)}{V_\pi}\right)\right) + 1 + \cos\left(\frac{\pi\left(V_s(t)+V_B\right)}{V_\pi}\right)\right. \\ &\left. + 2k\cos\left(\frac{\pi\left(V_c(t)-V_s(t)\right)}{2V_\pi}\right) + 2k\cos\left(\frac{\pi\left(V_c(t)+V_s(t)+2V_B\right)}{2V_\pi}\right)\right] \end{aligned} \tag{8.5}$$

If the MZMs are biased at the quadrature point ($V_B = -\frac{V_\pi}{2}$), equation 8.5 simplifies to:

$$\begin{aligned} I_{PD,1,2} = \frac{\mathcal{R}E_0^2}{8}&\left[k^2 \cdot \left(1+\sin\left(\frac{\pi\left(V_c(t)\right)}{V_\pi}\right)\right) + 1 + \sin\left(\frac{\pi\left(V_s(t)\right)}{V_\pi}\right)\right. \\ &\left. + 2k\cos\left(\frac{\pi\left(V_c(t)-V_s(t)\right)}{2V_\pi}\right) + 2k\sin\left(\frac{\pi\left(V_c(t)+V_s(t)\right)}{2V_\pi}\right)\right] \end{aligned} \tag{8.6}$$

The output current of the PD is converted to voltages by means of shunt feedback TIA, and in each branch, the output signal is filtered, which cancels all higher harmonics of the carrier signal, the DC component and the mixed terms in eq. 8.6. The output signals after filtering, and using the approximation $\sin(x) \approx x$, are given by:

$$V_{TIA,C} \propto V_c(t) = V_{0,c}\sin\left(\omega_{LO}t + \varphi\right) \tag{8.7}$$

$$V_{TIA,S} \propto V_s(t) \tag{8.8}$$

The carrier signal is upconverted to the desired transmit frequency and then multiplied with the arbitrary signal $V_s(t)$ by means of a conventional mixer for a BB signal or by a single-sideband mixer for a BP signal. The transmit signal in the frequency domain is given by:

$$V_{TX}(j\omega) = V_{0,TX}\left[V_S\left(j(\omega + N \cdot \omega_{LO})\right) + V_S\left(j(\omega - N \cdot \omega_{LO})\right)\right] \tag{8.9}$$

with the amplitude voltage of the transmit signal and the upconversion factor $N$. The amplitude of the transmit signal depends on the E-field, the responsivity of the PD, the gain of the TIA, and the gain of the frequency multipliers, mixers, and the power amplifier.

The received signal is a time-delayed replica of the transmitted signal and is given in the frequency domain by:

$$V_{RX}(j\omega) = G_{PL} \cdot V_{0,TX} \cdot \left[V_S\left(j(\omega + N \cdot \omega_{LO})\right) + V_S\left(j(\omega - N \cdot \omega_{LO})\right)\right] e^{j\omega\tau} \tag{8.10}$$

with the round trip delay $\tau$, and the free-space path loss multiplied by the transmit and antenna gain $G_{PL}$. Within the receiver frontend, the received signal is multiplied with the replica of the upconverted carrier signal. The demodulated IF IQ signal in the time domain is given by:

$$V_{RX,BB,I} = V_{RX,BB,0} \cdot \frac{V_S(t-\tau)}{2} \left[\cos\left(N\omega_{LO}\tau\right) - \cos\left(2N\omega_{LO}t - N\omega_{LO}\tau\right)\right] \quad (8.11)$$

$$V_{RX,BB,Q} = V_{RX,BB,0} \cdot \frac{V_S(t-\tau)}{2} \left[\sin\left(N\omega_{LO}\tau\right) + \sin\left(2N\omega_{LO}t - N\omega_{LO}\tau\right)\right] \quad (8.12)$$

with the amplitude of the baseband signal in the receive frontend $V_{RX,BB,0}$. The amplitude of the baseband signal depends on the free-space path loss, the antenna gain, the amplitude of the transmit signal, and the mixer gain.

The high frequency component is filtered by a LPF before the received signal is retransmitted to the central station by means of a coherent optical IQ return path.

### 8.2.2 Coherent Optical IQ Return Path

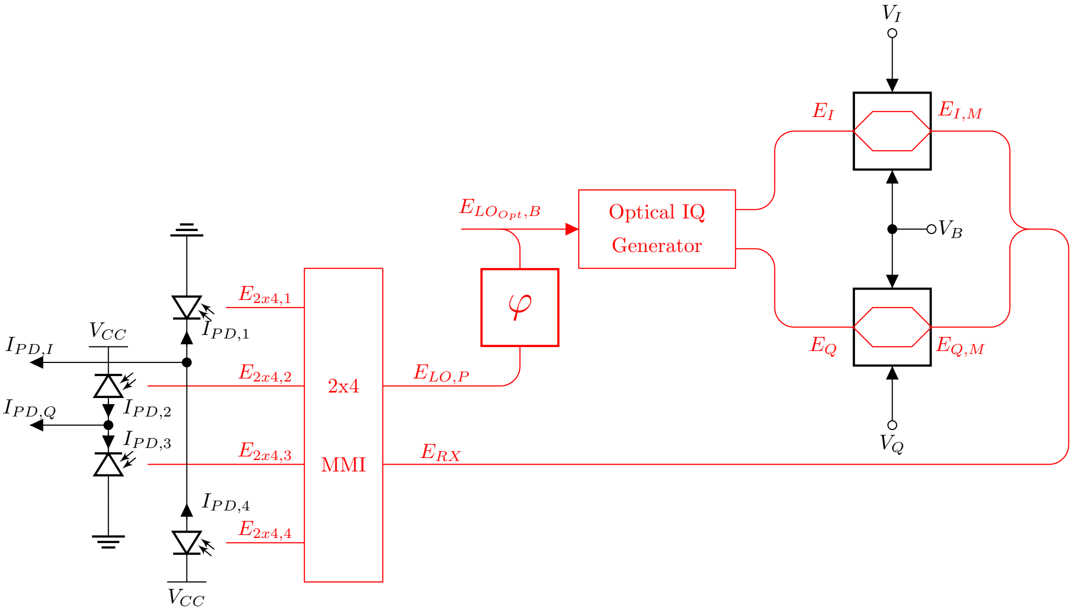

FIGURE 8.2: Coherent optical IQ return path

In a photonic radar system with an optical return path, the downconverted optical IF signals are transmitted via optical fibers to the central station. Typically, IQ demodulation of the received signal requires two fibers to establish the optical receive path from one RX frontend to the central station. This requirement can significantly increase the complexity and cost of large-aperture phased array radar systems. To mitigate this, a coherent optical IQ return path can be employed [132]. Figure 8.2 shows the coherent optical IQ return path.

The optical LO generation within the central station, the OE conversion, and the electrical parts of the TX and RX frontends remain consistent with previously analyzed photonic radar systems with optical LO distribution. Compared to these systems, a fraction of the distributed optical LO signal is bypassed and fed into an optical IQ generator with subsequent EO converters. Within the central station, a fraction of the optical LO signal is also bypassed, phase-adjusted, and fed into the optical RX. The optical RX consists of a 2x4 multimode interferometer (MMI) with PDs and TIAs [121].

The starting point for the analysis is the E-field of the optical signal [133]:

$$E_{LO_{Opt},B} = E \cdot e^{j(\omega_{opt}t+\varphi_0)} \tag{8.13}$$

where $E$ is the time-independent amplitude of the E-field, $\omega_{opt}$ is the optical angular frequency, and $\varphi_0$ is a random initial phase. The optical IQ generator splits the signal into the IQ signals:

$$E_I = \frac{E}{\sqrt{2}} \cdot e^{j(\omega_{opt}t+\varphi_0)} \tag{8.14}$$

$$E_Q = \frac{E}{\sqrt{2}} \cdot e^{j(\omega_{opt}t+\varphi_0+\frac{\pi}{2})} \tag{8.15}$$

The output signals of the IQ generator are modulated by MZMs with the corresponding downconverted electrical IQ signals [131]:

$$E_{I,M} = \frac{E}{\sqrt{2}} \cdot e^{j(\omega_{opt}t+\varphi_0)} \cdot \cos\left(\frac{\pi\left(V_I + V_B\right)}{2V_\pi}\right) \tag{8.16}$$

$$E_{Q,M} = j\frac{E}{\sqrt{2}} \cdot e^{j(\omega_{opt}t+\varphi_0)} \cdot \cos\left(\frac{\pi\left(V_Q + V_B\right)}{2V_\pi}\right) \tag{8.17}$$

The modulated signals are summed up and retransmitted to the central station. The received signal in the central station is given by:

$$E_{RX} = E \cdot e^{j(\omega_{opt}t+\varphi_0)} \cdot \left[\cos\left(\frac{\pi\left(V_I + V_B\right)}{2V_\pi}\right) + j\cos\left(\frac{\pi\left(V_Q + V_B\right)}{2V_\pi}\right)\right]. \tag{8.18}$$

The output E-field vector of the 2x4 MMI with the input signals $E_{RX}$ and the phase-shifted bypassed optical LO signal is given by [134]:

$$\underline{E_{2x4}} = \frac{e^{j\Xi}}{2} \cdot \begin{bmatrix} 1 & -e^{j\frac{\pi}{4}} \\ e^{j\frac{\pi}{4}} & 1 \\ -e^{j\frac{\pi}{4}} & 1 \\ 1 & e^{j\frac{\pi}{4}} \end{bmatrix} \cdot \begin{bmatrix} E_{RX} \\ E_{LO,P} \end{bmatrix} \tag{8.19}$$

with the phase shift of the MMI $\Xi$, the bypassed optical LO signal:

$$E_{LO,P} = d \cdot E \cdot e^{j(\omega_{opt}t+\varphi_P)} \tag{8.20}$$

with the phase shift $\varphi_P$.

The photocurrent vector of the four PDs is given by:

$$\underline{I_{PD}} = i_{PD,0} \cdot \left[\left(|s(t)|^2 + d^2\right)\underline{1} + 2d\begin{bmatrix} -\Re\{s(t)\}\cos\left(\Delta+\frac{\pi}{4}\right) - \Im\{s(t)\}\sin\left(\Delta+\frac{\pi}{4}\right) \\ \Re\{s(t)\}\sin\left(\Delta+\frac{\pi}{4}\right) + \Im\{s(t)\}\sin\left(\Delta-\frac{\pi}{4}\right) \\ -\Re\{s(t)\}\sin\left(\Delta+\frac{\pi}{4}\right) - \Im\{s(t)\}\sin\left(\Delta-\frac{\pi}{4}\right) \\ \\ \Re\{s(t)\}\cos\left(\Delta+\frac{\pi}{4}\right) + \Im\{s(t)\}\sin\left(\Delta+\frac{\pi}{4}\right) \end{bmatrix}\right] \tag{8.21}$$

with $\underline{1}$ the vector of ones, $i_{PD,0}$ the amplitude of the of the photocurrent $\Delta\varphi = \varphi_0 - \varphi_P$, and:

$$s(t) = \cos\left(\frac{\pi\left(V_I + V_B\right)}{2V_\pi}\right) + j\cos\left(\frac{\pi\left(V_Q + V_B\right)}{2V_\pi}\right) \tag{8.22}$$

The amplitude of the photocurrent depends on the responsivity of the PD and the E-field.

If $\Delta\varphi = -\frac{\pi}{4} + 2\pi l,\ l \in \mathbb{N}_0$, the photocurrent vector results in:

$$\underline{I_{PD}} = i_{PD,0} \cdot |E|^2 \cdot \left[\left(|s(t)|^2 + d^2\right)\underline{1} + 2d\begin{bmatrix} -\Re\{s(t)\} \\ \Im\{s(t)\} \\ -\Im\{s(t)\} \\ \Re\{s(t)\}\end{bmatrix}\right] \tag{8.23}$$

If $V_B = -V_\pi$, and making use of $sin(x) \approx x$, the IQ signals can be regenerated via:

$$\begin{aligned} I_{PD,I} &= I_{PD,4} - I_{PD,1} && (8.24)\\ &= 4 \cdot d \cdot i_{PD,0} \cdot \cos\left(\frac{\pi\left(V_I + V_B\right)}{2V_\pi}\right) \approx 2 \cdot d \cdot i_{PD,0} \cdot \frac{\pi V_I}{V_\pi} && (8.25)\\ I_{PD,Q} &= I_{PD,2} - I_{PD,3} && (8.26)\\ &= 4 \cdot d \cdot i_{PD,0} \cdot \cos\left(\frac{\pi\left(V_Q + V_B\right)}{2V_\pi}\right) \approx 2 \cdot d \cdot i_{PD,0} \cdot \frac{\pi V_Q}{V_\pi} && (8.27) \end{aligned}$$

## 8.3 System Simulation

### 8.3.1 Photonic Software-Defined MIMO Radar System with Optical Signal Distribution

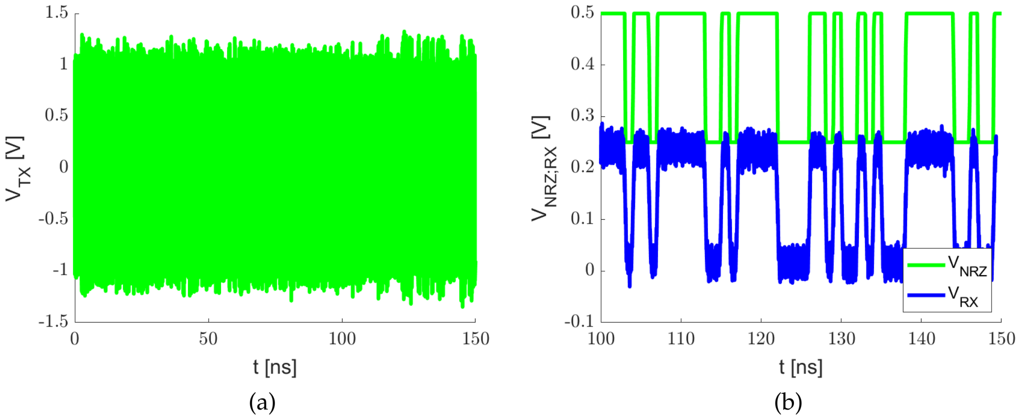

(a) (b)

FIGURE 8.3: Simulated (a) transmit signal in time domain; (b) pseudorandom non-return-to-zero sequence and the received signal after downconversion and optical receive part.

The simulation setup of the photonic software-defined MIMO radar system with optical signal distribution in Lumerical Interconnect closely resembles the photonic

FMCW MIMO radar system with optical LO distribution, presented in chapter 3.1, and is detailed in appendix E.

The simulated transmit signal in the time domain can be seen in figure 8.3a. Due to the finite time resolution of Lumerical Interconnect, only a small amplitude variation of the high-frequency carrier signal can be observed. Figure 8.3b shows a $50\,\mathrm{ns}$ time window of the pseudorandom non-return-to-zero sequence and the received signal after downconversion and optical receive part. The received signal is time-shifted by the time delay of the noiseless channel. It can be clearly observed that the arbitrary signal can be perfectly reconstructed.

### 8.3.2 Coherent Optical IQ Return Path

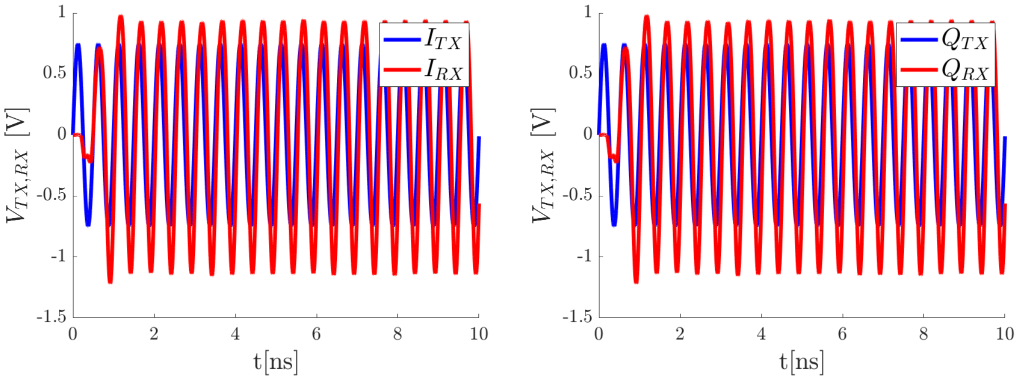

(a)

(b)

FIGURE 8.4: Simulation results of the (a) in-phase signal; (b) quadrature-phase signal before the coherent optical IQ return path (blue) and after the coherent optical IQ return path (red).

The simulation setup of the coherent optical IQ return path in Lumerical Interconnect is presented in appendix F.

The time-domain simulation results of the coherent optical IQ return path are presented in figure 8.4. After the transient response of the BPFs, both the in-phase and quadrature-phase signals are accurately reconstructed. Only a slight phase shift is observed between the input and output signals, which is also attributed to the BPFs.

## 8.4 Conclusion

In this chapter, a photonic software-defined MIMO radar systems with optical signal distribution was presented. In this system, a single fiber is used to distribute both the wireless carrier and an arbitrary IF signal from the central station to the RF frontends. Additionally, the system repurposes the optical LO signal to enable a coherent optical receive path. The system, together with the coherent optical IQ return path, was analyzed mathematically, and simulation results were presented using the optical design software Lumerical Interconnect by Ansys. The analysis and simulation demonstrate the system's potential to realize a large-aperture photonic radar with optical signal distribution and arbitrary transmit signals.

It should be noted that all components can be integrated using low-cost, mass-market silicon technology.

The system, its analysis, and the underlying model were previously published by the author in [54, 71].

# Chapter 9

# Photonic FMCW Multiband Radar System with Optical LO Distribution

In the previous chapter, photonic software-defined MIMO radar systems with optical signal distribution were presented. In this chapter, an additional photonic radar system featuring optical LO distribution is introduced. This system utilizes nonlinear EO conversion and photodiode-based signal beating to realize a *multiband* photonic radar architecture with optical LO distribution.

## 9.1 System Overview

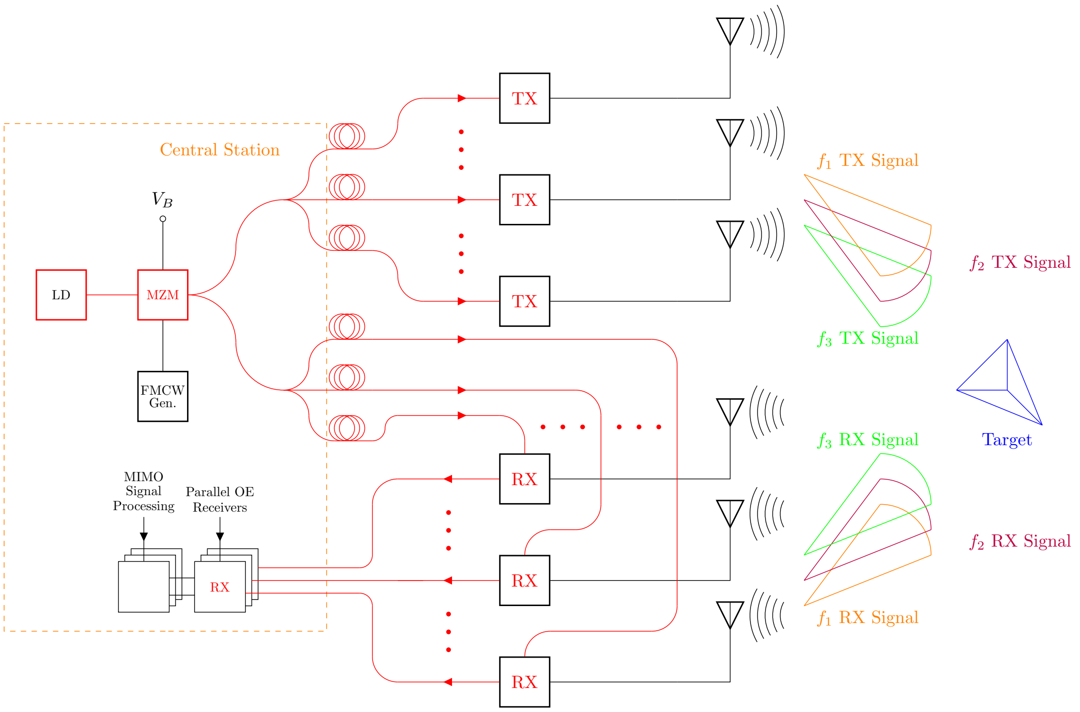

FIGURE 9.1: Simplified block diagram of the photonic FMCW multiband radar system with optical LO distribution.

The photonic multiband radar system with optical LO distribution—whose simplified block diagram is shown in figure 9.1—is inspired by previous publications on Nyquist pulses [135, 136]. Similar to previous photonic radar architectures, this system features a central station where the optical FMCW LO signal is generated using an EO modulator driven by an FMCW generator. The EO modulator is externally biased via the bias voltage $V_B$. From the central station, the optical LO signal is distributed to both the TX and RX frontends.

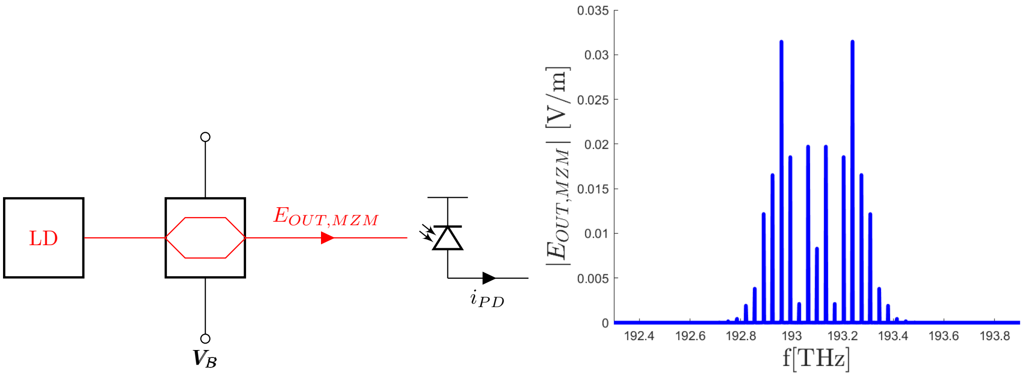

(a) (b)

FIGURE 9.2: (a) Simplified block diagram of the harmonic generation; (b) Output E-field of the MZM.

Harmonic generation in the photonic multiband radar system is achieved through EOE conversion by means of a CW laser, MZM, and beating in a PD. The simplified block diagram of the harmonic generation is shown in figure 9.2a. Within the central station, the amplitude of the electrical FMCW signal and the bias voltage of the EO modulator are properly adjusted. Through beating in a PD, the resulting E-field $E_{OUT,MZM}$, shown in figure 9.2b, is converted into an electrical current $i_{PD}$ that contains the three harmonics. As will be shown in chapter 9.2, by fine-tuning the bias point and drive amplitude of the EO modulator within the central station, three FMCW chirps with equal peak power can be generated after the OE conversion. Since the harmonics are generated via EOE conversion, the frontend design can be significantly simplified.

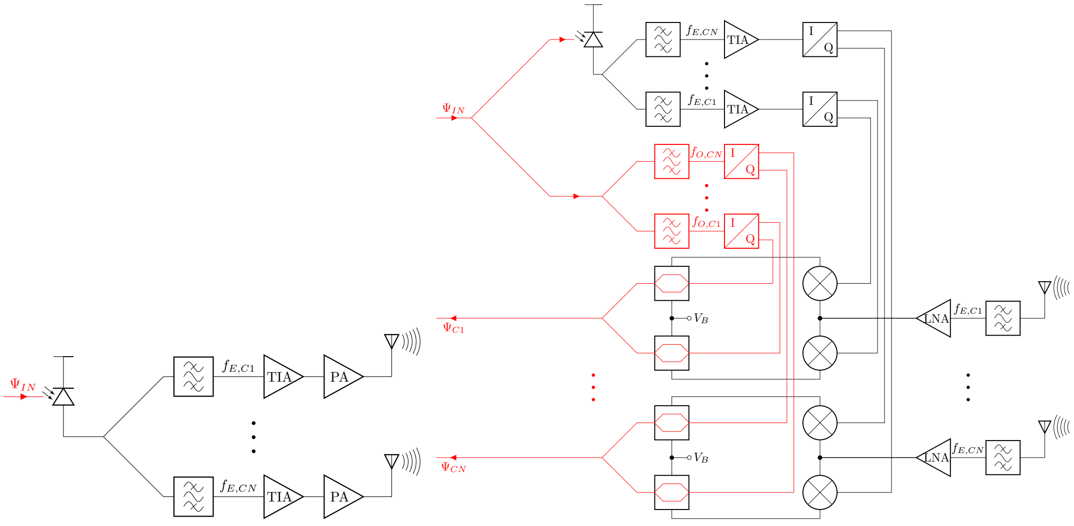

(a) (b)

FIGURE 9.3: Simplified block diagram of the (a) TX frontend; (b) RX frontend of a photonic multiband radar with optical LO distribution.

Figure 9.3a shows the simplified block diagram of the TX frontend. Within the frontend, the optical signal is converted to an electrical signal by means of a PD and split into the different branches, one branch for each band. The desired band of each branch is filtered by means of BPFs before amplification by means of a TIA. The filtered and amplified signal is further amplified using PAs and transmitted via transmit antennas optimized for each band.

The three radar signals are reflected by an obstacle and received by the RX frontend array, which is fed by the same optical LO signal.

Within the RX frontend, shown in figure 9.3b, the received signal, provided by receive antennas, is amplified by means of LNAs after the desired band is selected by a BPF. In each band, the amplified signal is downconverted to the baseband by a direct downconversion IQ mixer. The IQ signal for each band is provided by an electrical IQ network. The LO input signal of the IQ network is converted from the optical LO by means of a PD, TIA, and BPFs, similar to the OE conversion and band selection in the TX frontend. The electrical output signal of the IQ mixer is converted to the optical domain by EO modulators, biased at the quadrature point, and fed by single line of the optical LO signal. To reduce the number of optical fibers, the optical LO signal is reused as optical signal for the receive path, and an optical IQ modulation (see section 8.1) can be used.

Within the central station, the optical signal is converted back to an electrical signal by several parallel OE RX before further MIMO processing is performed.

It should be noted that the OE conversion of each band, consisting of a PD, BPF, and TIA, can be implemented by one optical NB receiver (see section 4.1) for each band.

## 9.2 Analysis

The starting point for deriving the photonic FMCW multiband radar system, shown in figure 9.1 and figure 9.3, with an electro-optical modulator is the output intensity of a MZM given in eq. 2.1. The output power of the PD within the TX frontend is given by:

$$\begin{aligned}
P_{PD,TX} &= 2P_{PD,TX,0}\left[1+\cos\left(\frac{\pi\left[V_S(t)+V_B\right]}{V_\pi}\right)\right]^2 \\
&= P_{PD,TX,0}\left[3+4\cos\left(\frac{\pi\left(V_s(t)+V_B\right)}{V_\pi}\right)+\cos\left(\frac{2\pi\left(V_s(t)+V_B\right)}{V_\pi}\right)\right] \\
&= P_{PD,TX,0}\left[3+4\cos\left(\frac{\pi V_B}{V_\pi}\right)\cos\left(\frac{\pi V_s(t)}{V_\pi}\right)-4\sin\left(\frac{\pi V_B}{V_\pi}\right)\sin\left(\frac{\pi V_s(t)}{V_\pi}\right)\right. \\
&\quad\left.+\cos\left(\frac{2\pi V_B}{V_\pi}\right)\cos\left(\frac{2\pi V_s(t)}{V_\pi}\right)-\sin\left(\frac{2\pi V_B}{V_\pi}\right)\sin\left(\frac{2\pi V_s(t)}{V_\pi}\right)\right] \qquad (9.1)
\end{aligned}$$

with the amplitude of the output power of the PD $P_{PD,TX,0}$. The amplitude By making use of the substitutions:

$$
\begin{aligned}
V_s(t) &= V_0 \cos\left(\Xi(t)\right) && (9.2)\\
\Xi(t) &= \left[\omega_{LO} + \frac{\mu t}{2}\right] t && (9.3)\\
\hat{V_0} &= \frac{\pi V_0}{V_\pi} && (9.4)\\
\hat{V_B} &= \frac{\pi V_B}{V_\pi} && (9.5)
\end{aligned}
$$

Eq. 9.1 simplifies to:

$$
\begin{aligned}
P_{PD,TX} = P_{PD,TX,0} \Big[ & 3 + 4\cos\left(\hat{V_B}\right)\cos\left(\hat{V_0}\cos\left(\Xi(t)\right)\right) - 4\sin\left(\hat{V_B}\right)\sin\left(\hat{V_0}\cos\left(\Xi(t)\right)\right)\\
& + \cos\left(2\hat{V_B}\right)\cos\left(2\hat{V_0}\cos\left(\Xi(t)\right)\right) - \sin\left(2\hat{V_B}\right)\sin\left(2\hat{V_0}\cos\left(\Xi(t)\right)\right)\Big] \quad (9.6)
\end{aligned}
$$

Using the Jacobi-Anger expansions results in:

$$
\begin{aligned}
P_{PD,TX} = P_{PD,TX,0} \Bigg[ & 3 + 4\cos\left(\hat{V_B}\right)\left[J_0\left(\hat{V_0}\right) + 2\sum_{n=1}^{\infty}(-1)^n J_{2n}\left(\hat{V_0}\right)\cos\left(2n\Xi(t)\right)\right]\\
& + 8\sin\left(\hat{V_B}\right)\sum_{n=1}^{\infty}(-1)^n J_{2k-1}\left(\hat{V_0}\right)\cos\left(\left[2n-1\right]\Xi(t)\right)\\
& + \cos\left(2\hat{V_B}\right)\left[J_0\left(2\hat{V_0}\right) + 2\sum_{n=1}^{\infty}(-1)^n J_{2n}\left(2\hat{V_0}\right)\cos\left(2n\Xi(t)\right)\right]\\
& +2\sin\left(2\hat{V_B}\right)\sum_{n=1}^{\infty}(-1)^n J_{2k-1}\left(2\hat{V_0}\right)\cos\left(\left[2n-1\right]\Xi(t)\right)\Bigg] \quad (9.7)\\
P_{PD,TX} = P_{PD,TX,0} \Big[ & 3 + 4\cos\left(\hat{V_B}\right)J_0\left(\hat{V_0}\right) + \cos\left(2\hat{V_B}\right)J_0\left(2\hat{V_0}\right)\\
& - 2\left[4\sin\left(\hat{V_B}\right)J_1\left(\hat{V_0}\right) + \sin\left(2\hat{V_B}\right)J_1\left(2\hat{V_0}\right)\right]\cos\left(\Xi(t)\right)\\
& - 2\left[4\cos\left(\hat{V_B}\right)J_2\left(\hat{V_0}\right) + \cos\left(2\hat{V_B}\right)J_2\left(2\hat{V_0}\right)\right]\cos\left(2\Xi(t)\right)\\
& +2\left[4\sin\left(\hat{V_B}\right)J_3\left(\hat{V_0}\right) + \sin\left(2\hat{V_B}\right)J_3\left(2\hat{V_0}\right)\right]\cos\left(3\Xi(t)\right) + \mathcal{O}\left(4\Xi(t)\right)\Big]\\
& \qquad (9.8)
\end{aligned}
$$

With $\mathcal{O}$ representing the big-O notation. Equation 9.8 orders the terms according to the DC term and the first three harmonics. Resubstituting $\hat{V_B}$, $\hat{V_0}$, and $\Xi$, eq. 9.8 results in:

$$
P_{PD,TX} = P_{PD,TX,0}\left[3 + P_{0th} + 2\sum_{n=1}^{3} P_{nth}\cos\left(n\left[\omega_{LO} + \frac{\mu t}{2}\right]t\right) + \mathcal{O}\left(4\left[\omega_{LO} + \frac{\mu t}{2}\right]t\right)\right] \quad (9.9)
$$

with:

$$
P_{nth} = 4\cos\left(\frac{\pi V_B}{V_\pi} + \frac{n\pi}{V_\pi}\right)J_n\left(\frac{\pi V_0}{V_\pi}\right) + \cos\left(\frac{2\pi V_B}{V_\pi} + \frac{n\pi}{V_\pi}\right)J_n\left(\frac{2\pi V_0}{V_\pi}\right) \quad (9.10)
$$

Eqs. 9.9 and 9.10 show that the amplitude of the harmonics is a function of the EO modulator bias voltage $V_B$ and the amplitude of the FMCW chirp amplitude $V_0$. The optimal point would be defined as the bias and amplitude point where $P_{1st} = P_{2nd} = P_{3rd}$.

Numerically it can be shown that a photonic multiband radar can be implemented with the previously proposed architecture if the amplitude mismatch is minimized:

$$\varepsilon = \min\left\{\frac{\Delta P}{\overline{P}}\right\} \tag{9.11}$$

while the amplitudes are maximized:

$$P_{max} = \max\left\{\overline{P}\right\} \tag{9.12}$$

In eq. 9.11, $\Delta P$ is defined as:

$$\Delta P = \max\left\{\left[\|P_{nth} - P_{mth}\|\, n, m \in \{1,2,3\}\right]\right\} \tag{9.13}$$

and

$$\overline{P} = \frac{1}{3}\sum_{n=1}^{3} P_{nth} \tag{9.14}$$

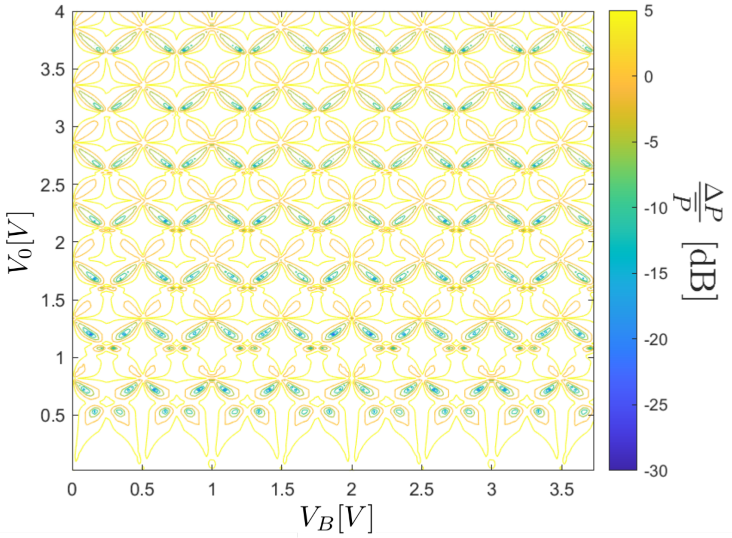

FIGURE 9.4: Contour plot of the maximum intensity mismatch between the first three harmonics as a function of $V_B$ and $V_S$ for an MZM with $V_\pi = 2\,\mathrm{V}$.

A contour plot of $\Delta P$ as a function of $V_B$ and $V_0$ is shown in Fig. 9.4. It can be observed that parameter combinations can be found where the maximum amplitude mismatch is minimized.

In the case of a perfect BPF in each branch and the same gain of the TIAs ($G_{TIA}$), the output signals of the three branches result in:

$$P_{TIA,n} = G_{TIA} P_{nth} \cos\left(n\left[\omega_{LO} + \frac{\mu t}{2}\right] t\right)\bigg|_{n \in 1,2,3} \tag{9.15}$$

The result of eq. 9.15 shows an FMCW multiband radar chirp, with one chirp in each branch.

In the RX frontend, the input signal of the LNA results, in the case of a perfect BPF, in:

$$P_{RX,k} = G_{PL} \cdot P_{kth} \cdot \cos\left(n\left[\omega_{LO} + \frac{\mu t}{2}\right]t\right)\Bigg|_{k\in 1,2,3} \tag{9.16}$$

with the free-space path loss multiplied by the transmit and receive antenna gains $G_{PL}$. The received signal in eq. 9.16 is, for each band, again an FMCW chirp. Each chirp can be downconverted and transmitted back to the central station as presented in the previous sections for a single carrier FMCW photonic radar system.

## 9.3 System Simulation

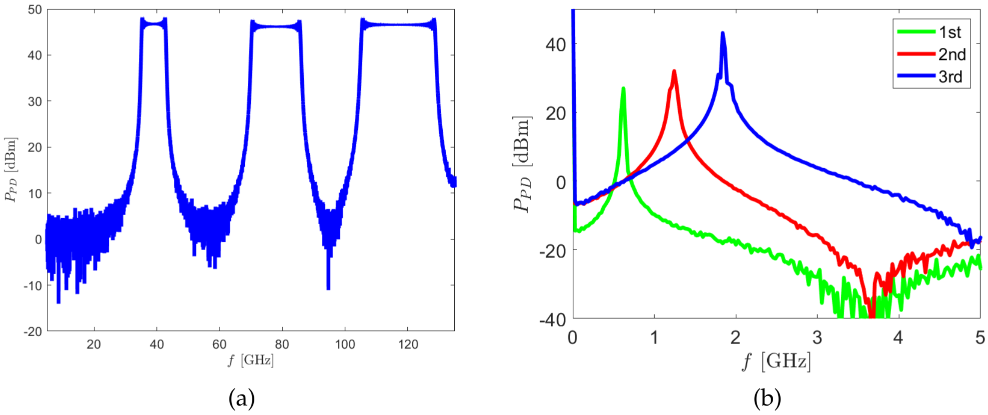

(a) (b)

FIGURE 9.5: Simulated multiband (a) FMCW transmit chirp; (b) IF spectrums for a round trip delay of $3\,\mathrm{ns}$.

The simulation setup of the photonic FMCW multiband radar aystems with optical LO distribution in Lumerical Interconnect is provided in appendix G.

The simulated transmitted multiband FMCW chirps in the frequency domain with $V_{B,MZM} = 0.8V_\pi$, and $V_0 = 1.66V_\pi$ are shown in figure 9.5a. It can be clearly observed that the three chirps have almost the same amplitude $\left(\overline{P} = 46.63\,\mathrm{dB\,m}\right.$ at $\left.\varepsilon = -26.73\,\mathrm{dB}\right)$, while the BW of each chirp scales linearly with the order of harmonics.

The simulations of the received IF signals after OE conversion in the central station, for a round-trip delay $\tau$ of $3\,\mathrm{ns}$, are shown in figure 9.5b. The target is clearly visible in all three IF frequency signals, each corresponding to a specific band. In figure 9.5b, the fundamental frequency chirp is represented in green, the second harmonic in red, and the third harmonic in blue. The amplitude imbalances result from the $1/\lambda$ behavior of the radar cross-section [137] implemented in the wireless channel. The wavelength dependence of the free-space path loss was omitted in the simulation.

## 9.4 Conclusion

In this chapter, a photonic multiband radar system with optical LO distribution was presented. The system utilizes the nonlinear transfer function of the MZM in conjunction with beating in a PD to generate the first three harmonics of a fundamental FMCW signal. Simulations showed that there is no point at which the first three harmonics exhibit equal amplitude. Nonetheless, it was proven by simulations that there exists an $\varepsilon$ for which the amplitude mismatch is minimized. The subsequent simulation in Lumerical Interconnect by Ansys validated the theoretical findings. The simulation demonstrated the three harmonics of the carrier signal and the three distinct IF signals, one corresponding to each band.

It should be noted that all components can be integrated using low-cost, mass-market silicon technology.

The system, its analysis, and the simulation model in Lumerical Interconnect by Ansys were previously published by the author in [60, 64].

# Chapter 10

# Lidar-Radar Combined Sensor System

In the previous chapters, different photonic radar systems with optical signal distribution were presented. In this chapter, the optical LO signal is reused to build a lidar system that operates coherently to the radar. In addition, it shows same Doppler shift as the radar although the carrier frequencies are orders of magnitude different.

## 10.1 System Overview

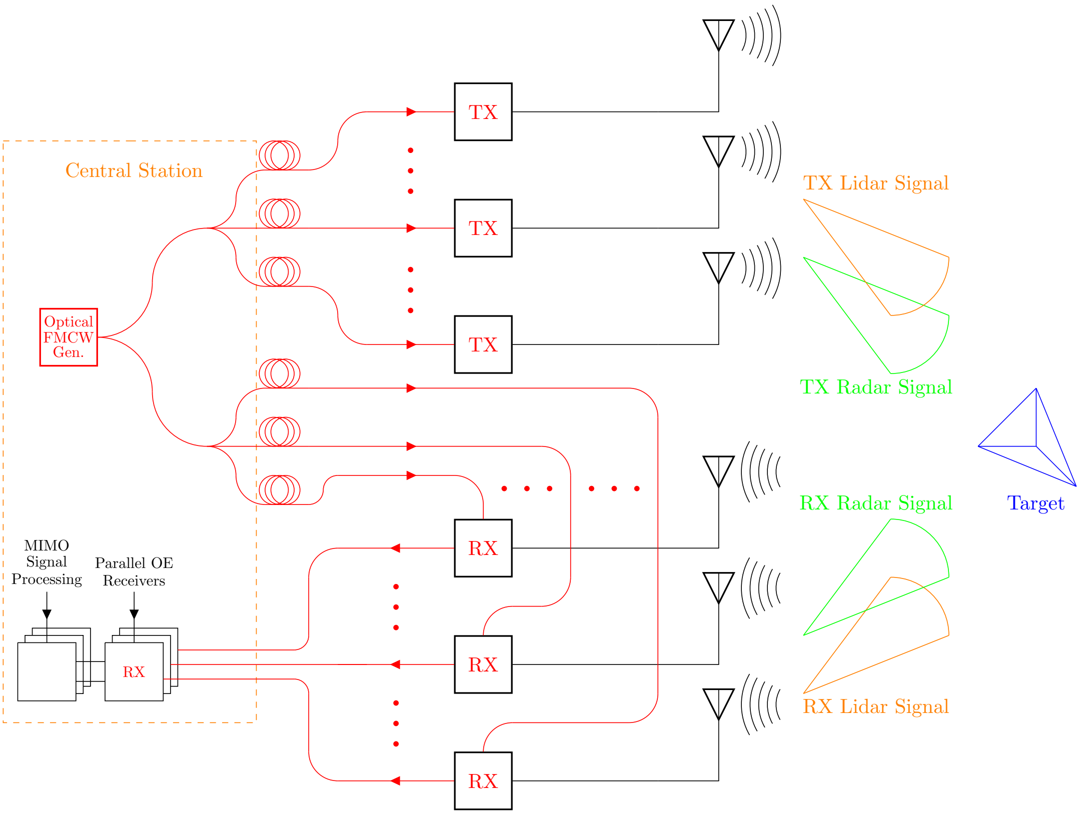

Figure 10.1: Simplified block diagram of the lidar-radar combined sensor system with optical return path.

The simplified block diagram of the lidar-radar combined sensor system is shown in figure 10.1. The overall block diagram is similar to the multiband radar system. Within a central station, an optical FMCW chirp is generated using an MZM biased at its minimum transmission point. The optical LO signal is distributed via optical fibers to the TX and RX frontends. Instead of several radar bands, as in the multiband radar, the TX frontend generates a radar and a lidar chirp.

Since an MZM delivers low optical power at this bias point, an alternative approach using two lasers detuned relative to each other can also be employed. In this case, the desired microwave signal is generated by beating the two laser signals in a photodiode [138].

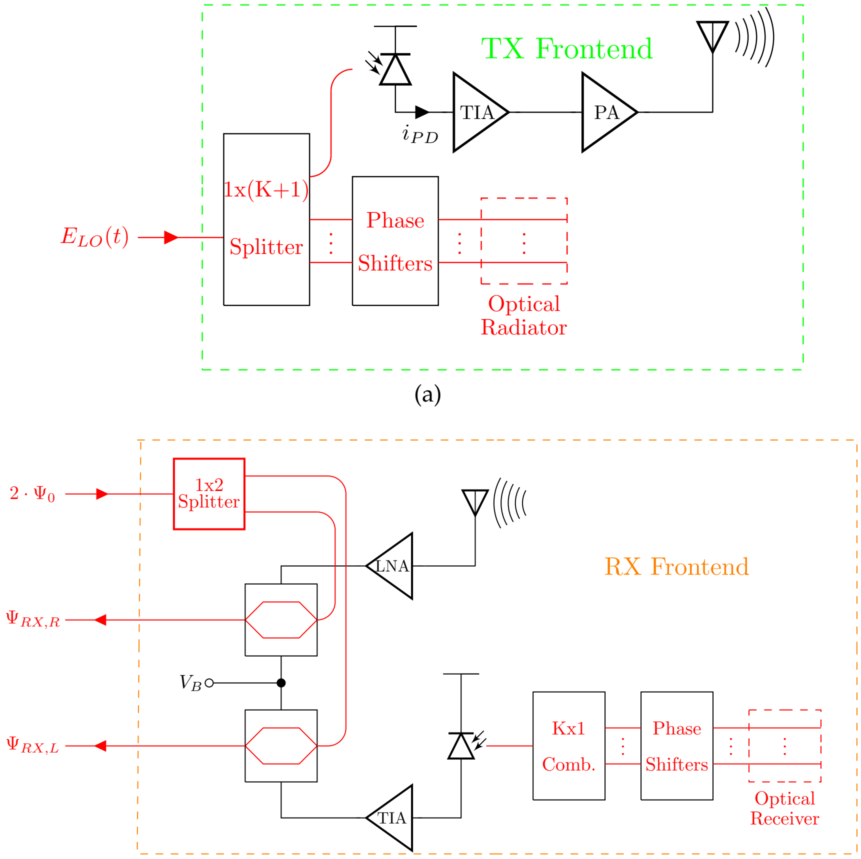

(a)

(b)

FIGURE 10.2: Simplified block diagram of the (a) TX frontend; (b) RX frontend of the lidar-radar combined sensor system.

Within the TX frontend, shown in figure 10.2a, the optical signal is split into a lidar path and a radar path. In the lidar path, the optical signal is transmitted by means of optical phase shifters and optical radiators, implementing an optical phased array (OPA) [139]. Alternatively, a MIMO approach with optical antennas can be realized. In the radar path, the optical LO signal is converted to an electrical signal by means of a PD and a TIA. The electrical signal is amplified using a PA, and transmitted via a transmit antenna.

Within the RX frontend, shown in figure 10.2b, the optical LO signal is split into an optical radar receive path and an optical lidar receive path. In the radar path, the received signal, provided by a receive antenna, is amplified by means of an LNA and fed to an MZM. The MZM is biased by the bias voltage $V_B$ in such a way that the MZM acts as an EO downconversion mixer. In the lidar path, the optical sensing signal from a certain direction is received by optical antennas, and converted to an electrical signal by means of a PD and a TIA. This electrical signal is mixed with the optical LO signal by means of a second MZM, similar to the radar receive path.

The optical radar and lidar signals are fed to the central station via an optical receive path, where parallel OE conversion is performed, followed by MIMO signal processing.

## 10.2 Analysis

The starting point for the derivation of the lidar-radar combined sensor system, shown in figure 10.1 and figure10.2, is the electric field of the optical LO signal, given by:

$$E_{LO}(t) = E_0 \cdot \left[ e^{j(\omega_{opt} - \Xi(t))t} - e^{j(\omega_{opt} + \Xi(t))t} \right] \tag{10.1}$$

The optical signal is transmitted via fibers to the TX and RX frontends. Within the TX frontend, the optical signal is divided into a lidar path and a radar path. In the radar path, the electrical signal is converted to the photocurrent [24]:

$$i_{PD} = c \cdot \mathcal{R} \left\| E_0 \right\|^2 \cdot (1 - \cos(2\Xi(t)t)) \tag{10.2}$$

with the proportionality factor $c$, which accounts for fiber losses and the splitting ratio. The photocurrent is converted to a voltage in a reference impedance system by means of a TIA. The transmitted radar signal is given by:

$$P_{TX}(t) = P_{0,TX} \cos^2(2\Xi(t)t) \tag{10.3}$$

with the amplitude of the transmit signal $P_{0,TX}$. If:

$$\Xi(t) = \frac{1}{2} \left( \omega_{LO} + \frac{\mu t}{2} \right) \tag{10.4}$$

Eq. 10.3 simplifies to:

$$P_{TX}(t) = P_{0,TX} \cos^2 \left( \left( \omega_{LO} + \frac{\mu t}{2} \right) t \right) \tag{10.5}$$

which is the normal FMCW radar signal.

The radar signal is reflected at an obstacle and then coupled into the RX frontend. The resulting driving voltage of the MZM is:

$$V_{MZM,R} = V_{0,R} \cos \left( \left( \omega_{LO} + \frac{\mu [t - \tau]}{2} \right) [t - \tau] \right) \tag{10.6}$$

with the amplitude of the driving voltage of the MZM in the radar path $V_{0,R}$. The amplitude of the driving voltage $V_{0,R}$ depends on the free space path loss, the transmit power, the receiver gain, and the radar cross section of the obstacle.

The output intensity of the MZM, biased at the quadrature point, of the optical radar receive path is given by:

$$\Psi_{RX,R} = \Psi_0 \left( 1 - \cos \left( \left[ \omega_{LO} + \frac{\mu t}{2} \right] t \right) \right) \cdot \left\{ 1 + \sin \left( \frac{\pi V_0}{V_\pi} \cos \left( \left( \omega_{LO} + \frac{\mu [t - \tau]}{2} \right) [t - \tau] \right) \right) \right\} \tag{10.7}$$

With the amplitude of the optical $\Psi_0$.

For a small amplitude of the driving voltage $V_0$, $\sin(x) \approx x$. This results in:

$$\Psi_{RX,R} \approxeq \Psi_0 \left(1 - \cos\left(\left[\omega_{LO} + \frac{\mu t}{2}\right] t\right)\right) \cdot \left\{1 + \frac{\pi V_0}{V_\pi} \cos\left(\left(\omega_{LO} + \frac{\mu\left[t-\tau\right]}{2}\right)\left[t-\tau\right]\right)\right\} \tag{10.8}$$

$$\begin{aligned}\approxeq \Psi_0 \Bigg\{ & 1 + \frac{\pi V_0}{V_\pi} \cos\left(\left(\omega_{LO} + \frac{\mu\left[t-\tau\right]}{2}\right)\left[t-\tau\right]\right) - \cos\left(\left[\omega_{LO} + \frac{\mu t}{2}\right] t\right) \\ & - \frac{\pi V_0}{2V_\pi}\left[\cos\left(\mu t\tau + \omega_{LO}\tau - \frac{\mu\tau^2}{2}\right) + \cos\left(2\omega_{LO}t + \mu t^2 - \mu t\tau - \omega_{LO}\tau + \frac{\mu\tau^2}{2}\right)\right]\Bigg\}\end{aligned} \tag{10.9}$$

If the PD and the subsequent TIA within the central station suppress the higher frequency components, the output voltage of the TIA is given by:

$$V_{TIA,R} = V_{0,T,R}\left\{1 - \frac{\pi V_0}{2V_\pi}\cos\left(\mu t\tau + \omega_{LO}\tau - \frac{\mu\tau^2}{2}\right)\right\} \tag{10.10}$$

with the amplitude of the output voltage of the TIA in the radar path $V_{0,T,R}$. The amplitude depends on the optical intensity, the responsivity of the PD, and the TIA gain. The MZM can act in conjunction with the PD in the central station as a downconversion mixer.

In the lidar part of the TX frontend, the optical LO signal is transmitted via an optical phased array. The lidar signal is reflected at an obstacle and received by an optical phased array receiver. The received electric field is given by:

$$E_{RX}(t,\tau) = G_{PL}E_0\left[e^{j(\omega_{opt} - \Xi(t-\tau))(t-\tau)} - e^{j(\omega_{opt} + \Xi(t-\tau))(t-\tau)}\right] \tag{10.11}$$

with the free-space path loss multiplied by the antenna gains. The output driving voltage of the MZM after the PD and TIA results in:

$$V_{MZM,L} = V_{0,L}\cos\left(\left(\omega_{LO} + \frac{\mu\left[t-\tau\right]}{2}\right)\left[t-\tau\right]\right) \tag{10.12}$$

with the amplitude of the driving voltage of the MZM in the lidar path $V_{0,L}$. The driving voltage in eq. 10.12 is same driving voltage as in the radar case except for proportionality factors. Following the same derivation for the optical receive path like in the radar branch, the low-frequency output voltage of the TIA in the central station is given by:

$$V_{TIA,L} = V_{0,T,L}\left\{1 - \frac{\pi V_0}{2V_\pi}\cos\left(\mu t\tau + \omega_{LO}\tau - \frac{\mu\tau^2}{2}\right)\right\} \tag{10.13}$$

with the amplitude of the output voltage of the TIA in the lidar path $V_{0,T,L}$. The amplitude depends on the optical intensity, the responsivity of the PD, and the TIA gain. This is exactly the same received signal as in the radar case except for proportionality factors. This means that the IF signal of the radar and the lidar are coherent and exhibit same Doppler frequency.

### 10.2.1 Doppler Analysis of a Lidar-Photonic Radar Combined Sensor System

A common disadvantage of lidar-radar combined sensor systems is the unequal single-carrier Doppler shift of the two measurement principles. The Doppler frequency of a single-carrier system is given by [140]:

$$|f_D| \leq \frac{2\nu_r f_0}{c_0} \tag{10.14}$$

with the relative speed difference $\nu_r$, and the carrier frequency of the lidar $f_0$. Since radar systems operate in the GHz regime and lidar systems in the THz domain, the Doppler frequency of a single-carrier lidar system is at least three orders of magnitude higher compared to a radar system. Since the Doppler frequency is several orders of magnitude greater in the lidar case than in the radar case, this leads to different range Doppler ambiguities. In the multi-target case, the signals with the different ambiguity functions must be superimposed in the sensor fusion in a complex manner.

As previously mentioned, the optical FMCW generator in the central station generates two optical lines, and beating in PDs is performed either in the lidar RX or in the radar TX frontend. The following derivations address the Doppler frequency of a two-carrier lidar system with beating in the PD.

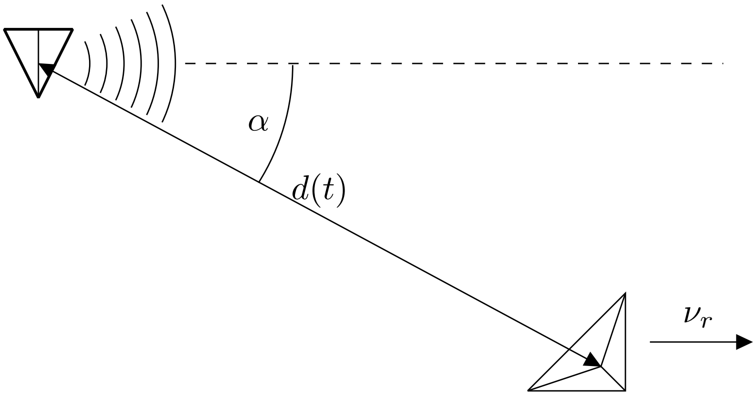

Figure 10.3: Scenario for the derivation of the Doppler shift of the radar and lidar signal.

The starting point of the derivation of the lidar Doppler shift is the received E-field signal, given by eq. 10.11. For this derivation, the free-space scenario shown in figure 10.3 is assumed. An obstacle with a relative speed $\nu_r$ departs over time under the angle $\alpha$ from the TX. The distance from the antenna to the obstacle is given by:

$$d(t) = d_0 + \nu_r t \cos(\alpha) \tag{10.15}$$

with an arbitrary starting distance $d_0$. From basic radar or lidar theory, it is well known that the reflected signal is received after:

$$\tau(t) = \frac{2d_0}{c_0} + \frac{2\nu_r t}{c_0}\cos(\alpha) = \tau_0 + \tau_\nu t \tag{10.16}$$

Inserting eq. 10.16 into eq. 10.11 leads to:

$$E_{RX}(t,\tau) = G_{PL}E_0\left[e^{j(\omega_{opt}-\Xi(t-\tau_0-\tau_\nu t))[t-\tau_0-\tau_\nu t]} - e^{j(\omega_{opt}+\Xi(t-\tau_0-\tau_\nu t))[t-\tau]}\right] \tag{10.17}$$

Factoring out $e^{j\omega_{opt}[(1-\tau_\nu)t-\tau_0]}$ results in:

$$E_{RX}(t,\tau) = -2jG_{PL}E_0e^{j\omega_{opt}[(1-\tau_\nu)t-\tau_0]}\sin\left(\Xi\left\{[1-\tau_\nu]t-\tau_0\right\}\left([1-\tau_\nu]t-\tau_0\right)\right) \tag{10.18}$$

The photocurrent of the PD in the lidar receiver is given by:

$$i_{PD,L} = \mathcal{R}\left|E_{RX}(t,\tau)\right|^2 = i_{PD,L,0}\left[1-\cos\left(2\Xi\left\{[1-\tau_\nu]t-\tau_0\right\}\left([1-\tau_\nu]t-\tau_0\right)\right)\right] \tag{10.19}$$

with the amplitude of the photocurrent of the PD in the LiDAR RX $i_{PD,L,0}$. The amplitude of the photocurrent depends on the free-space path loss, the antenna gain, and the amplitude of the E-field.

The output voltage of the TIA, with DC compensation, results in:

$$V_{MZM,L} = V_{0,L}\cos\left(2\Xi\left\{[1-\tau_\nu]t-\tau_0\right\}\left([1-\tau_\nu]t-\tau_0\right)\right) \tag{10.20}$$

By inserting eq. 10.16 into eq. 10.6, and making use of eq. 10.4, the drive voltage of the MZM of the radar branch results in:

$$V_{MZM,R} = V_{0,R}\cos\left(2\Xi\left\{[1-\tau_\nu]t-\tau_0\right\}\left([1-\tau_\nu]t-\tau_0\right)\right) \tag{10.21}$$

Comparing eq. 10.20 with eq. 10.21 shows that the MZM driving voltage of the lidar branch is exactly the same as the driving voltage of the radar branch except for the amplitudes for $V_{0,L}$ and $V_{0,R}$. The Doppler shift for the radar and lidar sensor is then given by:

$$f_d = \frac{4\nu_r f_E}{c_0}\cos(\alpha) \tag{10.22}$$

with $f_E$ being one half of the radar carrier frequency.

This difference between the single-carrier Doppler shift from eq. 10.14 and the Doppler shift of at least two carrier signals is visualized in figure 10.4. In the single-carrier lidar system, the absolute frequency shift is then given as [140]:

$$f_{d,single\ carrier} = \frac{2\nu_r f_0}{c_0}\cos(\alpha) \tag{10.23}$$

In the case of beating of the transmitted single-carrier signal with the received signal carrier, the absolute frequency shift would be observed.

Similarly to the single-carrier system, each carrier of the two-carrier lidar system has an absolute frequency shift of

$$f_{d,1} = \frac{2\nu_r f_1}{c_0}\cos(\alpha) \tag{10.24}$$

$$f_{d,2} = \frac{2\nu_r f_2}{c_0}\cos(\alpha) \tag{10.25}$$

with $f_1 = f_0 - f_E/2$, and $f_2 = f_0 + f_E/2$.

Since beating is performed with respect to the two carriers, only the relative frequency shift is important. The relative frequency shift is given by

$$f_d = \frac{2\nu_r\left(f_2-f_1\right)}{c_0}\cos(\alpha) = \frac{2\nu_r f_E}{c_0}\cos(\alpha) \tag{10.26}$$

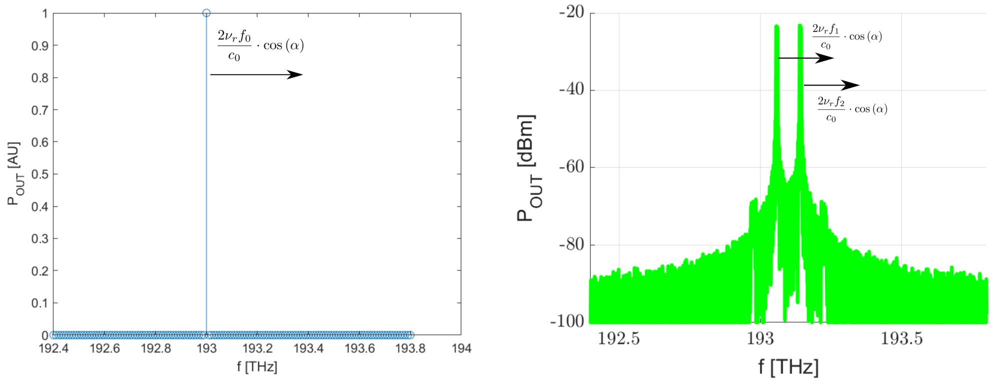

(a) (b)

FIGURE 10.4: Visualization of the Doppler shift for a (a) single carrier; (b) two carrier wireless system.

Due to the $|.|^2$ characteristic of the PD, the Doppler shift is doubled. For the radar sensor, the RF frequency is twice the difference of the two optical carrier signals.

## 10.3 System Simulation

The simulation setup of the lidar radar combined sensor system is presented in appendix H.

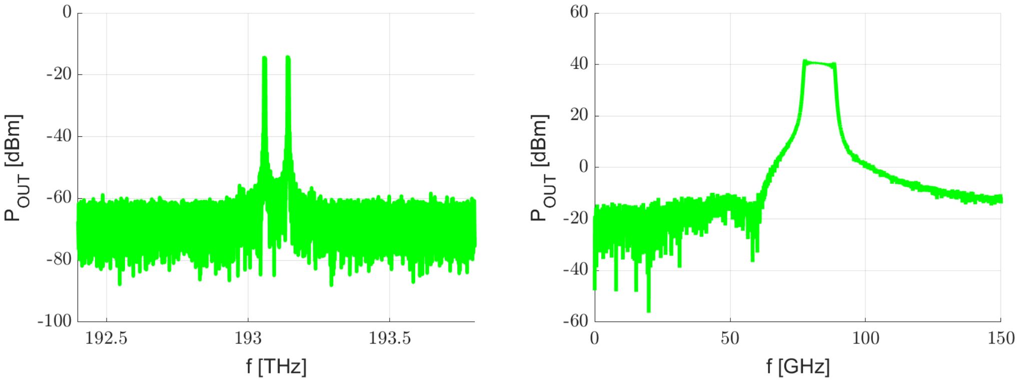

(a) (b)

FIGURE 10.5: Simulated spectrum of the (a) lidar; (b) radar transmit signal.

The simulated lidar and radar FMCW transmit chirps in the frequency domain are shown in figure 10.5. In the lidar spectrum, shown in figure 10.5a, the FMCW chirp is not visible. This is because the chirp bandwidth is much smaller than the carrier frequency. In contrast, in the radar spectrum, shown in figure 10.5b, the FMCW chirp is clearly visible.

The simulated IF signal after the OE conversion in the central station of the lidar-radar combined sensor system for a round trip delay of 5 ns and 10 ns is shown in figure 10.6. The target can be clearly observed in both the lidar band and the radar band.

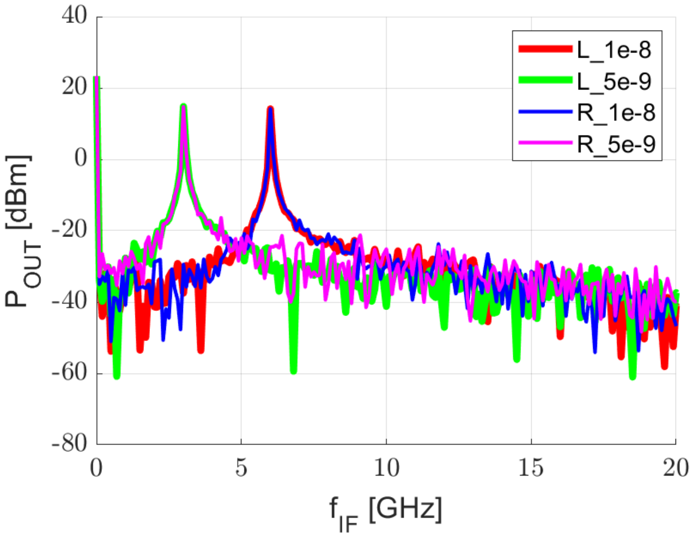

FIGURE 10.6: Simulated IF spectrum of the lidar and radar sensor for a round trip delay (RTD) of 10 ns and 5 ns. [Lidar RTD=10 ns (L_1e-8): red; lidar RTD=5 ns (L_5e-9): green; radar RTD=10 ns (R_1e-8): blue; radar RTD=5 ns (R_5e-9): purple]

Such a system, which generates the same IF signal for both the lidar and the radar corresponding to the same round-trip time, offers advantages in signal processing in addition to redundancy benefits. In state-of-the-art approaches, data from radar and lidar sensors are first preprocessed separately before sensor fusion is applied [141]. However, valuable information may be lost during the preprocessing stage. Using the same IF frequency for both lidar and radar with identical round-trip delays and Doppler frequencies enables sensor fusion without the need for extensive preprocessing.

## 10.4 Conclusion

In this chapter, a combined lidar-radar sensor system was presented. The system repurposes the optical LO signal to construct a lidar subsystem. A mathematical analysis was conducted, demonstrating the identity of the IF signals from the radar and lidar even under Doppler shift conditions. This coherence is ensured by the specific characteristics of the optical LO signal.

In a single-carrier lidar system, the Doppler shift depends on the absolute optical frequency. In contrast, in a dual-carrier lidar system, the Doppler shift depends solely on the relative frequency shift between the carriers—similar to the behavior observed in radar systems.

The simulation validated the proposed theory and highlighted the potential of such a system to reduce the complexity of sensor fusion.

It should be noted that all components can be integrated using low-cost, mass-market silicon technology.

The system, its analysis, and the simulation in Lumerical Interconnect by Ansys were previously published by the author in [55, 59, 72].

# Chapter 11

# Conclusion and Future Work

Within this thesis, for the first time a mm-wave photonic FMCW MIMO radar system with optical LO distribution was presented, mathematically modeled, including phase noise, and simulated in an optical and electrical design environment. In addition, the photonic radar system was modeled in an electronic design environment, and a behavioral model of a photonic radar TRX chipset in silicon photonics technology was introduced.

Furthermore, novel circuit architectures, namely a NB optical RX and a NB four-quadrant electro-optical mixer, were analyzed and demonstrated. Such circuit architectures can be useful as the first stage of the TRX frontends for a photonic FMCW MIMO radar with optical LO distribution.

In addition, within this thesis, the world's first photonic radar TRX chipset in IHP's pre-production silicon photonics technology [32, 33] was presented. Unfortunately, the maximum output power shifted to 67 GHz, which was caused by a decrease in the germanium PD BW, thereby reducing the overall TIA BW by 2.5 GHz. This led to a reduction of 10 GHz at the output of the frequency quadrupler. Nevertheless, a large coherent MIMO radar system demonstrator was presented by collaboration partners using our chips, achieving an angular resolution of 0.4°, which is close to the theoretical limit of 0.3° for the presented demonstrator.

Finally, additional photonic radar architectures and a novel lidar-radar combined sensor system were presented, mathematically modeled, and simulated within an optical design environment. The photonic software-defined radar with optical LO distribution enables the transmission of arbitrary waveforms in a large-aperture phased array MIMO system. The multiband architecture simultaneously generates three harmonics of adjustable signal strength from a single optical LO source. The unique architecture of the lidar-radar combined sensor system produces a coherent IF signal between the radar and lidar channels, which is preferable for signal processing. It should be noted that all systems are compatible with low-cost, high-volume silicon photonics technology and are well-suited for operation under harsh environmental conditions, such as those encountered in automotive applications.

The next step is to redesign the TRX chipset using the proposed NB optical RX. This thesis has demonstrated that the proposed NB optical RX offers excellent robustness against variations in PD parameters. Alternatively, the chipset could be redesigned with the novel NB four-quadrant electro-optical mixer, functioning as a frequency doubler. A future research question could be: which architecture is preferable with respect to additive phase noise—the proposed NB optical RX followed by a frequency doubler, or the novel NB four-quadrant electro-optical mixer acting directly as a frequency doubler?

Furthermore, to address mass-market applications such as the automotive sector, the TRX chipset must be completely redesigned using a scalable photonic CMOS technology, such as the 45 nm silicon photonic CMOS SOI platform from GlobalFoundries. Potential research questions for this integration include:

- What is the achievable output power at 77 GHz in a 45 nm photonic CMOS SOI technology?
- How can the temperature dependency of the transmitter and receiver chips be minimized?
- What is the minimum achievable noise figure at 77 GHz in a 45 nm photonic CMOS SOI technology?
- What is the minimum additive phase noise of a 77 GHz photonic radar chipset in this technology?

In addition, the other photonic radar architectures presented in this work—based on the photonic FMCW MIMO radar system with optical LO distribution—need to be implemented. In the following sections, future research questions are posed for the various photonic radar systems.

Possible research questions for the photonic software-defined MIMO radar systems with optical signal distribution include:

- What does the link budget look like, and how does it scale with the number of TRX frontends?
- Is a homodyne or heterodyne TRX architecture preferable?
- How can power consumption be reduced to enable low-power, large-aperture MIMO radar systems?
- Is a single TRX chip solution feasible, or is a two-chip approach with separate TX and RX chips more advantageous?

Possible research questions for the photonic FMCW multiband radar systems with optical LO distribution include:

- How can the architecture be adapted to meet regulatory requirements?
- What impact does nonlinear EO and OE conversion—used to generate the three harmonics—have on the system's phase noise?
- Is a system with three harmonics of equal amplitude beneficial, or is an approach with unequal amplitudes preferable?
- How does the multiband approach affect the sparsity of the overall system?

Possible research questions for the lidar-radar combined sensor system include:

- Is the output power of a MZM at its minimum point sufficient for both radar and lidar, or is a dual-laser beating approach preferable?
- Is an optical phased array preferable for lidar, or should conventional lens-based systems be used?
- What impact do mechanical vibrations have on the system's coherence?
- How much processing gain can be achieved with a combined sensor system

# Appendix A

# Higher Order Analysis of the Photonic FMCW Radar System with Optical LO Distribution

In chapter 2.2, the eq. 2.11 was simplified by considering only the DC component and the first-order Bessel function. This appendix provides a more comprehensive analysis of the photonic FMCW radar system with optical LO distribution, incorporating higher-order harmonics into the model. This extended approach also explains the ghost targets observed during simulations conducted with ADS Ptolemy (see chapter 3.2).

As the first OE conversion takes place in the TX front end, the modeling of the central station's transmitter section is not repeated here. A detailed description and analysis of the transmitter architecture can be found in chapter 2.2.3.

## A.1 TX Frontend

Within the TX frontend, shown in figure 2.2a, the optical LO signal is converted to an electrical one. By inserting $\Psi_{FMCW,TRX}(t)$ from eq. 2.14 into $\Psi_0(t)$ from eq. 2.4, and redo the analysis until eq. 2.11, the output voltage of the TIA results, neglecting the DC component, to:

$$\begin{aligned} V_{TIA}(j\omega) = 2 \cdot \frac{G(j\omega) Z_F(j\omega) \mathcal{R} \Psi_0}{G(j\omega) + j Z_F(j\omega) C_D \omega + 1} \\ \cdot \mathcal{F}\left\{ \sum_{n=1}^{\infty} (-1)^n J_{2n-1}\left(\frac{\pi V_{FMCW,0}}{V_\pi}\right) \cos\left[(2n-1)\left(\omega_{LO} + \frac{\mu t}{2} t\right) t\right]\right\}(j\omega). \end{aligned} \tag{A.1}$$

Within the mm-wave part of the TX frontend, the electrical signal is upconverted to the mm-wave band by means of a multiplication factor $k$. The mm-wave output signal of the frequency multipliers is filtered and amplified. The transmit signal is given by:

$$\begin{aligned} P_{TX}(j\omega) = 2 \cdot G_{TX}(j\omega) \cdot \frac{G(j\omega) Z_F \mathcal{R} \Psi_0}{G(j\omega) + j Z_F C_D \omega + 1} \\ \cdot \mathcal{F}\left\{ \sum_{n=1}^{\infty} (-1)^n J_{2n-1}\left(\frac{\pi V_{FMCW,0}}{V_\pi}\right) \cos\left[k \cdot (2n-1)\left(\omega_{LO} + \frac{\mu t}{2} t\right) t\right]\right\}(j\omega). \end{aligned} \tag{A.2}$$

with the gain of the TX antenna $G_{TX}(j\omega)$, the gain of the frequency multipliers and the PA $G_{PA}(j\omega)$, and the transfer function of the BPF $G_{BPF}(j\omega)$.

## A.2 RX Frontend

Within the RX frontend, shown in fig. 2.2b, the received signal, provided by a receive antenna, is filtered and amplified by an LNA before downconversion is performed. In mathematical words, this is a multiplication of the transmitted signal, given in eq. A.2, with a time delayed version of the transmitted signal, given in eq. A.2.

$$\begin{aligned} V_{IF}(j\omega) = 2 \cdot G_{TX}(j\omega) \cdot G_{RX}(j\omega) \cdot G_C(j\omega) \cdot \frac{G(j\omega) \cdot Z_F(j\omega) \cdot \mathcal{R}(\lambda)\Psi_0}{G(j\omega) + j\omega C_D Z_F(j\omega) + 1} \\ \cdot \mathcal{F}\left\{ \left[ \sum_{n=1}^{\infty} (-1)^n J_{2n-1}\left(\frac{\pi V_{FMCW,0}}{V_\pi}\right) \cos\left[k \cdot (2n-1)\left(\omega_{LO} + \frac{\mu t}{2}\right) t\right]\right] \right. \\ \left. \cdot \left[ \sum_{m=1}^{\infty} (-1)^m J_{2m-1}\left(\frac{\pi V_{FMCW,0}}{V_\pi}\right) \cos\left[k \cdot (2m-1)\left(\omega_{LO} + \frac{\mu (t-\tau)}{2}\right)(t-\tau)\right]\right] \right\} (j\omega) \end{aligned} \tag{A.3}$$

with the overall gain of the RX frontend $G_{RX}(j\omega)$, and the round trip delay $\tau$.

By making use of the Cauchy product formula [81]

$$\left(\sum_{n=0}^{\infty} a_n\right) \cdot \left(\sum_{m=0}^{\infty} b_m\right) = \sum_{n=0}^{\infty}\sum_{p=0}^{\infty} a_p b_{n-p}, \tag{A.4}$$

the mathematical transformation $\sum_{\nu=0}^{\infty} x_\nu = x_0 + \sum_{\nu=1}^{\infty} x_\nu$

$$\left(\sum_{n=1}^{\infty} a_n\right) \cdot \left(\sum_{m=1}^{\infty} b_m\right) = \left(-a_0 + \sum_{n=0}^{\infty} a_n\right) \cdot \left(-b_0 + \sum_{m=0}^{\infty} b_m\right) \tag{A.5}$$

$$= a_0 \cdot b_0 - a_0 \cdot \sum_{m=0}^{\infty} b_m - b_0 \cdot \sum_{n=0}^{\infty} a_n + \left(\sum_{n=0}^{\infty} a_n\right) \cdot \left(\sum_{m=0}^{\infty} b_m\right) \tag{A.6}$$

$$\left(\sum_{n=1}^{\infty} a_n\right) \cdot \left(\sum_{m=1}^{\infty} b_m\right) = a_0 \cdot b_0 - a_0 \cdot \sum_{m=0}^{\infty} b_m - b_0 \cdot \sum_{n=0}^{\infty} a_n + \sum_{n=0}^{\infty}\sum_{p=0}^{\infty} a_p b_{n-p}, \tag{A.7}$$

$$J_{-1}(x) = -J_1(x), \tag{A.8}$$

and

$$(-1)^p \cdot (-1)^{n-p} = (-1)^n, \tag{A.9}$$

the electrical IF signal is given by:

$$V_{IF}(j\omega) = 2 \cdot G_{TX}(j\omega) \cdot G_{RX}(j\omega) \cdot G_C(j\omega) \cdot \frac{G(j\omega) \cdot Z_F(j\omega) \cdot \mathcal{R}(\lambda)\Psi_0}{G(j\omega) + j\omega C_D Z_F(j\omega) + 1} \cdot \mathcal{F}\left\{a_0 b_0 + a_0 \cdot \sum_{m=0}^{\infty} b_m + b_0 \cdot \sum_{n=0}^{\infty} a_n + \sum_{n=0}^{\infty} (-1)^n \sum_{p=0}^{\infty} a_p \cdot b_{n-p}\right\}(j\omega). \tag{A.10}$$

with

$$a_0 = J_1\left(\frac{\pi V_{FMCW,0}}{V_\pi}\right) \cos\left(k \cdot \left[\omega_{LO} + \frac{\mu t}{2}\right] t\right), \tag{A.11}$$

$$b_0 = J_1\left(\frac{\pi V_{FMCW,0}}{V_\pi}\right) \cos\left(k \cdot \left[\omega_{LO} + \frac{\mu (t-\tau)}{2}\right] (t-\tau)\right), \tag{A.12}$$

$$a_n = (-1)^n J_{2n-1}\left(\frac{\pi V_{FMCW,0}}{V_\pi}\right) \cdot \cos\left[k \cdot (2n-1)\left(\omega_{LO} + \frac{\mu t}{2}\right) t\right], \tag{A.13}$$

$$b_m = (-1)^m J_{2m-1}\left(\frac{\pi V_{FMCW,0}}{V_\pi}\right) \cdot \cos\left[k \cdot (2m-1)\left(\omega_{LO} + \frac{\mu (t-\tau)}{2}\right)(t-\tau)\right], \tag{A.14}$$

and

$$\begin{aligned} a_p \cdot b_{n-p} = {} & \frac{1}{2} J_{2p-1}\left(\frac{\pi V_{FMCW,0}}{V_\pi}\right) \cdot J_{2(n-p)-1}\left(\frac{\pi V_{FMCW,0}}{V_\pi}\right) \\ & \cdot \left\{\cos\left\{k \cdot (2p-1)\left(\omega_{LO} + \frac{\mu t}{2}\right) t + k \cdot [2(n-p)-1]\left[\mu t + \frac{\mu\tau}{2} - \omega_{LO}\right]\tau\right\}\right. \\ & \left. + \cos\left\{k \cdot (2p-1)\left(\omega_{LO} + \frac{\mu t}{2}\right) t + k \cdot [2(n-p)-1]\left[\mu t - \frac{\mu\tau}{2} + \omega_{LO}\right]\tau\right\}\right\}. \end{aligned} \tag{A.15}$$

In eq. A.10, the noise of the wireless channel is neglected. In order to realize an optical receive path, the electrical IF signal is converted into an optical signal by means of an EO conversion unit.

## A.3 Receive Part of the Central Station

Within the receive part of the central station, the optical IF signal is converted to an electrical signal by an OE conversion unit. The optical IF signal $\Psi_{IF}$ results from inserting eq. A.10 into eq. 2.3. Inserting $\Psi_{IF}$ into $\Psi_0(t)$ from eq. 2.4, and redo the analysis until eq. 2.11, the output voltage of the TIA in the central station results to:

$$V_{TIA,RX,ECU} = 2 \cdot \frac{G_{ECU}(j\omega) Z_{F,ECU}(j\omega) \mathcal{R}_{ECU} \Psi_{0,OR}}{G_{ECU}(j\omega) + j\omega C_{D,ECU} Z_{F,ECU}(j\omega) + 1} \cdot \left[-\pi\delta(\omega) + \mathcal{F}\left\{\sin\left(\frac{\pi V_{IF}(t)}{V_\pi}\right)\right\}(j\omega)\right]. \tag{A.16}$$

with the voltage gain of the core amplifier of the shunt feedback TIA of the central station $G_{ECU}(j\omega)$, the feedback impedance of the TIA of the central station $Z_{F,ECU}(j\omega)$, the responsivity of the PD of the central station $\mathcal{R}_{ECU}$, the optical amplitude of the optical receive path $\Psi_{0,OR}$, and the capacitance of the PD of the central station $C_{D,ECU}$.

## Appendix B

# Derivation of the OE Power Gain of a TIA

In chapter 4.1.1, it was claimed that the OE power gain of any TIA is negative in dB up to a certain input power. This section provides a mathematical proof of this claim and applies the proposed theory to the NB and BB TIA designs presented in chapter 4.1.1 and chapter 4.1.2.

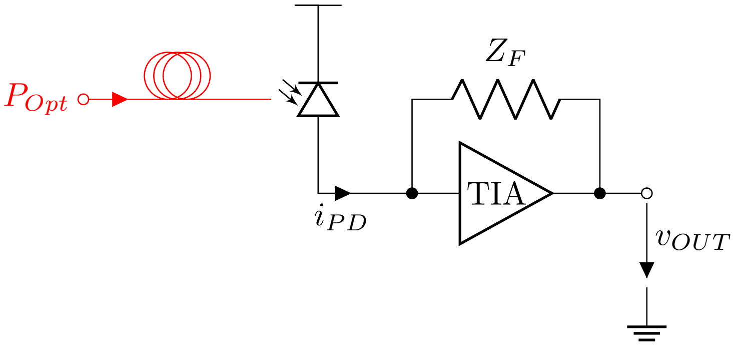

FIGURE B.1: Simplified block diagram of a TIA

The derivation is based on the simplified generic block diagram of a shunt feedback TIA shown in figure B.1. The output power of such a generic TIA is expressed as:

$$P_{EL} = Re\left\{v_{OUT} \cdot i_{OUT}^{*}\right\} \tag{B.1}$$

where $\Xi^*$ denotes the complex conjugate of $\Xi$. Substituting $i_{OUT} = \frac{v_{OUT}}{Z_0}$, with $Z_0$ being the output reference impedance of the TIA, the output power becomes:

$$P_{EL} = Re\left\{\frac{v_{OUT} \cdot v_{OUT}^{*}}{Z_0^{*}}\right\} \tag{B.2}$$

$$P_{EL} = Re\left\{\frac{|v_{OUT}|^2}{Z_0^{*}}\right\} \tag{B.3}$$

By substituting $v_{OUT} = i_{PD} \cdot Z_F$, the output power simplifies to:

$$P_{EL} = Re\left\{\frac{|i_{PD} \cdot Z_F|^2}{Z_0^{*}}\right\} \tag{B.4}$$

Assuming that the dark current of the PD is negligible, the photocurrent of the PD can be expressed as $i_{PD} = \mathcal{R} \cdot P_{OPT}$ [79]. With this simplification, the output power of the TIA becomes:

$$P_{EL} = Re\left\{\frac{|\mathcal{R}\cdot P_{OPT}\cdot Z_F|^2}{Z_0^*}\right\} \tag{B.5}$$

Since responsivity and optical power are real-valued, eq. B.5 reduces to:

$$P_{EL} = Re\left\{\frac{|Z_F|^2}{Z_0^*}\right\}\cdot\mathcal{R}^2\cdot P_{OPT}^2 \tag{B.6}$$

Eq. B.6 reveals a quadratic relationship with its root at $P_{OPT} = 0$.

Converting eq. B.6 into decibel form yields:

$$P_{EL,dBW} = 10\cdot\log_{10}\left(\frac{P_{EL}}{1\,\mathrm{W}}\right) \tag{B.7}$$

$$P_{EL,dBW} = 10\cdot\log_{10}\left(Re\left\{\frac{|Z_F|^2}{Z_0^*}\right\}\cdot\mathcal{R}^2\cdot\frac{P_{OPT}^2}{1\,\mathrm{W}}\right) \tag{B.8}$$

Applying the mathematical rules $\log_\Xi(a\cdot b) = \log_\Xi(a) + \log_\Xi(b)$ and $\log_\Xi(a^n) = n\log_\Xi(a)$ [81], eq. B.8 simplifies further:

$$P_{EL,dBW} = 10\cdot\log_{10}\left(Re\left\{\frac{|Z_F|^2}{Z_0^*}\right\}\right) + 20\cdot\log_{10}(\mathcal{R}) + 20\cdot\log_{10}\left(\frac{P_{OPT}}{1\,\mathrm{W}}\right) \tag{B.9}$$

Since $10\cdot\log_{10}\left(\frac{P_{OPT}}{1\,\mathrm{W}}\right) = P_{Opt,dBW}$, eq. B.9 transforms to:

$$P_{EL,dBW} = 10\cdot\log_{10}\left(Re\left\{\frac{|Z_F|^2}{Z_0^*}\right\}\right) + 20\cdot\log_{10}(\mathcal{R}) + 2\cdot P_{OPT,dBW} \tag{B.10}$$

The OE unity power gain in dB is given by:

$$P_{EL,dBW} = P_{OPT,dBW} = 10\cdot\log_{10}\left(Re\left\{\frac{Z_0^*}{|Z_F|^2}\right\}\right) - 20\cdot\log_{10}(\mathcal{R}) \tag{B.11}$$

and in linear scale

$$P_{EL} = P_{OPT} = \frac{1}{\mathcal{R}^2}\cdot Re\left\{\frac{Z_0^*}{|Z_F|^2}\right\} \tag{B.12}$$

For any $P_{OPT} < \frac{1}{\mathcal{R}^2}\cdot Re\left\{\frac{Z_0^*}{|Z_F|^2}\right\}$, the OE conversion gain in dB is negative. It should be emphasized that no assumptions regarding the TIA topology were made during the derivation.

# Appendix C

# An Ultra Low Phase Noise 77 GHz Frequency Synthesizer with Optical Output

This chapter presents a collaborative work by Meysam Bahmanian, Vijayalakshmi Surendranath Shroff, and Stephan Kruse. The opto-electronic phased locked loop (OEPLL) was developed by Meysam Bahmanian and Vijayalakshmi Surendranath Shroff, while the frequency multiplier architecture were contributed by Stephan Kruse.

Phase noise in FMCW radar has a significant impact on the resolution and overall performance of the system, as it appears as noise sidebands around the target and can obscure weak nearby reflections [88]. In chapter 2.3, the phase noise of a short-range photonic FMCW radar system with optical LO distribution was derived and is given by:

$$\mathcal{L}_{IF}(f_m) = 2 \cdot \mathcal{L}_{TX}(f_m) \cdot \left[1 - \cos\left(2\pi f_m \left\{\frac{2R}{c_0} - \frac{\Delta L}{c_f}\right\}\right)\right]. \tag{C.1}$$

The oscillator plays a crucial role in determining the overall phase noise of the system. Especially, in long-range radar or bistatic radar configurations, the phase noise of the transmitted signal and the phase noise of the received signal are only weakly correlated or completely uncorrelated, meaning they do not cancel out in the mixer [87].

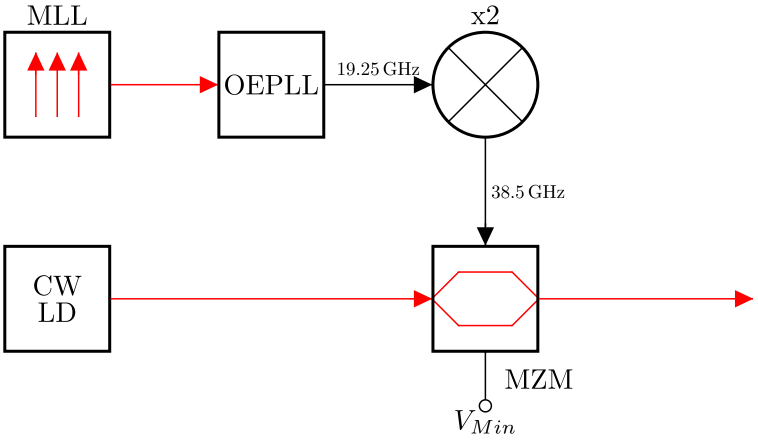

FIGURE C.1: Simplified block diagram of the ultra low phase noise 77 GHz frequency synthesizer with optical output.

The simplified block diagram of the ultra-low phase noise 77 GHz frequency synthesizer with optical output is shown in figure C.1. An OEPLL locks onto one harmonic of the mode locked laser (MLL) pulse train. The block diagram of the OEPLL is presented in figure C.2 [142].

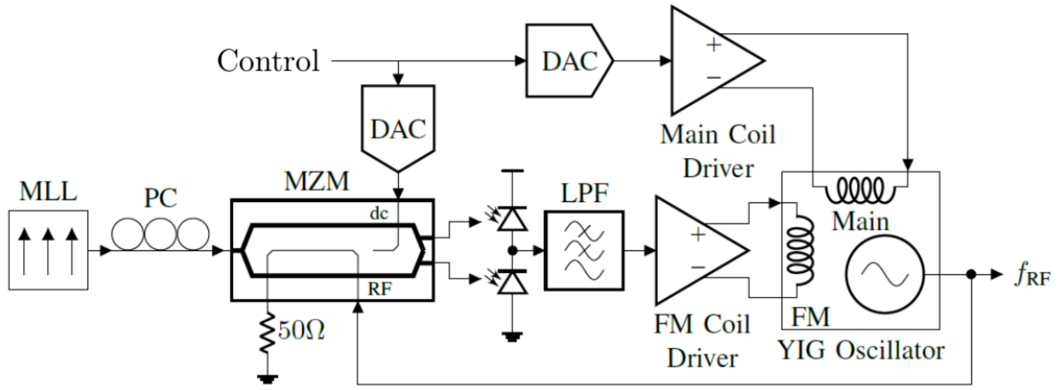

FIGURE C.2: Block diagram of the OEPLL [142].

An OE phase detector, implemented using a balanced MZM with complementary output and a balanced PD, provides an output signal proportional to the relative phase difference between the RF signal—generated by a Yttrium Iron Garnet (YIG) oscillator—and the desired harmonic of the MLL. The photocurrent, supplied by the PDs, is integrated by the loop filter and fed back into the oscillator. Additional details on the OEPLL and its principle of operation can be found in [142].

The OEPLL generates frequencies up to 20 GHz. The oscillator's output signal is fed into an electronic frequency doubler, whose output then drives a second MZM biased at its minimum point and fed by a CW laser. The MZM, biased at the minimum point, generates two components with a difference frequency equal to twice the input frequency. In a subsequent PD, beating is performed to obtain an electrical signal at 19.25 GHz. The output signal of the MZM can serve as the optical LO signal in photonic FMCW MIMO radar systems with optical LO distribution, as described in chapter 2.1. Since each TX and RX front end utilizes a photodiode in conjunction with a TIA to convert the optical LO signal into an electrical LO signal, beating occurs within the PD. Furthermore, a NB optical RX, such as the one presented in chapter 4.1, may offer advantages, as it eliminates the bandwidth-limiting PD capacitance through the use of a transmission line.

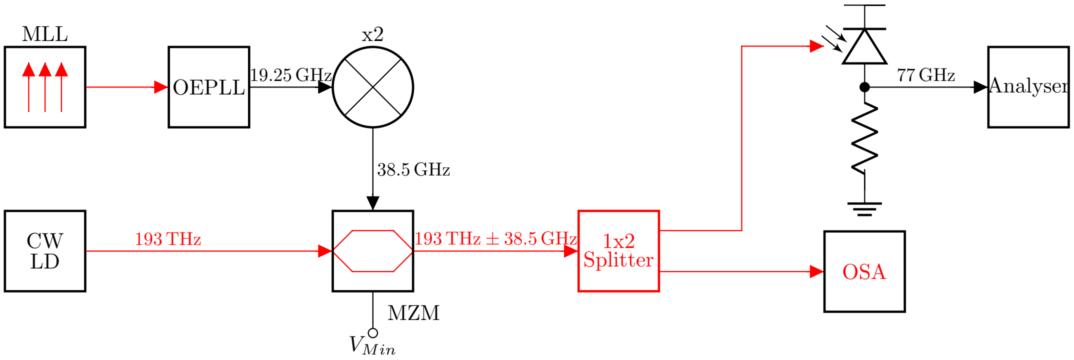

FIGURE C.3: Block diagram of the measurement setup of the 77 GHz frequency synthesizer.

The simplified measurement setup of the proposed ultra-low phase noise 77 GHz frequency synthesizer with optical output is shown in figure C.3. The optical output of the frequency synthesizer is split into two branches: one branch is used to observe the optical spectrum at the output of the MZM with an optical spectrum analyzer, while the other converts the optical signal into an electrical signal using a PD, enabling further analysis with a spectrum analyzer.

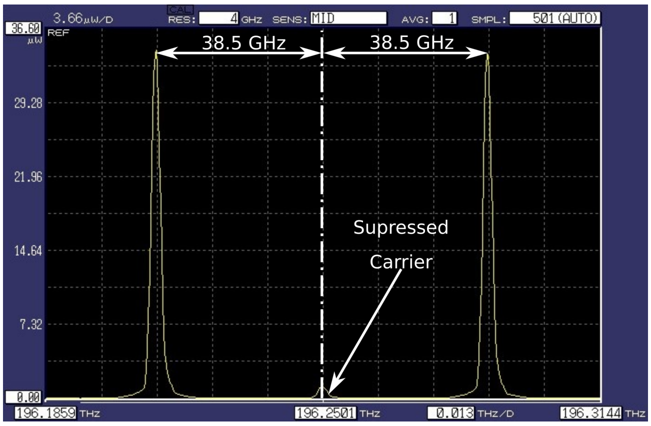

FIGURE C.4: Optical output spectrum of the frequency synthesizer with optical output.

Since the 77 GHz electrical signal is generated through optical beating in a photodiode, the suppression of the optical carrier at the second harmonic of the OEPLL output is a critical parameter. Figure C.4 shows the output spectrum of the MZM, which is biased at its minimum transmission point. The optical spectrum analyzer used has a resolution bandwidth of 4 GHz. The optical carrier at 196.25 THz is suppressed by approximately two orders of magnitude relative to the desired sidebands at 196.2115 THz and 196.2885 THz.

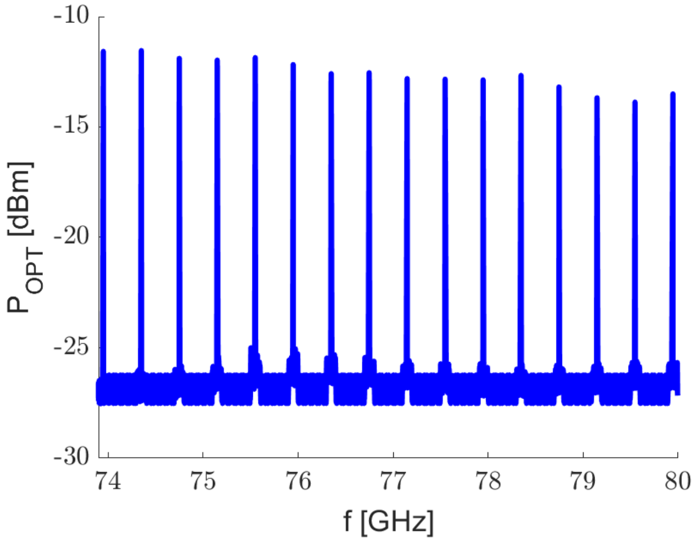

FIGURE C.5: Superimposed optical beat spectrum from multiple single-frequency measurements of the frequency synthesizer with optical output.

The combined optical output spectrum, corresponding to the beat frequency of the ultra-low phase noise frequency synthesizer with optical output, is presented in

Figure C.5. To obtain this spectrum, results from separate single-frequency measurements were superimposed. The optical signal was converted into an electrical signal using a photodiode and subsequently analyzed with a spectrum analyzer. Using the relationship, derived in appendix B

$$P_{EL} = Re\left\{\frac{|\mathcal{R}\cdot P_{OPT}\cdot Z_F|^2}{Z_0}\right\}, \tag{C.2}$$

the optical spectrum was calculated from the electrical spectrum. As mentioned previously, the OEPLL locks onto harmonics of the MLL, which has a repetition rate of 100 MHz. This leads to a channel spacing of 100 MHz for the OEPLL and 400 MHz after optical signal beating in a PD. The amplitude variations across the entire frequency band from 74 GHz to 80 GHz remain below 2.5 dB.

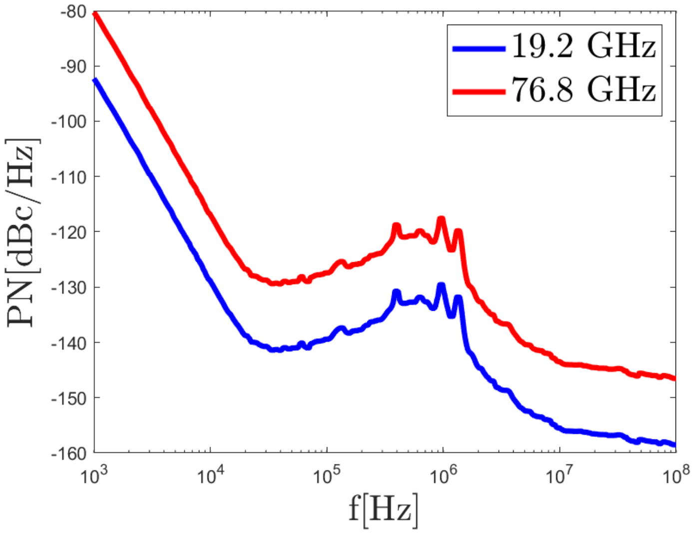

FIGURE C.6: Phase noise measurement at $f_{OEPLL} = 19.2$ GHz and expected value at $f_{Beat} = 76.8$ GHz.

Figure C.6 presents the phase noise measurement results of the OEPLL at 19.2 GHz. The OEPLL demonstrates excellent phase noise performance, reaching $-135$ dBc/Hz at a 1 MHz offset. The phase noise at 77 GHz was approximated using the theoretical minimum [87]:

$$\mathcal{L}_{77GHz}(f_m) = 4\cdot\mathcal{L}_{OEPLL}(f_m). \tag{C.3}$$

As previously noted, the current OEPLL can only lock onto integer harmonics of the MLL. While these harmonic steps are too large for FMCW radar applications, continuous tuning is currently under development at the Heinz Nixdorf Institute.

## Appendix D

# An Ultra Low Phase Noise 77 GHz Frequency Synthesizer

This chapter presents a collaborative work by Meysam Bahmanian, and Stephan Kruse. The OEPLL was developed by Meysam Bahmanian, while the frequency multiplier chip and architecture were contributed by Stephan Kruse.

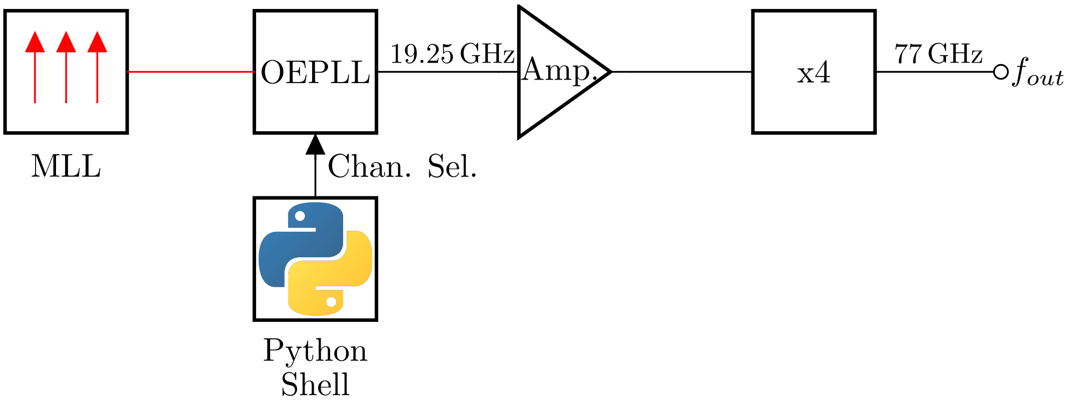

FIGURE D.1: Simplified block diagram of the 77 GHz frequency synthesizer.

In appendix C, an ultra-low phase noise 77 GHz frequency synthesizer with optical output was introduced. This chapter presents a 77 GHz frequency synthesizer with ultra-low phase noise and an electrical output. The output signal of the OEPLL, shown in figure C.2 [142], is amplified before being fed into a frequency multiplier chip. The block diagram of the frequency synthesizer is shown in figure D.1.

The frequency multiplier chip, previously published in [53], depicted in figure D.2, consists of two bootstrapped Gilbert cell frequency doublers [122] with delay lines between the RF and LO inputs of the Gilbert cell, along with an additional output buffer. To minimize the active chip area, the ESD bond pads [111] and the ultra-compact delay lines, presented in chapter 5.1.2, were utilized. The chip occupies an overall area of 947 µm × 1193 µm and consumes 91.5 mW from a 3.3 V source. The 19.25 GHz input features a GSSG configuration, while the 77 GHz output port adopts a GSGSG pad configuration. The chip was fabricated using IHP's 130 nm SiGe BiCMOS technology [143] with $f_T/f_{MAX} = 240\,\text{GHz}/340\,\text{GHz}$. It was optimized for 77 GHz long-range radar applications in Europe and the USA.

The block diagram of the measurement setup is shown in figure D.3a. The output signal of the OEPLL undergoes further amplification before the single-ended signal from the OEPLL and amplifier is converted into a differential signal using a balun. The output of the balun then drives the frequency quadrupler chip. One output of the frequency quadrupler chip is connected to a spectrum analyzer, while the

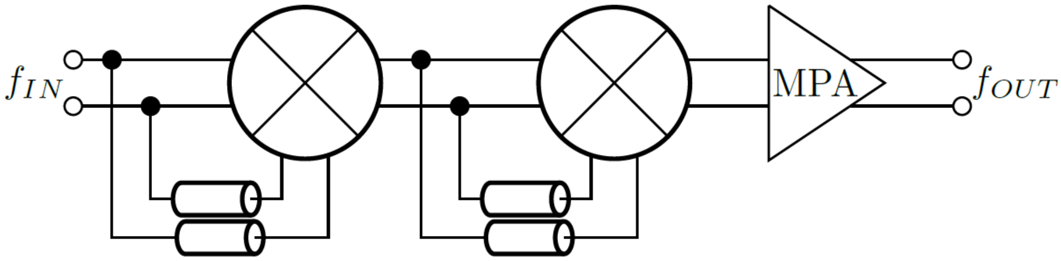

(a)

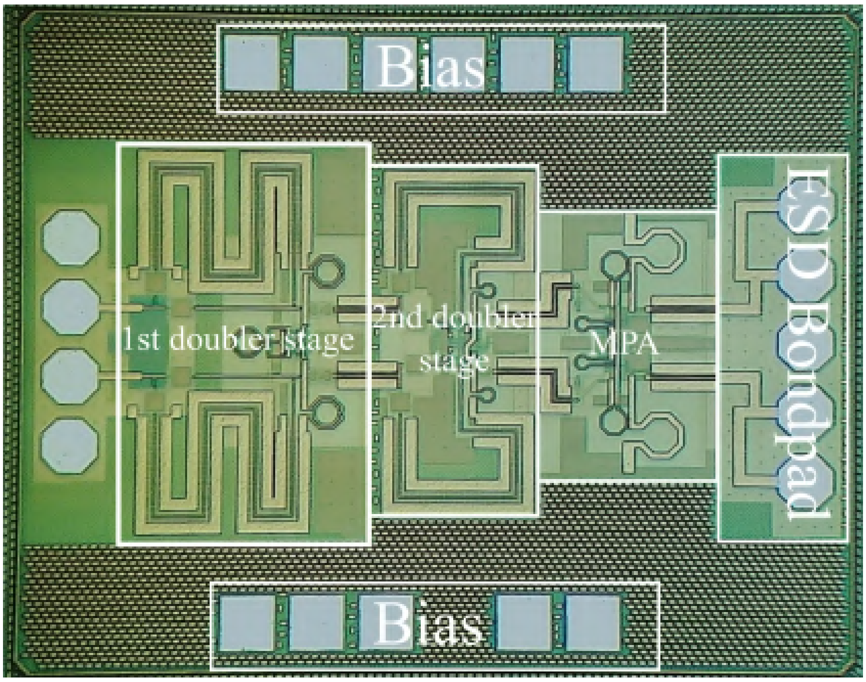

(b)

Figure D.2: (a) Simplified block diagram of the frequency quadrupler chip; (b) Chip micro photograph of the frequency quadrupler chip.

second output is linked to the cross-correlation unit [144] shown in figure D.3b. The chip's output signal is fed into a magic tee in a power divider configuration (see appendix I.2) before undergoing downconversion via subharmonic mixers, which convert the 77 GHz signal to an IF-frequency of 1.5 GHz. To ensure sufficient output power, the signal from the subharmonic mixers is amplified using low additive phase noise amplifiers powered by two independent sources. The amplified signals are then analyzed using a phase noise analyzer where cross-correlation is performed.

The combined optical output spectrum is shown in figure D.4. As mentioned in appendix C, the OEPLL locks onto harmonics of the MLL, which, in this experiment, has a repetition rate of 250 MHz. This results in a channel spacing of 250 MHz for the OEPLL and 1 GHz after the frequency quadrupler chip.

Figure D.5 presents the measured phase noise of the frequency synthesizer at 77 GHz. A peak can be observed at offset frequencies close to the carrier, caused by leakage from one of the signal generators used as the LO. The output phase noise of the OEPLL demonstrates excellent performance, reaching $-136.34\,\mathrm{dBc/Hz}$ at a 1 MHz offset frequency. Above an offset frequency of 3 MHz, the noise induced by the amplifier becomes noticable. The phase noise at the output frequency of the multiplier up to 10 MHz offset follows the theoretical minimum [87]:

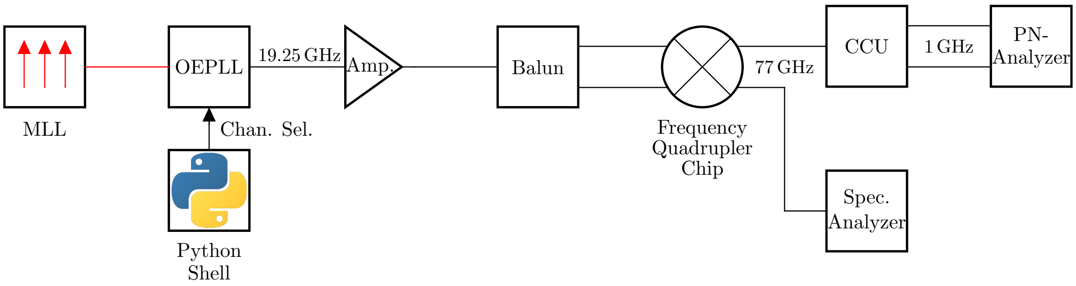

(a)

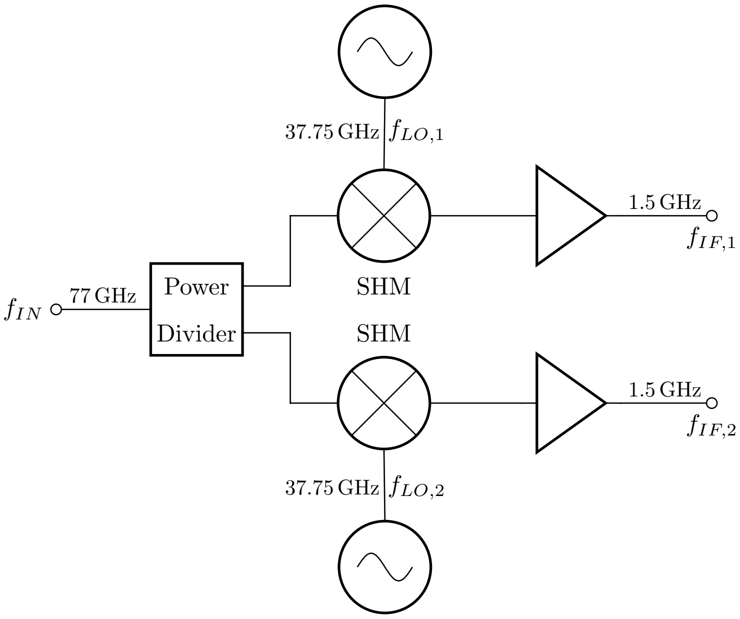

(b)

FIGURE D.3: (a) Block diagram of the measurement setup for simultaneous output power and phase noise analysis; (b) Block diagram of the cross correlation unit (CCU) with subharmonic mixers (SHMs).

$$\mathcal{L}_{theo.min} = \mathcal{L}_{Amp} + 12\,\mathrm{dB} \tag{D.1}$$

Beyond this offset frequency, the phase noise of the chip's output settles at $-135\,\mathrm{dBc/Hz}$ at a 100 MHz offset frequency. Additional measurements indicate that the additive phase noise of the chip remains below 3 dB across the entire 76 GHz to 78 GHz long-range radar band.

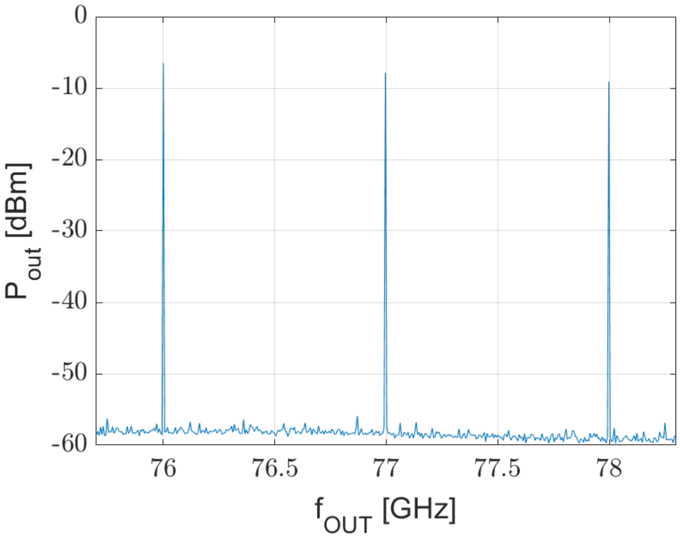

FIGURE D.4: Combined output spectrum of the three frequency output frequencies.

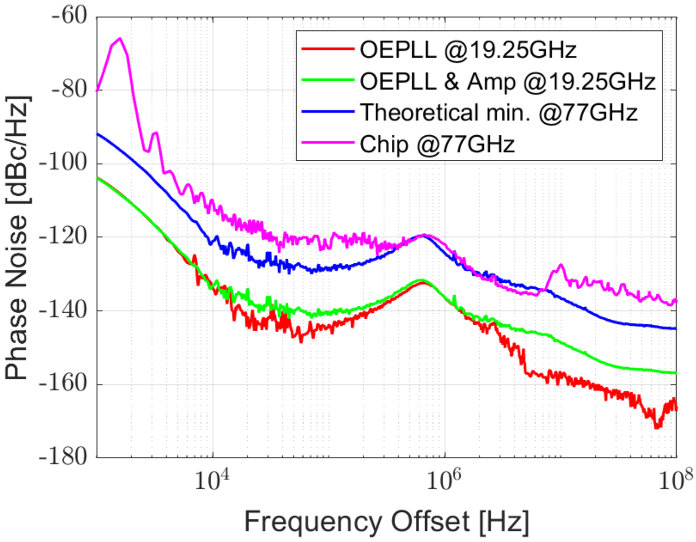

FIGURE D.5: Phase Noise measurement @$f_{OEPLL}$ = 19.25 GHz and $f_{out}$ = 77 GHz.

# Appendix E

# System Simulations of the Photonic Software-Defined MIMO Radar System with Optical Signal Distribution in Lumerical Interconnect

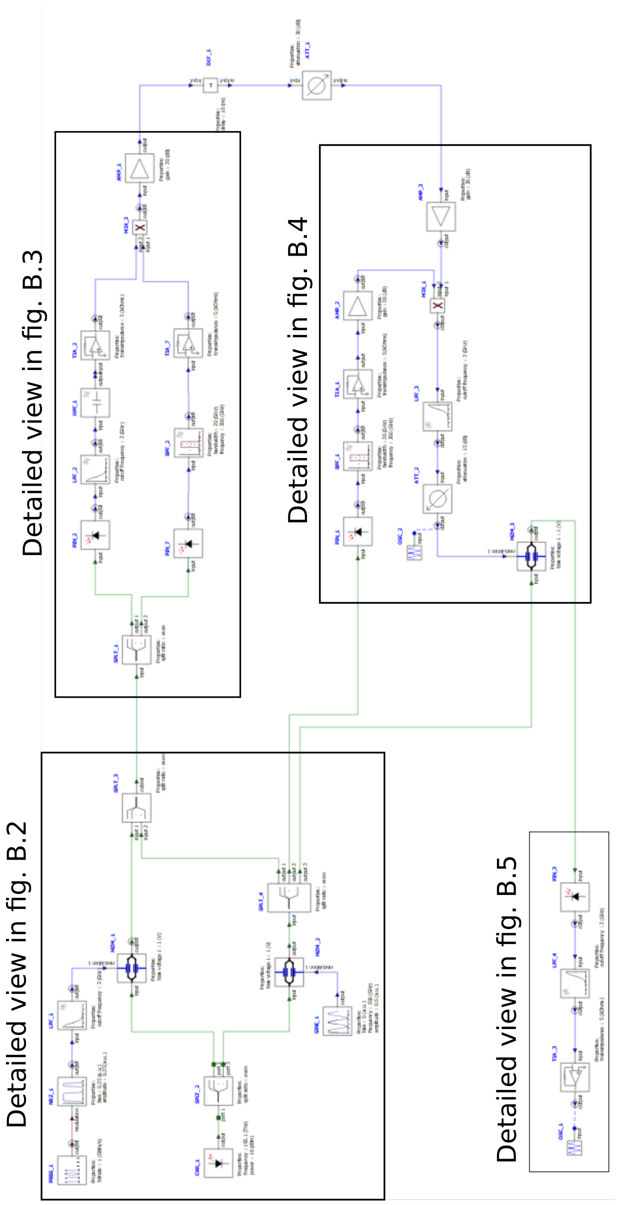

FIGURE E.1: Overall simulation setup of the photonic software-defined radar system with optical signal distribution. (High resolution images in [145]).

In chapter 8, the photonic software-defined MIMO radar system with optical signal distribution was introduced and analyzed, and corresponding simulation results were presented. In this appendix, the simulation model within the optical design environment Lumerical Interconnect by Ansys is presented.

Figure E.1 shows the overall simulation setup of the photonic software-defined radar system with optical signal distribution in the optical design environment Lumerical Interconnect. The setup includes the optical carrier and signal generation, the TX frontend, the noiseless channel, the RX frontend with the optical receive path, and the optical receiver in the central station.

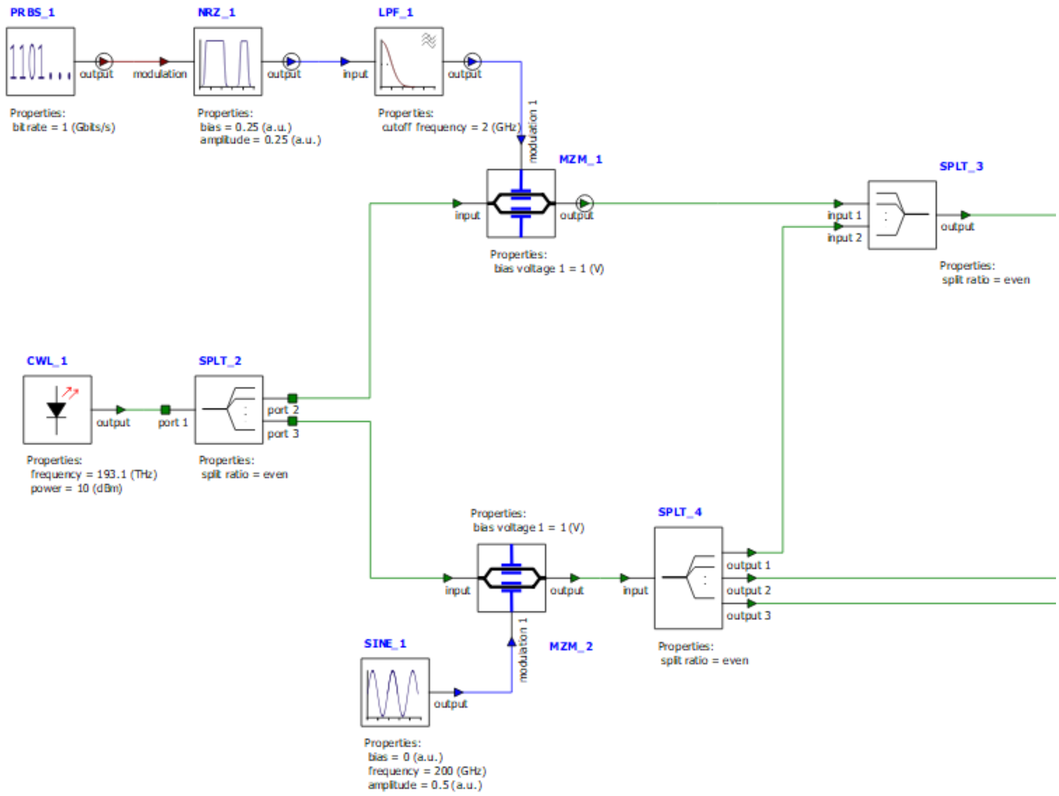

FIGURE E.2: Implementation of the optical signal generation in Lumerical Interconnect

The implementation of the optical signal generation in the optical design environment Lumerical Interconnect is shown in figure E.2. The output signal of a continuous wave laser (CWL_1) is split by an optical splitter (SPLT_2) into a carrier path and an arbitrary signal path. Within the arbitrary signal path, a pseudo-random bit sequence generator (PRBS_1) generates a bit stream with a data rate of $1\,\mathrm{Gbit/s}$. The bit stream is converted into a non-return-to-zero linear code by the code block NRZ_1. To suppress the high-frequency components of the ideal non-return-to-zero signal, a low-pass filter (LPF_1) was added at the output of the code block. The output signal of the low-pass filter finally drives the first MZM (MZM_1), which is biased at the quadrature point and fed by the output signal of the optical splitter. In the carrier path, the second MZM (MZM_2), which is also biased at the quadrature point, and fed by the second output signal of the optical splitter, is driven directly by an electrical continuous wave source (SINE_1). The peak driving amplitudes of the MZMs is $V_p/V_\pi = 1/8$. The output signal of the second MZM is split into three optical paths by an optical splitter (SPLT_4). One output of the optical splitter is fed into the optical combiner (SPLT_3) which sums up the arbitrary signal and the carrier signal. The other two outputs are fed to the RX frontend for the optical carrier distribution, and as a carrier signal for the optical receive path.

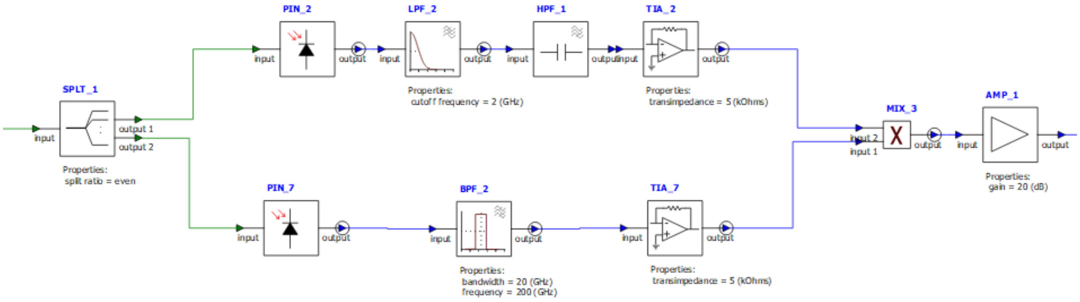

FIGURE E.3: Implementation of the TX frontend of the software-defined radar system in Lumerical Interconnect.

Figure E.3 shows the implementation of the TX frontend in the optical design environment Lumerical Interconnect. The optical signal is split into the low frequency path and the high frequency path by an optical splitter (SPLT_1). In the low frequency path, the optical input signal is converted to an electrical signal by a PD (PIN_2). To cancel the high frequency components and the DC offset, the output signal of the PD is filtered by a LPF (LPF_2) and a DC block component. The filtered output signal is finally further amplified by a TIA (TIA_2). In the high frequency path, the optical signal is also converted to an electrical signal by a PD (PIN_7). In contrast to the low frequency path, the high frequency carrier is filtered out of the photocurrent by a BPF (BPF_2). The output signal of the BPF is further amplified by a TIA (TIA_7). The output signal of the TIAs is multiplied by an electrical mixer (MIX_3) before the transmit signal is further amplified by an amplifier block (AMP_1).

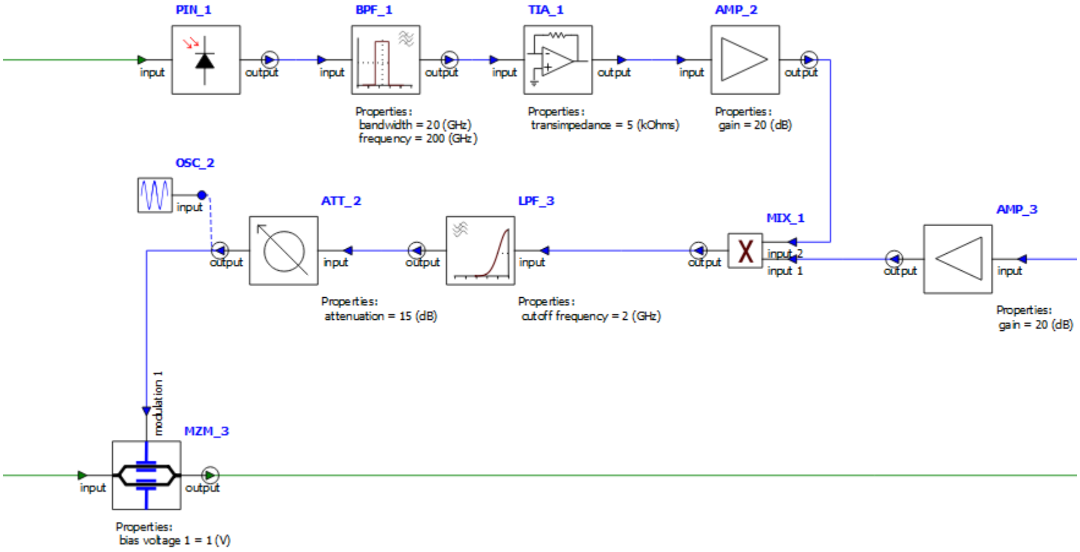

FIGURE E.4: Implementation of the RX frontend of the software defined radar system in Lumerical Interconnect.

The implementation of the RX frontend of the software-defined radar system in the optical design environment Lumerical Interconnect is shown in figure E.4. The RX frontend uses the same PD, TIA, BPF, and amplifier architecture as the high-frequency path of the TX frontend. The weak received signal is amplified by an amplifier block (AMP_3) before it is mixed with the high-frequency carrier by the mixer block MIX_1. The output signal is filtered by a LPF (LPF_3). The intensity of the output signal is adjusted by an attenuator block (ATT_2) before driving the MZM (MZM_3). The MZM is fed by the optical carrier signal.

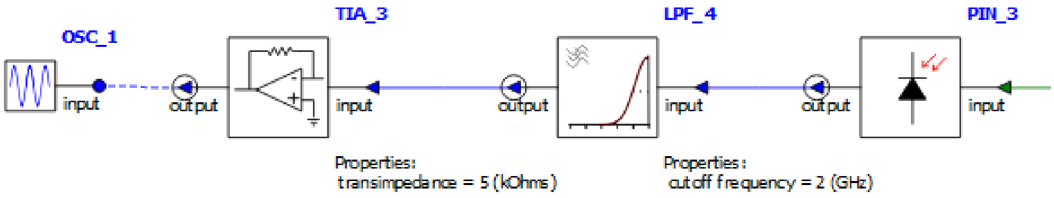

FIGURE E.5: Implementation of the receive part of the central station.

The modeled optical receiver in the central station is shown in figure E.5. The incident optical signal is converted to an electrical signal by a PD (PIN_3). The high-frequency components are filtered by a LPF (LPF_4) before the signal is amplified by a TIA (TIA_3). The final received signals are recorded by the oscilloscope block OSC_1.

The results of the simulation are presented in chapter 8.3.1.

# Appendix F

# System Simulations of the Coherent Optical IQ Return Path in Lumerical Interconnect

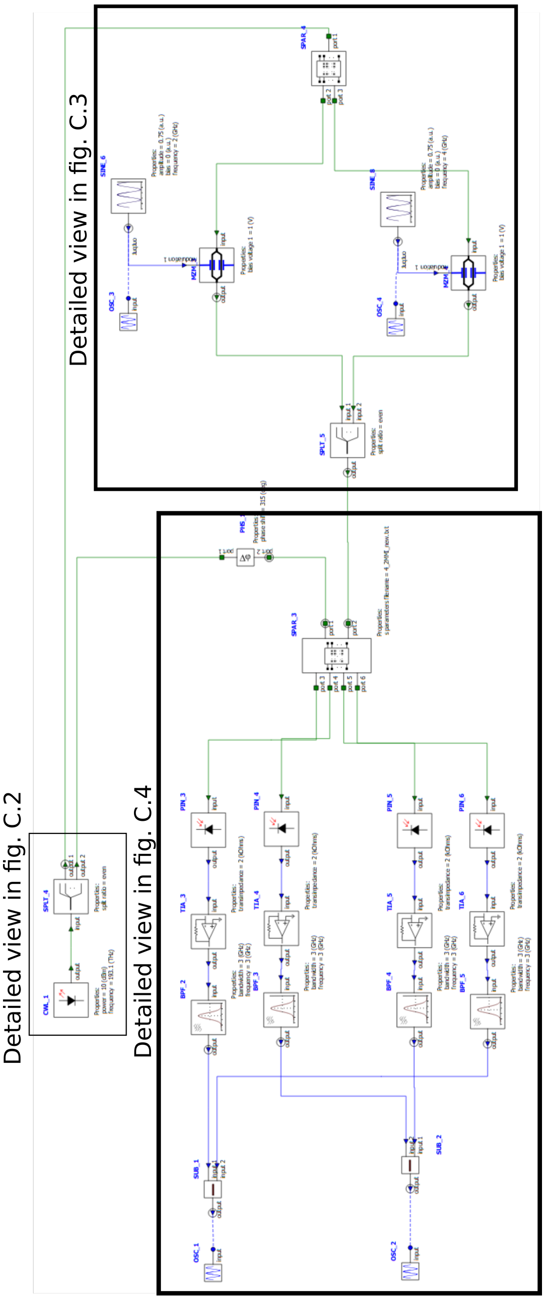

FIGURE F.1: Overall simulation setup of the coherent optical IQ return path. (High resolution images in [97].)

In chapter 8.2.2, the coherent optical IQ return path was introduced and analyzed, and corresponding simulation results were presented. In this appendix, the simulation model within the optical design environment Lumerical Interconnect by Ansys is presented.

Figure F.1 illustrates the overall simulation setup of the coherent optical IQ return path in the optical design environment Lumerical Interconnect by Ansys. For simplicity, the model includes only the coherent optical IQ return path, excluding the photonic software-defined radar with optical signal distribution.

Figure F.2 shows the implementation of the optical signal generation in Lumerical Interconnect. Since the simulation aims solely to validate the concept of the coherent optical IQ return path, the signal generation is reduced to its minimum. The output of the continuous wave laser (CWL_1) is fed into an optical splitter (SPLT_4). One output of the splitter is routed to the transmit part of the coherent optical IQ return path, while the other is directed to the receive part.

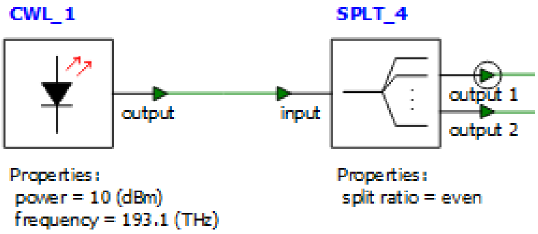

FIGURE F.2: Implementation of the simplified optical source in Lumerical Interconnect.

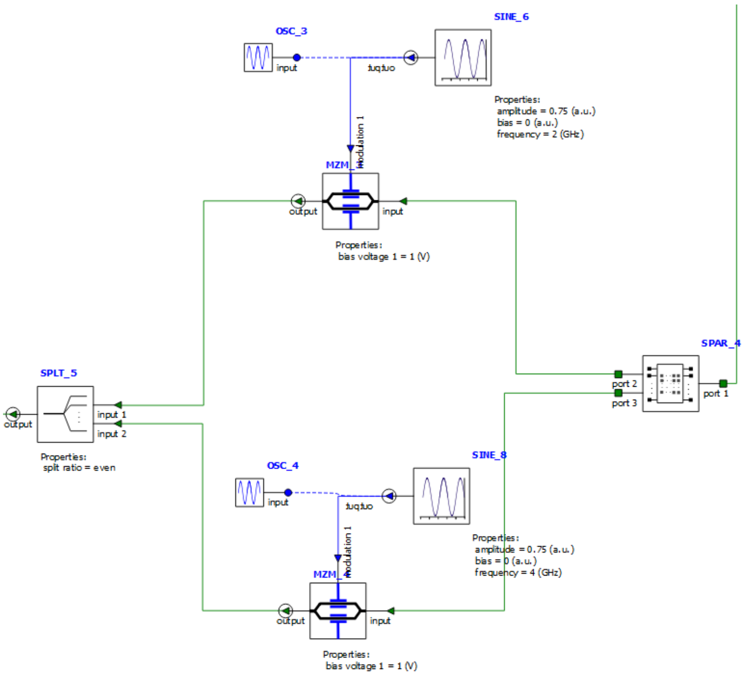

FIGURE F.3: Implementation of the transmit part of the coherent optical IQ return path in Lumerical Interconnect.

The transmit part of the coherent optical IQ return path is depicted in figure F.3. The optical IQ generator is implemented using the optical S-parameter box SPAR_4. To validate the IQ return path concept, each MZM (MZM_3 and MZM_4) is driven by a sinusoidal source at different frequencies. The two output signals from the MZMs are then combined using the SPL_5 block. Figure F.4 shows the receive part of the coherent optical IQ return path. The 2x4 MMI is implemented using the optical S-parameter block SPAR_3, which is fed by the received optical signal and a phase-shifted version of the continuous wave laser signal. The phase shift is introduced via the phase shifter block PHS_1. The output of SPAR_3 is converted into an electrical signal using four PDs (PIN_3–PIN_6) and four TIAs (TIA_3–TIA_6). To suppress unwanted harmonics induced by the MZMs, four BPFs (BPF_2–BPF_5) are placed after the OE conversion. The electrical IQ signal is then reconstructed by subtracting the output of BPF_5 from BPF_2, and BPF_4 from BPF_3.

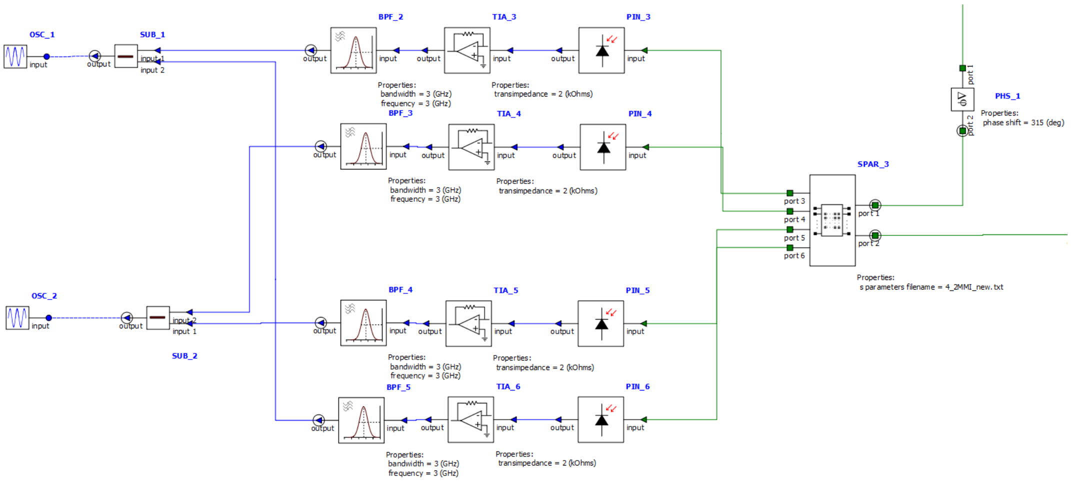

Figure F.4: Implementation of the receive part of the coherent optical IQ return path in Lumerical Interconnect.

The results of the simulation are presented in chapter 8.3.2.

# Appendix G

# System Simulations of the Photonic FMCW Multiband Radar System with Optical LO Distribution in Lumerical Interconnect

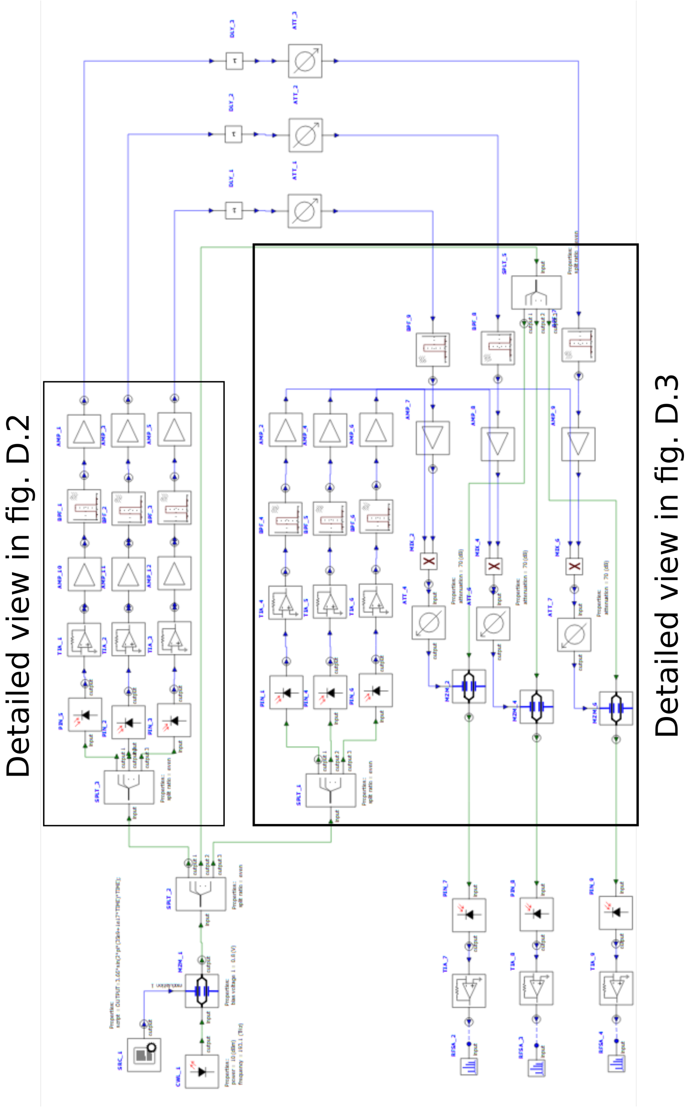

FIGURE G.1: Overall simulation setup of the photonic FMCW multiband radar systems with optical LO distribution. (High resolution images in [146].)

In chapter 9, the photonic FMCW multiband radar system with optical LO distribution was introduced and analyzed, and corresponding simulation results were presented. In this appendix, the simulation model within the optical design environment Lumerical Interconnect by Ansys is presented.

Figure G.1 shows the overall simulation setup of the photonic FMCW multiband radar systems with optical LO distribution in the optical design environment Lumerical Interconnect. The setup includes the optical LO generation, the TX frontend, the noiseless channel, the RX frontend with optical receive path, and the optical receiver in the central station.

The optical LO generation is implemented similarly to the one shown in figure 3.2a. The minor difference is that the power divider (SPLT_1) has three outputs instead of four, one for the TX frontend, one for the LO distribution to the RX frontend, and one for the optical receive path. The bias voltage of the MZM is $V_B/V_\pi = 0.8$. The scripted source generates a $35.9\,\mathrm{GHz}$ FMCW chirp with the amplitude $V_0/V_\pi = 3.66$, and $\mu = 1 \cdot 10^{17}\ \mathrm{s}^{-2}$. Similar to the photonic FMCW radar system with optical LO distribution, the high chirp rate is motivated by the finite frequency resolution of Lumerical Interconnect.

The implemented multiband radar TX frontend is shown in figure G.2. Within the TX, the incident optical LO signal is split into three paths. This is motivated by the lack of electrical power splitters in Lumerical Interconnect. The optical signal is converted in each path to an electrical signal by means of PDs (PIN_2, PIN_3 & PIN_5), TIAs (TIA_1, TIA_2 & TIA_3), preamplifiers (AMP_10, AMP_11 & AMP_12), and BPFs, similar to the photonic FMCW radar system with optical LO distribution. The BPFs filter the desired harmonic in each path before the signal is finally amplified by AMP_1, AMP_3, and AMP_5.

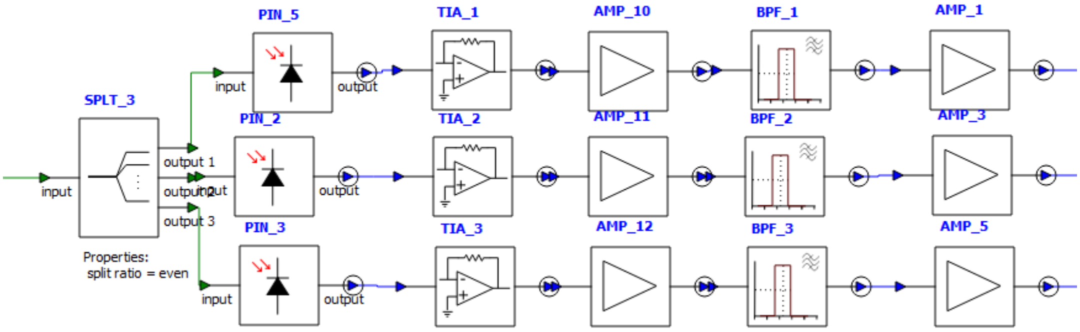

FIGURE G.2: Implementation of the TX frontend in Lumerical Interconnect.

For each radar band, an individual wireless channel was implemented. In each radar band, the noiseless wireless channel is modeled similarly to that of the photonic FMCW radar system with optical LO distribution. To model the $1/\lambda$ behavior [137] of the radar cross-section, the attenuation was properly adjusted in each path.

Figure G.3 shows the implemented RX frontend of the photonic multiband radar system. The frontend uses the same PD (PIN_1, PIN_4 & PIN_6), TIA (TIA_4, TIA_5 & TIA_6), BPF (BPF_4, BPF_5 & BPF_6), and amplifier (AMP_2, AMP_4 & AMP_6) architecture as the TX frontend for the OE conversion of the optical LO signal. In the receiver chain, the separation of the three radar bands is implemented by BPFs (BPF_7, BPF_8 & BPF_9). The weak received signal is amplified by the amplifier chain AMP_7, AMP_8, and AMP_9 before it is directly downconverted to the baseband by mixers (MIX_2, MIX_4 & MIX_6). The intensity of the downconverted signal is

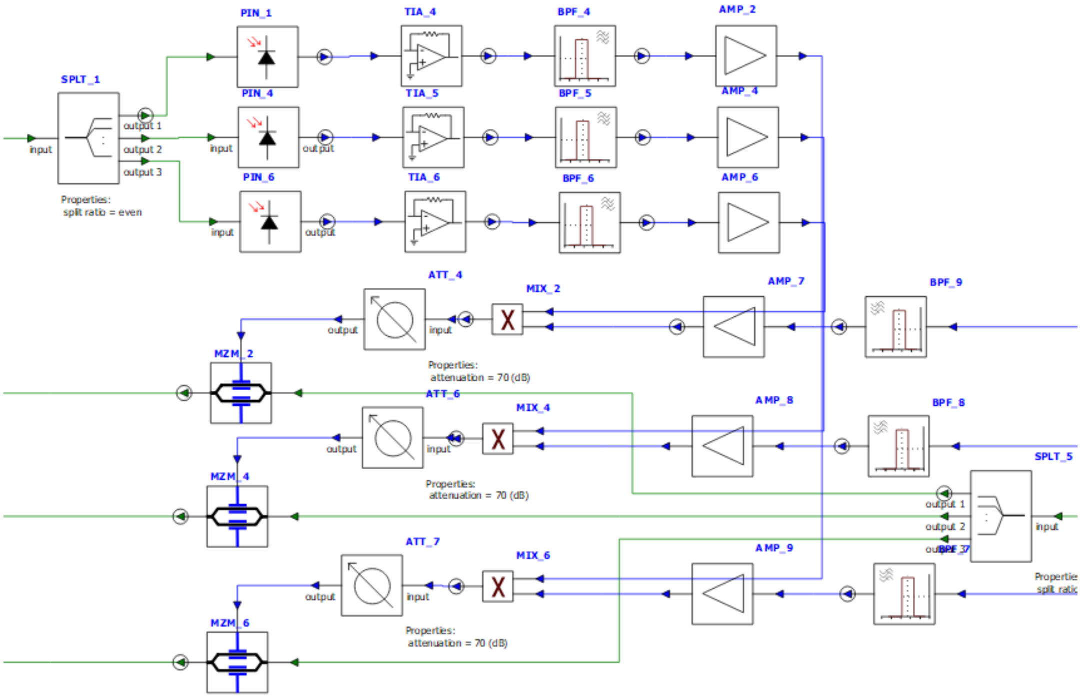

Figure G.3: Implementation of the RX frontend in Lumerical Interconnect.

attenuated to drive the MZMs in the linear region by attenuators (ATT_4, ATT_6 & ATT_7). The electrical IF signal is finally converted to an optical signal via MZMs (MZM_2, MZM_4, MZM_6).

The OE conversion in the central station is simply implemented by PDs and TIAs, each for one radar band.

The results of the simulations are shown in chapter 9.3.

# Appendix H

# System Simulations of the Lidar-Radar Combined Sensor System in Lumerical Interconnect

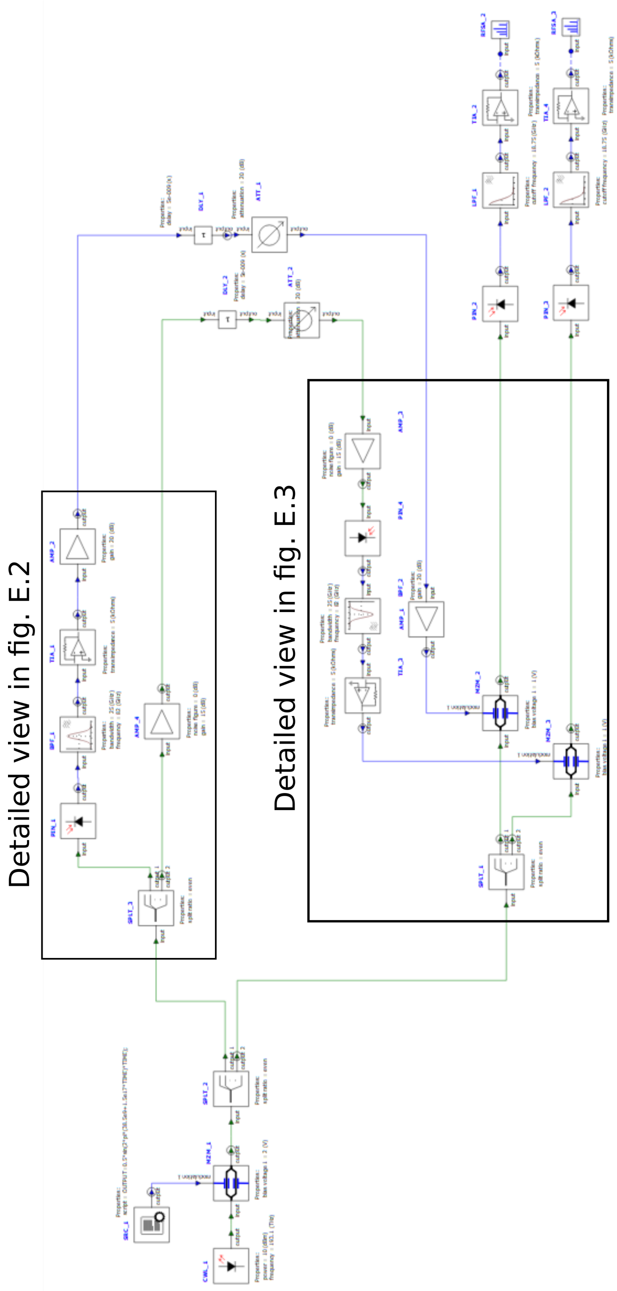

FIGURE H.1: Overall simulation setup of the Lidar-Radar combined sensor system in Lumerical Interconnect (High resolution images in [147].)

In chapter 10, the lidar-radar combined sensor system was introduced and analyzed, and corresponding simulation results were presented. In this appendix, the simulation model within the optical design environment Lumerical Interconnect by Ansys is presented.

Figure H.1 shows the overall simulation setup of the lidar-radar combined sensor system in the optical design environment Lumerical Interconnect. The setup includes the optical LO generation, the lidar and radar parts of the TX and RX frontends, the optical receive path of the RX frontend, and the optical receiver in the central station.

The optical LO generation is implemented similar as shown in figure 3.2a. The only difference to figure 3.2a is that the power divider (SPLT_1) has two outputs instead of four outputs, one for the TX frontend, and one for the RX frontend. The MZM for the lidar-radar combined sensor system is biased at the minimum point. The scripted source generates a $38.5\,\mathrm{GHz}$ FMCW chirp with the amplitude $V_0/V_\pi = 1/8$, and $\mu = 1.5\cdot10^{17}\,\mathrm{s}^{-2}$. Similar to the photonic FMCW radar system with LO distribution, the high chirp rate is motivated by the finite frequency resolution of Lumerical Interconnect.

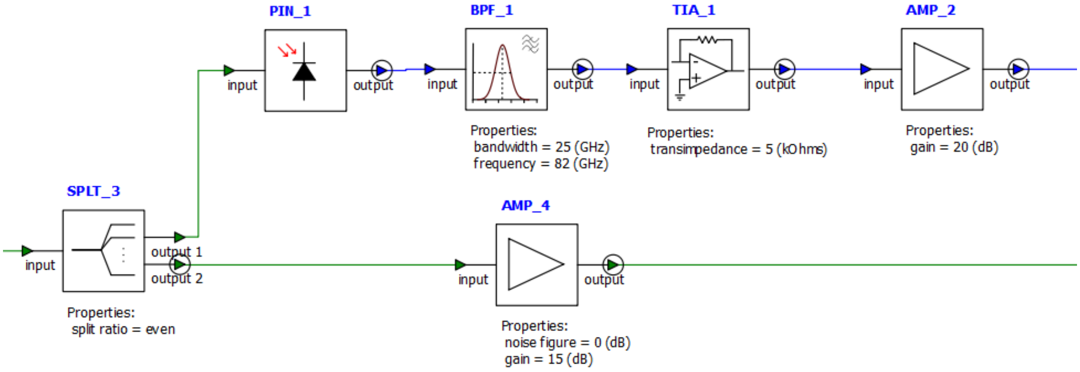

FIGURE H.2: Implementation of the lidar-radar combined sensor system in Lumerical Interconnect.

The implemented TX frontend of the lidar-radar combined sensor system is shown in figure H.2. The incident optical LO signal is split into the lidar and radar paths by means of an optical splitter (SPLT_3). Within the radar part, the optical LO signal is converted to an electrical signal by means of a PD (PIN_1), a BPF (BPF_1), a TIA (TIA_1), and an amplifier (AMP_2), similar to the TX frontend of the photonic FMCW radar system with optical LO distribution. In the lidar path, the optical LO signal is amplified by an optical amplifier (AMP_4), which models the optical antenna gain.

For the lidar and radar signals, an individual noiseless optical channel, similar to the one shown in figure 3.3, was implemented.

The implemented lidar-radar combined RX frontend is shown in figure H.3. Within the radar path, the weak received signal is amplified by the amplifier AMP_1. In the lidar part, the weak optical signal is also amplified by an optical amplifier (AMP_3) before the optical signal is converted to an electrical signal by means of a PD (PIN_4), a BPF (BPF_2), and a TIA (TIA_3). The output signals of the lidar and radar paths drive the MZMs MZM_2 for the radar signal and MZM_3 for the lidar signal. Both MZMs are biased at the quadrature point. The optical splitter SPLT_1 feeds the MZMs with the optical LO signal.

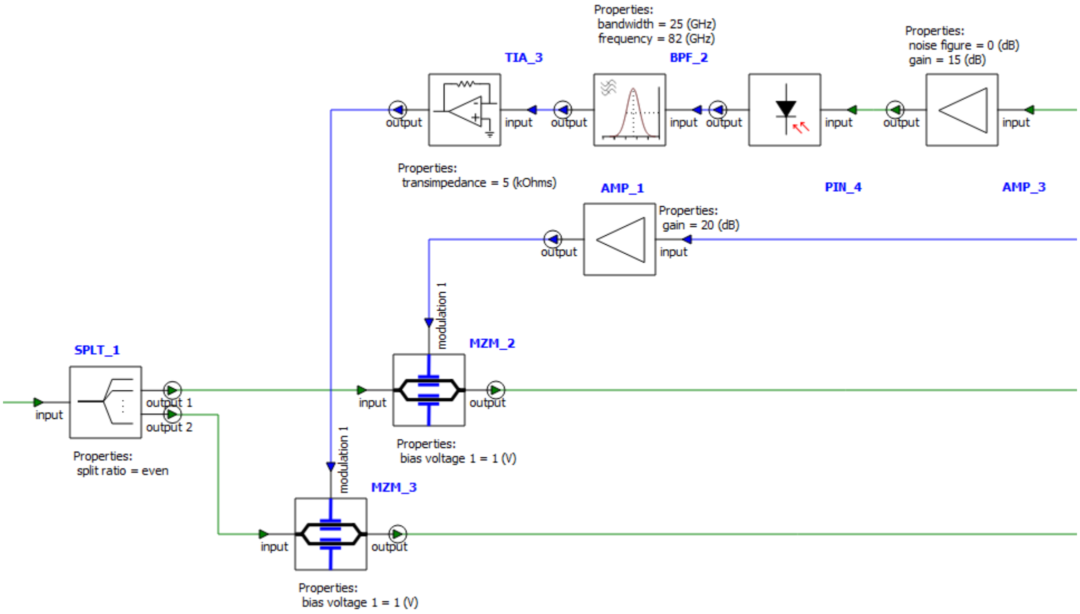

FIGURE H.3: Implementation of the RX frontend of the lidar-radar combined sensor system in Lumerical Interconnect.

The OE conversion in the central station is implemented by a PD and TIA, one for each measurement technique.

The results of the simulation are presented in chapter 10.3.

# Appendix I

# Magic Tee in Balun and Power Divider Configuration

## I.1 Balun

In chapter 6.2, the single-ended 77 GHz RF signal provided by the VNA, in CW signal generator configuration, is converted into a differential signal using a magic tee in balun configuration. To the best of the author's knowledge, the mathematical description has not been published before and is detailed for the first time in this appendix.

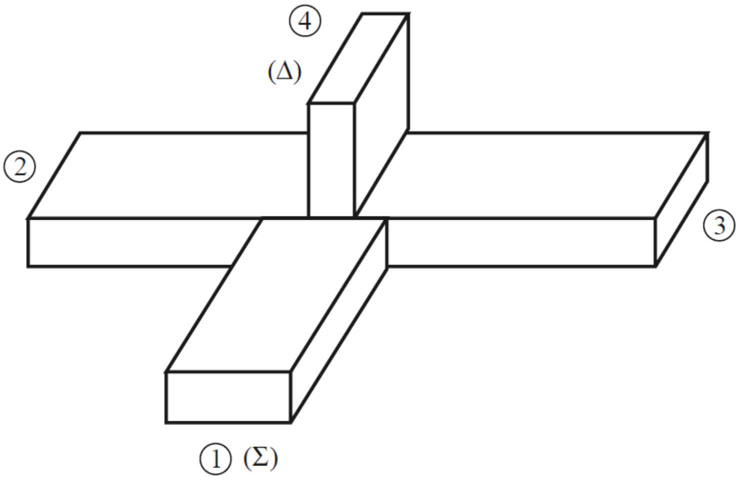

FIGURE I.1: A waveguide hybrid junction or magic tee [110].

The magic tee, shown in figure I.1, is a waveguide implementation of a 180° hybrid [110]. The S-parameter of the magic tee are [110]

$$S = -\frac{j}{\sqrt{2}} \begin{bmatrix} 0 & 1 & 1 & 0 \\ 1 & 0 & 0 & -1 \\ 1 & 0 & 0 & 1 \\ 0 & -1 & 1 & 0 \end{bmatrix}. \tag{I.1}$$

For an incident wave vector $\vec{a} = [0\ 0\ 0\ 1]^T$, the output wave vector is given as $\vec{b} = \left[0\ \frac{j}{\sqrt{2}}\ -\frac{j}{\sqrt{2}}\ 0\right]^T$. In this configuration, the output at ports 2 and 3 have the same amplitude and are 180° out of phase.

## I.2 Power Divider

In Appendix D, the magic tee is utilized in a power divider configuration within the cross-correlation unit. This section derives the power divider configuration.

The S-parameter parameters of the magic tee are given by [110]:

$$S = -\frac{j}{\sqrt{2}} \begin{bmatrix} 0 & 1 & 1 & 0 \\ 1 & 0 & 0 & -1 \\ 1 & 0 & 0 & 1 \\ 0 & -1 & 1 & 0 \end{bmatrix}. \tag{I.2}$$

For an incident wave vector $\vec{a} = [1\;0\;0\;0]^T$, the output wave vector is given by: $\vec{b} = \left[0\; -\frac{j}{\sqrt{2}}\; -\frac{j}{\sqrt{2}}\; 0\right]^T$. In this configuration, the outputs at ports 2 and 3 have equal amplitudes and are in phase.

# Bibliography

[1] G. E. Moore, “Cramming more components onto integrated circuits, Reprinted from Electronics, volume 38, number 8, April 19, 1965, pp.114 ff.,” *IEEE Solid-State Circuits Society Newsletter*, vol. 11, no. 3, pp. 33–35, 2006. DOI: `10.1109/N-SSC.2006.4785860`

[2] M. M. Zaman, I. H. Shibly, M. S. Hossain, and M. S. Rahman Shanto, “Advancements in Radar Technology for Enhanced Adaptive Cruise Control Systems,” in *2024 IEEE International Conference on Power, Electrical, Electronics and Industrial Applications (PEEIACON)*, 2024, pp. 1–6. DOI: `10.1109/PEEIACON63629.2024.10800208`

[3] S. Rajendar and V. K. Kaliappan, “Recent Advancements in Autonomous Emergency Braking: A Survey,” in *2021 5th International Conference on Electronics, Communication and Aerospace Technology (ICECA)*, 2021, pp. 1027–1032. DOI: `10.1109/ICECA52323.2021.9675885`

[4] K. V. Mishra, A. Kruger, and W. F. Krajewski, “Compressed sensing applied to weather radar,” in *2014 IEEE Geoscience and Remote Sensing Symposium*, 2014, pp. 1832–1835. DOI: `10.1109/IGARSS.2014.6946811`

[5] M. Vogt and M. Gerding, “Silo and Tank Vision: Applications, Challenges, and Technical Solutions for Radar Measurement of Liquids and Bulk Solids in Tanks and Silos,” *IEEE Microwave Magazine*, vol. 18, no. 6, pp. 38–51, 2017. DOI: `10.1109/MMM.2017.2711978`

[6] Y. Álvarez López, M. García Fernández, R. Grau, and F. Las-Heras, “A Synthetic Aperture Radar (SAR)-Based Technique for Microwave Imaging and Material Characterization,” *Electronics*, vol. 7, no. 12, 2018, ISSN: 2079-9292. DOI: `10.3390/electronics7120373`

[7] J. Blanche, D. Mitchell, R. Gupta, A. Tang, and D. Flynn, “Asset Integrity Monitoring of Wind Turbine Blades with Non-Destructive Radar Sensing,” in *2020 11th IEEE Annual Information Technology, Electronics and Mobile Communication Conference (IEMCON)*, 2020, pp. 0498–0504. DOI: `10.1109/IEMCON51383.2020.9284941`

[8] Rayleigh, *XXXI. Investigations in optics, with special reference to the spectroscope*, Oct. 1879. DOI: `10.1080/14786447908639684`

[9] S. Lischke, D. Knoll, L. Zimmermann, Y. Yamamoto, M. Fraschke, A. Trusch, A. Krüger, M. Kroh, and B. Tillack, “Low dark current Ge PIN photodiode for a high-performance, photonic BiCMOS process for radio-over-fiber applications,” in *IEEE Photonics Conference 2012*, 2012, pp. 628–629. DOI: `10.1109/IPCon.2012.6358778`

[10] S. Preussler, F. Schwartau, J. Schoebel, and T. Schneider, “Optical Signal Generation and Distribution for Large Aperture Radar in Autonomous Driving,” in *2019 12th German Microwave Conference (GeMiC)*, 2019, pp. 154–157. DOI: `10.23919/GEMIC.2019.8698119`

[11] I. Barabas, A. Todorut, N. Cordos, and A. Molea, “Current challenges in autonomous driving,” *IOP Conference Series: Materials Science and Engineering*, vol. 252, no. 1, p. 012 096, Oct. 2017. DOI: `10.1088/1757-899X/252/1/012096`

[12] The Event Horizon Telescope Collaboration et al., “First M87 Event Horizon Telescope Results. I. The Shadow of the Supermassive Black Hole,” *The Astrophysical Journal Letters*, vol. 875, no. 1, p. L1, Apr. 2019. DOI: `10.3847/2041-8213/ab0ec7`

[13] M. E. Warren, “Automotive LIDAR Technology,” in *2019 Symposium on VLSI Circuits*, 2019, pp. C254–C255. DOI: `10.23919/VLSIC.2019.8777993`

[14] M. Murad, I. Bilik, M. Friesen, J. Nickolaou, J. Salinger, K. Geary, and J. S. Colburn, “Requirements for next generation automotive radars,” in *2013 IEEE Radar Conference (RadarCon13)*, 2013, pp. 1–6. DOI: `10.1109/RADAR.2013.6586127`

[15] C. Waldschmidt, J. Hasch, and W. Menzel, “Automotive Radar — From First Efforts to Future Systems,” *IEEE Journal of Microwaves*, vol. 1, no. 1, pp. 135–148, 2021. DOI: `10.1109/JMW.2020.3033616`

[16] D. Pan, Z. Duan, B. Wu, Y. Wang, D. Huang, Y. Wang, L. Sun, P. Gui, and L. Cheng, “A 76–81-GHz Four-Channel Digitally Controlled CMOS Receiver for Automotive Radars,” *IEEE Transactions on Circuits and Systems I: Regular Papers*, vol. 68, no. 3, pp. 1091–1101, 2021. DOI: `10.1109/TCSI.2020.3042976`

[17] H.-H. Ko, K.-W. Cheng, and H.-J. Su, “Range resolution improvement for FMCW radars,” in *2008 European Radar Conference*, 2008, pp. 352–355.

[18] S. Neemat, F. Uysal, O. Krasnov, and A. Yarovoy, “Reconfigurable Range-Doppler Processing and Range Resolution Improvement for FMCW Radar,” *IEEE Sensors Journal*, vol. 19, no. 20, pp. 9294–9303, 2019. DOI: `10.1109/JSEN.2019.2923053`

[19] F. S. Minko, “ON-CHIP AND HYBRID LNA INTEGRATION AT MM-WAVE FREQUENCIES,” Ph.D. dissertation, UNIVERSITY OF PRETORIA, Sep. 2021.

[20] K. Czuba and D. Sikora, “Phase drift versus temperature measurements of coaxial cables,” in *18-th INTERNATIONAL CONFERENCE ON MICROWAVES, RADAR AND WIRELESS COMMUNICATIONS*, 2010, pp. 1–3.

[21] J. Zhang, H. Gao, Z. Zhao, J. Cheng, B. Zhao, B. Luo, and S. Yu, “Ultra-Stable RF Transmission Over Coaxial Cables via Phase Fluctuation Compensation,” *IEEE Microwave and Wireless Technology Letters*, vol. 33, no. 12, pp. 1678–1681, 2023. DOI: `10.1109/LMWT.2023.3326483`

[22] Y. Tamura, H. Sakuma, K. Morita, M. Suzuki, Y. Yamamoto, K. Shimada, Y. Honma, K. Sohma, T. Fujii, and T. Hasegawa, “The First 0.14-dB/km Loss Optical Fiber and its Impact on Submarine Transmission,” *Journal of Lightwave Technology*, vol. 36, no. 1, pp. 44–49, 2018. DOI: `10.1109/JLT.2018.2796647`

[23] S. Addanki, I. Amiri, and P. Yupapin, “Review of optical fibers-introduction and applications in fiber lasers,” *Results in Physics*, vol. 10, pp. 743–750, 2018, ISSN: 2211-3797. DOI: `https://doi.org/10.1016/j.rinp.2018.07.028`

[24] M. Kottmeier, “Design of a mm-Wave Transmitter based on Photonic Mixing using Silicon Photonics,” M.S. thesis, Paderborn University, 2018.

[25] P. Hannan, "The element-gain paradox for a phased-array antenna," *IEEE Transactions on Antennas and Propagation*, vol. 12, no. 4, pp. 423–433, 1964. DOI: `10.1109/TAP.1964.1138237`

[26] Y. Liu and H. Hu, "Silicon optical phased array with a 180-degree field of view for 2D optical beam steering," *Optica*, vol. 9, no. 8, pp. 903–907, Aug. 2022. DOI: `10.1364/OPTICA.458642`

[27] A. Ganis, E. M. Navarro, B. Schoenlinner, U. Prechtel, A. Meusling, C. Heller, T. Spreng, J. Mietzner, C. Krimmer, B. Haeberle, S. Lutz, M. Loghi, A. Belenguer, H. Esteban, and V. Ziegler, "A Portable 3-D Imaging FMCW MIMO Radar Demonstrator With a $24 \times 24$ Antenna Array for Medium-Range Applications," *IEEE Transactions on Geoscience and Remote Sensing*, vol. 56, no. 1, pp. 298–312, 2018. DOI: `10.1109/TGRS.2017.2746739`

[28] A. Dürr, D. Schwarz, F. Roos, P. Hügler, S. Bucher, P. Grüner, and C. Waldschmidt, "On the Calibration of mm-Wave MIMO Radars Using Sparse Antenna Arrays for DoA Estimation," in *2019 49th European Microwave Conference (EuMC)*, 2019, pp. 984–987. DOI: `10.23919/EuMC.2019.8910838`

[29] D. Mateos-Núñez, M. A. González-Huici, R. Simoni, F. B. Khalid, M. Eschbaumer, and A. Roger, "Sparse array design for Automotive MIMO Radar," in *2019 16th European Radar Conference (EuRAD)*, 2019, pp. 249–252.

[30] C. Vasanelli, R. Batra, and C. Waldschmidt, "Optimization of a MIMO radar antenna system for automotive applications," in *2017 11th European Conference on Antennas and Propagation (EUCAP)*, 2017, pp. 1113–1117. DOI: `10.23919/EuCAP.2017.7928056`

[31] J. Massen, M. Frei, W. Menzel, and U. Möller, "A 79 GHz SiGe short-range radar sensor for automotive applications," *International Journal of Microwave and Wireless Technologies*, vol. 5, no. 1, pp. 5–14, 2013. DOI: `10.1017/S1759078712000669`

[32] S. Lischke, D. Knoll, L. Zimmermann, P. Rito, A. C. Ulusoy, A. Awny, D. Petousi, I. G. Lopez, C. Mai, M. Kroh, B. Heinemann, H. Rücker, R. Barth, J. Katzer, M. A. Schubert, M. Kaynak, and A. Mai, "Photonic BiCMOS technology — Enabler for Si-based, monolithically integrated transceivers towards 400 Gbps," in *2016 46th European Microwave Conference (EuMC)*, 2016, pp. 1385–1388. DOI: `10.1109/EuMC.2016.7824611`

[33] S. Lischke, D. Knoll, C. Mai, A. Awny, G. Winzer, M. Kroh, K. Voigt, and L. Zimmermann, "Monolithic photonic BiCMOS technology for high-speed receiver applications," in *2017 19th International Conference on Transparent Optical Networks (ICTON)*, 2017, pp. 1–4. DOI: `10.1109/ICTON.2017.8024829`

[34] D. Knoll, H. H. Richter, B. Heinemann, S. Lischke, Y. Yamamoto, L. Zimmermann, and B. Tillack, "Substrate Design and Thermal Budget Tuning for Integration of Photonic Components in a High-Performance SiGe:C BiCMOS Process," *ECS Transactions*, vol. 50, no. 9, p. 297, Mar. 2013. DOI: `10.1149/05009.0297ecst`

[35] K. Giewont, K. Nummy, F. A. Anderson, J. Ayala, T. Barwicz, Y. Bian, K. K. Dezfulian, D. M. Gill, T. Houghton, S. Hu, B. Peng, M. Rakowski, S. Rauch, J. C. Rosenberg, A. Sahin, I. Stobert, and A. Stricker, "300-mm Monolithic Silicon Photonics Foundry Technology," *IEEE Journal of Selected Topics in Quantum Electronics*, vol. 25, no. 5, pp. 1–11, 2019. DOI: `10.1109/JSTQE.2019.2908790`

[36] M. Rakowski, C. Meagher, K. Nummy, A. Aboketaf, J. Ayala, Y. Bian, B. Harris, K. Mclean, K. McStay, A. Sahin, L. Medina, B. Peng, Z. Sowinski, A. Stricker, T. Houghton, C. Hedges, K. Giewont, A. Jacob, T. Letavic, D. Riggs, A. Yu, and J. Pellerin, "45nm CMOS — Silicon Photonics Monolithic Technology (45CLO) for Next-Generation, Low Power and High Speed Optical Interconnects," in *2020 Optical Fiber Communications Conference and Exhibition (OFC)*, 2020, pp. 1–3.

[37] S. Lewis, J. Sandenbergh, and M. Inggs, "Evaluating an off-the-shelf white rabbit system to synchronise network radar via optic fibre," in *2017 IEEE Radar Conference (RadarConf)*, 2017, pp. 1657–1662. DOI: `10.1109/RADAR.2017.7944473`

[38] D. Griffiths, G. Donlan, J. Kannanthara, M. Jahangir, C. Baker, M. Antoniou, and Y. Singh, "Phase Synchronization of Bistatic Radar by Exploiting the Urban Scene," *IEEE Transactions on Aerospace and Electronic Systems*, vol. 61, no. 3, pp. 6083–6097, 2025. DOI: `10.1109/TAES.2025.3526900`

[39] S. Lewis and M. Inggs, "Synchronization of coherent netted radar using white rabbit compared with one-way multichannel gpsdos," *IEEE Transactions on Aerospace and Electronic Systems*, vol. 57, no. 3, pp. 1413–1422, 2021. DOI: `10.1109/TAES.2020.3043530`

[40] Y. Cai, J. Zhang, Y. Sun, F. Yang, X. Jiang, C. Zi, C. He, and S. Cui, "The novel transmission scheme with CAT Ethernet cable and SFP for White Rabbit," *Radiation Detection Technology and Methods*, vol. 5, no. 2, pp. 290–296, Jun. 2021, ISSN: 2509-9949. DOI: `10.1007/s41605-021-00247-8`

[41] P. J. Beasley, N. Peters, C. Horne, and M. A. Ritchie, "Global Navigation Satellite Systems disciplined oscillator synchronisation of multistatic radar," *IET Radar, Sonar & Navigation*, vol. 18, no. 1, pp. 23–40, 2024. DOI: `https://doi.org/10.1049/rsn2.12475` eprint: `https://ietresearch.onlinelibrary.wiley.com/doi/pdf/10.1049/rsn2.12475`.

[42] J. Sandenbergh and M. Inggs, "Synchronizing network radar using all-in-view GPS-disciplined oscillators," in *2017 IEEE Radar Conference (RadarConf)*, 2017, pp. 1640–1645. DOI: `10.1109/RADAR.2017.7944470`

[43] S. Preussler, F. Schwartau, J. Schoebel, and T. Schneider, "Photonically synchronized large aperture radar for autonomous driving," *Opt. Express*, vol. 27, no. 2, pp. 1199–1207, Jan. 2019. DOI: `10.1364/OE.27.001199`

[44] F. Falconi, S. Melo, F. Scotti, M. N. Malik, M. Scaffardi, C. Porzi, L. Ansalone, P. Ghelfi, and A. Bogoni, "A Combined Radar & Lidar System Based on Integrated Photonics in Silicon-on-Insulator," *Journal of Lightwave Technology*, vol. 39, no. 1, pp. 17–23, 2021. DOI: `10.1109/JLT.2020.3023496`

[45] S. Li, Z. Cui, X. Ye, J. Feng, Y. Yang, Z. He, R. Cong, D. Zhu, F. Zhang, and S. Pan, "Chip-Based Microwave-Photonic Radar for High-Resolution Imaging," *Laser & Photonics Reviews*, vol. 14, no. 10, p. 1 900 239, 2020. DOI: `https://doi.org/10.1002/lpor.201900239`

[46] S. Melo, F. Falconi, P. Ghelfi, F. Scotti, C. Porzi, and A. Bogoni, "A Silicon Integrated Photonics-based Radar Operating in Multiple Bands," in *2020 International Topical Meeting on Microwave Photonics (MWP)*, 2020, pp. 47–49. DOI: `10.23919/MWP48676.2020.9314602`

[47] J. Li, S. Yang, H. Chen, X. Wang, M. Chen, and W. Zou, "Fully integrated hybrid microwave photonic receiver," *Photon. Res.*, vol. 10, no. 6, pp. 1472–1483, Jun. 2022. DOI: `10.1364/PRJ.452631`

[48] A. W. Mohammad, C. G. Roeloffzen, P. W. van Dijk, L. Wevers, P. Ghelfi, M. Reza, T. Otto, H. Mohammadhoseini, R. Heuvink, F. Sahin, and E. Klein, "Design, Fabrication, and Characterization of a Hybrid Integrated Photonic Module for a Synthetic Aperture Radar Receiver," *Journal of Lightwave Technology*, vol. 42, no. 2, pp. 760–770, 2024.

[49] S. Kruse, S. Gudyriev, T. Schwabe, P. Kneuper, H. G. Kurz, and J. C. Scheytt, "Silicon Photonic Radar Transmitter IC for mm-Wave Large Aperture MIMO Radar Using Optical Clock Distribution," *IEEE Microwave and Wireless Components Letters*, vol. 31, no. 6, pp. 783–786, 2021. DOI: `10.1109/LMWC.2021.3062112`

[50] S. Kruse, S. Gudyriev, P. Kneuper, T. Schwabe, M.-M. Meinecke, H. G. Kurz, and J. C. Scheytt, "Silicon Photonic Radar Receiver IC for mm-Wave Large Aperture MIMO Radar Using Optical Clock Distribution," *IEEE Microwave and Wireless Components Letters*, vol. 32, no. 12, pp. 1447–1450, 2022. DOI: `10.1109/LMWC.2022.3186432`

[51] S. Kruse, J. C. Greitens, T. Schwabe, P. Kneuper, M.-M. Meinecke, H. G. Kurz, and J. C. Scheytt, "A Narrowband Four-Quadrant Electro-Optical Mixer for Microwave Photonics," *IEEE Microwave and Wireless Technology Letters*, vol. 33, no. 11, pp. 1552–1555, 2023. DOI: `10.1109/LMWT.2023.3315315`

[52] S. Kruse, M. Bahmanian, P. Kneuper, C. Kress, H. G. Kurz, T. Schneider, and J. C. Scheytt, "Phase Noise Investigation for a Radar System with Optical Clock Distribution," in *2020 17th European Radar Conference (EuRAD)*, 2021, pp. 26–29. DOI: `10.1109/EuRAD48048.2021.00018`

[53] S. Kruse, J. C. Scheytt, and H. G. Kurz, "An Area Efficient 19.25 GHz to 77 GHz Gilbert Cell Frequency Quadrupler with 55% Shrinked Delay Lines in 130nm SiGe BiCMOS," in *2019 IEEE MTT-S International Microwave and RF Conference (IMARC)*, 2019, pp. 1–5. DOI: `10.1109/IMaRC45935.2019.9118726`

[54] S. Kruse, P. Kneuper, T. Schwabe, M.-M. Meinecke, H. G. Kurz, and J. C. Scheytt, "Distributed System Architecture for Software-Defined Radio / Radar with Optical Signal Distribution," in *2023 24th International Radar Symposium (IRS)*, 2023, pp. 1–8. DOI: `10.23919/IRS57608.2023.10172470`

[55] S. Kruse, M.-M. Meinecke, P. Kneuper, T. Schwabe, H. G. Kurz, and J. C. Scheytt, "Analysis and Simulation of a Coherent FMCW Lidar-Photonic Radar Combined Sensor System for Large Aperture Phased Array MIMO," in *2023 20th European Radar Conference (EuRAD)*, 2023, pp. 419–422. DOI: `10.23919/EuRAD58043.2023.10289439`

[56] S. Kruse, C. Kress, H. G. Kurz, T. Schneider, and J. C. Scheytt, "Analysis and Simulation of a Wireless Phased Array System with Optical Carrier Distribution and an Optical IQ Return Path," in *2020 German Microwave Conference (GeMiC)*, 2020, pp. 140–143.

[57] S. Kruse, T. Schwabe, P. Kneuper, M.-M. Meinecke, H. G. Kurz, and J. Christoph Scheytt, "Nonlinear S-Parameter Behavioral Model of a Photonic Radar Transceiver Chipset for Automotive Applications," in *2023 24th International Radar Symposium (IRS)*, 2023, pp. 1–10. DOI: `10.23919/IRS57608.2023.10172395`

[58] S. Kruse, M. Bahmanian, S. F. Fard, M.-M. Meinecke, H. G. Kurz, and J. C. Scheytt, “A Low Phase Noise 77 GHz Frequency Synthesizer for Long Range Radar,” in *2022 19th European Radar Conference (EuRAD)*, 2022, pp. 289–292. DOI: `10.23919/EuRAD54643.2022.9924677`

[59] S. Kruse, J. Brockmeier, P. Kneuper, T. Schwabe, H. G. Kurz, M.-M. Meinecke, and J. C. Scheytt, “Doppler Analysis of a Lidar-Photonic Radar Combined Sensor System,” in *2024 International Radar Symposium (IRS)*, 2024, pp. 70–73.

[60] S. Kruse, T. Schwabe, P. Kneuper, H. G. Kurz, M.-M. Meinecke, and J. C. Scheytt, “Analysis and Simulation of a Photonic Multiband FMCW Radar Sensor System Using Nyquist Pulses,” in *2024 15th German Microwave Conference (GeMiC)*, 2024, pp. 201–204. DOI: `10.23919/GeMiC59120.2024.10485320`

[61] S. Kruse, P. Kneuper, T. Schwabe, H. G. Kurz, M.-M. Meinecke, M. A. Gonzalez-Huici, and J. C. Scheytt, “Phase Noise Analysis of Photonic Radar Systems with Optical LO Distribution,” in *ICMIM 2024; 7th IEEE MTT Conference*, 2024, pp. 57–60.

[62] C. Greiff, D. Mateos-Núñez, R. Simoni, M. González-Huici, S. Kruse, J. C. Scheytt, K. Kolk, C. Höller, H. G. Kurz, M.-M. Meinecke, and T. Gisder, “Calibration of Large Coherent MIMO Radar Arrays: Channel Imbalances and 3D Antenna Positions,” in *2023 24th International Radar Symposium (IRS)*, 2023, pp. 1–10. DOI: `10.23919/IRS57608.2023.10172475`

[63] M.-M. Meinecke, T. Gisder, R. Simoni, M. A. González-Huici, C. Greiff, D. Mateos-Nunez, A. Danklmayer, S. Kruse, J. Ladan, and H. G. Kurz, “Antennenvorrichtung zum Aussenden von elektromagnetischer Strahlung für ein Kraftfahrzeug sowie Kraftfahrzeug,” DE102023208400A1, 2023.

[64] H. G. Kurz, M.-M. Meinecke, T. Schwabe, S. Kruse, and C. Scheytt, “Mehrband-Sensorsystem zur Umfelderfassung, sowie Verfahren und Kraftfahrzeug,” DE102023204354A1, 2023.

[65] M.-M. Meinecke, H. G. Kurz, T. Gisder, S. Kruse, and C. Scheytt, “Verfahren zum Erzeugen eines frequenzmodulierten Sendesignals für eine Sendeeinrichtung, Computerprogrammprodukt, computerlesbares Speichermedium, Sendeeinrichtung sowie Detektionsvorrichtung,” DE102023205100A1, 2023.

[66] S. KRUSE and J. C. SCHEYTT, “ELEKTROOPTISCHER MISCHER,” EP000004457561A1, 2023.

[67] S. KRUSE and J. C. SCHEYTT, “System mit optischer Trägerverteilung,” DE102020202771A1, 2020.

[68] S. KRUSE and J. C. SCHEYTT, “Elektrooptischer Regelkreis,” DE102020207050A1, 2020.

[69] S. KRUSE and J. C. SCHEYTT, “Elektrooptischer Mischer,” DE102020213283A1, 2020.

[70] S. KRUSE and J. C. SCHEYTT, “Elektrooptischer Mischer,” DE102022201070B4, 2023.

[71] M.-M. Meinecke, H. G. Kurz, C. Scheytt, and S. Kruse, “Verfahren zum Betreiben einer elektrooptischen Übertragungsvorrichtung für beliebige Signale, Computerprogrammprodukt sowie Datenübertragungsvorrichtung,” DE102022201312B4, 2022.

[72] S. Kruse, C. Scheytt, M.-M. Meinecke, and H. G. Kurz, “Funk-Optisches Sensorsystem für die Umfelderfassung,” DE102022212165A1, 2022.

[73] S. KRUSE and J. C. SCHEYTT, "Optoelektronischer Oszillator und Anordnung mehrerer elektrooptischer Wandlereinheiten weiterhin aufweisendend einen solchen optoelektronischen Oszillator," DE102022214163B4, 2022.

[74] M.-M. Meinecke, A. Aal, H. Kurz, S. Kruse, and C. Scheytt, "Radarsystem mit CMOS-Elektronikkomponenten," DE102023200606A1, 2023.

[75] S. KRUSE and J. C. SCHEYTT, "Elektrooptische PLL," DE102023203698B4, 2023.

[76] H. G. Kurz, M.-M. Meinecke, T. Schwabe, S. Kruse, and C. Scheytt, "Mehrband-Software-Defined-Radio-System zur Umfelderfassung, sowie Verfahren und Kraftfahrzeug," DE102023204352B4, 2023.

[77] J. Svarny and S. Chladek, "Model-Based Bias Controller for a Mach-Zehnder Intensity Modulator," *Journal of Lightwave Technology*, vol. 40, no. 3, pp. 720–727, 2022. DOI: `10.1109/JLT.2021.3122460`

[78] M. Schwengelbeck, "Design and Implementation of a Bias-Point Controller for Discrete and Integrated Mach-Zehnder Modulators Using a ESP-32-Microcontroller Board," M.S. thesis, Paderborn University, 2023.

[79] L. Chrostowski and M. Hochberg, *Silicon Photonics Design: From Devices to Systems*. Cambridge University Press, 2015.

[80] B. Razavi, *Design of Integrated Circuits for Optical Communications*. John Wiley & Sons, 2012, ISBN: 978-1-118-33694-6.

[81] I. N. Bronstein, K. A. Semendjajew, G. Grosche, and V. Ziegler, *Taschenbuch der Mathematik*. Nauka, Moskau & BSB B.G. Teubner Verlagsgesellschaft, Leipzig, 1979.

[82] A. Aubry, A. D. Maio, V. Carotenuto, and A. Farina, "Radar Phase Noise Modeling and Effects-Part I : MTI Filters," *IEEE Transactions on Aerospace and Electronic Systems*, vol. 52, no. 2, pp. 698–711, 2016. DOI: `10.1109/TAES.2015.140549`

[83] J. Beas, G. Castanon, I. Aldaya, A. Aragon-Zavala, and G. Campuzano, "Millimeter-Wave Frequency Radio over Fiber Systems: A Survey," *IEEE Communications Surveys & Tutorials*, vol. 15, no. 4, pp. 1593–1619, 2013. DOI: `10.1109/SURV.2013.013013.00135`

[84] F. Timofeev, S. Bennett, R. Griffin, P. Bayvel, A. Seeds, R. Wyatt, R. Kashyap, and M. Robertson, "High spectral purity millimetre-wave modulated optical signal generation using fibre grating lasers," in *1998 IEEE MTT-S International Microwave Symposium Digest (Cat. No.98CH36192)*, vol. 3, 1998, 1221–1224 vol.3. DOI: `10.1109/MWSYM.1998.700594`

[85] J. Pan, "21 GHz wideband fiber optic link," in *1988., IEEE MTT-S International Microwave Symposium Digest*, 1988, pp. 977–978. DOI: `10.1109/MWSYM.1988.22194`

[86] P. Hartmann, X. Qian, A. Wonfor, R. Penty, and I. White, "1-20 GHz Directly Modulated Radio over MMF Link," in *2005 International Topical Meeting on Microwave Photonics*, 2005, pp. 95–98. DOI: `10.1109/MWP.2005.203548`

[87] K. Siddiq, R. J. Watson, S. R. Pennock, P. Avery, R. Poulton, and B. Dakin-Norris, "Phase noise analysis in FMCW radar systems," in *2015 European Radar Conference (EuRAD)*, 2015, pp. 501–504. DOI: `10.1109/EuRAD.2015.7346347`

[88] K. Siddiq, M. K. Hobden, S. R. Pennock, and R. J. Watson, "Phase Noise in FMCW Radar Systems," *IEEE Transactions on Aerospace and Electronic Systems*, vol. 55, no. 1, pp. 70–81, 2019. DOI: `10.1109/TAES.2018.2847999`

[89] J. Taylor, S. Datta, A. Hati, C. Nelson, F. Quinlan, A. Joshi, and S. Diddams, "Characterization of Power-to-Phase Conversion in High-Speed P-I-N Photodiodes," *IEEE Photonics Journal*, vol. 3, no. 1, pp. 140–151, 2011. DOI: `10.1109/JPHOT.2011.2109703`

[90] D. Leeson, "A simple model of feedback oscillator noise spectrum," *Proceedings of the IEEE*, vol. 54, no. 2, pp. 329–330, 1966. DOI: `10.1109/PROC.1966.4682`

[91] L. Kang and B. H. Kolner, "Characterization of AM-to-PM Conversion in Silicon p-i-n Photodiodes," *IEEE Photonics Technology Letters*, vol. 31, no. 13, pp. 1001–1004, 2019. DOI: `10.1109/LPT.2019.2914607`

[92] K. Siddiq, R. J. Watson, S. R. Pennock, P. Avery, R. Poulton, and S. Martins, "Analysis of sampling clock phase noise in homodyne FMCW radar systems," in *2016 IEEE Radar Conference (RadarConf)*, 2016, pp. 1–4. DOI: `10.1109/RADAR.2016.7485302`

[93] N. Da Dalt, M. Harteneck, C. Sandner, and A. Wiesbauer, "On the jitter requirements of the sampling clock for analog-to-digital converters," *IEEE Transactions on Circuits and Systems I: Fundamental Theory and Applications*, vol. 49, no. 9, pp. 1354–1360, 2002. DOI: `10.1109/TCSI.2002.802353`

[94] T. N. Guo, "Unique Measurement and Modeling of Total Phase Noise in RF Receiver," *IEEE Transactions on Circuits and Systems II: Express Briefs*, vol. 60, no. 5, pp. 262–266, 2013. DOI: `10.1109/TCSII.2013.2251966`

[95] I. Fatadin, D. Ives, and M. Wicks, "Numerical simulation of intensity and phase noise from extracted parameters for CW DFB lasers," *IEEE Journal of Quantum Electronics*, vol. 42, no. 9, pp. 934–941, 2006. DOI: `10.1109/JQE.2006.880117`

[96] P. Martin, F. Gays, E. Grellier, A. Myko, and S. Menezo, "Modeling of silicon photonics devices with Verilog-A," in *2014 29th International Conference on Microelectronics Proceedings - MIEL 2014*, 2014, pp. 209–212. DOI: `10.1109/MIEL.2014.6842123`

[97] S. Kruse, J. C. Scheytt, T. Schwabe, and P. Kneuper, *Extended Material: Analysis and Simulation of a Wireless Phased Array System with Optical Carrier Distribution and an Optical IQ Return Path*, Zenodo, Oct. 2025. DOI: `10.5281/zenodo.17430874.`

[98] S. Yuan and H. Schumacher, "90–140 GHz frequency octupler in Si/SiGe BiCMOS using a novel bootstrapped doubler topology," in *2014 9th European Microwave Integrated Circuit Conference*, 2014, pp. 158–161. DOI: `10.1109/EuMIC.2014.6997816`

[99] S. S. Kruse, J. C. Scheytt, T. Schwabe, and P. Kneuper, *Extended Material: Nonlinear S-Parameter Behavioral Model of a Photonic Radar Transceiver Chipset for Automotive Applications*, Zenodo, Oct. 2025. DOI: `doi:10.5281/zenodo.17424081.`

[100] C. Kress, T. Schwabe, H. Rhee, and J. Christoph Scheytt, "Compact, High-Speed Mach-Zehnder Modulator With On-Chip Linear Drivers in Photonic BiCMOS Technology," *IEEE Access*, vol. 12, pp. 64 561–64 570, 2024. DOI: `10.1109/ACCESS.2024.3396877`

[101] R. Yadav, P. K. Dahiya, and R. Mishra, "A high performance 76.5 GHz FMCW RADAR for advanced driving assistance system," in *2016 3rd International Conference on Signal Processing and Integrated Networks (SPIN)*, 2016, pp. 383–388. DOI: `10.1109/SPIN.2016.7566724`

[102] B. Razavi, *RF Microelectronics*. London, U.K.: Pearson Education, Sep. 22, 2011, 960 pp., ISBN: 0137134738.

[103] R. Frevert, J. Haase, R. Jancke, U. Knöchel, P. Schwarz, R. Kakerow, and M. Darianian, *Modeling and Simulation for RF System Design*. Springer New York, 2005.

[104] C. Rapp, "Effects of HPA-nonlinearity on a 4-DPSK/OFDM-signal for a digital sound broadcasting signal," in *ESA, Second European Conference on Satellite Communications (ECSC-2)*, 1991.

[105] A. Saleh, "Frequency-Independent and Frequency-Dependent Nonlinear Models of TWT Amplifiers," *IEEE Transactions on Communications*, vol. 29, no. 11, pp. 1715–1720, 1981. DOI: `10.1109/TCOM.1981.1094911`

[106] A. Ghorbani and M. Sheikhan, "The effect of solid state power amplifiers (sspas) nonlinearities on mpsk and m-qam signal transmission," in *1991 Sixth International Conference on Digital Processing of Signals in Communications*, 1991, pp. 193–197.

[107] M. Berroth, "Schaltkreissimulator for heterostrukturfeldeffekttransistoren," Ph.D. dissertation, Ruhr-Universität Bochum, 1991.

[108] J.-M. Lee, M. Kim, S. Lischke, L. Zimmernman, S.-H. Cho, and W.-Y. Choi, "Photodetection frequency response characterization for high-speed Ge-PD on Si with an equivalent circuit," in *2016 21st OptoElectronics and Communications Conference (OECC) held jointly with 2016 International Conference on Photonics in Switching (PS)*, 2016, pp. 1–3.

[109] T. Fukazawa, T. Hirano, F. Ohno, and T. Baba, "Low Loss Intersection of Si Photonic Wire Waveguides," *Japanese Journal of Applied Physics*, vol. 43, no. 2R, p. 646, Feb. 2004. DOI: `10.1143/JJAP.43.646`

[110] D. M. Pozar, *Microwave engineering*. Hoboken, NJ: Wiley, 2012.

[111] R. Berenguer, G. Liu, and Y. Xu, "A Low Power 77 GHz Low Noise Amplifier With an Area Efficient RF-ESD Protection in 65 nm CMOS," *IEEE Microwave and Wireless Components Letters*, vol. 20, no. 12, pp. 678–680, 2010. DOI: `10.1109/LMWC.2010.2087015`

[112] K. Ogawa, *Integrated Silicon-based Optical Modulators: 100 Gb/s and Beyond*. SPIE, 2019.

[113] S. Voinigescu, *High-Frequency Integrated Circuits*. Cambridge University Press, 2013.

[114] W. Bakalski, W. Simburger, H. Knapp, H.-D. Wohlmuth, and A. Scholtz, "Lumped and distributed lattice-type LC-baluns," in *2002 IEEE MTT-S International Microwave Symposium Digest (Cat. No.02CH37278)*, vol. 1, 2002, 209–212 vol.1. DOI: `10.1109/MWSYM.2002.1011595`

[115] S. Gudyriev, J. C. Scheytt, L. Yan, C. Meuer, and L. Zimmermann, "Fully-differential, DC-coupled, self-biased, monolithically-integrated optical receiver in 0.25um photonic BiCMOS Technology for multi-channel fiber links," in *2017 IEEE Bipolar/BiCMOS Circuits and Technology Meeting (BCTM)*, 2017, pp. 110–113. DOI: `10.1109/BCTM.2017.8112922`

[116] A. Ramaswamy, M. Piels, N. Nunoya, T. Yin, and J. E. Bowers, "High Power Silicon-Germanium Photodiodes for Microwave Photonic Applications," *IEEE Transactions on Microwave Theory and Techniques*, vol. 58, no. 11, pp. 3336–3343, 2010. DOI: `10.1109/TMTT.2010.2076630`

[117] Z. Li, Y. Shi, M. Zou, Y. Yu, and X. Zhang, "Ultrahigh-power germanium photodetector enabling amplifier-free wireless communication," *Laser & Photonics Reviews*, vol. 19, no. 5, p. 2 401 469, 2025. DOI: `https://doi.org/10.1002/lpor.202401469`

[118] D. A. Tulchinsky, J. B. Boos, D. Park, P. G. Goetz, W. S. Rabinovich, and K. J. Williams, "High-Current Photodetectors as Efficient, Linear, and High-Power RF Output Stages," *Journal of Lightwave Technology*, vol. 26, no. 4, pp. 408–416, 2008. DOI: `10.1109/JLT.2007.912503`

[119] L. Virot, L. Vivien, J.-M. Fédéli, Y. Bogumilowicz, J.-M. Hartmann, F. Bœuf, P. Crozat, D. Marris-Morini, and E. Cassan, "High-performance waveguide-integrated germanium PIN photodiodes for optical communication applications," *Photon. Res.*, vol. 1, no. 3, pp. 140–147, Oct. 2013. DOI: `10.1364/PRJ.1.000140`

[120] R. Dehghani and S. Atarodi, "A new low voltage precision CMOS current reference with no external components," *IEEE Transactions on Circuits and Systems II: Analog and Digital Signal Processing*, vol. 50, no. 12, pp. 928–932, 2003. DOI: `10.1109/TCSII.2003.820239`

[121] S. Gudyriev, C. Kress, H. Zwickel, J. N. Kemal, S. Lischke, L. Zimmermann, C. Koos, and J. C. Scheytt, "Coherent ePIC Receiver for 64 GBaud QPSK in 0.25 um Photonic BiCMOS Technology," *Journal of Lightwave Technology*, vol. 37, no. 1, pp. 103–109, 2019. DOI: `10.1109/JLT.2018.2881107`

[122] S. Kueppers, K. Aufinger, and N. Pohl, "A fully differential 100 – 140 GHz frequency quadrupler in a 130 nm SiGe:C technology for MIMO radar applications using the bootstrapped Gilbert-Cell doubler topology," in *2017 IEEE 17th Topical Meeting on Silicon Monolithic Integrated Circuits in RF Systems (SiRF)*, 2017, pp. 37–39. DOI: `10.1109/SIRF.2017.7874364`

[123] T. Hancock, I. Gresham, and G. Rebeiz, "A differential sub-nanosecond high-isolation absorptive active SiGe 24 GHz switch for UWB applications," in *2004 IEE Radio Frequency Integrated Circuits (RFIC) Systems. Digest of Papers*, 2004, pp. 497–500. DOI: `10.1109/RFIC.2004.1320665`

[124] I. Haroun, C. Plett, Y.-C. Hsu, and D.-C. Chang, "Compact 60-GHz IPD-Based Branch-Line Coupler for System-on-Package V-Band Radios," *IEEE Transactions on Components, Packaging and Manufacturing Technology*, vol. 2, no. 7, pp. 1070–1074, 2012. DOI: `10.1109/TCPMT.2012.2186450`

[125] T. Cheung and J. Long, "Shielded passive devices for silicon-based monolithic microwave and millimeter-wave integrated circuits," *IEEE Journal of Solid-State Circuits*, vol. 41, no. 5, pp. 1183–1200, 2006. DOI: `10.1109/JSSC.2006.872737`

[126] Y. Sun, G. G. Fischer, and J. C. Scheytt, "A Compact Linear 60-GHz PA With 29.2% PAE Operating at Weak Avalanche Area in SiGe," *IEEE Transactions on Microwave Theory and Techniques*, vol. 60, no. 8, pp. 2581–2589, 2012. DOI: `10.1109/TMTT.2012.2202684`

[127] S. Joo, T.-Y. Choi, and B. Jung, "A 2.4-GHz Resistive Feedback LNA in 0.13-$\mu$m CMOS," *IEEE Journal of Solid-State Circuits*, vol. 44, no. 11, pp. 3019–3029, 2009. DOI: `10.1109/JSSC.2009.2031912`

[128] N. Sarmah, P. R. Vazquez, J. Grzyb, W. Foerster, B. Heinemann, and U. R. Pfeiffer, "A wideband fully integrated SiGe chipset for high data rate communication at 240 GHz," in *2016 11th European Microwave Integrated Circuits Conference (EuMIC)*, 2016, pp. 181–184. DOI: `10.1109/EuMIC.2016.7777520`

[129] N. Sarmah, J. Grzyb, K. Statnikov, S. Malz, P. Rodriguez Vazquez, W. Föerster, B. Heinemann, and U. R. Pfeiffer, "A Fully Integrated 240-GHz Direct-Conversion Quadrature Transmitter and Receiver Chipset in SiGe Technology," *IEEE Transactions on Microwave Theory and Techniques*, vol. 64, no. 2, pp. 562–574, 2016. DOI: `10.1109/TMTT.2015.2504930`

[130] B. Dehlink, H.-d. Wohlmuth, K. Aufinger, F. Weiss, and A. L. Scholtz, "An 80 GHz SiGe Quadrature Receiver Frontend," in *2006 IEEE Compound Semiconductor Integrated Circuit Symposium*, 2006, pp. 197–200. DOI: `10.1109/CSICS.2006.319962`

[131] J. Zhang, J. Yu, X. Li, K. Wang, W. Zhou, J. Xiao, L. Zhao, X. Pan, B. Liu, and X. Xin, "200 Gbit/s/$\lambda$ PDM-PAM-4 PON system based on intensity modulation and coherent detection," *Journal of Optical Communications and Networking*, vol. 12, no. 1, A1–A8, 2020. DOI: `10.1364/JOCN.12.0000A1`

[132] K. Kikuchi, "Fundamentals of Coherent Optical Fiber Communications," *Journal of Lightwave Technology*, vol. 34, no. 1, pp. 157–179, 2016. DOI: `10.1109/JLT.2015.2463719`

[133] S. Dahiya and Asha, "Performance analysis of millimeter wave-based radio over fiber system for next generation networks," *Journal of Optics*, vol. 53, no. 3, pp. 2174–2182, Jul. 2024, ISSN: 0974-6900. DOI: `10.1007/s12596-023-01472-8`

[134] C. Kress, "Modellierung und Entwurf eines monolitisch-integrierten kohärenten Empfängers für 56GBaud in 0.25um Photonic-BiCMOS," M.S. thesis, Paderborn University, 2017.

[135] M. A. Soto, M. Alem, M. Amin Shoaie, A. Vedadi, C.-S. Brès, L. Thévenaz, and T. Schneider, "Optical sinc-shaped Nyquist pulses of exceptional quality," *Nature Communications*, vol. 4, no. 1, p. 2898, Dec. 2013, ISSN: 2041-1723. DOI: `10.1038/ncomms3898`

[136] S. De, A. Misra, R. Das, T. Kleine-Ostmann, and T. Schneider, "Analysis of Non-Idealities in the Generation of Reconfigurable Sinc-Shaped Optical Nyquist Pulses," *IEEE Access*, vol. 9, pp. 76 286–76 295, 2021. DOI: `10.1109/ACCESS.2021.3082847`

[137] M. T. T. Eugene Knott John F. Schaeffer, *Radar Cross Section*. Artech House Publishers, 1992.

[138] G. Kervella, J. Maxin, M. Faugeron, P. Berger, H. Lanctuit, G. Pillet, L. Morvan, F. van Dijk, and D. Dolfi, "Laser sources for microwave to millimeter-wave applications," *Photon. Res.*, vol. 2, no. 4, B70–B79, Aug. 2014. DOI: `10.1364/PRJ.2.000B70`

[139] J. Sun, E. Timurdogan, A. Yaacobi, Z. Su, E. S. Hosseini, D. B. Cole, and M. R. Watts, "Large-Scale Silicon Photonic Circuits for Optical Phased Arrays," *IEEE Journal of Selected Topics in Quantum Electronics*, vol. 20, no. 4, pp. 264–278, 2014. DOI: `10.1109/JSTQE.2013.2293316`

[140] Z. Hongping, L. Quanbo, C. Dapeng, C. Wenliang, and S. Fei, "Doppler Shift and Height Detection of Obstacle Based on FMCW Radar Sensor," in *2015 International Conference on Cyber-Enabled Distributed Computing and Knowledge Discovery*, 2015, pp. 399–402. DOI: `10.1109/CyberC.2015.64`

[141] D. Göhring, M. Wang, M. Schnürmacher, and T. Ganjineh, "Radar/lidar sensor fusion for car-following on highways," in *The 5th International Conference on Automation, Robotics and Applications*, 2011, pp. 407–412. DOI: `10.1109/ICARA.2011.6144918`

[142] M. Bahmanian and J. C. Scheytt, "A 2–20-GHz Ultralow Phase Noise Signal Source Using a Microwave Oscillator Locked to a Mode-Locked Laser," *IEEE Transactions on Microwave Theory and Techniques*, vol. 69, no. 3, pp. 1635–1645, 2021. DOI: `10.1109/TMTT.2020.3047647`

[143] H. Rucker, B. Heinemann, W. Winkler, R. Barth, J. Borngraber, J. Drews, G. G. Fischer, A. Fox, T. Grabolla, U. Haak, D. Knoll, F. Korndorfer, A. Mai, S. Marschmeyer, P. Schley, D. Schmidt, J. Schmidt, K. Schulz, B. Tillack, D. Wolansky, and Y. Yamamoto, "A 0.13um SiGe BiCMOS technology featuring fT/fmax of 240/330 GHz and gate delays below 3 ps," in *2009 IEEE Bipolar/BiCMOS Circuits and Technology Meeting*, 2009, pp. 166–169. DOI: `10.1109/BIPOL.2009.5314251`

[144] E. Rubiola and R. Boudot, "The effect of AM noise on correlation phase-noise measurements," *IEEE Transactions on Ultrasonics, Ferroelectrics, and Frequency Control*, vol. 54, no. 5, pp. 926–932, 2007. DOI: `10.1109/TUFFC.2007.338`

[145] S. Kruse, T. Schwabe, P. Kneuper, and J. C. Scheytt, *Extended Material: Distributed System Architecture for Software-Defined Radio / Radar with Optical Signal Distribution*, Zenodo, Oct. 2025. DOI: `10.5281/zenodo.17431271`

[146] S. Kruse, T. Schwabe, P. Kneuper, and J. C. Scheytt, *Extended Material: Analysis and Simulation of a Photonic Multiband FMCW Radar Sensor System Using Nyquist Pulses*, Zenodo, Oct. 2025. DOI: `10.5281/zenodo.17431867.`

[147] S. Kruse, P. Kneuper, T. Schwabe, and J. C. Scheytt, *Extended Material: Analysis and Simulation of a Coherent FMCW Lidar-Photonic Radar Combined Sensor System for Large Aperture Phased Array MIMO*, Zenodo, Oct. 2025. DOI: `10.5281/zenodo.17432016.`

# Das Heinz Nixdorf Institut – Interdisziplinäres Forschungszentrum für Informatik und Technik

Das Heinz Nixdorf Institut ist ein Forschungszentrum der Universität Paderborn. Es entstand 1987 aus der Initiative und mit Förderung von Heinz Nixdorf. Damit wollte er Ingenieurwissenschaften und Informatik zusammenführen, um wesentliche Impulse für neue Produkte und Dienstleistungen zu erzeugen. Dies schließt auch die Wechselwirkungen mit dem gesellschaftlichen Umfeld ein.

Die Forschungsarbeit orientiert sich an dem Programm „Dynamik, Vernetzung, Autonomie: Neue Methoden und Technologien für die intelligenten technischen Systeme von morgen“. In der Lehre engagiert sich das Heinz Nixdorf Institut in Studiengängen der Informatik, der Ingenieurwissenschaften und der Wirtschaftswissenschaften.

Heute wirken am Heinz Nixdorf Institut acht Professoren/in mit insgesamt 120 Mitarbeiterinnen und Mitarbeitern. Pro Jahr promovieren hier etwa 15 Nachwuchswissenschaftlerinnen und Nachwuchswissenschaftler.

# Heinz Nixdorf Institute – Interdisciplinary Research Centre for Computer Science and Technology

The Heinz Nixdorf Institute is a research centre within the University of Paderborn. It was founded in 1987 initiated and supported by Heinz Nixdorf. By doing so he wanted to create a symbiosis of computer science and engineering in order to provide critical impetus for new products and services. This includes interactions with the social environment

Our research is aligned with the program "Dynamics, Networking, Autonomy: New methods and technologies for intelligent technical systems of tomorrow". In training and education the Heinz Nixdorf Institute is involved in many programs of study at the University of Paderborn. The superior goal in education and training is to communicate competencies that are critical in tomorrows economy.

Today eight Professors and 120 researchers work at the Heinz Nixdorf Institute. Per year approximately 15 young researchers receive a doctorate.

## Zuletzt erschienene Bände der Verlagsschriftenreihe des Heinz Nixdorf Instituts

Bd. 410 Rüddenklau, N.: *Hardware-in-the-Loop-Simulation von HD-Scheinwerfer-Steuergeräten zur Entwicklung von Lichtfunktionen in virtuellen Nachtfahrten*, Dissertation. Fakultät für Maschinenbau, Universität Paderborn: Verlagsschriftenreihe des Heinz Nixdorf Instituts, Paderborn, 2023, Band 410, ISBN: 978-3-947647-29-3

Bd. 411 Biemelt, P.: *Entwurf und Analyse modellprädiktiver Regelungsansätze zur Steigerung des Immersionsempfindens in interaktiven Fahrsimulationen*, Dissertation. Fakultät für Maschinenbau, Universität Paderborn: Verlagsschriftenreihe des Heinz Nixdorf Instituts, Paderborn, 2023, Band 411, ISBN: 978-3-947647-30-9

Bd. 412 Haake, C.-J., Meyer auf der Heide, F., Platzner, M., Wachsmuth, H. und Wehrheim, H.: *On-The-Fly Computing: Individualized IT-services in dynamic markets: Collaborative Research Centre 901 (2011 - 2023)*. Verlagsschriftenreihe des Heinz Nixdorf Instituts, Paderborn, 2023, Band 412, ISBN: 978-3-947647-31-6

Bd. 413 Dumitrescu, R. und Hölzle, K.: *Vorausschau und Technologieplanung: 17. Symposium für Vorausschau und Technologieplanung, 14. und 15. September 2023, Berlin*. Berlin-Brandenburgische Akademie der Wissenschaften, Berlin: Verlagsschriftenreihe des Heinz Nixdorf Instituts, Paderborn, 2023, Band 413, ISBN: 978-3-947647-32-3

Bd. 414 Abughannam, S.: *Low-power Direct-detection Wake-up Receiver at 2.44 GHz for Wireless Sensor Networks*, Dissertation. Fakultät für Elektrotechnik, Informatik und Mathematik, Universität Paderborn: Verlagsschriftenreihe des Heinz Nixdorf Instituts, Paderborn, 2023, Band 414, ISBN: 978-3-947647-33-0

Bd. 415 Reinhold, J.: *Systematik zur musterbasierten Transformation von Wertschöpfungssystemen für Smart Services*, Dissertation. Fakultät für Maschinenbau, Universität Paderborn: Verlagsschriftenreihe des Heinz Nixdorf Instituts, Paderborn, 2023, Band 415, ISBN: 978-3-947647-34-7

Bd. 416 Yang, X.: *Eine Methode zur Unterstützung von Entscheidungen bei der Entwicklung modularer Leichtbauprodukte*, Dissertation. Fakultät für Maschinenbau, Universität Paderborn: Verlagsschriftenreihe des Heinz Nixdorf Instituts, Paderborn, 2023, Band 416, ISBN: 978-3-947647-35-4

Bd. 417 Gräler, M.: *Entwicklung adaptiver Einrichtassistenzsysteme für Produktionsprozesse*, Dissertation. Fakultät für Maschinenbau, Universität Paderborn: Verlagsschriftenreihe des Heinz Nixdorf Instituts, Paderborn, 2023, Band 417, ISBN: 978-3-947647-36-1

Bd. 418 Rösmann, D.: *Menschenzentrierte Montageplanung und -steuerung durch fähigkeitsorientierte Aufgabenzuordnung*, Dissertation. Fakultät für Maschinenbau, Universität Paderborn: Verlagsschriftenreihe des Heinz Nixdorf Instituts, Paderborn, 2024, Band 418, ISBN: 978-3-947647-37-8

Bd. 419 BAHMANIAN, M.: *Optoelectronic Phase-Locked Loop, Theory and Implementation*, Dissertation. Fakultät für Elektrotechnik, Informatik und Mathematik, Universität Paderborn: Verlagsschriftenreihe des Heinz Nixdorf Instituts, Paderborn, 2024, Band 419, ISBN: 978-3-947647-38-5

Bd. 420 HEIHOFF-SCHWEDE, J.: *Spezifikationstechnik zur Analyse, Gestaltung und Bewertung von Engineering-IT-Architekturen*, Dissertation. Fakultät für Elektrotechnik, Informatik und Mathematik, Universität Paderborn: Verlagsschriftenreihe des Heinz Nixdorf Instituts, Paderborn, 2024, Band 420, ISBN: 978-3-947647-39-2

Bd. 421 MEYER, M.: *Systematik zur Planung und Verwertung von Betriebsdaten-Analysen in der strategischen Produktplanung*, Dissertation. Fakultät für Elektrotechnik, Informatik und Mathematik, Universität Paderborn: Verlagsschriftenreihe des Heinz Nixdorf Instituts, Paderborn, 2024, Band 421, ISBN: 978-3-947647-40-8

---

Bezugsadresse:
Heinz Nixdorf Institut
Universität Paderborn
Fürstenallee 11
33102 Paderborn

## Zuletzt erschienene Bände der Verlagsschriftenreihe des Heinz Nixdorf Instituts

Bd. 422 MALENA, K.: *Konzipierung, Analyse und Realumsetzung eines mehrstufigen modellprädiktiven Lichtsignalanlagenregelungssystems*, Dissertation. Fakultät für Maschinenbau, Universität Paderborn: Verlagsschriftenreihe des Heinz Nixdorf Instituts, Paderborn, 2024, Band 422, ISBN: 978-3-947647-41-5

Bd. 423 GÖTTE, R.-S.: *Online-Schätzung von Modellungenauigkeiten zur automatischen Modelladaption unter Beibehaltung einer physikalisch-technischen Interpretierbarkeit*, Dissertation. Fakultät für Maschinenbau, Universität Paderborn: Verlagsschriftenreihe des Heinz Nixdorf Instituts, Paderborn, 2024, Band 423, ISBN: 978-3-947647-42-2

Bd. 424 PIERENKEMPER, C.: *Systematik zur Entwicklung Leistungsstufen-basierter Industrie 4.0-Strategien*, Dissertation. Fakultät für Elektrotechnik, Informatik und Mathematik, Universität Paderborn: Verlagsschriftenreihe des Heinz Nixdorf Instituts, Paderborn, 2024, Band 424, ISBN: 978-3-947647-43-9

Bd. 425 DUMITRESCU, R. und HÖLZLE, K.: *Vorausschau und Technologieplanung*. 18. Symposium für Vorausschau und Technologieplanung, Heinz Nixdorf Institut, 5./6. Dezember 2024, Berlin-Brandenburgische Akademie der Wissenschaften, Berlin, Verlagsschriftenreihe des Heinz Nixdorf Instituts, Paderborn, 2024, Band 425, ISBN: 978-3-947647-44-6

Bd. 426 HESSE, M.: *Interaktive Inbetriebnahme von Steuerungen und Regelungen für partiell bekannte dynamische Systeme mittels Gauß-Prozess-Regression*, Dissertation. Fakultät für Maschinenbau, Universität Paderborn: Verlagsschriftenreihe des Heinz Nixdorf Instituts, Paderborn, 2024, Band 426, ISBN: 978-3-947647-45-3

Bd. 427 PREUß, D.: *Methodik zur automatisierten Extrahierung, Formalisierung und Handhabung von Änderungen technischer Anforderungen*, Dissertation. Fakultät für Maschinenbau, Universität Paderborn: Verlagsschriftenreihe des Heinz Nixdorf Instituts, Paderborn, 2024, Band 427, ISBN: 978-3-947647-46-0

Bd. 428 JUNKER, A.: *Datengetriebene Modellbildung für nicht lineare mechatronische Systeme in regelungstechnisch verwertbarer Form*, Dissertation. Fakultät für Maschinenbau, Universität Paderborn: Verlagsschriftenreihe des Heinz Nixdorf Instituts, Paderborn, 2024, Band 428, ISBN: 978-3-947647-47-7

Bd. 429 THIELE, H.: *Technologievorausschau auf Basis mathematischer Modellierung*, Dissertation. Fakultät für Maschinenbau, Universität Paderborn: Verlagsschriftenreihe des Heinz Nixdorf Instituts, Paderborn, 2025, Band 429, ISBN: 978-3-947647-48-4

Bd. 430 TIMMERMANN, J., JUNKER, A., GÖTTE, R. S., HESSE, M. und SCHWARZER, L.: *DART - Datengetriebene Methoden in der Regelungstechnik*. Fakultät für Maschinenbau, Universität Paderborn: Verlagsschriftenreihe des Heinz Nixdorf Instituts, Paderborn, 2025, Band 430, ISBN: 978-3-947647-49-1

Bd. 431 DUMITRESCU, R. und HÖLZLE, K.: *Vorausschau und Technologieplanung*. 19. Symposium für Vorausschau und Technologieplanung, Heinz Nixdorf Institut, 23./24. Oktober 2025, Berlin-Brandenburgische Akademie der Wissenschaften, Berlin: Verlagsschriftenreihe des Heinz Nixdorf Instituts, Paderborn, 2025, Band 431, ISBN: 978-3-947647-50-7

Bd. 432 WIECHEL, D.: *Modellbasierte Wirkkettenanalyse zur Bewertung technischer Änderungen*, Dissertation. Fakultät für Maschinenbau, Universität Paderborn: Verlagsschriftenreihe des Heinz Nixdorf Instituts, Paderborn, 2025, Band 432, ISBN: 978-3-947647-51-4

Bd. 433 WELLER, J. L.: *Spezifikationstechnik für Prescriptive Analytics Lösungen in der Produktion*, Dissertation. Fakultät für Elektrotechnik, Informatik und Mathematik, Universität Paderborn: Verlagsschriftenreihe des Heinz Nixdorf Instituts, Paderborn, 2026, Band 433, ISBN: 978-3-947647-52-1

---

Bezugsadresse:
Heinz Nixdorf Institut
Universität Paderborn
Fürstenallee 11
33102 Paderborn

The angular resolution of a phased array antenna is inversely proportional to it's aperture size. The high electrical losses limit the aperture size of modern all-electric radar systems to a few cm. This poses a significant problem for a variety of applications, especially for high resolution radar systems. In this doctoral thesis, various novel photonic radar systems are presented and mathematically analyzed. Furthermore, the different systems are simulated in the optical design environment Lumerical Interconnect. Since all other photonic radar architectures presented are based on the FMCW MIMO radar system with optical LO distribution and optical return path, this system is also simulated in the electrical design environment ADS. After a successful analysis, novel circuit topologies for the different photonic radar systems will be presented, including an novel optoelectronic mixer. Subsequently, the first transceiver chipset of a photonic radar system with optical LO distribution will be presented. A demonstrator based on this chipset, with an aperture size of 50 cm, achieves an angular resolution of 0.4°, which is close to the theoretically possible limit of 0.3°. The appendix of this work also presents two 77 GHz frequency synthesizers with extremely low phase noise – one with an optical output, the other with an electrical output. In addition, the appendix contains further mathematical considerations.